Multiscale mechanical investigations of the human anulus fibrosus

Diana Pham

BSc, BEng (Biomed, Hons)

Thesis submitted in total fulfilment
of the requirements for the degree of
Doctor of Philosophy
in Biomedical Engineering

The Medical Device Research Institute (MDRI)
School of Computer Science, Engineering and Mathematics
Flinders University, South Australia

October 2015

Contents

List of Figures

List of Tables

Abbreviations

A	anterior
AF	anulus fibrosus
AFM	atomic force microscope
AL	anterolateral
ANOVA	analysis of variance
E	Young's Modulus of Elasticity
E_T	toe modulus
L	lateral
MRI	magnetic resonance imaging
NP	nucleus pulposus
PG	proteoglycan
P	posterior
PL	posterolateral
PBS	phosphate-buffered saline
VB	vertebral body
VE	vertebral endplate
ϵ_M	extensibility
ϕ	phase shift

Abstract

Low-back pain is a commonly reported musculoskeletal disorder, with one possible cause being intervertebral disc degeneration. Presently, this disease is incurable, whilst the available treatments are not always effective and aim to alleviate the symptomatic pain instead of targeting the root cause. A more solid understanding of the mechanisms underlying disc degeneration could potentially lead to the development of more effective treatments.

One region that notably contributes to the disc's loading response is the anulus fibrosus (AF), which lies on the periphery of the disc, and consists of fibrous, collagen-type-I-rich layers, or lamellae. Previous studies have investigated the mechanical properties of multiple and single lamella sections of the AF. It has been observed that disc degeneration does not significantly affect the mechanical behaviour of multiple or single lamellae, though lamellae in the anterior region tend to have higher Young's Moduli. Moreover, an increased strain rate correlates with an increased Young's Modulus and lower hysteresis.

To provide a more comprehensive, multiscale analysis of the disc, and clarify the effect that disc degeneration might have upon the different components within the disc, it would be pertinent to investigate its mechanical properties at lower hierarchical levels, such as the microscale and nanoscale. These are the two main foci of this research.

The microscale study investigated the collagen type I bundles which constitute the AF lamellae. Individual fibre bundles were extracted from healthy and degenerate human outer AF in four different anatomical regions: posterolateral, lateral, anterolateral and anterior. Each sample was tensile tested under hydrated conditions and subjected to slow (0.1%/s), medium (1%/s) and fast (10%/s) strain rates. Four mechanical parameters were measured: toe modulus, Young's Modulus of Elasticity, extensibility and phase shift. It was found that disc degeneration and anatomical

region had no significant effect on these parameters, though increased strain rate produced higher Young's Moduli and lower phase shifts. The phase shifts of the fibre bundles were also smaller in magnitude than those at the lamella level.

The nanoscale study investigated collagen type I fibrils extracted from the fibre bundles used in the microscale study. Young's Modulus was indirectly derived by nanoindenting the fibrils in ambient conditions using an atomic force microscope. Due to limitations with nanoindentation, no other parameters were considered at the nanoscale. As in the microscale study, it was found that disc degeneration and anatomical region had no significant effect upon the Young's Moduli of the fibrils.

The results from these two studies indicate that disc degeneration did not affect the microscale nor nanoscale of the AF. Moreover, the regional inconsistencies observed at the lamella level were not evident at the fibre bundle or fibril level, suggesting that the properties of the disc become more uniform when more homogeneous structures are considered, and that their intra-lamellar arrangement could influence the overall mechanical properties of the lamellae. Finally, the smaller phase shifts at the microscale demonstrate that the fibre bundles exhibited more elastic behaviours than the lamellae.

This research was constrained by relatively small sample sizes and limitations in the testing apparatus; thus, the results need to be interpreted with caution. Nonetheless, this body of work may provide a precedent for future investigations into AF mechanics at the microscale and nanoscale, two hierarchical levels that were previously unexplored.

Declaration

I certify that this thesis does not incorporate without acknowledgement any material previously submitted for a degree or diploma in any university; and that to the best of my knowledge and belief, it does not contain any material previously published or written by another person except where due reference is made in the text.

Diana Pham

Acknowledgements

The Greek philosopher Socrates famously remarked that the only true wisdom is in knowing you know nothing. Oh, how these words echo my own sentiments at this very moment. I've come to realise that PhDs really are a tiny, tiny speck in the vast universe of human knowledge. And knowing nothing takes a great deal of effort.

Dr John Costi is one of those truly dedicated researchers who genuinely loves what he does and gets super excited when you show him an interesting graph. I'd like to thank him for being such a caring supervisor and friend, and for giving me many valuable opportunities to develop my research skills over the years. I feel honoured to be his first PhD student, and I am tremendously grateful for his guidance, generosity and infectious enthusiasm.

A massive thanks goes to Prof Joe Shapter, one of the most cool-headed professors I've ever met. On many occasions he managed to put things into perspective for me, and taught me a lot about being an effective communicator. I also thank him enormously for opening up the doorway to working in science education. Special thanks go to Prof Karen Reynolds and Emeritus Prof Trevor Hearn, who are like the Research Gods all the biomeds kind of worship. I'd also like to thank the academics in the School of CSEM, who had a hugely positive influence on me during my undergrad and postgrad years; and my Science21 colleagues, who cheered me on from the sidelines.

Along the pathway to nothingness, I enlisted the help of a number of people who so generously offered their time and expertise. Richard Stanley gave me much-needed help in the biomechanics lab, even when he was short on time and had more important things to do! I learned a lot from him, and our lab conversations made cutting up cadavers that little bit more bearable. Meanwhile, Dr Chris Gibson was a huge help in the AFM lab and was always willing to offer his expert advice. I'd also like to acknowledge Dr Sharon Byers for her help with collagen extraction, and

Pawel Skuza, our go-to stats specialist.

Flinders University was, well, my second home for a long time, and made infinitely more enjoyable thanks to my wonderful research buddies: Bryant Roberts, Fabian Lim, Melissa Ryan, Tony Carlisle, Emily Anderson, Laura Diment, Roshida Ab. Lazid, Brianna Martin, Kelly Knight and David Hobbs. I will be forever grateful for our office/lab/hallway conversations, Lucky Lupita lunches, and all-important PhD whinge sessions. A big shout-out goes to Aaron Mohtar for offering me valuable help and advice when I ran into technical/LaTeX/life issues! It's good to know I have my goat farm in Nepal to turn to if this science thing doesn't work out.

My beloved best friends and I make up a rather peculiar group. It's chiefly made up of psychologists and engineers - with a few writers, teachers and mime artists thrown into the mix - and many of us chose to endure the cruelties of the PhD, making us all quite specialised in our little fields. Maybe that's why our team got the wooden spoon prize at that quiz night long ago. Anyway, the completion of this PhD certainly wouldn't have been achievable without them. Life-saving therapy in the form of coffee debriefs, silly dancing, Fringe, WOMAD, picnics and croquet was administered regularly under the direction of Drs. Rachel 'DJ' Stephens and Anastasia 'Nasty' Ejova: the remaining arms of the Nightclub Trio (although now it's probably more like the Tea and Boardgames Trio). They have been by my side the whole time, provided much-needed distraction when the sky was a little grey, and continue to inspire me with their tremendous academic successes. Resident wise owl, Cheryl Goult always managed to recharge our souls with her kind words, Pulitzer-grade stories and delectable dinner parties. And, of course, the wonderful company of Suzie Cosh, Kim Pfitzner, Ertimiss Eshkevari, Sarah Williams, Christian Baker, Fernando Marmolejo-Ramos, Daniel Oates, Paul Campbell and little sister Maria Ejova made the postgraduate chapter of my life a truly memorable one. I must also thank my dear friends Silvana Niutta, Prema Thavaneswaran, Nyla Sarwar, Yuko Morita and Julie Woerner for their endless support, even from afar.

With immeasurable love and gratitude, I would like to finally acknowledge my family, without whom my achievements to date would not have been possible. My mother Suong, father Thanh and sister Clarabelle are the very essence of me, and taught me that anything is achievable, even if you have very little to begin with. Their unwavering support and dedication is both humbling and empowering, and

I feel incredibly fortunate to have them in my life. My heartfelt thanks also goes to my wonderful brother-in-law Guo-Rong and godmother Patricia Huxtable, who make up our little extended family. I thank them all for the countless times they had to sit there and nod as I bored them with the finer details of collagen stretching; for providing me with dinner when thesis mode prevented me from being a functioning member of society; and for teaching me the value of hard work and perseverance.

I dedicate this thesis to my mother, whose patience, selflessness and infinite wisdom helped me conquer the PhD mountain. Thanks, Mum. The view is quite nice from here.

Conference Papers

Invited Speaker

Pham DT, Shapter JG and Costi JJ. Multiscale mechanical investigations of the human anulus fibrosus. *Adelaide Centre for Spinal Research (ACSR), Symposium XI*. Mt Lofty, SA, Australia; 8-10 August 2013.

Pham DT, Shapter JG and Costi JJ. Micro-tensile testing of individual fibre bundles from healthy human anulus fibrosus. *Adelaide Centre for Spinal Research (ACSR), Symposium X*. Barossa Valley, SA, Australia; 2-4 August 2012.

Pham DT, Shapter JG and Costi JJ. Multiscale characterisation of collagen type I in the intervertebral disc. *Adelaide Biomechanics Seminars, UniSA*. Adelaide, SA, Australia; 13 April 2011.

Pham DT, Shapter JG and Costi JJ. Multiscale mechanical testing of collagen type I in the intervertebral disc. *Sixth Clare Valley Bone Meeting, PhD Student Session*. Clare Valley, SA, Australia; 26-30 March 2010.

Peer-Reviewed Conference Papers

Pham DT, Shapter JG and Costi JJ. Microtensile properties of individual fibre bundles in healthy and degenerate human anulus fibrosus [poster presentation]. *8th Combined Meeting of Orthopaedic Research Societies (CORS)*. Venice, Italy; 13-16 October 2013.

Pham DT, Shapter JG and Costi JJ. Viscoelastic properties of individual fibre bun-

dles in human anulus fibrosus [oral presentation]. *Australian and New Zealand Orthopaedic Research Society (ANZORS), 19th Annual Scientific Meeting.* Sydney, NSW, Australia; 4-5 September 2013.

Pham DT, Shapter JG and Costi JJ. Microtensile properties of individual fibre bundles in healthy and degenerate human anulus fibrosus [oral presentation]. *Spine Society of Australia (SSA), 24th Annual Scientific Meeting.* Perth, WA, Australia; 19-21 April 2013.

Pham DT, Shapter JG and Costi JJ. A novel nano-tensile testing technique for determining the Young's Modulus of collagen type I fibrils in the intervertebral disc [oral presentation]. *XXIII Congress of the International Society of Biomechanics (ISB).* Brussels, Belgium; 3-7 July 2011.

Other Presentations

Pham DT, Shapter JG and Costi JJ. Multiscale characterisation of collagen type I tensile material properties within the intervertebral disc [oral presentation]. *Scanning Probe Microscopy Workshop.* Adelaide, SA, Australia; 19 July 2010.

Three-Minute Thesis (3MT) Competition, Flinders University. First place prize for School level and Faculty level.

Journal Manuscripts in Preparation

Pham DT, Shapter JG and Costi JJ. Microtensile properties of collagen fibre bundles in the human anulus fibrosus. To be submitted to the *Journal of Biomechanics.*

Pham DT, Shapter JG and Costi JJ. A multiscale analysis of human anulus fibrosus mechanics. To be submitted to the *Journal of Biomechanics.*

Pham DT, Shapter JG and Costi JJ. The development of a novel nano-tensile testing technique using atomic force microscopy. To be submitted to *Nanoscience Methods.*

Part I

Introduction

Chapter 1

Background

1.1 The Anatomy of the Spine

1.1.1 Vertebral Column

The vertebral column forms the skeleton of the spine, and comprises approximately 30 bony segments called vertebrae (Figure 1.1). It can be divided into five anatomical regions: cervical (C1-C7), thoracic (T1-T12), lumbar (L1-L5), sacral (5 fused vertebrae, S1-S5), and coccygeal (3-5 fused vertebrae). Although the entire spinal column is important for trunk function, this research will have a particular focus on the lumbar region, as it tends to undergo the most degenerative change.

Each lumbar vertebra features three functional components: the vertebral body, posterior elements and pedicles (Figure 1.2). At the anterior end lies the vertebral body, whose flat, cylindrical shape maximises the contact area between the adjacent vertebrae, making it ideal for sustaining longitudinally applied loads [2]. The cross-hatched trabeculae, which constitute the internal structure of the vertebral body, act as struts and cross-beams that convert the load into vertical compression and transverse tension, making the vertebrae highly resilient to the compressive forces exerted upon the spine. Towards the caudal end of the spine, the body mass that needs to be supported increases. The lumbar spine needs to withstand the weight of the thorax as well as any load carried in the upper limbs [4]. To accommodate this load, lumbar vertebral bodies tend to be wider and thicker, which effectively gives them higher ultimate compressive strengths [5].

At the posterior end of the vertebra are the posterior elements, which lock to-

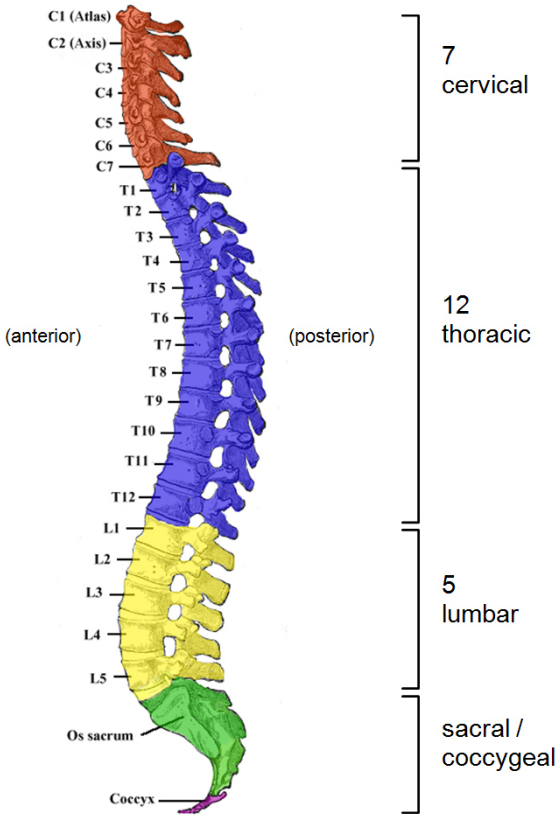

Figure 1.1: The human vertebral column. The five anatomical regions are cervical, thoracic, lumbar, sacral and coccygeal. (Modified from Gille (2006) [1].)

gether with adjacent posterior elements to form zygapophysial joints. These complex articulations resist forward sliding and transverse rotation of the vertebrae, whilst allowing flexion (11-13°), extension (3-5°) and lateral bending (10°) [2, 6].

Finally, the pedicles are two thick processes on the lateral sides of the vertebra that connect the vertebral body to the posterior elements, and form the sides of a canal called the vertebral foramen that surrounds and protects the entire length of the spinal cord.

1.1.2 Ligaments and Muscles

To help maintain spinal stability and prevent excessive motion that could be potentially damaging, the lumbar vertebrae are interconnected by a number of ligaments. These ligaments can be classified into three groups according to the anatomical regions that they connect; i.e. vertebral bodies, posterior elements and other regions (Figure 1.3). The vertebral bodies are connected by the anterior longitudinal liga-

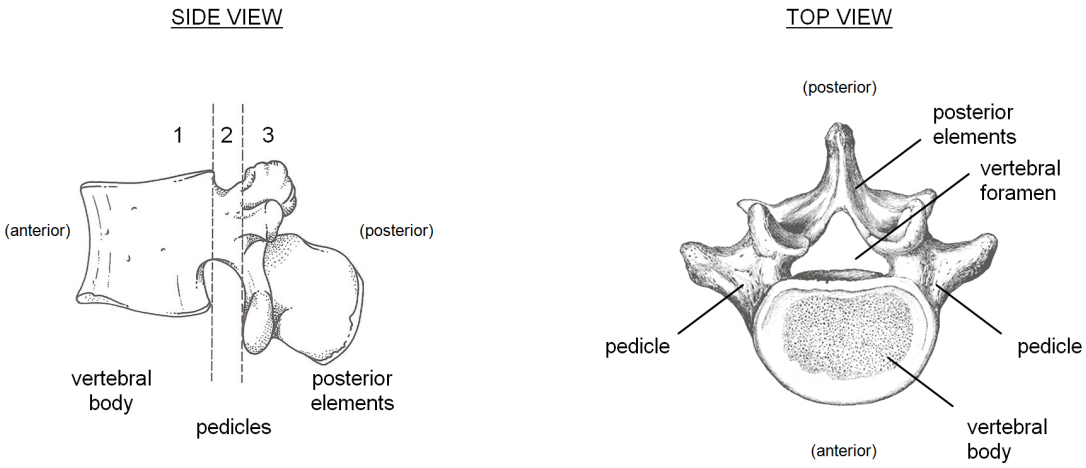

Figure 1.2: Three functional components of a lumbar vertebra, viewed from the side and top. (Modified from Bogduk (2002) [2] and Gray [3].)

ment and posterior longitudinal ligament; and posterior elements by the ligamentum flavum, interspinous ligaments and supraspinous ligament [2]. The remaining regions of the vertebra are connected by other ligaments, such as the iliolumbar ligaments that connect the lowest lumbar vertebra to the ilium.

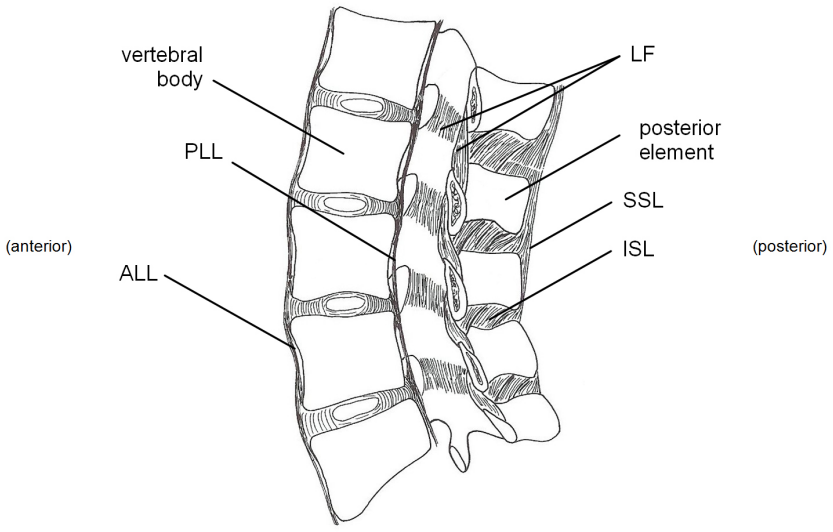

Figure 1.3: Ligaments connecting the vertebral bodies and posterior elements. ALL: anterior longitudinal ligament; PLL: posterior longitudinal ligament; LF: ligamentous flavum; ISL: interspinous ligaments; SSL: supraspinous ligament. (Modified from Bogduk (2002) [2].)

Our ability to bend the spine and lift objects is attributable to the numerous muscles that are inserted into various parts of the vertebral column. The muscles of the lumbar spine (Figure 1.4) can be categorised into three groups according to position and function:

1. *Psoas major*, which attaches to the anterolateral region of the vertebral bodies and is the primary flexor muscle of the hip joint;

2. *Quadratus lumborum* and *intertransversarii laterales*, which cover the anterior aspects of the transverse processes (part of the posterior elements) and act as lateral flexors;

3. *Lumbar back muscles*, which lie behind the posterior elements and all contribute to extension and rotation [2, 7].

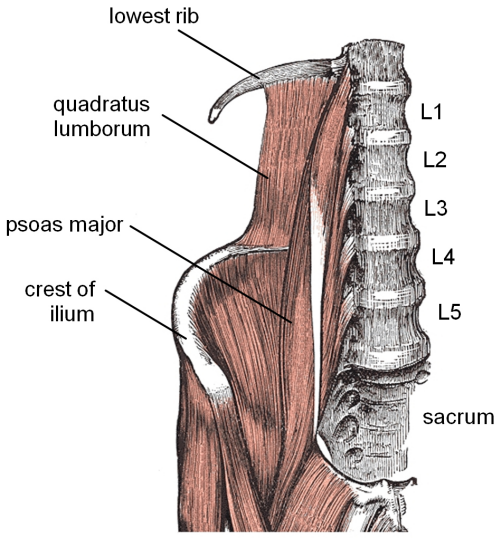

Figure 1.4: Psoas major and quadratus lumborum muscles of the lumbar spine (Modified from Gray (2008) [8].)

1.1.3 Intervertebral Discs

Finally, the intervertebral discs ('discs'), which are the focus of this research, are the avascular, multi-regional structures which are interposed between the vertebral bodies of C2 to S1 (Figure 1.5). Section 1.2 describes the functional role and structure of lumbar discs in detail.

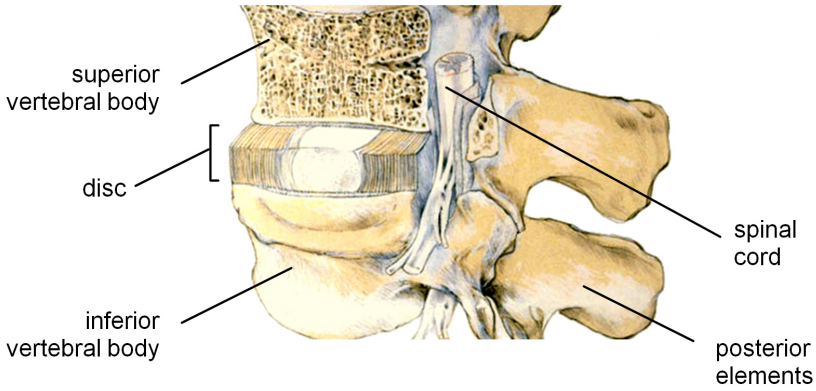

Figure 1.5: Location of the intervertebral disc in relation to superior and inferior vertebral bodies, spinal cord and posterior elements. (Modified from Urban (2003) [9].)

1.2 Lumbar Intervertebral Discs

1.2.1 Structure and Function

The lumbar disc has two main practical purposes [10]:

1. To provide a strong, flexible junction between the vertebral bodies of adjacent vertebrae;

2. To cushion and redistribute the longitudinal forces imparted on the spine.

Though its dimensions vary with each individual, the height and lateral diameter of the lumbar disc are usually around 12.5 and 45 mm, respectively [2]. It should be noted that this chapter describes lumbar discs only. Discs in the cervical and thoracic regions have slightly different morphologies because they have different mechanical demands [11, 12].

Two different anatomical regions comprise intervertebral discs: the nucleus pulposus and anulus fibrosus (Figure 1.6). Whilst their molecular compositions contain similar elements (see Table 1.1), both regions are distinct in their physical properties and mechanical behaviour. Optimal disc functionality is achieved when they work in conjunction with each other.

Nucleus Pulposus

The nucleus pulposus (NP), located at the centre of the disc, is a highly hydrated, incompressible gel [4]. Its major component is water, which, in healthy specimens,

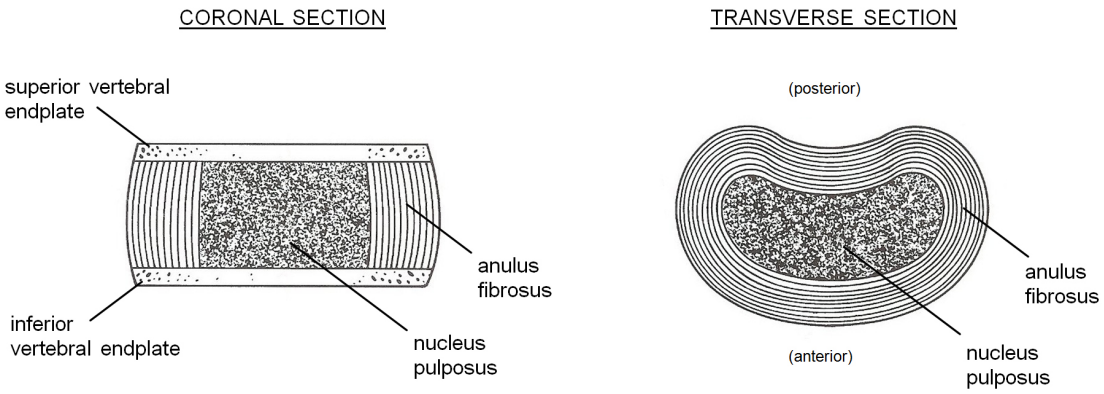

Figure 1.6: Coronal and transverse sections of the human intervertebral disc. (Modified from Bogduk (2002) [2].)

Table 1.1: Structural comparison of the nucleus pulposus and anulus fibrosus.

Description	**Nucleus pulposus**	**Anulus fibrosus**
Location	Inner region	Outer region
Structure	Highly hydrated semi-fluid mass with gel-like consistency	Concentric fibrous layers with alternating fibre orientation
Composition	Collagen (4%) - 15-20% dry weight - Primarily type II - Small amount of type I, III, IV, IX, XI Proteoglycans (14%) Water (70-90%) Elastic fibres Enzymes Non-collagenous proteins Chondrocyte-like cells	Collagen (50%) - 60-70% dry weight - Primarily type I - Small amount of type II, III, V, VI Proteoglycans (5%) Water (60-70%) Elastic fibres Enzymes Non-collagenous proteins Fibroblast cells

makes up 70-90% of its structure. Round-shaped cartilage cells called chondrocytes are responsible for synthesising the proteins that make up the nucleus matrix, chiefly proteoglycans and collagen [2].

Proteoglycans constitute 65% of the nucleus (dry weight), and exist as either freely dispersed units or aggregates composed of 8-10 units strung together. Proteoglycan units are composed of a core protein strand to which glycosaminoglycans (GAGs) are attached. The secondary forces between the core protein and GAGs give way to the proteoglycan's coiled structure (Figure 1.7). The negative charges on the sulphate groups in the GAGs attract and retain water molecules, demonstrating the integral role proteoglycans play in maintaining disc hydration [4].

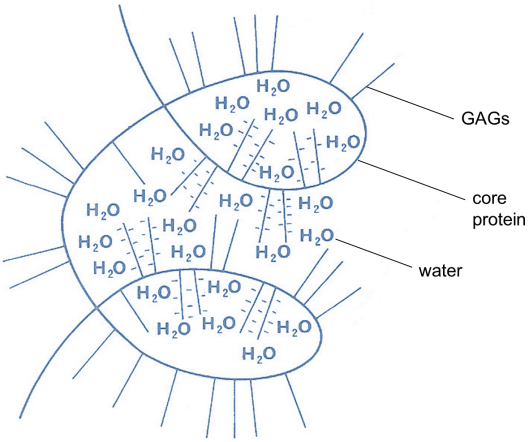

Figure 1.7: Proteoglycan interaction with water. (From Bogduk (2002) [2].)

The NP contains a high percentage of large, hydrophilic, space-filling proteoglycans, such as aggrecan, which help give the disc its hydrodynamic, weight-bearing properties [13].

The structure-reinforcing, fibrous protein collagen comprises up to four percent of the NP (20 percent dry weight). Though small amounts of collagen type I, III, VI, IX and XI are present, the primary subtype in the nucleus is collagen type II, which exists as spindly fibrils interspersed amongst the matrix, and helps hold the proteoglycan aggregates together. Due to its elastic nature, collagen type II is typically found in tissues that tend to be subjected to pressure-related processes [2], hence its prevalence in the nucleus pulposus.

The remainder of the matrix is composed of non-collagenous proteins, elastic fibres and proteolytic enzymes called matrix metalloproteinases, which play a key role in matrix degradation and renewal [2, 14].

Anulus Fibrosus

The anulus fibrosus (AF), which surrounds the nucleus pulposus, is typically made up of 10 to 20 concentric layers called lamellae that contain highly organised collagen fibre bundles (Figure 1.8) held together by a proteoglycan-rich matrix, or ground substance. Small proteoglycans, such as biglycan and decorin, are more prevalent in the AF, as they help with crosslinking the collagen fibrils, maintaining their arrangement [13, 15].

These collagen fibre bundles are arranged in an oblique, parallel pattern whose

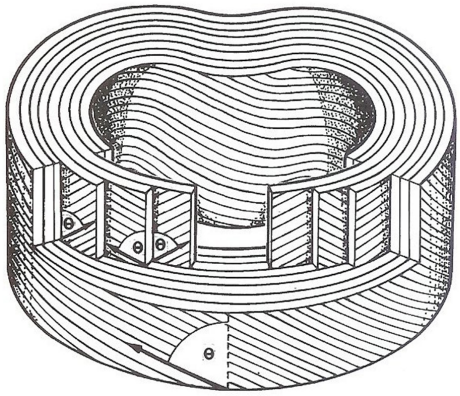

Figure 1.8: Layered structure of the anulus fibrosus. The 65-degree orientation of the fibre bundles, θ, alternates with each successive layer. (From Bogduk [2].)

65-degree orientation (relative to the vertical axis) alternates with each successive lamellae, making the AF extremely resilient to torsional motion [2, 16]. Note that whilst Figure 1.8 depicts distinct lamellae, around 40 percent of them will be incomplete; i.e. they will terminate without passing around the complete circumference of the disc.

A significant portion of the AF's composition is collagen type I, with small amounts of type II, III, V and VI also present. Collagen type I is the main focus of this research, and is discussed in detail in Section 1.3. As the AF progresses from the outer to inner region, the percentage of collagen type I diminishes and is replaced with collagen type II [17]. At the transition zone, where the AF and NP coalesce, the fibrous lamellar characteristics of the AF gradually transform into the gel-like properties of the NP. The lamellae also become significantly thicker with closer proximity to the nucleus [16].

Vertebral Endplate

A thin layer of hyaline cartilage called the vertebral endplate forms the interface between the discs and vertebral bodies. It is weakly bonded to the porous, cortical bone of the vertebral body and collagen fibres in the anulus and nucleus [2], and plays an important role in nutrient delivery [18]. Furthermore, the osmotic swelling pressure generated by the proteoglycans gives rise to the inward and outward movement of fluid, regulating the pressure within the disc [18].

1.2.2 Weight-Bearing

Intervertebral discs are constantly subjected to six-degree-of-freedom motion; i.e. horizontal, sagittal and coronal translations and rotations about each axis. When a compressive force is applied, the height of the nucleus is reduced, and due to its incompressible, semi-fluid-like disposition, it expands radially towards the surrounding anulus. The anulus resists this expansion by undergoing radial and circumferential tension and bulging. Since the nucleus is constrained in the radial and axial direction, it must exert pressure on the endplates, which effectively transmits the load onto the next (inferior) vertebra (Figure 1.9). Though the magnitude of the force remains the same, the rate at which the forces are transmitted from one vertebra to the next is attenuated due to the momentary diversion of energy used to stretch the anulus. By slowing down the rate of transmission, intervertebral discs are able to protect the underlying vertebrae, and it is for this reason that the spine as a whole is often compared to a shock absorber; i.e. a device that dissipates or converts kinetic energy into another form.

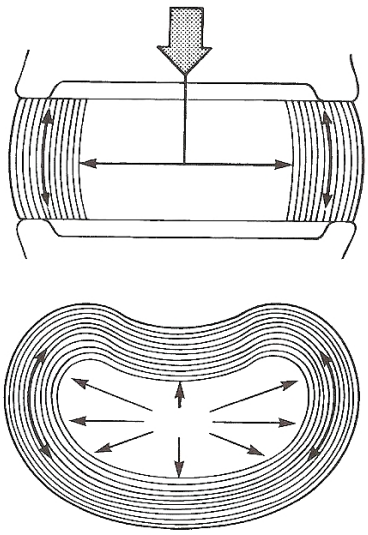

Figure 1.9: Weight transmission in the lumbar disc, as viewed from the side (top image) and top (bottom image). The compressive force causes the nucleus to expand radially and circumferentially, but is constrained by the anulus, which undergoes tension and bulging. As a result, the nucleus must exert pressure on the anulus, which transmits the load to the next vertebra. (From Bogduk (2002) [2].)

Being bi-phasic in structure (i.e. both solid and fluid), the disc's response to loading depends on a number of factors, including the deformational degree of freedom (e.g. compression, bending, torsion, shear), frequency at which the load is applied, and grade of degeneration. For example, Costi et al. (2008) [19] found that the disc became stiffer with increased frequency, particularly for deformation modes where fluid flow-dependent interactions were more prevalent (i.e. compression, lateral bending, flexion/extension).

1.3 Collagen Type I

1.3.1 Introduction

Collagen type I is the most prevalent protein in the anulus fibrosus, and is likely to be an important contributor to the disc's function as a whole. It is for this reason that collagen type I is of particular interest in this research.

Collagen, like other fibrous proteins, has a complex, hierarchical structure that spans from the molecular level to the aggregate level; thus, it has the ability to optimise its behaviour and mechanically adapt at every structural level [20]. It is the most abundant protein in the human body [21, 22], and is the main component of connective tissue, which includes skin, bone, cartilage, ligaments, tendons and intervertebral discs [23–25]. In humans, 28 types of collagen have been discovered [20], 11 of which are found in connective tissue alone [2]. The collagens are labelled as type I, II, III, etc. and are categorised according to their structure and function.

In the intervertebral disc, collagen type I constitutes up to 15 percent (50 percent dry weight) of the anulus fibrosus (Table 1.1). It is thought that collagen type I, shown to have viscoelastic properties and high tensile strength, forms the structural framework of the anulus, and is largely responsible for its highly resilient, tension-resisting properties [2, 26].

The structures that comprise each collagen hierarchy vary considerably in size, and can be ambiguous to define. As a result, nomenclature tends to be inconsistent between studies. For clarification, this paper will refer to four different hierarchical levels in collagen type I: *tropocollagen*, *microfibril*, *fibril* and *fibre* (Figure 1.10).

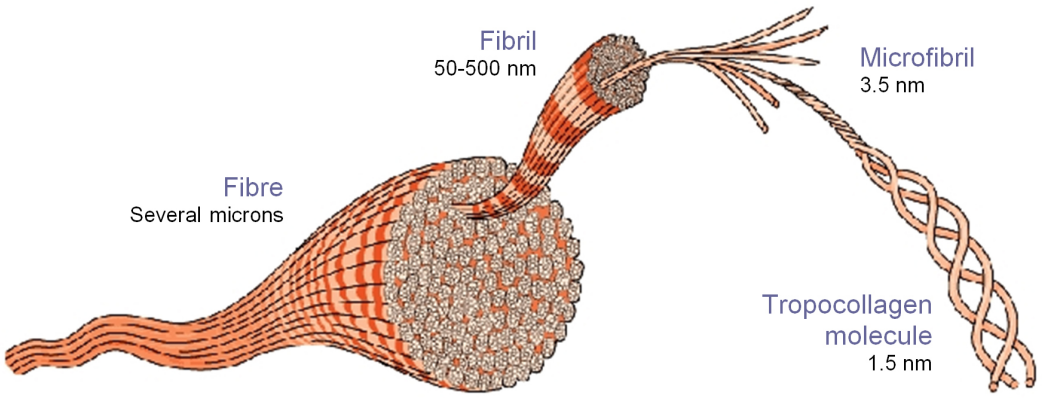

Figure 1.10: Hierarchical breakdown of collagen type I: tropocollagen molecule, microfibril, fibril and fibre. Their respective diameters are shown. (Modified from Mallery [27].)

1.3.2 Tropocollagen

At their most primitive level, all types of collagen take the form of tropocollagen molecules, consisting of three polypeptide monomer chains intertwined in a right-handed helical conformation, measuring approximately 300 nm in length.

Each one of these polypeptides, or *alpha chains*, is a string of amino acids. All alpha chains in collagen feature the amino acid triplet sequence *Gly-X-Y*, where *Gly* is glycine, and X and Y are other amino acids, though these are often proline and hydroxyproline, respectively [28]. There exist numerous kinds of alpha chains, distinguished by the types of amino acids that constitute X and Y, and each alpha chain consists of over 1000 amino acid residues.

Tropocollagen molecules in each collagen type are uniquely composed of different combinations of these alpha chains. Tropocollagen can be categorised as heterotrimeric, wherein two or three of its alpha chains are different, or homotrimeric, wherein all three chains are the same. Collagen type I is heterotrimeric, and is composed of two alpha-1 chains and one alpha-2 chain [25].

1.3.3 Microfibrils and Fibrils

At collagen's supramolecular structural level, tropocollagen molecules congregate to form what are known as microfibrils. Here, tropocollagen molecules run parallel with one another, five molecules abreast, and are longitudinally distributed in a quarter-

stagger array (i.e. overlap intervals are approximately one quarter of the molecule length). These form a microfibril 3.5 nm in diameter [29]. The three-dimensional arrangement of the tropocollagen molecules is not clearly understood, though it is has been postulated that they form a left-handed spiral due to electrostatic forces between the tropocollagen chains (Figure 1.11) [30, 31].

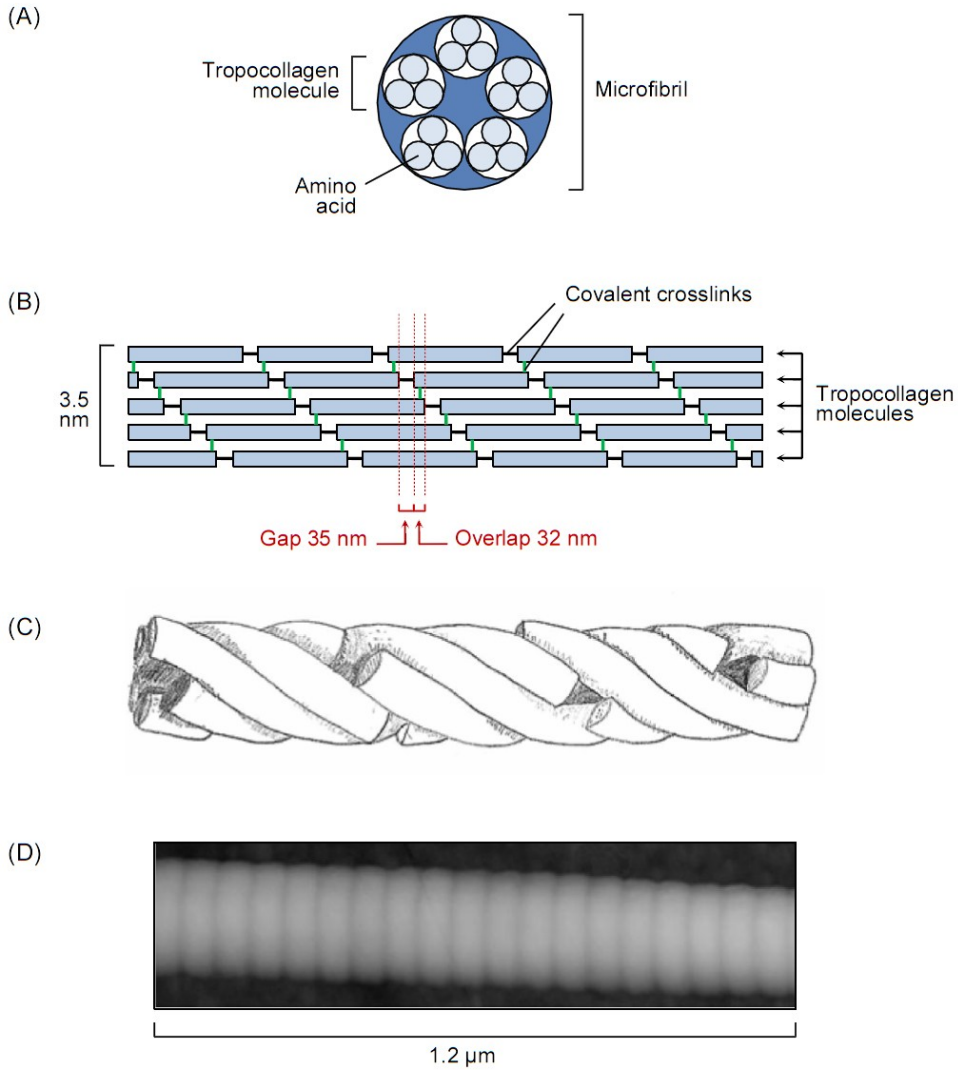

Figure 1.11: Collagen microfibril structure. (A) Cross-sectional view of microfibril, showing five parallel triple helices; (B) side view of quarter-stagger array of tropocollagen molecules held together side-by-side and end-to-end by covalent crosslinks (highlighted in green and black, respectively); (C) 3-D representation of the left-handed spiral arrangement of tropocollagen molecules; (D) atomic force microscope image of collagen microfibril. (Modified from van der Rijt (2006) [32] and Heim (2006) [33].)

This highly ordered arrangement of molecules is stabilised by various types of covalent crosslinks, such as pyridinoline and deoxypyridinoline [34–36]. The quarter-stagger array is a significant structural feature, as it gives rise to the 67 nm banding characteristic to all fibrous collagens. When viewed from the side, there appear to be 35 nm 'gap' regions and 32 nm 'overlap' regions. These correspond to the characteristic light and dark stripes, respectively (Figure 1.11).

Microfibrils aggregate laterally and longitudinally to form fibrils, much in the same way tropocollagen molecules bundle into microfibrils. Likewise, covalent crosslinks provide inter-microfibrillar stabilisation. Fibrillar diameter can range from 50 to 500 nm, depending upon the region where the collagen is located [20].

1.3.4 Fibres

The final hierarchical level of interest is the fibres, whose size and structural integrity is entirely dependent upon the size and length of the fibrils, and most importantly, the way that the fibrils are arranged and bound together by the inter-fibrillar matrix. The fibre level signifies the point at which collagen's morphology and mechanical properties diversify and become tissue-specific; i.e. sub-fibrillar structures are common between all collagenous tissues.

Collagen fibres can take a multitude of different forms, each with different mechanical properties. One collagen fibre may consist of fibrils oriented longitudinally, laterally and transversely, which impart isotropic or anisotropic characteristics. In the anulus fibrosus, the fibres take the form of long, fibrous ropes, in which the fibrils are interspersed with a proteoglycan-rich matrix. Small, leucine-rich repeat (LRR) proteoglycans, such as decorin and fibromodulin, form cross-bridges between the collagen fibrils to help stabilise the fibrillar network [37–39]. The fibres then band together side by side to form fibre bundles, which are the distinct feature of the anulus fibrosus lamellae (Figure 1.12).

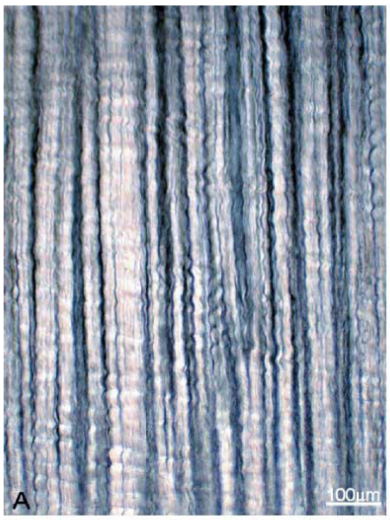

Figure 1.12: Differential intereference contrast (DIC) light microscopy image of collagen fibre bundles in the anulus fibrosus. (From Pezowicz et al. (2005) [40].)

1.4 Disc Degeneration

1.4.1 Characteristics

The structural features detailed in Section 1.2 describe a healthy lumbar intervertebral disc. The features of a degenerated intervertebral disc are quite distinct by comparison.

A recent review of the pathophysiology of disc degeneration by Hadjipavlou et al. (2008) [14] concluded that it can be characterised by a number of biochemical and microscopic features (Table 1.2).

Table 1.2: Biochemical and microscopic characteristics of disc degeneration, which become more prominent with increased severity. NP = nucleus pulposus; AF = anulus fibrosus; VE = vertebral endplate. (From Hadjipavlou (2008) [14].)

Features	**NP**	**AF**	**VE**
Biochemical	Fewer, less aggregated proteoglycans Lower pH (↑ acidity) Dehydration	Cross-linking of collagen fibrils	Fewer, less aggregated proteoglycans
Microscopic	Cracks Tears Fibrosis	Delamination Tears (peripheral, radial, circumferential) Fissures Thickening	Thickening Cracks Fractures

1.4.2 Association with Low-Back Pain

Between 2011 and 2012, over three million Australians experienced some form of back pain, making it the nation's second most commonly reported musculoskeletal disorder after arthritis [41]. Between 2008 and 2009, the direct cost of low back pain in Australia was estimated to be $1.2 billion, a figure that takes into account the costs of hospital admitted patient services, out-of-hospital medical services and prescription pharmaceuticals [42]. However, if all indirect costs were also considered, such as those associated with loss of earnings and productivity for the patients, relatives and employers, the figure could exceed $8 billion, demonstrating the enormous economic burden low back pain places upon society [43].

The question of whether a causal relationship exists between disc degeneration and low back pain remains unanswered. In order to determine whether the disc is the source of a patient's back pain, the physician may use discography, in which a radioactive contrast dye is injected into the nucleus of the disc. The purpose of the dye is two-fold: to infiltrate, and hence highlight, any structural defects in the disc (observed using CT), and provoke the sensation of pain, which the patient will then rate in terms of intensity [44]. The use of this procedure for investigating low back pain and disc degeneration is extensive in the literature, but the results are varied and inconsistent. For example, Luoma et al. (2000) [45] showed that for a group of 164 male subjects, the incidence of low back pain was greater in the presence of degenerative symptoms. Conversely, Jensen et al. (1994) [46] found that signs of degeneration were exhibited in a group of asymptotic subjects. The validity of discography as a diagnostic tool for low back pain is also questionable, as a number of factors, such as the patient's psychosocial profile, can increase the likelihood of false-positive results, suggesting that discography is only effective on certain patients, and should only be used after proper screening procedures have been performed [47]. Furthermore, the discograph itself has been shown to cause degeneration due to needle puncture, suggesting that the risks and benefits of this technique should be carefully considered before it is administered to patients [48].

Fagan et al. (2003) [49] found disc innervation to be meagre, and that the richest areas of innervation were the central endplate and perianular connective tissue on the outer edge of the anulus; no nerves were detected in the nucleus and inner anulus. Yet, despite this lack of innervation, the mere presence of nerves suggests that there

may be a link between intervertebral discs and low back pain, especially since pain sensitivity has been shown to be more significantly influenced by receptor threshold rather than density [49].

It is apparent that the origins of low-back pain are not fully understood and need to be investigated further, and whilst this is outside the scope of this study, an understanding of its relationship with disc degeneration could potentially change the way that low-back pain is diagnosed and treated.

1.4.3 Disc Structural Failure

Severe disc degeneration can lead to the development of other medical conditions, many of which are closely associated with discogenic pain. Some of these conditions are described in the following sections.

Disc Herniation

Disc herniation, or prolapse, can occur when the integrity of the anulus fibrosus is severely compromised due to radial fissures and/or endplate fractures [50]. The result is the extrusion of the nucleus pulposus into the area surrounding the anulus. This can lead to the compression and irritation of spinal nerves, which are associated with pain, numbness and muscle weakness [51]. The nucleus may even herniate through the fractures in the endplate causing a Schmorl's Node, in which the vertebral bone becomes inflamed and possibly necrotic [52].

Internal Disc Disruption

Severe fractures in the endplate cause it to deform more under load, effectively reducing the pressure in the nucleus and making it less effective at resisting compressive forces. So, as a compensatory mechanism, these applied forces must be resisted by the surrounding anulus and apophyseal joints, which can cause the innermost layers of the anulus to collapse into the nucleus [53]. This condition is referred to as internal disc disruption, and has been shown to be strongly associated with discogenic pain [4].

Disc Narrowing, Radial Bulging and Vertebral Osteophytes

Dehydration of the nucleus during degeneration reduces its height, and as a consequence, the anulus must bear a greater compressive load. Analyses of the disc under compressive loading show that degenerated discs tend to have higher stress concentrations in the outer anulus due to greater load-bearing responsibility [54]. In some circumstances, the inner and outer lamellae of the anulus buckle inwards and outwards respectively, forcing lamellae separation, or 'delamination', a condition that may lead to concentric anular tears [55]. The anulus' height collapses, reducing the separation between the posterior edges of the vertebral foramen (neural arches) of adjacent vertebrae. As the neural arches come in contact with one another, they become responsible for resisting over 50 percent of the compressive forces exerted upon the spine. A direct association has been found between severe disc narrowing and osteoarthritis, vertebral osteophytes (small, bony projections), and sclerosis of the vertebral endplates [52].

1.4.4 Diagnosis

Disc degeneration can be diagnosed in a clinical or experimental environment.

Clinical Diagnosis

The clinical diagnosis of disc degeneration in patients requires the use of medical imaging technology such as radiography, computed tomography (CT) or magnetic resonance imaging (MRI). The images produced by these diagnostic techniques highlight any degenerative changes, allowing the physician to determine the morphologic grade of the disc.

Today, MRI is widely used due to its high accuracy, short scanning time, good signal-to-noise ratio and minimal motion artefact [57]. In an MR image, degeneration is denoted by a decrease in signal intensity, reduced height and/or the presence of fissures [58]. Macroscopic anomalies, such as disc herniation, are also clearly distinguishable (Figure 1.13).

The degree of degeneration can then be deduced from the images using one of the various classification systems that have been developed to help standardise the diagnosis procedure. For example, Pfirrmann et al. (2001) [57] developed a five-

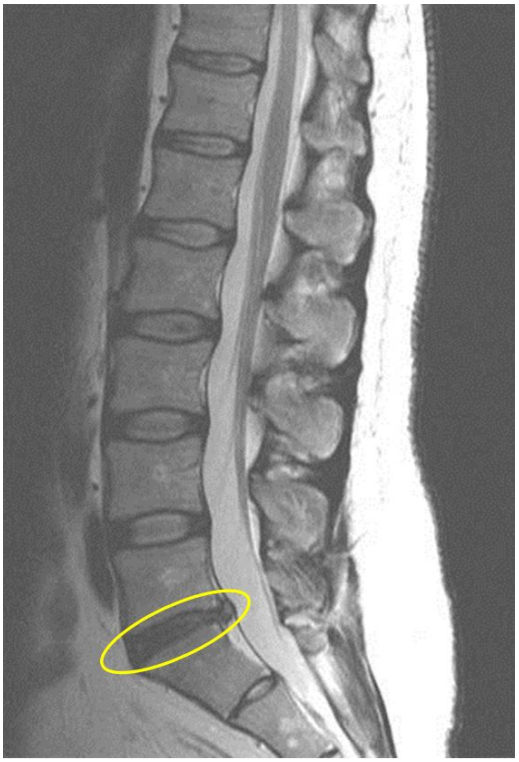

Figure 1.13: Mid-sagittal MR image of the lumbar spine with herniated disc. The herniated disc (circled) is much darker in appearance and has a posterior bulge. (From Wang (2009) [56].)

point scale that categorises discs according to the presence of structural features observed on MR images. According to this grading scheme, a disc is deemed to be more degenerated, and is therefore given a higher value on the scale, if the MR image contains certain visual features, such as a darker, inhomogeneous appearance, an unclear distinction between the nucleus and anulus, and a collapsed disc space (Table 1.3).

Standard MRI techniques can only be used for the *qualitative* characterisation of disc degeneration. However, a number of studies have also explored the use of MR imaging for *quantitative* assessments. Qualitative assessments are generally performed using T2-weighted MR imaging; however, Martin et al. (2015) [59] showed that quantitative information can be derived from population average T2 image maps taken pre- and post-injury. The pre-injury image acts as the control to which subsequent post-injury images are compared, allowing the degree of deviation to be measured. Similarly, Nguyen et al. (2008) [60] demonstrated that T1ρ-weighted MR imaging of the human NP had a positive linear correlation with swelling pressure and

proteoglycan content - two strong markers of disc degeneration. These quantitative assessment techniques are still being developed, though they hold much promise for future clinical diagnoses.

Table 1.3: The Pfirrmann Scale. This grading system was specifically designed to be used with clinical investigations using MRI. NP = nucleus pulposus; AF = anulus fibrosus. (From [57])

Grade	**Structure**	**NP and AF distinction**	**Signal intensity**	**Height of disc**
I	Homogeneous, bright white	Clear	Hyperintense, isointense to cerebrospinal fluid	Normal
II	Inhomogeneous with or without horizontal bands	Clear	Hyperintense, isointense to cerebrospinal fluid	Normal
III	Inhomogeneous, grey	Unclear	Intermediate	Normal to slightly decreased
IV	Inhomogeneous, grey to black	Lost	Intermediate to hypointense	Normal to moderately decreased
V	Inhomogeneous, black	Lost	Hypointense	Collapsed disc space

Experimental Diagnosis

Degeneration can be measured experimentally in cases where the disc has been removed, either due to a surgical procedure (e.g. spinal fusion; see Section 1.4.6) or post-mortem for research purposes. A number of grading schemes have been developed for interlaboratory examination, and are based upon transverse or sagittal sections using morphologic or radiographic methods [62, 63]. This research uses the Thompson scale [61], a commonly used five-point grading scheme, which is based upon the physical characteristics of the nucleus, anulus, vertebral endplates and vertebral body. It identifies degeneration by features such as anular fissures, osteophytes, a fibrous nucleus and irregular endplate thickness (Table 1.4).

Current standard grading schemes for disc degeneration are discontinuous and subject to interpretation. A more objective, continuous system is required, but yet to be developed [58].

Table 1.4: The Thompson Scale. This grading system can be used for determining the morphologic grade of the disc in experimental investigations. NP = nucleus pulposus; AF = anulus fibrosus; VE = vertebral endplate; VB = vertebral body. (From Thompson (1990) [61].)

Grade	**NP**	**AF**	**VE**	**VB**
I	Bulging gel	Discrete fibrous bundles	Hyaline, uniformly thick	Margins rounded
II	White fibrous tissue peripherally	Mucinous material between lamellae	Thickness irregular	Margins pointed
III	Consolidated fibrous tissue	Extensive mucinous infiltration; loss of anular nuclear demarcation	Focal defects in cartilage	Early chondrocytes or osteophytes at margins
IV	Horizontal clefts parallel to endplate	Focal disruptions	Fibrocartilage extending from subchondral bone; irregularity and focal sclerosis on subchondral bone	Ostephytes less than 2 mm
V	Clefts extend through nucleus and anulus		Diffuse sclerosis	Osteophytes greater than 2 mm

1.4.5 Aetiology

The aetiology of disc degeneration is multi-factorial, but one contributing factor is the excessive or insufficient production of one or more molecular components, which leads to an imbalance between matrix synthesis and degradation. Hadjipavlou et al. (2008) [14] postulated that the following factors are amongst the many that could play a role in the development of disc degeneration.

Genetic Factors

Degeneration has been found to be significantly linked to the individual's genetic makeup, or more specifically, the genes that give rise to proteins that regulate the composition of the disc [64, 65].

One example is the gene that encodes the proteoglycan-degrading enzyme, matrix metalloproteinase-3 (MMP-3). In some instances, this gene contains five adenosine amino acids rather than six, which dramatically increases its transcription ability. A study by Takahashi et al. (2001) [66] found that elderly people with this

genetic mutation tended to show more signs of disc degeneration.

Battie et al. (2009) [67] investigated the discrepancies in disc morphology between twin siblings, and found that heredity was linked to disc degeneration, with twins exhibiting similar morphologies despite being subjected to completely different physical loading conditions in their daily lives.

Ageing

Disc ageing is marked by a number of different molecular changes. The number of cells and the rate at which they are synthesised decreases, particularly in the anulus. Proteoglycans are smaller, less abundant and less aggregated, so there are fewer polar groups to which water can bind, and the disc becomes dehydrated, more fibrous and more cartilaginous. Collagen type II is replaced by type I, making the transition zone between the anulus and nucleus less distinct. The cause of these effects is unknown, but there may be associations with poorer nutrition, fatigue failure and/or an accumulation of degraded matrix components [2, 68].

Nutrition

The disc is avascular, and thus does not receive nutrients directly from the blood stream. Cells in the outer anulus obtain nutrients from the blood vessels present in the surrounding soft tissue, whereas those in the nucleus and inner anulus rely on the diffusion of nutrients through the endplate from the capillaries in the vertebral bodies [69]. Consequently, the presence of toxins in the bloodstream could also be transported to the disc, leading to adverse effects. For example, a study on bovine specimens showed that the presence of nicotine in the blood inhibited cell proliferation, reducing the rate of protein synthesis in the disc [70].

Given that it acts as a nutrient pathway, the occlusion of the endplate - due to conditions such as artery disease or endplate calcification - could be deleterious. A lack of nutrients in the disc has been shown to cause oxidative stress, which could lead to a decrease in proteoglycan synthesis [71]. Though, interestingly, other studies have indicated that low oxygen tension actually improves the restoration of NP cells, and promotes higher mRNA expression and more uniform matrix elaboration [72]. These contrasting results may be attributable to a number of experimental factors, such as the culture duration and cell source, and further clarification is necessary.

Mechanical Factors

Disc degeneration tends to be more prevalent in the lumbar region of the spine, which supports the highest magnitude of weight compared to more superior spinal regions [73]. This suggests that the mechanics and physical demands of the disc may be major determinants of disc degeneration.

Intervertebral discs are designed to withstand mechanical loading, and it is this physiological stimulus that promotes matrix renewal - a vital part of maintaining disc health [74]. However, if the magnitude, frequency and/or duration of loading lies outside a particular homeostatic threshold, the effect could be ultimately damaging.

Compression

Excessive compressive loading, either in the form of a sudden, severe load or a moderate, cyclic load, will make the vertebral endplate highly amenable to fracture. For example, Adams et al. (2000) [53] found that endplate damage occurred after applying a mean±SD compressive force of 6.7±2.5 kN (range: 3-11.7 kN). The body's inflammatory response to bone fracture is to develop a callous, but whilst this may mend the damaged endplate, the diffusion pathways that provide nutrients to the nucleus and inner anulus can become occluded [2].

Additionally, it has been shown that disc cells are highly sensitive to loading frequency and magnitude. Studies on compression in rat tail specimens demonstrated that loads with a frequency below 0.1 Hz and/or a magnitude above 0.9 MPa resulted in increased cell apoptosis [75, 76].

Torsion

The alternating orientation of the collagen fibres in the anulus fibrosus makes them highly effective at resisting torsional motion, during which half of the fibres are in tension, and the remaining ones are slack. If the fibres are subjected to longitudinal strains greater than 4% (corresponding to around 3° axial rotation of one spinal segment), damage to the disc may ensue. As a preventative measure, the zygapophysial joints and ligaments limit the movement of the segments; however, in the case of damaged joints or a flexed spine, the torsional constraint of the joints is reduced, and axial rotation may exceed this physiological threshold. Excessive rotation has been found to cause nucleus migration, disc narrowing, anular fissures and periph-

eral tears, which then propagate into radial tears oriented towards the centre of the disc [77].

Whole-Body Vibration

There is evidence to suggest that whole-body vibration can impair disc metabolism, particularly if it is equal to the resonant frequency of the spine (4-6 Hertz) [78]. Some studies, such as that by Bovenzi et al. (1992) [79], have found that people exposed to extended periods of whole-body vibrational motion, such as helicopter pilots and vehicle operators, tend to be more susceptible to low-back pain. This theory is still being explored, but it is likely that low-back pain is attributable to a combination of different factors, rather than vibration alone.

1.4.6 Current Treatments

Disc degeneration is not curable; however, there exist a number of treatment options that can help alleviate the symptomatic pain that may accompany it. Depending upon the individual and the severity of their condition, the physician may recommend non-surgical or surgical treatment strategies.

Non-Surgical Treatments

In cases where the patient experiences mild pain, it is often sufficient to prescribe a non-surgical treatment, such as heat application, anti-inflammatory medication, gentle exercise or acupuncture; or a minimally invasive procedure, such as transcutaneous nerve stimulation or an epidural steroid injection [80, 81]. The effectiveness of these treatments varies with each individual; some patients may be much more responsive than others. If these treatments are ineffective, the physician may need to resort to surgical methods.

Surgical Treatments

Spinal Fusion

A common, albeit controversial, procedure is spinal fusion, in which the damaged disc is removed and the two interfacing vertebrae are fused together, often with the aid of bone grafts. Spinal fusion, performed in the anterior, posterior or posterolat-

eral regions, is based upon the premise that motion at the defective joint is the cause of back pain, and that joint stabilisation will provide pain relief [82]. The clinical outcomes of this procedure can vary considerably [83]. Whilst some studies have shown fusion surgery to be an effective treatment for discogenic pain (determined by factors such as patient satisfaction, general function and radiographic results), the procedure has been known to have frequent perioperative complications and could even promote further degeneration of the discs at adjacent levels [83]. Moreover, in some cases, equal or better clinical outcomes could be achieved using cheaper, less invasive treatments, such as intradiscal electrothermal therapy and cognitive rehabilitation programs [83–85]. Due to such inconsistent results, the efficacy of spinal fusion as a treatment option is still being reviewed.

Disc Prostheses

Artificial disc implantation is the newest type of surgical procedure used in clinical practice, and whilst it is still being refined, it has been described as having tremendous potential as a treatment for disc degeneration [80]. Disc prostheses are generating enormous research interest, though the task of developing a biomaterial that mimics the mechanical behaviour of the intervertebral disc is proving to be a challenge. Interestingly, the rationale behind the development of disc prostheses is 'dynamic stabilisation', which suggests that motion preservation, rather than fusion, is more effective at alleviating pain symptoms [86]. Being a relatively new concept, disc prostheses are yet to be validated in the long-term, though the results of short-term clinical trials have been generally promising [86, 87].

Further Research

Whilst these treatments merely aim to *relieve* the symptomatic pain, research into tissue engineering and biological treatment strategies - which aim to *repair* the degenerated disc matrix - is becoming more prolific.

A multitude of different strategies is being explored. Firstly, gene therapy, in which a gene of interest is introduced into target disc cells to initiate protein synthesis, holds considerable promise as a treatment for disc degeneration [88]. The use of stem cells has also been investigated, since they can develop into various specialised cell types and have been used in other tissue engineering applications.

For example, a study by Sobajima et al. (2008) [89] demonstrated the feasibility of stem cell therapy for the supplementation/replenishment of NP cells in degenerate discs. Numerous *in vivo* and *in vitro* studies suggest that growth factor injections may be used for the biological regeneration of disc tissue [90]. Similarly, the injection of platelet-rich plasma, contained inside biodegradable hydrogel microspheres, has been shown to significantly attenuate the rate of degeneration in rabbit NP tissue [91]. Finally, researchers from the University of Pennsylvania have made some promising advancements with electrospun tissue-engineered composites seeded with anulus fibrosus cells in an attempt to create biomaterials with properties identical to those in healthy biological tissue [92].

These emerging techniques are still in their developmental stages, and will not be used in clinical practice for some time; however, they are making considerable progress and have a common preventative focus. Spinal fusion techniques and prostheses have the potential to help sufferers of discogenic pain, but these treatments are administered after disc degeneration has reached an advanced stage. A more ideal and efficient method of treatment would be to target the disease at its onset, to prevent it from reaching a more serious, symptomatic state. **The development of such a treatment could be assisted by better understanding the multiscale mechanical behaviour of the disc's components and the pathogenesis of disc degeneration. These will be the foci of this thesis.**

Chapter 2

Mechanical Testing Review

2.1 Introduction

Objects can be described in terms of their *structural* or *mechanical* properties [93]. The structural properties refer to the object as a whole (e.g. a whole vertebra), and consider the way that the object's material and geometric characteristics contribute to its load-deformation response. The mechanical properties refer to the intrinsic characteristics of the materials that make up the object (e.g. the bone that constitutes the vertebra), and consider factors such as biochemical composition and molecular organisation. This research is primarily concerned with the intervertebral disc's mechanical properties.

The mechanical properties of biological tissue can be described using various parameters, including the following:

- **Young's Modulus, E [Pascals, Pa]; Toe Modulus, E_T [Pascals, Pa]; Extensibility, ϵ_M [%]**

  Young's Modulus, E, is a measure of an isotropic material's elasticity, and describes the linear load-deformation response when a load acts in a direction perpendicular to the cross-sectional area. It is represented by Equation 2.1.

$$E = \frac{\sigma}{\epsilon} \tag{2.1}$$

  where σ is stress (force per unit area, expressed in Pa) and ϵ is strain (change

in length relative to original length). Stress and strain are given by Equations 2.2 and 2.3, respectively. E is therefore the gradient of the stress-strain relationship.

$$\sigma = \frac{F}{A} \tag{2.2}$$

$$\epsilon = \frac{\Delta L}{L_O} \tag{2.3}$$

F is the resultant force after displacement is applied, expressed in Newtons (N). A is the cross-sectional area of the sample, expressed in square metres (m^2). L_O is the original sample length, expressed in metres (m), before any displacement is applied. ΔL is the change in sample length relative to L_O.

For elastic materials, the stress-strain relationship prior to yielding will be linear, and both loading (extend) and unloading (retract) phases will be coincident; i.e. they will be in phase. However, viscoelastic materials will be time-dependent, and the stress and strain will be out of phase. This gives rise to a curved stress-strain plot, and the area inside the stress-strain loop (hysteresis) is the energy absorbed during that loading-unloading cycle [94]. Figure 2.1 shows examples of these two different curves. It should be noted that, by definition, Young's Modulus refers to elastic materials, and biological tissue is characteristically viscoelastic. Notwithstanding, the use of the term Young's Modulus is still commonly used in the literature for describing biological tissue's ultimate elasticity within the most linear region, so this thesis will refer to it as such.

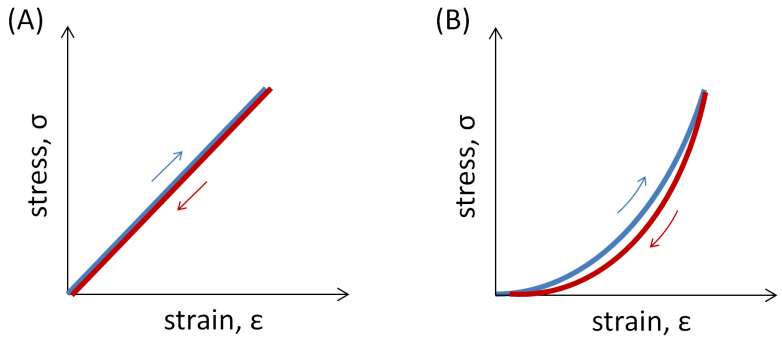

Figure 2.1: Examples of stress-strain curves and (A) elastic and (B) viscoelastic materials. Blue=extend cycle; red=retract cycle.

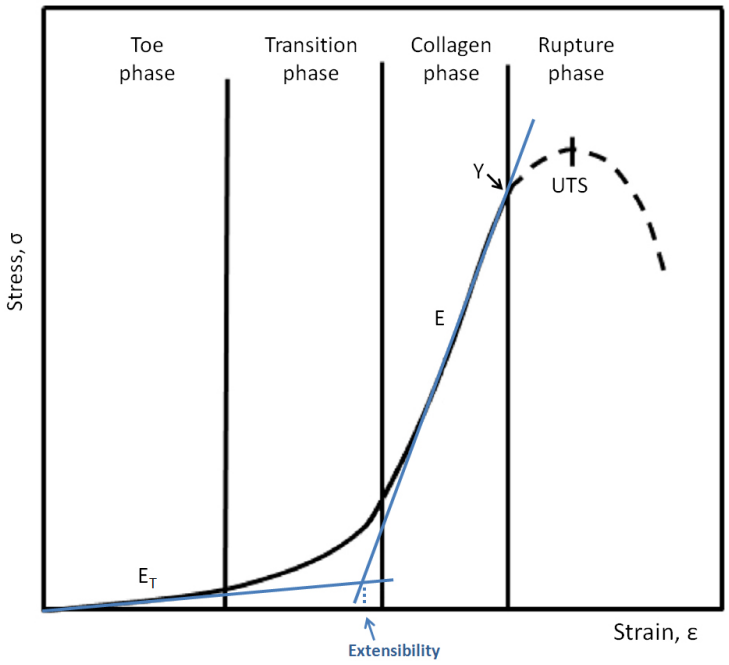

Figure 2.2: Example of stress-strain extend curve for a viscoelastic material pulled to failure, showing four different phases: the toe phase (from which the toe modulus (E_T) is derived), transition phase, collagen phase (from which Young's Modulus (E) is derived) and rupture phase. The yield point (Y) denotes the point at which non-recoverable plastic deformation occurs. The ultimate tensile strength (UTS) represents the maximum stress reached before failure occurs. The extensibility (ϵ_M) is the point where E_T and E intersect. (Modified from Hasan et al. (2014) [95]).

It can be observed that the typical non-linear stress-strain relationship for biological materials no longer yields a single gradient that can be considered to be E. Instead, the relationship can be described as having four main phases, as shown in Figure 2.2. The initial linear *toe phase* represents the straightening of crimped collagen fibres and elongation of elastin fibres, and is the region from

which the linear toe modulus, E_T, can be calculated. This is followed by the non-linear *transition phase*, which could represent the continued uncrimping and straightening of the collagen fibres and the transfer of force from elastin to collagen. This leads into a linear *collagen phase*, wherein the collagen and elastin fibres are straightened and bear the load together, and the equivalent E is calculated. The *yield point* represents the first deviation from linearity, after which non-recoverable plastic deformation/strain occurs when the load is removed. Finally, the *rupture phase* represents the breakage of fibres and failure of the tissue, where the ultimate tensile strength (UTS) is the maximum stress that the material can withstand before failure [95]. The extensibility, ϵ_M, is the strain that corresponds to the intersection between E_T and E, and describes the transition between the two moduli and the uncrimping of collagen fibres [96].

- **Phase Shift, ϕ [Degrees, $^\circ$]**

  Phase shift is the amount of energy dissipated by a material relative to that which it stores; i.e. a measure of viscoelasticity. With regards to load-deformation, the phase shift is calculated by measuring the lag in force response relative to the applied displacement. For purely elastic materials, this shift is 0°; for purely viscous materials, it is 90°. Viscoelastic materials have a phase shift between 0 and 90°.

- **Poisson's Ratio, ν**

  Poisson's Ratio considers the two-dimensional strain on an object as it undergoes deformation. This quantity is equal to the ratio of the lateral strain (in the transverse direction relative to the object's axis) and the longitudinal strain (in the direction of the object's axis). In general, the longitudinal strain and the resultant lateral strain are opposite in sign; i.e. as the object is stretched longitudinally, it will contract laterally.

2.2 The Mechanical Properties of the AF

As mentioned previously, AF lamellae can be considered to be composite layers consisting of collagen fibre bundles bound together by a proteoglycan-rich ground substance. In the outer AF lamellae, these fibre bundles are predominantly composed of collagen type I fibrils [97]. The lamellae themselves are crosslinked to form the concentric layers.

This type of structure is analogous to a brick wall, where the bricks are the collagen fibre bundles, the ground substance is the mortar, and together they create a brick wall-like structure, which is the AF lamella. Although this is a very simplified analogy, it allows one to visualise the collagen and ground substance interaction (Figure 2.3).

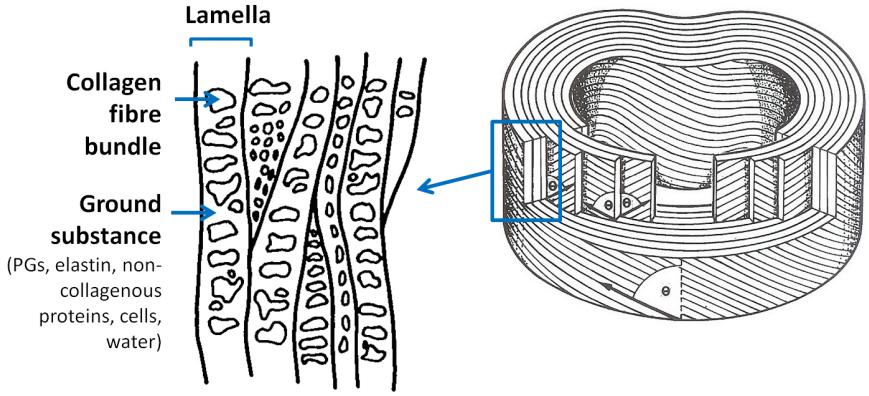

Figure 2.3: Cross-section of lamellae showing collagen fibre bundle and ground substance composition. (Modified from Marchand & Ahmed (1990) [16] and Bogduk (2002) [2])

Various hierarchical levels within the AF (see Section 1, Figure 1.10) have been studied in the literature, and although some levels, such as the individual collagen fibre bundles, are yet to be explored, considerable progress has been made over the past few decades. This chapter will review the techniques and findings of the studies that have explored E, E_T, ϵ_M and/or ϕ in *multiple lamellae*, *single lamellae* and *collagen fibrils*. Particular attention has been given to the effects of anatomical region, degenerative grade and strain rate. **Note that the collagen fibre bundle level, which lies between the single lamella and collagen fibril levels is yet to be explored in the literature, and is the focus of this current research.**

Table 2.1: Studies exploring the Young's Modulus, E, of multiple lamellae in the AF. PLANE OF TESTING: Circ=circumferential; Ax=axial; Rad=radial. ANATOMICAL REGION: PL=posterolateral; L=lateral; AL=anterolateral; A=anterior. DEGENERATIVE GRADE: H=healthy; D=degenerate. * denotes significantly different groups.

Specimen	**Author**	***E*, anatomical region**	***E*, degenerative grade**
Human, lumbar	Acaroglu et al. (1995) [98]	(Circ) outer PL: 14 MPa*, outer A: 28 MPa*	(Circ) No significant differences between degenerative grades
	Ebara et al. (1996) [99]	(Circ) outer PL: 20 MPa*, outer A: 49 MPa*	N/A
	Elliott and Setton (2001) [100]	(Circ) outer A: 17.45 MPa (Ax) outer A: 0.82 MPa (Rad) A: 0.45 MPa	N/A
	Fujita et al. (1997) [101]	(Rad) PL: 0.51 MPa, A: 0.49 MPa	N/A
	Guerin and Elliott (2006) [102]	N/A	(Circ) H: 29.35 MPa, D: 29.10 MPa
	O'Connell et al. (2009) [103]	N/A	(Circ) H: 20.9 MPa, D: 22.9 MPa (Rad) H: 0.29 MPa, D: 0.35 MPa
	Smith et al. (2008) [96]	(Rad) PL: 0.167 MPa, AL: 0.272 MPa	N/A
	Wagner and Lotz (2004) [104]	(Circ) outer A: 13.2 MPa	N/A
Human, thoracolumbar	Skrzypiec et al. (2007) [105]	(Circ) outer AL: 18.5 MPa	N/A
Porcine, cervical	Gregory and Callaghan (2010) [106]	(Circ) outer P: 6.85 MPa, outer A: 7.76 MPa (Ax) outer P: 6.30 MPa, outer A: 4.18 MPa	N/A
	Gregory and Callaghan (2011) [107]	(Circ) outer P: 3.97 MPa, outer A: 5.17 MPa	N/A

2.2.1 Multiple Lamellae

A considerable number of studies have looked at multiple lamellar mechanics. Table 2.1 summarises a range of tensile testing studies that have measured E in relation to anatomical region and degenerative grade. Note that *multiple* lamellae essentially refers to more than one lamella, though the exact number of lamellae in each sample was not often measured and/or specified. Thus, thicknesses and number of lamellae differed amongst the various studies. This may have contributed to the discrepancies between the studies' reported measurements.

Multiple lamella samples are generally tested using tensile testing apparatuses, such as MTS hydraulic material testing systems (MTS Systems Corporation, Minneapolis, USA) [98, 99, 101], Instron machines (Instron, Norwood, USA) [102, 103], Minimat miniature testing systems (Rheometric Scientific, Piscataway, USA) [105], and CellScale micromechanical testing systems (CellScale, Waterloo, Canada) [106, 107].

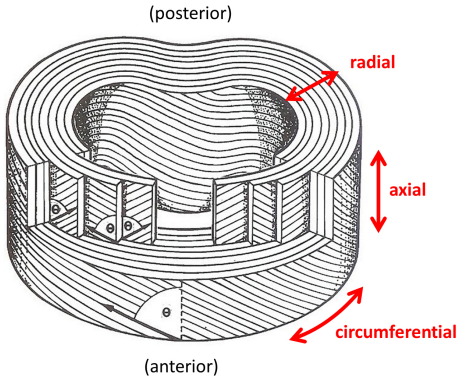

Figure 2.4: Testing orientations (radial, axial and circumferential) in the AF. The angle of the fibre bundles, θ, is approximately 65°. (Modified from Bogduk (2002) [2].)

Due to the specific, alternating orientation of the collagen fibre bundles *within* the lamellae and the complex cross-linking *between* the lamellae, inter- and intra-lamellar mechanics are of particular interest at this hierarchical level. The specific fibre bundle orientation and various disc loading directions also makes the testing orientation (i.e. circumferential, axial and radial) a critical factor (Figure 2.4). E has been shown to be greatest in the circumferential direction, which is expected, since the fibre bundles in the lamellae are orientated approximately 65° to the vertical

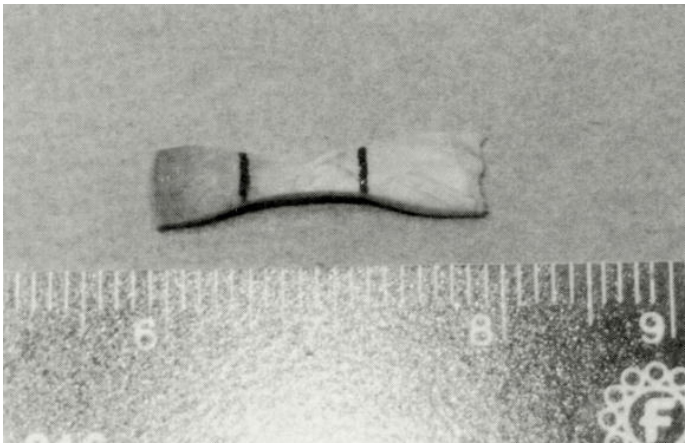

Figure 2.5: Multiple lamella sample for testing in the circumferential direction. (From Ebara et al. (1996) [99].)

(or 25° to the horizontal), and one would expect the lamellae to be stiffer if it is more closely aligned with the axis of the fibres. Figure 2.5 shows an example of a multiple lamella sample prepared for circumferential testing. In human specimens, E in the outer circumferential direction ranges from 13.2-49 MPa. For sections tested radially, E is at a minimum (<1 MPa) [96, 100, 101, 103], since this direction of testing represents the matrix in between the lamellae.

It is important to note that the *morphology* and *arrangement* of the collagen fibre bundles within the lamellae have been investigated in the literature, but their *mechanical behaviour* is yet to be quantified.

Only four studies have measured E_T in multiple lamellae specimens. These are summarised in Table 2.2. As expected, E_T tends to be much smaller in magnitude compared with E.

The results shown in Tables 2.1 and 2.2 will now be discussed in greater detail with respect to anatomical region, degenerative grade and strain rate.

Anatomical Region

Regarding anatomical region, the studies that conducted tensile tests in the circumferential direction have found that lamellar sections taken from the anterior region from human intervertebral discs have significantly higher E values than those taken from the posterolateral region [98, 99].

There are a number of theories that attempt to explain this regional variability.

- Marchand and Ahmed (1990) [16] found that there was a greater percentage

Table 2.2: Studies exploring the toe modulus, E_T, of multiple lamellae in the AF. PLANE OF TESTING: Circ=circumferential; Rad=radial. ANATOMICAL REGION: PL=posterolateral; A=anterior. DEGENERATIVE GRADE: H=healthy; D=degenerate. * denotes significantly different groups.

Specimen	**Author**	***E*, anatomical region**	***E*, degenerative grade**
Human, lumbar	Fujita et al. (1997) [101]	(Rad) PL: 0.18 MPa, A: 0.22 MPa	N/A
	Guerin and Elliott (2006) [102]	N/A	(Circ) H: 2.53 MPa, D: 5.68 MPa
	O'Connell et al. (2009) [103]	N/A	(Circ) H: 2.70 MPa, D: 4.20 MPa (Rad) H: 0.14 MPa*, D: 0.30 MPa*
	Smith et al. (2008) [96]	(Rad) PL: 0.055 MPa, AL: 0.096 MPa	N/A

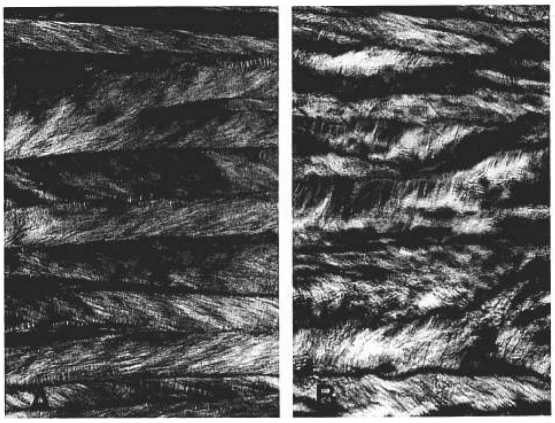

Figure 2.6: Polarised microphotographs of anterior (left image) and posterior (right image) lamellae. Anterior specimens tend to be more uniform and continuous in structure compared with posterior specimens. (From Tsuji et al. (1993) [108].)

of incomplete lamellae in the posterolateral region compared with those in the anterior region.

- It has been shown that the way in which the fibre bundles are arranged within the lamellae differ according to region. Tsuji et al. (1993) [108] conducted a morphological analysis of outer, middle and inner AF in healthy discs and found that the arrangement of the fibre bundles in the posterior/posterolateral region were more incomplete and discontinuous, fewer in number and more loosely connected compared with those in the anterior region (Figure 2.6).

- Continuous fibre bundles that extend from endplate to endplate could be an important contributor to anular stiffness and strength [40, 109, 110]. These long fibre bundles are strongly embedded at both ends in the cartilaginous endplate and/or vertebral bone, and are likely to provide the highest tensile strength. A number of studies have speculated about the existence of shorter fibre bundle lengths connected end-to-end with the proteoglycan-rich matrix (Figure 2.7), which would be comparatively lower in strength [109, 110]. A different theory, however, suggests that the apparent presence of these composite fibre bundles could merely be an artefact of the sectioning process. Given that the fibre bundles are tightly arranged, there is a possibility that the fibre bundles will be inadvertently severed or disrupted during sectioning [111]. The presence of these fibres is therefore questionable, and needs further clarification.

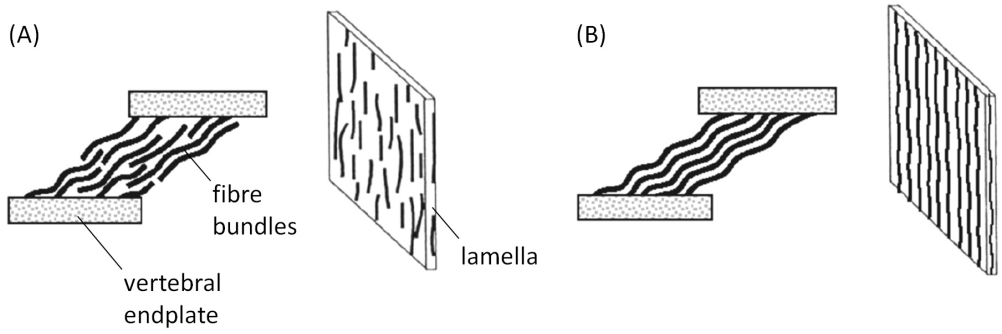

Figure 2.7: (A) Discontinuous fibre bundle arrangement, as seen in the posterior lamellae of the AF; (B) continuous fibre bundle arrangement, as seen in the anterior lamellae of the AF. (Modified from Pezowicz (2010) [109].)

Interestingly, two studies by Gregory and Callaghan [106, 107] did not find any significant regional differences for E. However, this contrary finding could be attributable to the use of a porcine model as opposed to the human models used in the other studies.

Only two studies by Fujita et al (1997) [101] and Smith et al. (2008) [96] considered the effect of anatomical region on E_T. Both studies tested in the radial direction, and found that there were no significant differences between posterolateral and anterior/anterolateral regions. This suggests that the difference in fibre arrangement does not affect the straightening of crimped collagen fibres and elongation of elastin during this initial toe phase. Smith et al. (2008) was the only study that measured ϵ_M, and found that ϵ_M in the posterolateral region (22.3%) was significantly higher than that in the anterolateral region (14.9%).

Degenerative Grade

Three studies have investigated the effects of degeneration on the elastic behaviour of multiple AF layers [98, 102, 103]. Although all three studies used the standard Thompson Scale to grade their disc specimens, the 'healthy' and 'degenerate' groups were categorised in different ways. Acaroglu et al. (1995) [98] separated their specimens into three groups: normal (Grade I), mildly degenerate (Grades II and III) and severely degenerate (Grades IV and V). In contrast, Guerin and Elliott (2006) [102] and O'Connell et al. (2009) [103] took the average grades of the discs and divided them into 'healthy' and 'degenerate' groups. All groups had modest sample

sizes, ranging from 6 to 17; thus, any significant findings should be interpreted with this in mind.

All studies found that E in multiple lamella samples, when tested in circumferential and radial directions, did not appear to be significantly affected by degeneration. This suggests that degeneration does not affect intra- nor inter-lamellar mechanics. This lack of change in mechanical behaviour appears to be inconsistent with the microscopic changes that are observed in degenerated AF, namely cracks, fissures, thickening of the lamellae and delamination (see Table 1.2). One would expect such dramatic structural changes to affect the mechanical behaviour of multiple lamella sections. However, it should be noted that Acaroglu at al. (1995) [98] reported a decreasing trend in the value of the circumferential Young's modulus with degeneration. Additionally, the statistical significance was reported as being 0.06, which could be considered marginal.

Only two studies by Guerin & Elliott (2006) [102] and O'Connell et al. (2009) [103] considered E_T of the stress-strain curve for healthy and degenerate specimens. Both studies found that, when stretched in the circumferential direction, degeneration had no significant effect on E_T. However, O'Connell et al. (2009) also tested radial segments, and found that degenerate specimens were significantly stiffer in this direction. This is perhaps an indication that degeneration only has an effect on inter-lamellar matrix during the uncrimping of the collagen; however, sample sizes for this study were relatively small (N=7 for healthy, N=6 for degenerate), so these results should be interpreted with caution.

Only one study by Sen et al. (2012) [112] measured phase shift in multiple lamella specimens and compared degenerative grades. The average force-displacement phase shift in healthy specimens, tested in the circumferential direction, was 6.76°, which decreased with a faster strain rate. This demonstrates the viscoelasticity and time-dependency of multiple lamellae, though the low phase angles (8° was the maximum reported value) indicate that the tissue behaviour closely resembles that of a non-linear, elastic solid. Disc degeneration did not have any significant effect on phase angle, suggesting that degeneration causes no change to the AF's ability to dissipate energy during loading. In comparison, Costi et al. (2008) [19] measured the phase shift of whole disc specimens in six degrees of freedom, and the average phase shift for each degree of freedom ranged from 5.1° to 8.6°, with a maximum reported

value of 12°. This indicates that even at higher structural levels, the disc displays predominantly elastic behaviour.

Strain Rate

The majority of the multiple lamella studies used one strain rate, which tended to be less than 1%/s. However, two studies considered the effect of different strain rates on the tissue's mechanical response. Fujita et al. (1997) [101] performed tensile testing on radial samples of human AF under four different strain rates: 0.005, 0.5, 5 and 50%/s, though no significant differences between the strain rates were observed. Gregory & Callaghan (2010) [106] tested porcine AF samples in circumferential and axial directions under three different strain rates: 1, 2 and 4%/s. Similarly, no differences in stiffness or maximum stress were observed between the strain rates, though this is expected, given that the three strain rates in these studies were not markedly different.

2.2.2 Single Lamellae

Single lamella mechanics have not been explored as widely as multiple lamellar mechanics. Due to the proteoglycan-rich matrix that permeates and surrounds the lamellae and binds them tightly together, the lamellae are difficult to prise apart and isolate, making these samples more challenging to prepare. To date, only two studies have explored E and E_T of human single lamella specimens. The results for E are summarised in Table 2.3.

Table 2.3: Studies exploring the Young's Modulus of single lamellae in the AF. ANATOMICAL REGION: P=posterior; PL=posterolateral; AL=anterolateral; A=anterior. * denotes significantly different groups.

Specimen	**Author**	***E*, anatomical region**
Human, lumbar	Holzapfel et al. (2005) [113]	Outer P: 64.8 MPa, outer AL: 77.6 MPa
	Skaggs & Weidenbaum (1994) [114]	Outer PL: 82 MPa*, outer A: 136 MPa*

Anatomical Region

Both studies examined the effects of anatomical region on Young's Modulus in human lumbar AF samples. Skaggs & Weidenbaum (1994) [114] found that the outer anterior lamellae had higher Young's Moduli than those in the posterolateral region. Holzapfel et al. (2005) [113] compared posterior and anterolateral regions, and though the latter region showed a slight increase in E, the difference was not deemed to be significant. This disagreement could be due to a number of factors. Firstly, the clamping and testing methods they employed were very distinct - Holzapfel et al. (2005) retained the vertebral bone at either end of the lamella (Figure 2.8), whereas Skaggs & Weidenbaum (1994) excised the soft tissue component only and attached squares of emery paper to either end.

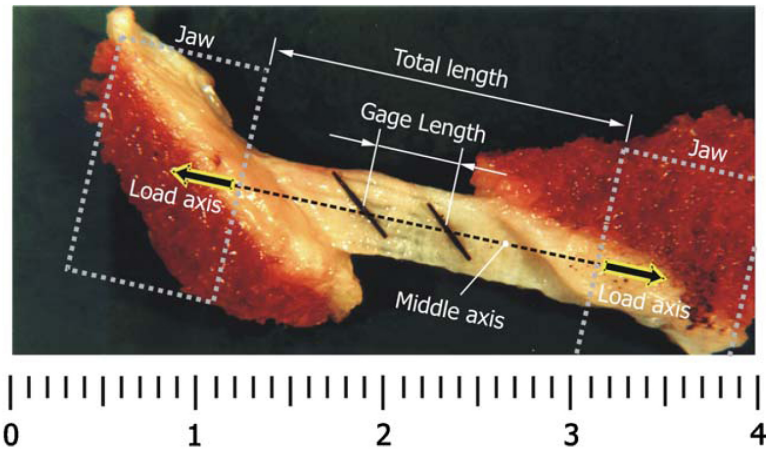

Figure 2.8: Single lamella specimen. Scale is in cm. (From Holzapfel et al. (2005) [113].)

Secondly, the specimens used by Skaggs & Weidenbaum (1994) were frozen and then thawed, whereas Holzapfel et al. (2005) used fresh tissue that was directly excised from human cadavers. There is evidence to suggest that freezing and thawing cycles do not affect the compressive properties of intervertebral disc tissue [115–117], though this has not been verified for the tensile properties of AF tissue, so it is fair to speculate that freezing may be an influencing factor.

Finally, both studies also had relatively small sample sizes (n<15) with considerable inter-specimen variance, and their methods for determining Young's Modulus were different. Holzapfel et al. (2005) took the tangential slope of the stress-strain curve at 75% of the failure strain, whereas Skaggs & Weidenbaum (1994) took the

slope of the curve between 0.5 and 1.0 MPa of stress. Although these two methods seem to refer to similar regions on the stress-strain curve, the final reported moduli could have been affected significantly.

Although there are noticeable differences between the two studies, the results suggest that regional variability could also be evident at the single lamella level, reinforcing the theory that fibre bundle arrangement and fibre-matrix interactions play an important role in intra-lamellar mechanics.

It is interesting to note that the values for E obtained at the single lamella level are generally higher than those at the multiple lamella level. This is most likely due to the orientation of the sample during testing. The two single lamella studies tested their samples along the axis of the fibre bundles, whereas the multiple lamella samples, orientated in the circumferential and axial direction, were not aligned with the axis of the fibre bundles. The fibre arrangement of the lamellae makes them anisotropic in nature. As such, one would expect the tensile modulus to be at a maximum for samples orientated in the fibre bundle direction, and a minimum for those orientated in the transverse direction [118].

Only Holzapfel et al. (2005) [113] considered E_T for single lamella specimens, and, like E, found that there were no significant differences between the anterolateral (5.96 MPa) and posterior (8.01 MPa) regions. As with E, the values for E_T at the single lamella level tended to be much higher than those at the multiple lamella level.

Degenerative Grade

To date, no studies have explored the effect of degenerative grade on single lamellar mechanics, though this is an area that needs to be investigated. It has been shown that degeneration does not affect multiple lamellae in the circumferential direction, but understanding its effect upon single lamellar mechanics would help verify the theory that degeneration only has an effect on inter-lamellar mechanics.

Strain Rate

Out of the two studies, only Holzapfel et al. (2005) [113] considered the rate-dependency of single lamella specimens. Three different displacement rates were used: 0.1 mm/min, 1 mm/min and 10 mm/min. It was found that the highest

strain rate caused a noticeable decrease in hysteresis, demonstrating more elastic behaviour. There was also moderate stiffening in the stress-strain response, but the difference was deemed to be insignificant. This relatively rate-insensitive behaviour is a characteristic of ligaments [119], which is understandable, given that they have a similar molecular composition to the outer AF [120]. From a physiological perspective, this may give ligaments the propensity to respond to joint loading in the same way regardless of how fast or slow the activity is, and suggests that the AF plays a similar strain-rate-regulating role in the disc.

2.2.3 Collagen Fibre Bundles

As mentioned in Section 2.2.1, the mechanical properties of individual collagen fibre bundles within the AF lamellae is yet to be explored.

2.2.4 Collagen Fibrils

Collagen type I fibrils are considered to be the elementary building blocks of collagenous tissues, and it is the way they are arranged that gives rise to the bespoke mechanical properties of the tissue as a whole [20]. In the outer AF, the collagen fibre bundles consist of collagen type I fibrils all aligned in the same direction and adjacently crosslinked via other proteins in the ground substance, such as decorin and biglycan, which are small, non-aggregating proteoglycans [15, 37, 121].

Collagen fibrils cannot be tensile tested using the testing systems used at the microscale because they are too small (their widths range from 50 to 500 nm) and cannot be physically clamped. Researchers have devised alternative methods for determining Young's Modulus at the nanoscale, and the testing system most commonly used is *atomic force microscopy (AFM)*. AFM is a microscopy method that can discern the mechanical properties of a sample through its interactions with a nanoscopic cantilever tip. The AFM's basic setup and modes of operation are covered in detail in Section 6.

Three main AFM methods have been explored in the literature: *tensile testing*, *bending* and *nanoindentation*. These AFM methods, and the studies that have employed them thus far, are summarised in Table 2.4. Note that *ambient* refers to tests conducted in air at room temperature, and hydrated refers to tests conducted

in PBS at 37°C.

Table 2.4: Studies using atomic force microscopy to explore the Young's Modulus of individual collagen type I fibrils.

Testing method	**Author**	**Specimen**	***E* [GPa]**	
			Ambient	**Hydrated**
Tensile testing	Graham et al. (2004) [23]	Human dermis	0.032	N/A
	van der Rijt et al. (2006) [32]	Bovine achilles tendon	2-7	0.2-0.8
	Yang et al. (2008, 2012) [122, 123]	Bovine achilles tendon	2.5	0.6
Bending	Heim et al. (2007) [124]	Sea cucumber dermis	10	N/A
	Yang et al. (2007) [125]	Bovine achilles tendon	1.4-5.4	N/A
Nanoindentation	Grant et al. (2009) [126]	Bovine achilles tendon	1.85	0.0012
	Heim and Matthews (2006) [33]	Sea cucumber dermis	1-2	N/A
	Strasser et al. (2007) [127]	Bovine dermis	1.2	N/A
	Wenger et al. (2007) [128]	Rat tail	5-11.5	N/A

Tensile Testing

In tensile testing, one end of the fibril is fixed to a substrate, and the other to the aforementioned cantilever tip (see Figure 2.9). The cantilever can then move up and down and stretch the fibril along its longitudinal axis, thereby allowing Young's Modulus to be determined directly. This direct method is the most ideal way to measure a fibril's elasticity, though the main caveat is the difficulty with carrying out these tests. Only three studies have successfully tensile tested collagen fibrils, and they used different tissues and methods for fixing the collagen fibril at its ends.

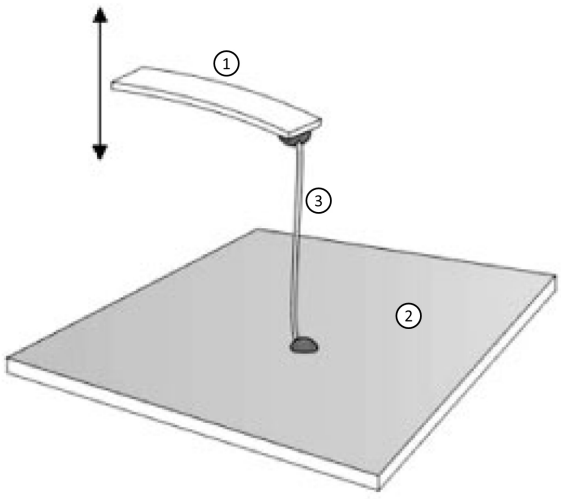

Figure 2.9: Tensile testing using AFM. (1) AFM cantilever, which moves up and down; (2) substrate, such as mica; (3) collagen fibril, fixed at both ends. (Modified from van der Rijt et al. (2006) [32].)

The studies by van der Rijt et al. (2006) [32] and Yang et al. (2012) [123] originated from the same research group, and both used collagen type I fibrils extracted from bovine achilles tendon. The fibrils were tested in ambient and hydrated conditions, with hydrated samples yielding Young's Modulus values several orders lower than ambient samples. The decrease in modulus could be due to the formation of water bridges between the collagen peptide chains [129]. The fibrils were fixed to the substrate and cantilever using epoxy glue, which was an effective method of attachment. However, the technique of tensile testing collagen fibrils needs to be further developed, because, despite yielding positive results, the gluing method appears to be very technically challenging and time-consuming; i.e. the surface of the substrate needs to be half-coated in Teflon, and the glue requires 12 hours of curing time. A separate study by Svensson et al. (2010) [130] (not shown in Table 2.4, as they did not measure E values) used a similar gluing technique, though the sample preparation seemed to be just as complex.

The method for tensile testing collagen fibrils needs to be further developed. It should be simpler, be suitable for standard AFM setups, not require any special sample substrate, allow for the possibility of testing in hydrated conditions, and be quicker to carry out.

Graham at al. (2004) [23] assembled collagen fibrils *in vitro* from human dermal collagen type I monomers. The fibrils, which were 10-30 nm in diameter - narrower than native fibrils - were attached to a glass slide substrate and AFM cantilever using non-covalent adsorption, demonstrating that collagen's inherent surface adhesion properties could be adequately strong for substrate and tip fixation. This adsorption method has also been used for a number of other tensile testing studies for collagen, though these were conducted at the monomer level [21, 24]. The stress-strain curve for these fibrils exhibited jagged regions that could be associated with monomer reorganisation. This jaggedness was not observed in the other tensile tests, possibly because the fibrils in this study were much narrower than fibrils in other studies (10-30 compared with approximately 300 nm), making the internal reorganisation more noticeable. These periodic drops in stress could also explain the lower Young's Modulus value (32 MPa).

Finally, researchers have also explored the use of micro-electrical-mechanical systems (MEMS) for collagen fibril testing [131, 132]. The two ends of the fibril were

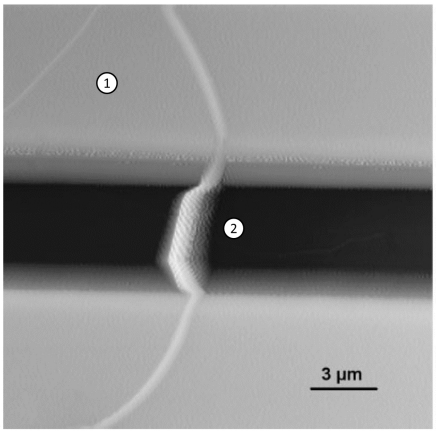

Figure 2.10: Example of bending test using AFM. (1) Edges of the nanoscopic channel; (2) collagen fibril. (From Yang et al. (2007) [125].)

glued to two pads, whose separation was controlled using an electrostatic actuator. The method yielded promising results, but the system was a custom-made and fabricated by the authors themselves. Using an AFM is advantageous because the instrumentation is widely available.

Bending

Two studies [124, 125] have used AFM to perform fibril bending, wherein the fibril is suspended over a nanoscopic channel or trough, and then the cantilever tip is pressed into its centre, effectively subjecting it to a three-point bending test (Figure 2.10). The force required to bend the fibril at the centre point can then be used to derive Young's Modulus using Equation 2.4.

$$E = \frac{l^3}{48I} \times \frac{dF}{dx} \tag{2.4}$$

where E is Young's Modulus, l is the length of the fibril spanning the channel; I is the moment of inertia, which, for a fibril of radius R, is equal to $1/4\pi R^4$; and $\mathrm{d}F/\mathrm{d}x$ is the slope of the force-indentation curve obtained from bending the middle point of the fibril.

This technique yielded Young's Moduli that were comparable with previously reported values, demonstrating its potential as a fibril-testing method. However, the studies were not able to test in fluid, possibly due to how the fibrils were deposited onto and bound to the surface of the channels.

Nanoindentation

The final AFM technique to be discussed is nanoindentation, whereby the surface of the collagen fibril is indented with the cantilever tip, and the force and indentation values are substituted into a model that relates these parameters to Young's Modulus. This method is arguably the simplest to execute; however, its disadvantage lies in the indirect way in which the modulus is derived. Thus, while the tensile and bending tests are technically challenging, their direct methods of E derivation render them favourable over nanoindentation.

Different models have been developed to relate indentation to elastic modulus. The simplest model that is used for collagen fibrils is the Hertz model (Equation 2.5) [133]. It was used by three of the four collagen nanoindentation studies [33, 126, 127].

$$E = \frac{3}{4}\frac{F(1-\nu^2)}{\sqrt{R}\delta^{3/2}} \tag{2.5}$$

where E is Young's Modulus of Elasticity; F is the applied force; ν is Poisson's Ratio; R is the tip radius; and δ is the nanoindentation. The model is valid under the following assumptions:

- The indenter is many orders of magnitude harder than the sample, and is shaped like a paraboloid. There are variations of the model for spherical, conical and pyramidal tip shapes; however, the differences are also negligible if the indentation is much smaller than the radius of the tip and stays within the elastic regime [134, 135]. This indentation range, which is generally around 5-10% of the sample thickness, ensures that the substrate, which is assumed to be many orders of magnitude harder than the sample, does not influence the calculations.

- The sample is a purely elastic, homogeneous, isotropic solid occupying an infinitely extending half-space.

- Both surfaces are smooth and frictionless, and there are no additional interactions between the indenter and the sample.

The use of the Hertz theory for biological tissue and cells is debatable, since these materials are known to be non-linear, heterogeneous, viscoelastic and anisotropic in

nature. However, despite its simplicity, it is an accepted model for representing the mechanics of biological materials provided the indentation stays within the elastic region of the material's response. It is also the most common model used for collagen fibril studies.

A number of alternative models exist, such as the Johnson, Kendall and Roberts (JKR) model [136], which calculates the modulus from the retract curve and takes the adhesion at the contact zone into account. This model is applicable for spherical tips and large radius compliant solids, and has been used for a number of studies on biological tissue, but has not been used on collagen fibrils. Oliver and Pharr (1992) [137] developed a model that considers the unloading portion of the nanoindentation curve and assumes that the sample deformation comprises both elastic and plastic contributions. However, it also assumes a high indentation depth and, like the other models, does not account for viscoelastic or creep behaviours. One collagen fibril study used this model [128], though the values for E were noticeably higher than those obtained in the other studies that used the standard Hertz model.

Only one study by Lewis et al. (2008) [138] has attempted to explore the nanomechanical properties of the AF. Rabbit intervertebral discs were micro-dissected into various transverse and axial sections, mounted onto glass slides, and then nanoindented under hydrated conditions. It was found that there were no differences in elastic moduli between posterior and anterior regions (in transverse and axial directions), and moduli ranged from 0.6-1.2 MPa. These values are noticeably lower than those obtained from single collagen fibrils, which is expected, since the entire section, including the inter-fibrillar matrix, was nanoindented, rather than just the fibrils themselves. Hence, whilst this study provided some useful insights into the transverse and axial behaviours of the disc and demonstrated that nanoindentation could be used on larger lamella sections, it would not be accurate to place this study in the same category as the single collagen fibril studies.

Investigating collagen fibrils in the human lumbar AF will broaden our understanding of the contributions that each hierarchical level makes to the AF's overall mechanical properties. Additionally, determining the effects that disc degeneration has on collagen fibrils could be pertinent to understanding the disease's origins, and assist in the development of improved therapies, such as tissue engineering.

Chapter 3

Research Aims

The aim of this research is to explore the mechanical properties of the human AF at two hierarchical levels:

1. Collagen type I **fibre bundles** at the microscale

2. Collagen type I **fibrils** at the nanoscale

Specifically, this will involve measuring toe modulus (E_T), Young's Modulus (E), extensibility (ϵ_M) and/or phase shift (ϕ) through micro- and nano-mechanical testing. The effects of the following three independent variables will be investigated:

1. Anatomical region

2. Degenerative grade

3. Strain rate

To date, the mechanical properties of fibre bundles and fibrils - with respect to these three parameters - have not been explored in the human AF. This information could clarify why regional differences in mechanical properties have been observed at higher structural levels; quantify the degree of viscoelasticity and strain rate dependence at the micro and nanoscale; and determine the point at which disc degeneration is discernible.

It is hypothesised that:

1. The effect of anatomical region on the AF's mechanical behaviour will be insignificant at the microscale and nanoscale, as the reported observations at the lamella level indicate that disc behaviours tend towards uniformity as more homogeneous structures are approached.

2. The effect of degeneration will not be significant at the microscale and nanoscale, as there have not been any reported differences at the lamella level.

3. When subjected to higher strain rates, the AF at the microscale will exhibit higher Young's Modulus values and more elastic behaviour, as these are common observations for viscoelastic materials.

It is anticipated that this research will broaden our understanding of how these hierarchical levels contribute to the function of the AF as a whole, and provide important information for the development of biomaterials and finite-element models. Furthermore, it could improve our knowledge of disc degeneration to instigate the development of more effective methods of treatment.

The remainder of this thesis is structured as follows:

Part II covers the microscale experiments that explored collagen fibre bundles. Chapter 4 describes the microscale materials and methods in which the mechanical properties of the fibre bundles were measured using a CellScale micromechanical testing system. Chapter 5 details the results and discussion of these experiments.

Part III covers the nanoscale experiments that explored collagen fibrils. Chapter 6 describes the nanoscale materials and methods in which nanoindentation was performed using AFM, followed by the results and discussion in Chapter 7. Chapter 8 describes an additional experiment that aimed to develop a novel nano-tensile testing technique, though it was not used to obtain the final data in this research.

Part IV concludes this thesis by summarising the main findings and future recommendations, and highlighting the significance of this research in the context of biomechanics.

Part V contains the appendices and references.

Part II

Microscale Experiments: Collagen Fibre Bundles

Chapter 4

Microscale: Materials and Methods

4.1 Introduction

The aim of this experiment was to determine the effect of degenerative grade, anatomical region and strain rate on E_T, E, ϵ_M and ϕ in collagen fibre bundles extracted from the outer AF.

4.2 Experimental Setup: The CellScale BioTester

4.2.1 Overview of the Apparatus

Tests were performed using a CellScale BioTester 5000 (CellScale, Ontario, Canada), a micromechanical testing system specially designed for the testing of biological materials. The tensile testing is conducted using a set of mechanical actuator arms which grip the sample and stretch it in uniaxial or biaxial directions.

The system consists of the following components (Figure 4.1):

1. An overhead charge-coupled device (CCD) camera, which records images and video of the sample as it is being stretched.

2. Overhead lamps to illuminate the sample.

3. Four actuator arms fitted with custom-made tissue clamps that hold the sample in place. Uniaxial testing uses two opposite arms; biaxial uses all four

arms. Details of the tissue clamps are shown in Chapter 4.2.2.

4. Load cells for measuring the force on the sample. The setup in this research used 2.5 N and 23 N load cells (±0.1% error), which were housed in protective compartments on the sides of the device. The load cells are oriented perpendicularly to each other, allowing tensile tests to be performed in uniaxial or biaxial directions.

5. A water bath, which sits on top of a heated platform.

6. A thermocouple, which can be placed in the water bath to monitor and control the temperature of the testing environment.

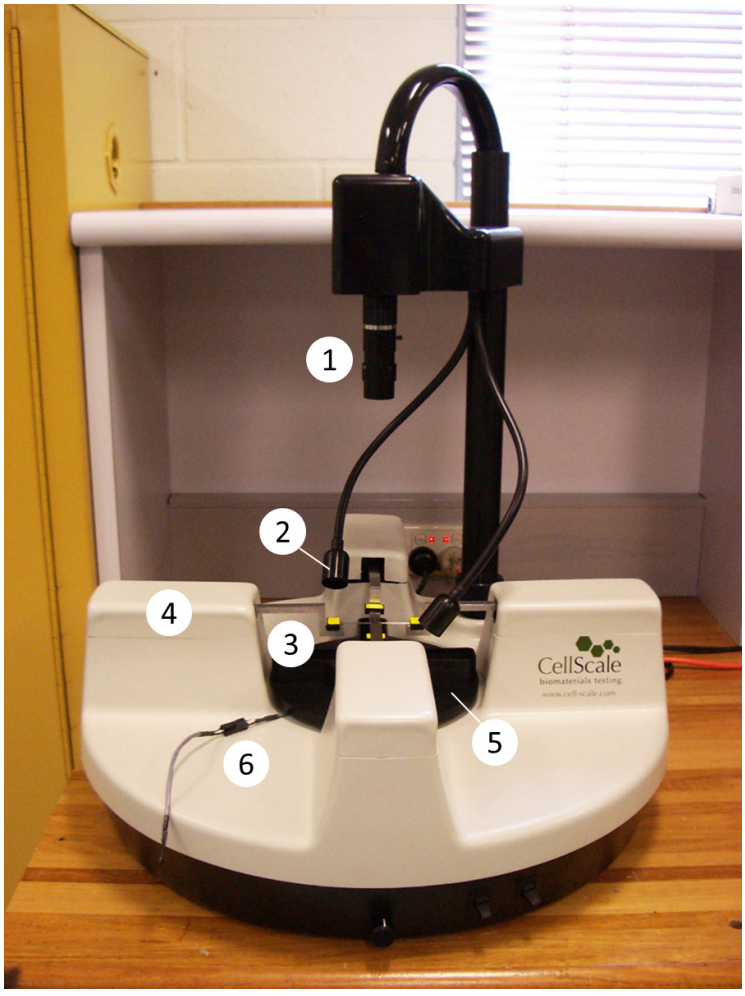

Figure 4.1: The CellScale BioTester. (1) Overhead CCD camera; (2) overhead lamps; (3) actuator arms and tissue clamps; (4) load cell housing; (5) heated platform and water bath; (6) temperature gauge.

4.2.2 Tissue Clamps

To hold the tissue sample, a pair of custom-made tissue clamps were designed and constructed (Figure 4.2). A 19 mm fold back clip (Celco, New South Wales, Australia) constituted the clamping mechanism. To improve their grip, the jaws of the clips were lined with small strips of P800 emery paper and glued using cyanoacrylate adhesive (Selleys Shock Proof, Selleys, New South Wales, Australia). One of the clip's metal arms was removed and a stainless steel plate glued to that side using a heavy duty cyanoacrylate adhesive (Loctite 454 Prism, Loctite, North Rhine-Westphalia, Germany). The plate was then screwed to the CellScale's calibration bracket provided with the system.

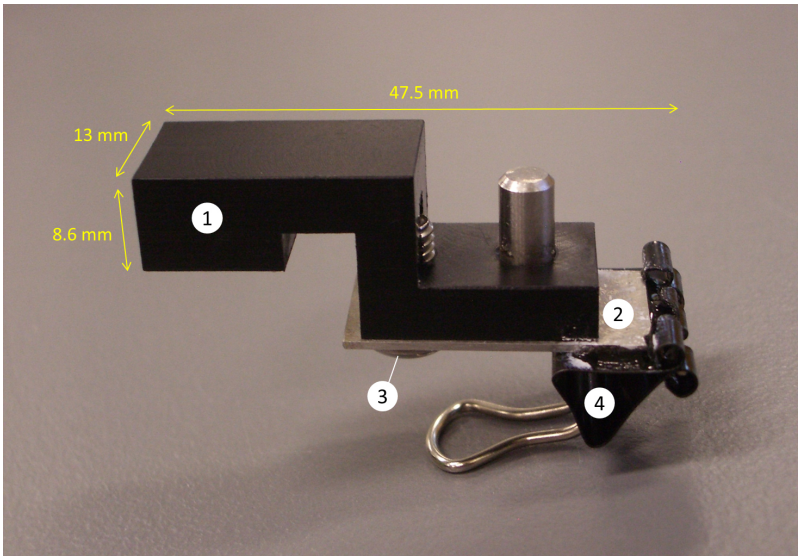

Figure 4.2: Custom-made tissue clamps. (1) Bracket, which locks onto the actuator arm; (2) stainless steel plate; (3) screw and washer; (4) fold back clip lined with emery paper.

4.3 Specimen Preparation

A total of 11 cadaveric human lumbar spines (mean age: 51 years, range: 16-91 years), divided into motion segments (i.e. the two adjacent vertebrae and intervening disc), were sourced from the National Disease Research Interchange (Pennsylvania, USA) and the Ray Last Laboratories, University of Adelaide (South Australia, Australia), sealed in plastic bags and stored at -30°C prior to use. Ethics approval

was granted by Southern Adelaide Clinical Human Research Ethics Committee (application number 184.11) for the duration of this research project.

The motion segments were then thawed for several hours at room temperature. Using a scalpel, the fascia surrounding the discs was removed until the diagonal fibres on the disc periphery could be seen. Intact discs were then dissected transversely using a scalpel and prised open. In some cases, the posterior elements were sawed off to allow the discs to be opened more easily. Disc cross-sections were graded by two independent observers using the Thompson criteria [61]. Discs graded as 1-3 were classified as healthy; those graded 4-5 were classified as degenerate. Only discs with sufficient height (i.e. greater than 5 mm) were used, as it was difficult to extract tissue from severely narrowed specimens. A total of 7 healthy and 7 degenerate discs were used in this study (Table 4.1).

Table 4.1: Parameters for healthy (N=7) and degenerate (N=7) specimens. Note that some lumbar spines yielded more than one usable disc.

	Reference number	**Sex**	**Age [years]**	**Disc level**	**Thompson grade**
Healthy (N=7)	H1	M	33	T12-L1	2
	H2			L5-S1	2
	H3			L4-L5	2
	H4	M	16	L4-L5	3
	H5	M	53	T12-L1	3
	H6			L1-L2	3
	H7			L3-L4	3
Degenerate (N=7)	D1	F	69	L4-L5	4
	D2	M	69	L5-S1	5
	D3	M	82	L4-L5	4
	D4	M	82	L3-L4	5
	D5	M	77	L3-L4	4
	D6	M	76	L1-L2	4
	D7	M	91	L2-L3	5

Using a scalpel, AF lamella sections were excised from the outer region of the discs at four different anatomical locations: posterolateral (PL), lateral (L), anterolateral (AL) and anterior (A), giving 56 samples in total (Figure 4.3). The lamella sections were placed in 0.15 M phosphate-buffered saline (PBS) solution (Australian Chemical Reagents, Queensland, Australia) for approximately 30 minutes to allow them to swell and soften. Individual, intact fibre bundles were then pulled from the lamella network using surgical tweezers, stored in vials containing PBS, and frozen

at -30°C prior to use.

Individual, intact fibre bundles were then pulled from the lamella network using surgical tweezers, stored in vials containing PBS, and frozen at -30°C prior to use. Care was taken to ensure that the fibre orientation within these bundles was consistently longitudinal, as verified by the overhead CCD camera of the CellScale BioTester set to 11μm/pixel image resolution (Figure 4.4A). Fibre bundles that were adjacent and parallel to each other were prised apart at the ground substance interface running between them, allowing individual fibre bundles to be isolated.

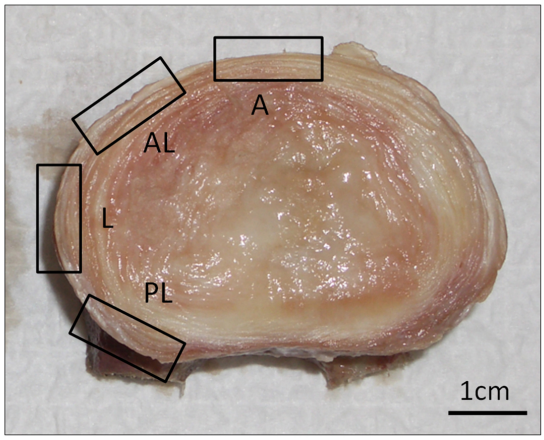

Figure 4.3: Transverse view of a dissected disc showing the four anatomical regions of interest: posterolateral (PL), lateral (L), anterolateral (AL) and anterior (A).

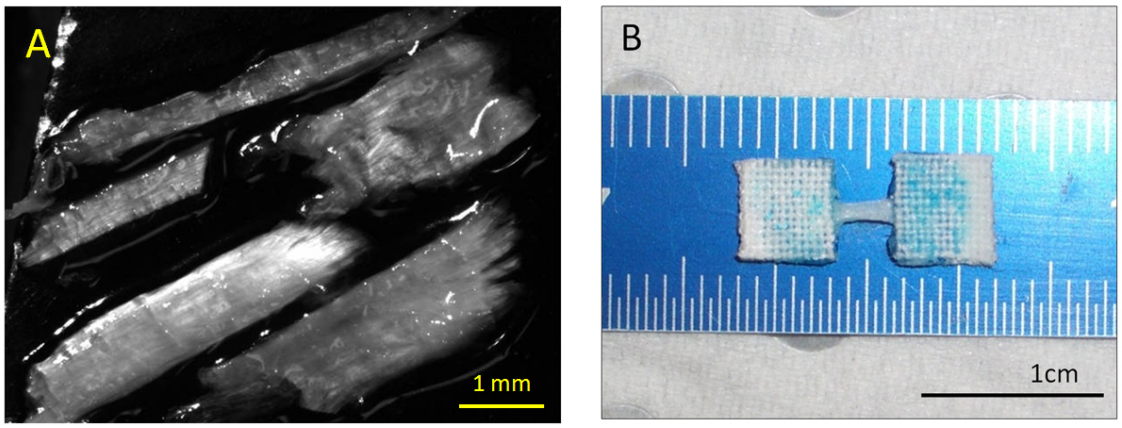

Figure 4.4: (A) Fibre bundles extracted from lamellae, showing consistent fibre direction; (B) fibre bundle with fabric tabs attached.

To improve gripping strength, cotton fabric tabs, measuring approximately 6×6 mm, were folded onto to the ends of the fibre bundles and fixed using cyanoacrylate

adhesive (Selleys Shock Proof, Selleys, New South Wales, Australia) that had been dyed to help with visibility. Care was taken to ensure that the glue was not applied to the length of sample between the two tabs (Figure 4.4B).

4.4 Tensile Testing

The tabs at either end of each sample were inserted into a pair of custom-made clamps such that the loading axis was aligned with the fibre orientation. The two clamps were then fixed to two opposing actuator arms on the BioTester fitted with 2.5 N or 23 N load cells (±0.1% accuracy), and secured in place using Hoffmann clamps (Figure 4.5). The clamped samples, orientated horizontally, were lowered into a PBS bath maintained at 37±1°C for the entire duration of the experiments.

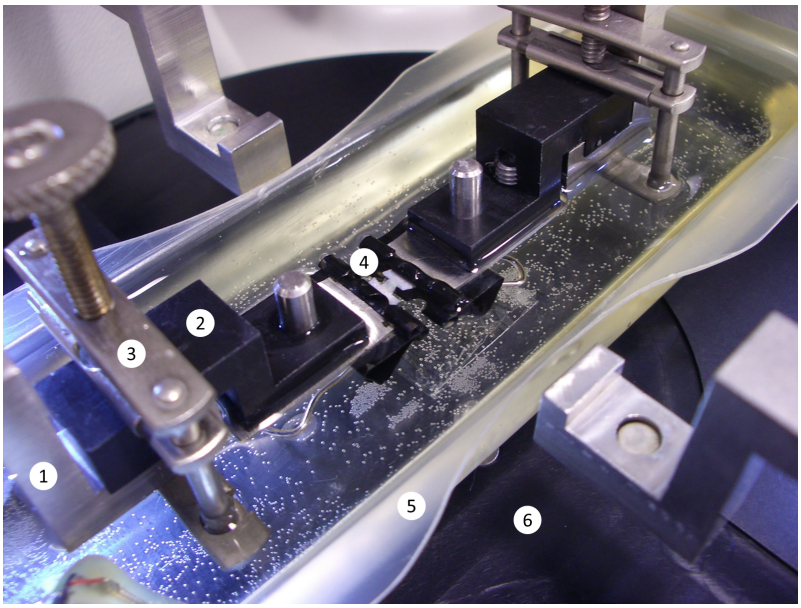

Figure 4.5: The CellScale BioTester's clamping setup. (1) Actuator arm; (2) tissue clamp; (3) Hoffmann clamp; (4) tissue sample; (5) water bath; (6) heated platform.

A preload of approximately 50 mN was applied for 10 minutes prior to testing. This preload was used, as pilot tests demonstrated that this load magnitude was substantial enough to overcome the initial unloaded 'slack' region for collagen fibre bundles.

The sample was then subjected to uniaxial tension under linear ramp displacement control. Displacement was applied until the linear region of the stress-strain response was reached without slipping out of the clamps.

Loading/unloading was performed at three different strain rates: 0.1%/s (slow), 1%/s (medium), and 10%/s (fast). Table 4.2 summarises the number of cycles, sample frequency and image frequency for each strain rate. The number of cycles for the slow strain rate was reduced to 10, due to the extended time taken to perform each test. LabJoy 2.0 software (CellScale, Ontario, Canada) was used to control the test parameters and collect the data. Images were captured by the BioTester's overhead CCD camera. The raw data were processed with MATLAB R2010b (MathWorks, Massachusetts, USA) using a custom-made program (Appendix A).

Table 4.2: Test parameters for the CellScale micromechanical experiments.

Strain rate	**Number of cycles**	**Sample frequency [Hz]**	**Image frequency [Hz]**
slow (0.1%/s)	10	1	1
medium (1%/s)	15	10	5
fast (10%/s)	15	100	5

4.5 Measurement of Dimensions

Sample width (W) and thickness (T) were measured photogrammetrically using the CCD camera. The camera was calibrated by photographing a steel plate whose dimensions were measured separately with a micrometer. Sample thickness was measured by placing the sample on a mounting plate in its hydrated state, turning the plate onto its side and imaging it. The average thickness was calculated from five evenly spaced thickness measurements taken along the mid-section of the sample between the fabric tabs (Figure 4.6).

4.6 Calculation of Moduli and Extensibility

E_T and E were calculated by taking the gradient of the linear toe phase and collagen phase of the extend stress-strain curve, respectively, as shown in Figure 2.2. To minimise any subjective ambiguity, the two moduli were calculated using moving cell linear regression to identify the most linear region having the largest coefficient of determination [96]. ϵ_M was then calculated from the intersection of these two moduli. All calculations were made using custom-written MATLAB programs (Appendix A).

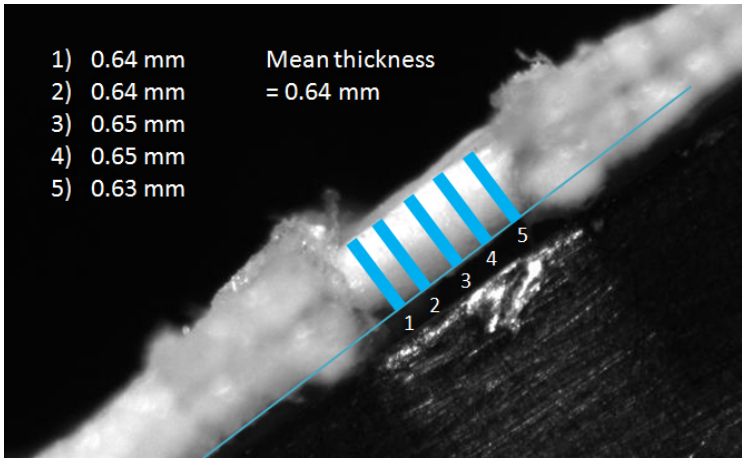

Figure 4.6: Measurements of collagen fibre bundle thickness. The average thickness was taken from five evenly spaced thickness measurements along the fibre bundle mid section between the fabric tabs.

The force, F, was measured by the load cells. A was the cross-sectional area of the sample, and was assumed to be rectangular in shape; thus, it was given by $W \times T$. Non-contact surface strains were measured by manually detecting two of the numerous visible marks close to mid-substance on the sample surface (Figure 4.7). Their relative positions were monitored over the course of the test using the CCD camera. L_O was the original separation between the marks before any displacement was applied; ΔL was the change in separation between the marks when maximum displacement had been reached.

Pilot tests showed that five cycles were sufficient for the tissue to reach steady-state hysteresis. As such, the last cycle in each set was used for the calculation of the two moduli; i.e. the 10th cycle for the slow rate and the 15th cycle for the medium and fast rates.

4.7 Calculation of Phase Shift

ϕ for each frequency was calculated between the input displacements and measured forces of the final five cycles of each stress-strain curve using the Cross Spectral Density Estimate function (`CSD.m`) in MATLAB.

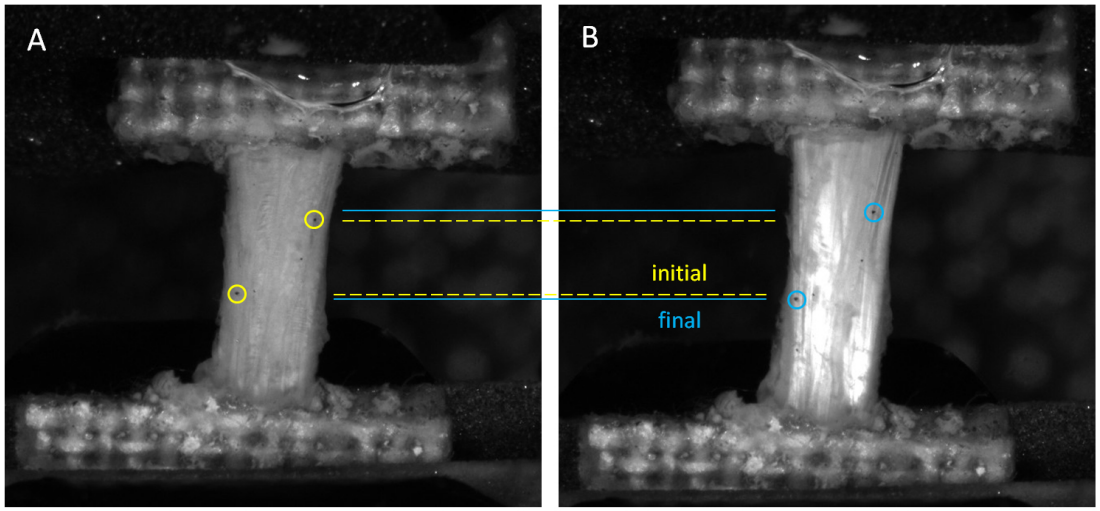

Figure 4.7: Measurement of non-contact surface strains on a fibre bundle sample (A) before any displacement is applied and (B) after maximum displacement has been reached. The relative position of two visible marks on the surface of the sample were detected to determine the actual displacement of the sample. The yellow circles highlight the initial position of the markers; the blue circles highlight the final position of the markers.

4.8 Statistical Analysis

All statistical analyses were performed using IBM SPSS v.20 (IBM, New York, USA) and were conducted under the advice of a statistician. To determine the effects of strain rate, degenerative grade and anatomical region (independent variables) on E_T, E, ϵ_M and ϕ (dependent variables), the data were analysed using a mixed-factor, repeated measures analysis of variance (ANOVA) with one between factor (degenerative grade) and two within factors (strain rate and anatomical region).

To check whether any of the mixed-factor, repeated measures ANOVA assumptions were violated, the following tests were conducted:

- Each group and its post-ANOVA standardised residuals were tested for normal distribution using a Shapiro-Wilk test, with any outliers noted.
- Homogeneity of variances within each group was verified using Levene's Test of Equality of Error Variances.
- Homogeneity of variances of the differences between the repeated groups was verified using Mauchly's Test of Sphericity.

Where appropriate, post-hoc analyses were performed using Bonferroni adjustments. In the case where sphericity was violated, the Greenhouse-Geiser adjustment was used for analysing within-subject effects. A p-value less than 0.05 was considered to be significant. Effect sizes were estimated using the partial eta squared (η^2) value given in SPSS. Small, medium and large effect sizes were defined as $0.01 \leq \eta^2 < 0.06$, $0.06 \leq \eta^2 < 0.14$ and $\eta^2 \geq 0.14$ respectively, in accordance with Kinnear & Gray (2010) [139].

Chapter 5

Microscale: Results and Discussion

5.1 Results

5.1.1 Overview

This chapter details the results of the micro-tensile tests on collagen fibre bundles, as described in Chapter 4.

The most notable findings, with respect to the independent variables, were as follows:

- Degenerative grade did not have a significant effect on E_T, E, ϵ_M or ϕ.
- Anatomical region did not have a significant effect on E_T, E, ϵ_M or ϕ.
- Strain rate had a significant effect on E and ϕ , but did not affect E_T or ϵ_M.

Full results and statistical analyses can be found under Appendix B.

5.1.2 Verification of Statistical Assumptions

For all four dependent variables, normal distributions were verified, except for two cases: the degenerate anterior group at a slow strain rate for E_T (p=0.030); and the degenerate anterior group at a fast strain rate for E (p=0.037). Upon analysing the standardised residuals, normal distributions were also verified, except for the anterior group at a fast strain rate for E_T (p=0.034).

Homogeneity of variances was verified for all 12 groups, except for the anterior group at a fast strain rate for ϕ.

Homogeneity of variances of the differences between the repeated measures was verified for all 12 groups, except for the interaction between strain rate and region for E_T and E.

Given that the assumptions were verified for the majority of the groups, it was assumed that the violations would have a negligible effect on the statistical outcome. As such, the mixed-factor, repeated measure ANOVA was deemed to be suitable.

Amongst the 96 groups (E_T, E, ϵ_M and ϕ, two degenerative grades, four regions, three strain rates), SPSS identified 19 groups as containing outliers. These are given in Appendix B.1. To the author's knowledge, there were no circumstances under which these points could be deemed invalid. None of the samples were considered to be unusual or damaged. A comparison of the original dataset with a revised dataset - with outliers removed - showed that the statistical outcome was not affected. Though there were some differences in the values for p and partial η^2 (main effects and interactions), the same significant relationships were present in the revised dataset. The differences in the main effects are shown in Appendix B.2.3. As such, the author felt it was unnecessary to remove the points that had been flagged as outliers.

5.1.3 The Effects of Disc Degeneration, Anatomical Region and Strain Rate

The mean±SD sample width and thickness of the extracted collagen fibre bundles were measured to be 1.75±0.44 mm and 0.50±0.15 mm, respectively. Full results are given in Appendix B.1.5. Note that the original width of the collagen fibre bundles was not always retained upon extraction. In some cases, the width needed to be trimmed slightly in order to obtain a sample with consistent fibre orientation. Thus, a statistical comparison between healthy and degenerate specimens was omitted, as it would not necessarily reflect the true dimensions of the collagen fibre bundles in each group.

Figure 5.1 shows typical stress-strain cycles for collagen fibre bundles at slow (green), medium (red) and fast (blue) rates.

Figures 5.2, 5.3, 5.4 and 5.5 show the main effect of strain rate on E_T, E, ϵ_M and ϕ, respectively.

Figures 5.6, 5.7, 5.8 and 5.9 show the interactive effects of degenerative grade, anatomical region and strain rate on E_T, E, ϵ_M and ϕ, respectively.

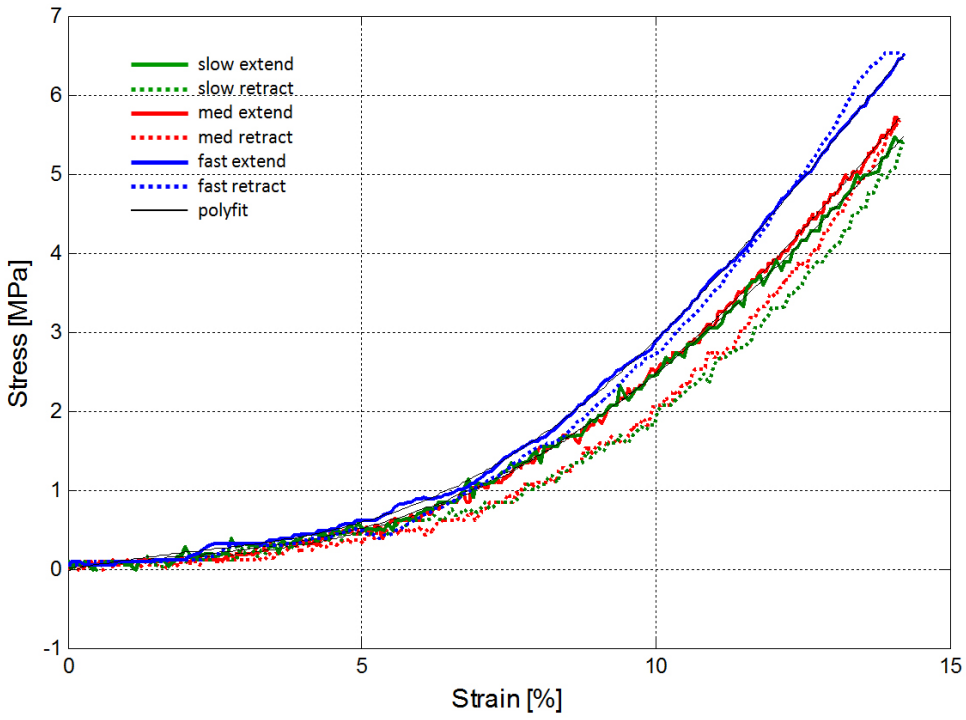

Figure 5.1: Typical stress-strain curves, at slow (0.1%/s), medium (1%/s) and fast (10%/s) strain rates, for collagen fibre bundles.

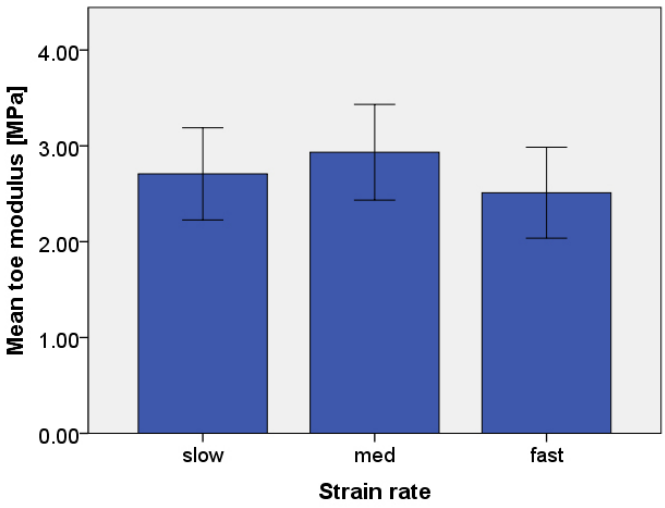

Figure 5.2: Main effect of strain rate (slow, med, fast) on toe modulus, E_T. Columns represent mean (95% CI). No significant differences observed.

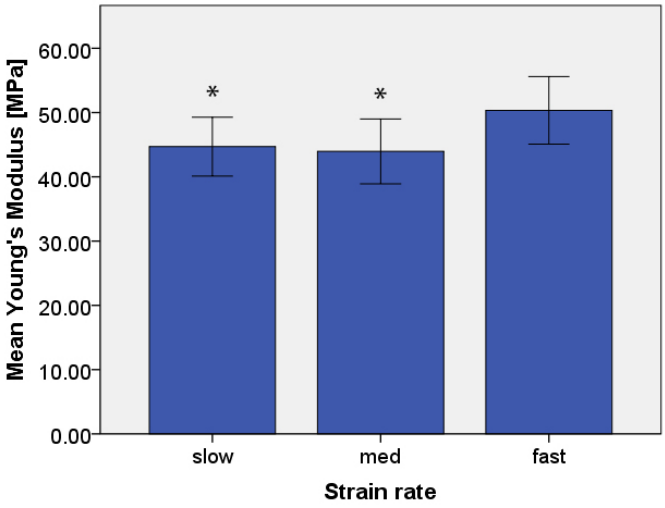

Figure 5.3: Main effect of strain rate (slow, med, fast) on Young's Modulus, E. Columns represent mean (95% CI). Asterisks denote strain rate groups that yielded significantly lower E values compared with the fast strain rate ($p<0.05$).

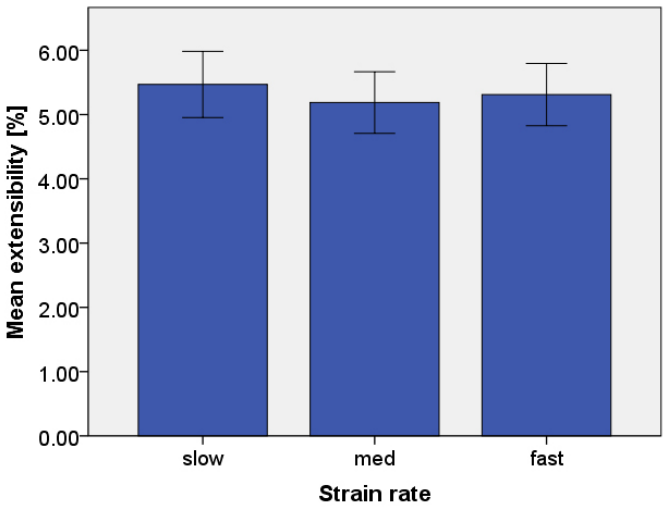

Figure 5.4: Main effect of strain rate (slow, med, fast) on extensibility, ϵ_M. Columns represent mean (95% CI). No significant differences observed.

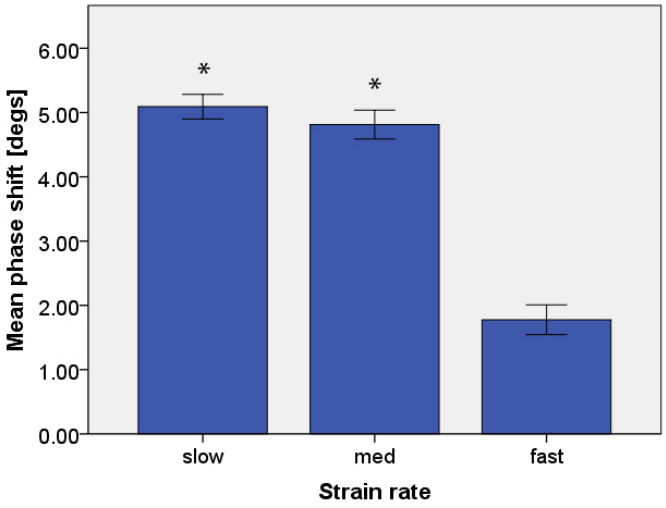

Figure 5.5: Main effect of strain rate (slow, med, fast) on phase shift, ϕ. Columns represent mean (95% CI). Asterisks denote strain rate groups that yielded significantly higher ϕ values compared with the fast strain rate ($p<0.05$).

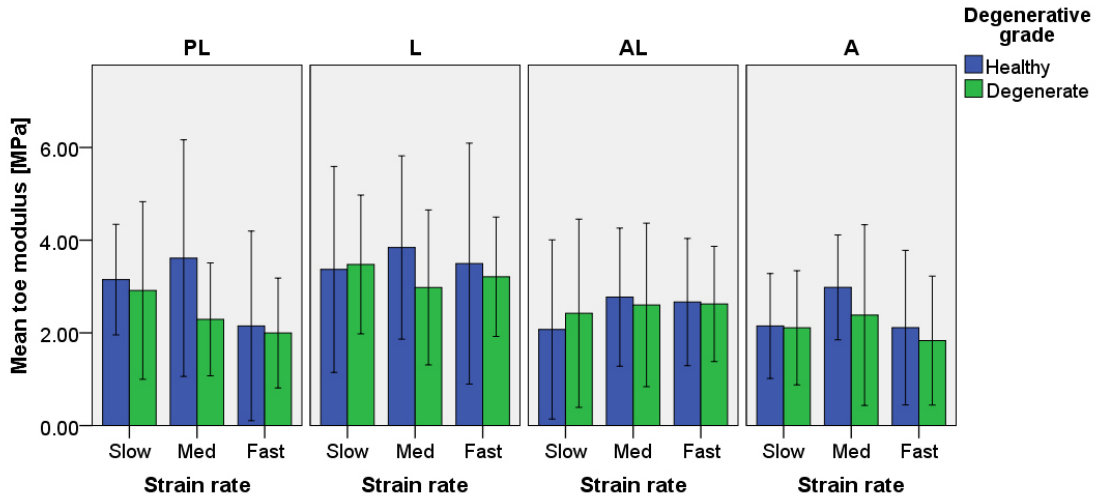

Figure 5.6: Mean (95% CI) toe modulus, E_T, with respect to degenerative grade (healthy, degenerate), anatomical region (PL=posterolateral, L=lateral, AL=anterolateral, A=anterior) and strain rate (slow, medium, fast).

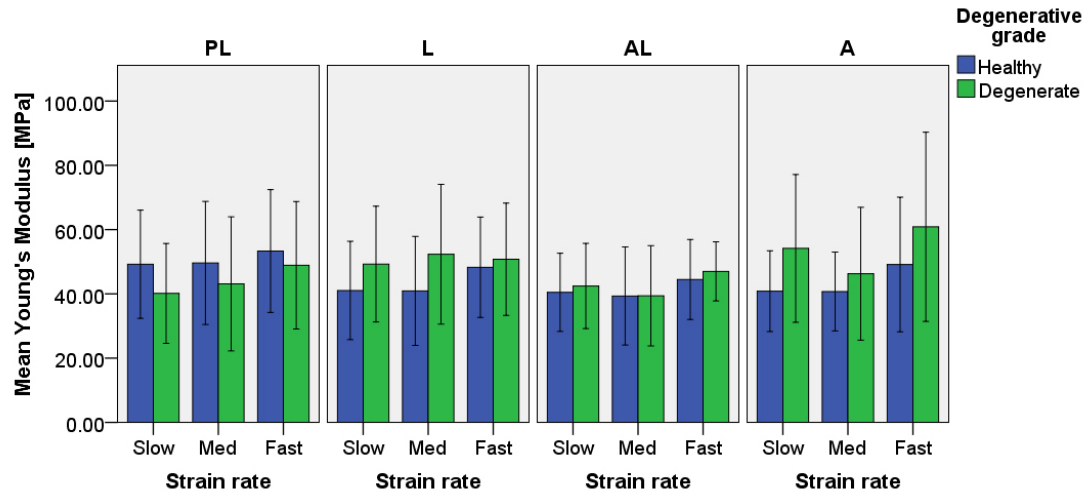

Figure 5.7: Mean (95% CI) Young's Modulus, E, with respect to degenerative grade (healthy, degenerate), anatomical region (PL=posterolateral, L=lateral, AL=anterolateral, A=anterior) and strain rate (slow, medium, fast).

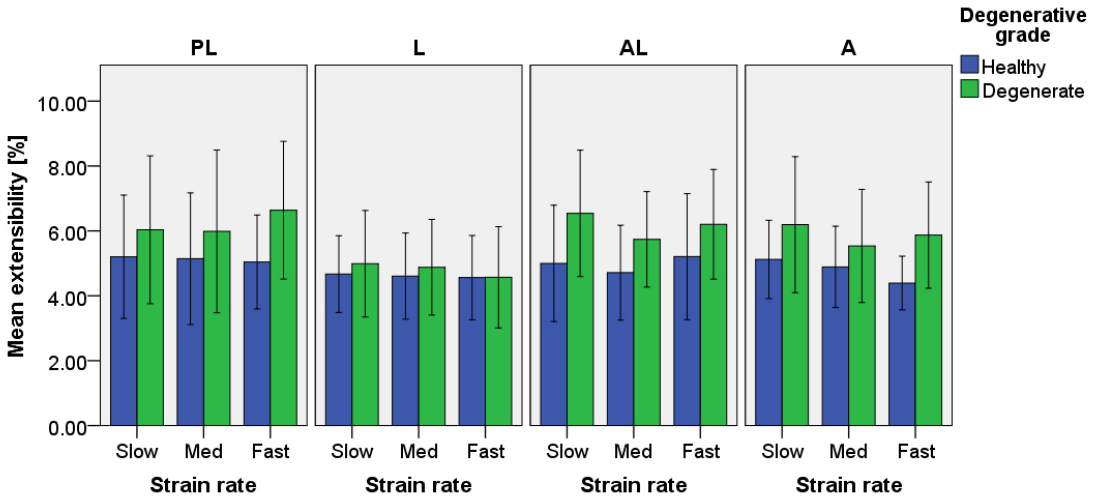

Figure 5.8: Mean (95% CI) extensibility, ϵ_M, with respect to degenerative grade (healthy, degenerate), anatomical region (PL=posterolateral, L=lateral, AL=anterolateral, A=anterior) and strain rate (slow, medium, fast).

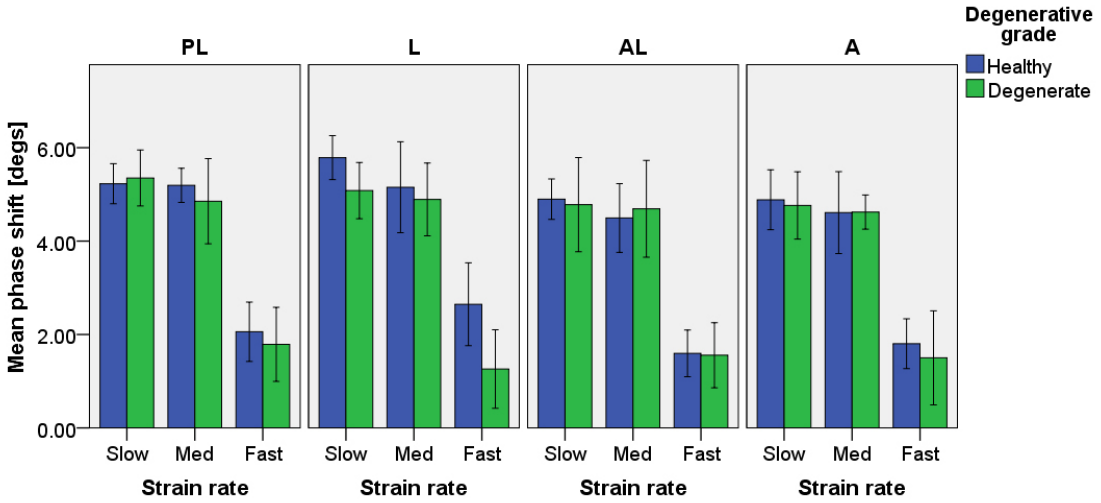

Figure 5.9: Mean (95% CI) phase shift, ϕ, with respect to degenerative grade (healthy, degenerate), anatomical region (PL=posterolateral, L=lateral, AL=anterolateral, A=anterior) and strain rate (slow, medium, fast).

As seen in Figures 5.2-5.5, the main effect for strain rate was not significant for E_T (p=0.284) or ϵ_M (p=0.071); however, E (p=0.003) and ϕ (p=0.000) were significantly affected. For E, pairwise comparisons showed that slow and medium strain rates had no significant differences (p=1.000), but the value of E at the fast rate was significantly higher than those at the slow rate (p=0.038) and medium rate (p=0.033). There was also a noticeable decrease in hysteresis with the fast rate. For ϕ, pairwise comparisons showed that there were no differences between slow and medium strain rates (p=0.110), but ϕ at the fast rate was much higher than the slow and medium rates (both p=0.000).

Thus, the fibre bundles exhibited the same loading response at slower strain rates (i.e. slow and medium). At faster strain rates, the toe and transition phase behaviours were unaffected, but there was an increase in stiffness and elasticity. This verifies the third hypothesis presented in Chapter 3.

No interactions between the independent factors had any significant effect on the four measured variables.

As seen in Figures 5.6-5.9, disc degeneration was not shown to have any significant effect on E_T (p=0.505), E (p=0.614), ϵ_M (p=0.121) or ϕ (p=0.172). Similarly, anatomical region did not significantly affect E_T (p=0.102), E (p=0.708), ϵ_M (p=0.437) or ϕ (p=0.117).

Thus, the toe, transition and collagen phase behaviours were consistent throughout the outer regions of the AF, regardless of degenerative grade, and exhibited the same degree of viscoelasticity. This verifies the first and second hypotheses presented in Chapter 3.

5.2 Discussion

5.2.1 Preparation

The fibre bundle samples were successfully obtained from the four regions within the disc. It was not possible to obtain posterior fibre bundles, as the disc height here tended to be small, making it difficult to work with, and the fibre bundles, when extracted, often comprised multiple layers or were too short to be clamped effectively

(a minimum length of approximately 5 mm was required for secure clamping). As such, the posterior region was abandoned. The posterolateral region also proved to be difficult to work with, but the fibre bundles were eventually extracted with success. Fibre bundle extraction was much easier in the remaining regions, as they tended to be longer and more intact. This observation is consistent with the findings by Tsuji et al. (1993) [108], which describe the disc as having shorter, discontinuous fibre bundles in the posterior/posterolateral region, and longer, continuous fibres in the anterior region.

An ideal tensile test would stretch the tissue to failure. However, despite using fabric tabs on the tissue and lining the clamps with emery paper, the failure point could not be reached without the tissue slipping from the jaws of the clamps. This was due to smooth surface of the tissue, combined with its high tensile strength and testing in fluid, which made it extremely slippery. Nonetheless, preliminary tests showed that the fabric tabs and lined clamps managed to grip the sample much more effectively than using bare clamps alone.

Due to this limitation, it was decided that the tissue would be stretched until it reached the linear collagen phase (see Section 2.1, Figure 2.2), which, for these samples, corresponded to approximately 30% strain. All samples reached this linear region without slipping out of the clamps.

5.2.2 The Effect of Anatomical Region

It is worthwhile revisiting the results from the studies that have examined the effect of anatomical region at the multiple and single lamella levels (refer to Section 2.2) and comparing them to the results from the current study. This is summarised in Table 5.1. This comparison suggests that the disc's mechanical behaviour, with regards to anatomical region, may not be uniform over all hierarchical levels.

Table 5.1: Summary of three hierarchical levels: does anatomical region affect the mechanical behaviour of the AF? Y=yes, as evidenced by at least one study; N=no evidence; blank=unknown.

Level	E_T	$\boldsymbol{E}$	ϵ_M	ϕ	References
Multiple lamellae		Y			[96, 98–101, 104–107]
Single lamella		Y			[113, 114]
Fibre bundles	N	N	N	N	Current study

Hitherto, no studies have considered the regional variability of E_T, ϵ_M and ϕ at the multiple and single lamella level, but the results for E indicate that the regional variability at the lamella levels are not evident at the collagen fibre bundle level. In essence, the lamellae ('brick walls') within the AF have higher E values in the anterior region, but the collagen fibre bundles ('bricks') within the lamellae do not change. The fibre bundles exhibit the same type of behaviour at the toe phase, transition phase and collagen phase, and have the same degree of viscoelasticity, regardless of their region of extraction.

As mentioned in Section 2.2.1, the arrangement of the collagen fibre bundles in the anterior region is much more uniform and continuous compared with that in the posterior region. Proteoglycan, water and elastin content has also been shown to be significantly lower in the anterior region [140, 141].

These differences in ground substance ('mortar') levels could be associated with the mechanical demands for each region. Higher tensile strength in the anterior region could be compensating for the lack of protection from the posterior elements. It has been shown that the anterior region is subjected to much lower levels of axial strain compared with the posterior region. For example, during flexion (i.e. bending forwards), the posterior region of the lumbar AF experiences axial strains of up to 60%, whereas the anterior region experiences only 3% strain during extension (i.e. bending backwards). Furthermore, during torsion, the strain on the collagen fibre bundles in the posterolateral region was greater than that in the anterior region by a factor of two [142]. Thus, while the dominant mechanical strength of the lamella is more likely to be derived from the completeness, endplate-to-endplate continuity and arrangement of the fibre bundles (discussed in Section 2.2.1), the inter- and intra-lamellar binding provided by the ground substance could play an important, albeit minor, role in the AF's ability to withstand strain. The differences in ground substance levels, combined with the *consistency* of collagen fibre bundle regional mechanics, and *inconsistency* of lamella regional mechanics, suggest that the interaction between collagen and the ground substance may also contribute to the mechanical strength of the lamellae [110, 143].

As mentioned in Section 2.2, E values at the multiple lamella level in the circumferential direction (13.2-49 MPa) were noticeably lower than those measured at the single lamella level (64.8-136 MPa). At the collagen fibre bundle level, E was

measured to be 44.7±17.1 MPa (mean±SD). Note that this pertains to the slow strain rate from this study, as the multiple and single lamella studies tended to use slow, quasi-static strain rates.

The reason for this decrease in stiffness at the collagen fibre bundle level could be the fibre bundles 'relaxing' as they are removed from the lamella. When bound within the lamella, the fibre bundles are held tightly in place by the ground substance. This intact network keeps the fibre bundles taut and immovable. Once they have been removed from this network, the fibre bundles - and the fibrils within them - become noticeably looser in structure. This suggests that maximum stiffness is achieved when the collagen fibre bundles are interwoven with the ground substance.

Although no significant differences were found amongst the four anatomical regions, it should be noted that partial η^2, a measure of effect size, was small for E (0.037) and moderate for ϵ_M (0.072), suggesting that a larger sample size may have produced significant differences between two or more of the different regions.

5.2.3 The Effect of Degeneration

The effect of degeneration on fibre bundles found in this study, compared with other hierarchical levels in the AF, is summarised in Table 5.2.

Table 5.2: Summary of three hierarchical levels: does disc degeneration affect the mechanical behaviour of the AF? Y=yes, as evidenced by at least one study; N=no evidence; blank=unknown.

Level	E_T	$\boldsymbol{E}$	ϵ_M	ϕ	References
Multiple lamellae	N	N			[98, 102, 103]
Single lamella					None
Fibre bundles	N	N	N	N	Current study

This comparison suggests that the AF's mechanical behaviour may not be affected by disc degeneration. In essence, the biochemical changes that occur in the AF as a result of disc degeneration do not appear to affect the AF's loading response at the multiple lamella level, nor the collagen fibre bundle level. However, as mentioned in Section 2.2.1, the results at the multiple lamella level should be interpreted cautiously, as there was a decreasing, albeit marginally non-significant, trend in E between healthy and degenerate specimens [98].

Given that disc degeneration is characterised by increased fibrosis and dehydration, a higher concentration of collagen type I, and a lower concentration of collagen type II [68, 97, 144, 145], the lack of change between the mechanics of healthy and degenerate collagen fibre bundles is understandable. Since the collagen fibre bundles already consist primarily of collagen type I in the outer samples tested in this study, a further increase in disc fibrosity would not likely affect their mechanical integrity or viscoelasticity.

This observation indicates that disc degeneration does not target these individual fibre bundles themselves, but could have a more profound effect upon the proteins in the ground substance that hold the fibre bundles together. Indeed, an interesting qualitative observation was that some degenerate fibre bundles were easier to prise apart and remove from the lamellae. The ground substance holding the fibres together in healthy samples seemed more solid and intact, compared with degenerate samples, where the ground substance was more gel-like and crumbly. Comparing the mechanical behaviour of healthy and degenerate single lamella specimens is yet to be explored in the literature, but could provide some clarity for these observations.

The effects of disc degeneration may also be more noticeable in other areas within the disc, such as the NP, which is rich in proteoglycans, collagen type II and water. It has been shown that degeneration causes a decrease in the compressive modulus of the NP; i.e. the NP becomes less effective at swelling and withstanding compressive loads [140, 146] and exhibits more solid-like, as opposed to fluid-like, behaviour [140].

It should be noted that partial η^2 for E_T and E were small (0.038 and 0.022, respectively), suggesting that a larger sample size may have produced significant differences between healthy and degenerate samples.

5.2.4 The Effect of Strain Rate

The effect of strain rate on fibre bundles found in this study, compared with other hierarchical levels in the AF, is summarised in Table 5.3.

Table 5.3: Summary of three hierarchical levels: does strain rate affect the mechanical behaviour of the AF? Y=yes, as evidenced by at least one study; N=no evidence; blank=unknown.

Level	E_T	$\boldsymbol{E}$	ϵ_M	ϕ	References
Multiple lamellae		N			[101, 106]
Single lamella		N			[113]
Fibre bundles	N	Y	N	Y	Current study

In the current study, the stiffness of the fibre bundles increased when they were subjected to a fast strain rate, though this was not observed at the other hierarchical levels. One explanation could be experimental design and the types of strain rates that were used. The fastest strain rate used in the current study was 10%/s; however, the fastest strain rate in the single lamella study was 10 mm/min. Given that the average length of the single lamella samples was approximately 13 mm, this would have been the equivalent of 1.3%/s, which is close to the current study's medium strain rate. As such, it is currently unknown whether strain rate dependency for single lamellae would be observed at higher strain rates.

Similarly, one of the two multiple lamella studies only used strain rates whose magnitudes were within the same order; i.e. 1, 2 and 4%/s [106]. However, it is interesting that the remaining multiple lamella study used four strain rates that ranged from 0.1 to 50%/s, and did not observe any significant differences [101]. It should be noted that only 10 samples were used in this pilot study, and the overall reported significance for the different strain rates was 0.11, which could be considered marginal.

It is worthwhile noting that a study by Costi et al. (2008) [19] investigated stiffness in human whole disc specimens undergoing three different displacements - compression, lateral bending and flexion-extension - at various strain rates. It was found that stiffness increased with higher strain rates, demonstrating that strain rate dependence is also present at the whole disc level.

The decrease in ϕ for the fibre bundles at the fast rate demonstrates that they exhibited more elastic, as opposed to viscoelastic, behaviour when loaded more quickly. This strain rate dependence is a typical characteristic of viscoelastic materials [20, 147]. It is postulated that when the collagen fibre bundles were subjected to tension at slow and medium rates, the tissue had time to adjust and adapt to the change in length, minimising the degree of tensile stress to which the tissue was

subjected. Under the fast strain rate, the tissue was given less time for this rearrangement to occur, and as a result, less energy was lost during the process (producing less hysteresis), but the tissue was subjected to a greater degree of stress.

Interestingly, the fast rate was not shown to have any significant effect on E_T, suggesting that the initial uncrimping of the fibre bundles remained the same for all three strain rates. However, it should be noted that partial η^2 for E_T was moderate (0.100), suggesting that a larger sample size may have produced significant differences between the various strain rates.

The same whole disc study by Costi et al. (2008) [19] investigated ϕ for the three aforementioned displacements. As with the fibre bundles, ϕ decreased with increasing strain rate. For example, for flexion-extension, the mean±SD ϕ ranged from 11.2±2.7 degrees at 0.001 Hz to 5.4±2.5 degrees at 1 Hz. These values are noticeably higher than the mean±SD ϕ measured in the current study, which were 5.09±0.71, 4.81±0.84 and 1.78±0.86 degrees for slow (0.1%/s), medium (1%/s) and fast (10%/s) strain rates, respectively. Thus, the disc as a whole exhibited more viscoelastic behaviours compared with the fibre bundles which were more elastic. This would be expected, since the whole disc study also considered the effects of the gel-like, incompressible NP, and this is likely to have contributed to viscoelasticity. Exploring ϕ at the multiple and single lamella level could verify this shift towards more elastic behaviours as more homogeneous structures are approached, and help clarify the ground substance's mechanical contributions.

5.2.5 Future Recommendations

The following recommendations have been made for tensile testing collagen fibre bundles in the AF.

- The power of the dataset was calculated using G*Power v3.1 [148] using the following conditions: ANOVA repeated measures (within-between interaction), α error probability = 0.05, non-sphericity correction = 1. The respective powers for the four dependent variables (E_T, E, ϵ_M and ϕ) were 0.07, 0.06, 0.20 and 0.16, which are all considerably lower than the standard, accepted power value of 0.8. In order to obtain adequate power with these experiments, the sample sizes would need to be 126, 218, 26 and 32, respectively. Obtaining

enough tissue to reach these sample sizes would be a challenge, given that human tissue was being used. However the author does acknowledge that the sample size used in this study was small, and given that the effect size was low to moderate in a number of cases, it is possible that a larger number of samples could have produced different statistical outcomes.

- The main limitation with this tensile testing technique was the inability to secure the tissue in a way such that stretching to failure could be successfully achieved. The critical area was the clamping of the sample. Despite trying to secure the sample using fabric tabs at both ends, the rupture phase in the stress-strain cycle could not be reached without the sample slipping out of the clamps. This problem with clamping is relatively common in AF studies [98, 99, 113, 114]. A clamping force that can exceed the ultimate tensile strength of the AF and allow it to fail mid-substance is necessary.

- The non-contact tracking method used to calculate strain monitored two points on the tissue's surface. Only two points were used, as it was difficult to find visible surface markers, and given that the tracking was done manually, a greater number of points was not attempted in these experiments. It has been shown that fibre bundles in tendon fascicles are discontinuous, and undergo significant interfibrillar sliding during loading. Indeed, interfibrillar load transfer is likely to be a fundamental part of the loading response [149]. Since there are structural parallels between tendons and AF tissue, it is possible that this interfibrillar sliding also exists between AF fibre bundles. Consequently, the use of only two surface markers may have introduced a degree of error to the strain measurements, and contributed to the variability between samples. Future investigations should perhaps consider using texture correlations to cover a larger portion of the surface area.

- This study tested all specimens in the same strain rate order - i.e. medium, slow, fast - as it was most time-efficient way of performing the tests with the CellScale apparatus. Some samples could be not used for the final dataset due to a number of reasons; e.g. they could not reach a minimum of 30% strain without slipping out of the clamps. The medium strain rate was the easiest strain rate to initially test the sample's suitability, since the slow rate

would take a long period of time, and the fast strain could have possibly led to rupturing. It is possible that the strain rate testing order could have affected the loading response of the tissue. Thus, a more randomised strain rate order would have eliminated any possible influence of strain rate order upon the tissue's loading response.

- This study used tissue that had been thawed from a frozen state, as this was the most practical way of obtaining, preparing and testing human cadaver tissue. Pilot tests indicated that when the samples were thawed, tested, frozen again, thawed again, and tested again, the loading response was not significantly affected. An example is given in Appendix B.2.4). Whilst this does not necessarily indicate that fresh tissue behaves in the same way as thawed tissue, it does indicate that multiple freezing cycles do not appear to affect the behaviour of the collagen fibre bundles. Ideally, this type of tensile testing should use freshly excised tissue to eliminate any possible effects of freezing, though this presents a number of practical challenges.

- Four different anatomical regions were considered in this study, though the posterior region was not included, as the fibre bundles here were not intact or too small to clamp in the apparatus. The posterior region in the disc specimens tended to be narrower (i.e. smaller in height) than the other regions. If it were possible, comparing posterior samples with the existing four regions would provide further insights to the effects of anatomical region. Though it would be challenging to obtain an adequate number of samples for each group, testing various degenerative grades - as opposed to merely categorising them as healthy or degenerate - could enable more comprehensive analyses, such as correlating the mechanical parameters with degenerative grade or age.

- This study was concerned with the behaviour of the outer AF, mainly because it contains the highest percentage of collagen type I [97], and this was the focus of the nanoscale experiments. Future studies could consider the behaviour of the inner AF to determine whether it possesses the same behavioural consistency as the outer AF. Given that the proportions of the collagen types change with proximity to the NP, the behaviour of the inner AF may well be very different. Investigating the lamellae located in the transition zone could also

clarify the effect that the NP has upon the AF fibre bundles in that region.

- A number of finite-element analyses of the disc consider its micromechanical properties, and in some cases, model the individual fibre bundles [150–152]. However, the material properties used to describe the AF collagen fibre bundles are commonly estimated from the properties of self-assembled fibres, or fibres extracted from other collagenous tissues, and some of these values are grossly overestimated. For example, Schroeder et al. (2006) [150] used an E value of 380.8 MPa, which was derived from a study investigating the elastic properties of self-assembled collagen fibres, vastly different in structure to AF fibre bundles [153]. Inputting material parameters that have been directly measured from human AF collagen fibre bundles could lead to more accurate loading predictions in these models.

- Finally, it would be useful to examine the relationships between the mechanical behaviour of the collagen fibre bundles and their biochemical composition in a single, cohesive study. Extracting the fibre bundles from the lamella network would have unbound them from the intra-lamellar ground substance; however, residual ground substance is likely to have remained attached and it is unknown whether this would have affected the fibre bundles' behaviour. Quantifying the types of protein present in the fibre bundles - such as the collagen types, proteoglycans and elastin - could lead to insightful correlations with anatomical region and degenerative grade. Indeed, elastin has been shown to enhance the mechanical integrity of radial lamella sections [96], so they could play a similar role within the fibre bundle structure.

5.3 Chapter Summary

This chapter of work has shown that the loading response of collagen fibre bundles is consistent throughout the outer AF, regardless of degenerative grade. This information provides insights to the components of the AF that are affected by disc degeneration, and could therefore narrow down what needs to be targeted if more effective methods of treatment are to be developed. Quantifying the AF's micromechanical behaviour could also assist in the development of more comprehensive finite-element

models of the disc, which could potentially lead to more accurate loading predictions at the whole-disc level.

With regard to strain rate dependence, the loading response of fibre bundles does not change at slow strain rates; however, they exhibit stiffer, more elastic behaviours when fast strain rates are applied. Under sedentary conditions, the AF would intrinsically endure slow, quasistatic tension. Conversely, fast activities, such as those associated with sport, would subject the AF to higher strain rates. Investigating this type of fast loading could allow us to determine the extent to which the disc and its components need to be loaded before damage occurs.

This work sheds light upon the mechanical behaviour of collagen fibre bundles, which has not yet been investigated. Exploring the disc at a deeper level - i.e. at the nanoscale - could provide even further insights to the disc's multiscale mechanical behaviour. This will be the focus of Part III.

Part III

Nanoscale Experiments: Collagen Fibrils

Chapter 6

Nanoscale: Materials and Methods

6.1 Introduction

The aim of the nanoscale experiments was to measure E in collagen fibrils.
Two techniques were explored:

- Nanoindentation
- Nano-tensile testing

The final results for the collagen fibril properties were obtained using nanoindentation, whose method and results will be described in this chapter and Chapter 7, respectively.

An additional experiment aimed to develop a novel nano-tensile testing technique for collagen fibrils, but was not used to obtain final data. It will be described in Chapter 8.

6.2 Experimental Setup: The Atomic Force Microscope

6.2.1 Basic Operation

Due to the miniscule size of the collagen fibrils, the nanoscale experiments required the use of an *atomic force microscope* (AFM). The AFM is a type of scanning probe microscope; i.e. it scans the surface of the sample using a probe, and then examines

the physical interactions between the probe and the sample to deduce the sample's topographical and mechanical properties. It does not rely upon light or an electron beam to illuminate and magnify the sample, which eliminates the limits of resolution associated with other microscope techniques, like optical microscopy. As such, the AFM is capable of resolving objects as small as 2 nm [154], making it highly suitable for exploring collagen at the fibril level.

The AFM used in this study was a Bruker MultiMode 8 with NanoScope V Controller (Bruker Corporation, Massachusetts, USA). The complete AFM setup, depicted in Figure 6.1A, comprises the following components:

- MultiMode 8 AFM unit;
- NanoScope V controller;
- PC and monitor with NanoScope Analysis 8.10 software.

The Multimode 8 AFM unit (Figure 6.1B) is composed of three main parts [155]:

1. *AFM chip*

   The AFM chip is the only part of the system in contact with the sample. Its critical features are the microscopic cantilever, which is suspended over its edge much like a diving board; and the tip, which is located at the distal end of the cantilever and serves as the probing mechanism. As the tip makes contact with the sample surface, the cantilever deflects, in accordance with Hooke's Law (Equation 6.1), where F is force, k is stiffness and x is displacement.

   $$F = -kx \tag{6.1}$$

   By measuring this deflection, in addition to other parameters, certain topographical and material properties about the sample, such as elastic modulus and hardness, can be ascertained. Depending on the application and mode of use, the shape, material and stiffness of the cantilever can vary, as can the geometry of the tip.

Figure 6.2 shows the dimension convention for cantilevers and tips, and Table 6.1 shows the specifications of the chips used in this research. Note that for Bruker MultiMode instruments, the AFM chip remains completely stationary, except for the cantilever deflecting in the vertical (z) direction.

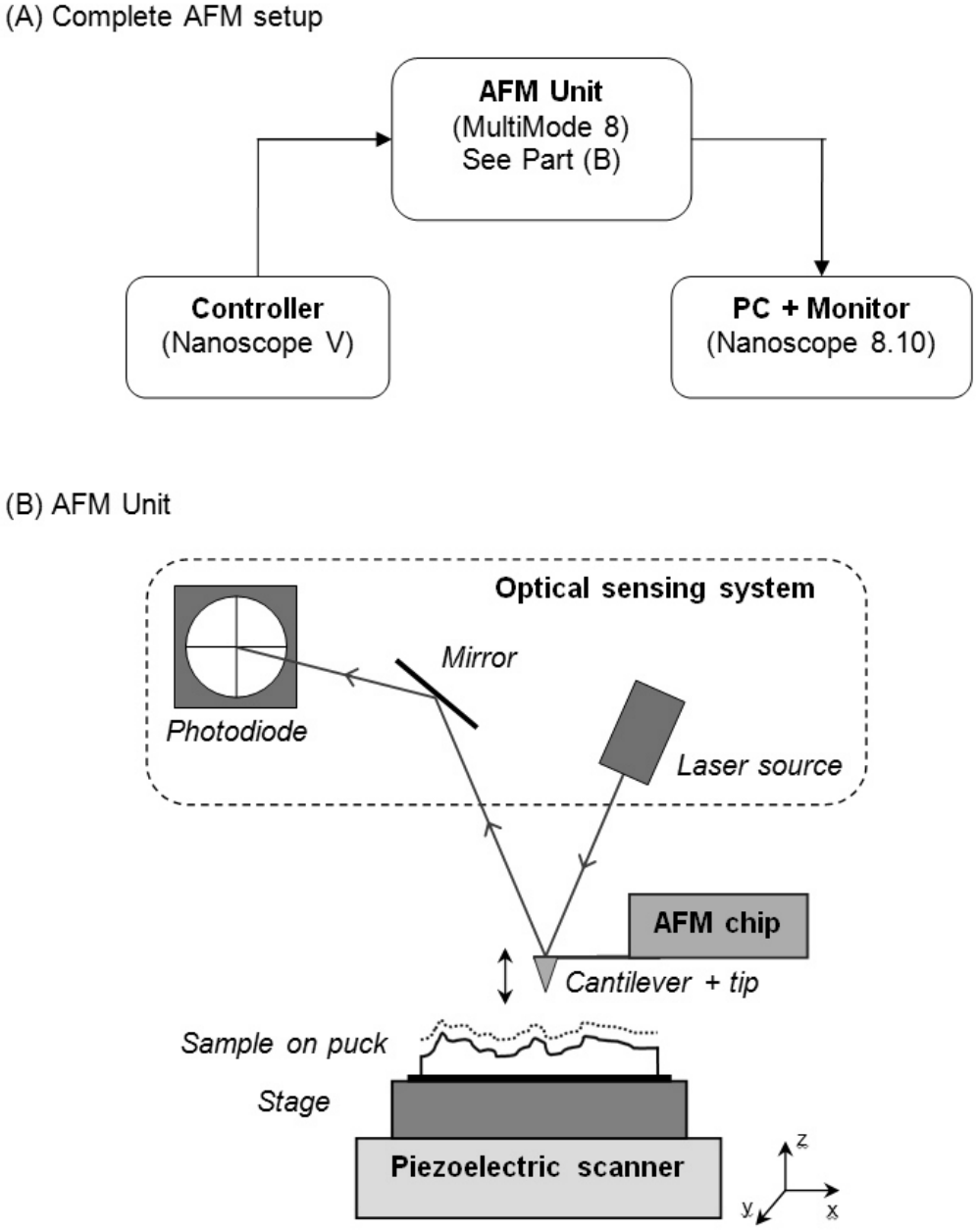

Figure 6.1: The atomic force microscope (AFM). (A) Complete AFM setup; (B) AFM unit. Note that diagram is not to scale.

Table 6.1: Specifications of AFM chips used in this research. k=cantilever spring constant; ν=resonant frequency; W_C=cantilever width; L_C=cantilever length; T_C=cantilever thickness; W_T=tip width; H_T=tip height. Note that given values are nominal, as quoted by the manufacturers.

Tip	**Operation mode**	**Cantilever geometry**	**Material**	***k* {min,max} [N/m]**	**ν {min,max} [kHz]**	**Dimensions**				
						W_C [μm]	L_C [μm]	T_C [μm]	W_T [nm]	H_T [μm]
Bruker OTR-8 [156]	Contact	Triangular	Silicon nitride cantilever and tip	0.15{0.07,0.3}	24{16,32}	30	200	0.8	15	2.5-3.5
Bruker SNL-10 [157]	Contact	Triangular	Silicon nitride cantilever, silicon tip	0.12{0.06,0.24}	23{16,28}	35	200	0.6	2	2.5-8.0
Bruker FMV [158]	Contact/ tapping	Rectangular	Antinomy -doped silicon	2.8{1,5}	75{50,100}	28	225	2.75	10	10-15
MikroMasch NSC15 [159]	Tapping	Rectangular	Silicon nitride cantilever and tip	40{20,80}	325{265,410}	35	125	4	10	20-25

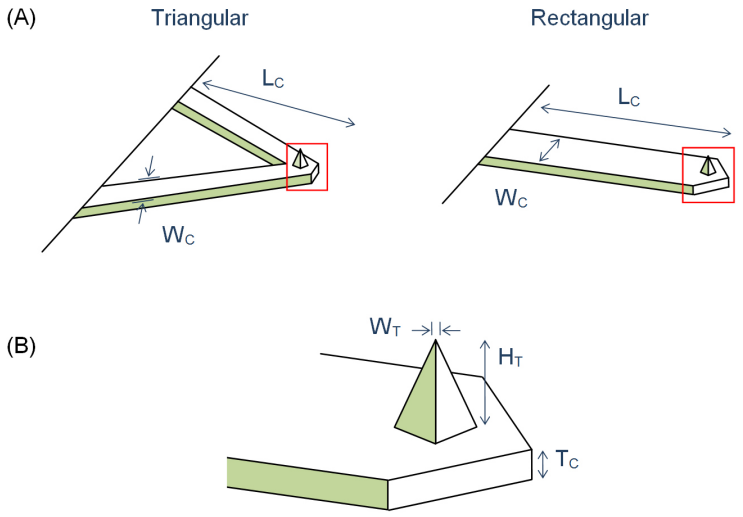

Figure 6.2: Diagram of the AFM (A) cantilever (triangular and rectangular), and (B) tip. W_C=cantilever width; L_C=cantilever length; T_C=cantilever thickness; W_T=tip width; H_T=tip height. Note that diagram is not to scale.

2. *Piezoelectric scanner*

The sample, mounted on a metal puck, is placed on a stage, which is controlled by a piezoelectric scanner capable of moving in three dimensions (x, y and z directions). The scanner, whose movements are controlled by the NanoScope V controller, is responsible for positioning the sample underneath the tip by moving the stage in the horizontal and vertical axes. The movement of the scanner is carried out by a piezoelectric crystal, which expands and contracts as a voltage is applied to it. The Bruker MultiMode features various interchangeable scanners. The E and J scanners were used in this research; their specifications are given in Table 6.2.

Table 6.2: Specifications of Bruker MultiMode scanners used in this research [154].

Model	**Scan size (x, y directions)**	**Vertical range (z direction)**
AS-12VLR (E vertical)	10 μm x 10 μm	2.5 μm
AS-130VLR (J vertical)	125 μm x 125 μm	5.0 μm

3. *Optical sensing system*

The optical sensing system measures the deflection of the cantilever as the tip interacts with the sample surface. A laser is shone onto the highly-reflective top surface of the cantilever, reflected off a mirror, and directed onto a photodiode, which precisely measures the cantilever deflection. This information is then sent to the PC, where it is processed and transformed into an image that we view on the monitor.

6.2.2 Modes of Use

This research used two modes of operation: topographical imaging and force spectroscopy. These are summarised in Figure 6.3.

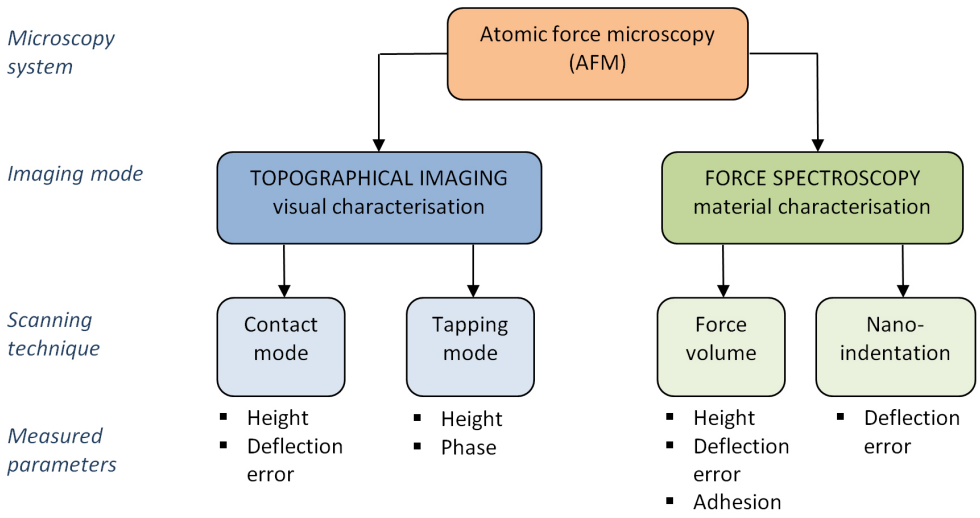

Figure 6.3: Breakdown of AFM techniques used in this research.

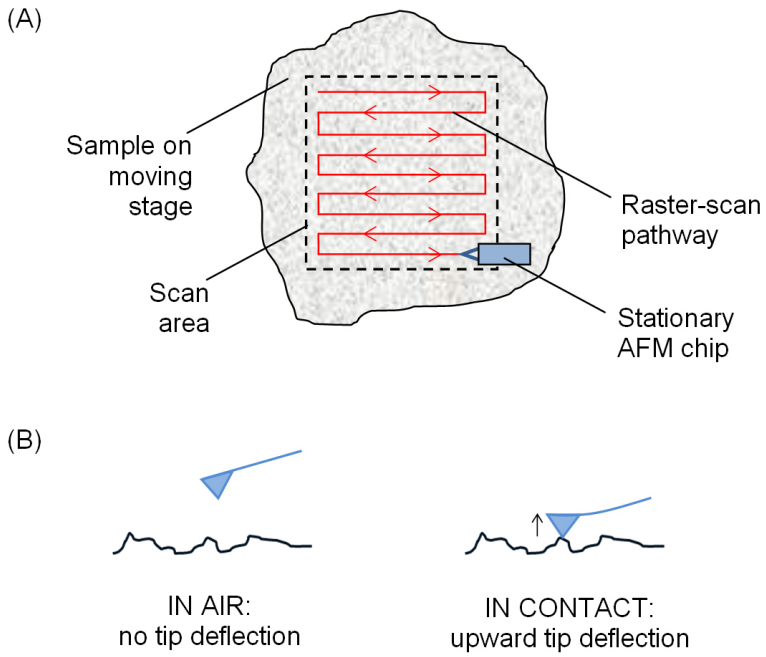

Figure 6.4: Tip-surface interactions. (A) The raster-scan pathway of the AFM tip over the sample surface; (B) the deflection of the cantilever as the tip makes contact with the surface.

Topographical Imaging

Topographical imaging is used for the purposes of visual characterisation, and the output is a two-dimensional (2-D) or three-dimensional (3-D) image of the sample surface. There exist several modes of operation for topographical imaging, and all have uses for different applications. Two particular modes were used for this research: *contact mode* and *tapping (intermittent) mode*. Their processes are described below.

Contact Mode

In this mode, the tip was brought into contact with the sample, and the scanner moved back and forth from top to bottom, raster-scanning the surface of the sample over a specified area (Figure 6.4A). The tip ran over the contours of the surface, causing the cantilever to deflect (Figure 6.4B). The controller then adjusted the z position of the sample such that a constant deflection (*deflection set-point*), as specified by the researcher, was maintained, allowing the tip to trace the surface without crashing into it.

Different parameters can be used to construct different topographical images.

The contact mode images in this research were constructed from *height data*, which corresponded to the change in scanner height needed to keep the cantilever deflection constant; and *deflection error data*, which represented the differential signal from the top and bottom segments of the photodiode relative to the deflection set-point specified by the researcher [154].

Tapping (Intermittent) Mode

In tapping made, the tip made intermittent contact with the sample, as opposed to continuous contact, as in contact mode. The tip was held above the surface whilst it oscillated at its resonant frequency with a particular amplitude. This oscillatory amplitude decreased as the tip was brought into contact with the surface.

The tip was raster-scanned over the surface, as in contact mode, and was brought into contact with the surface until the oscillatory amplitude was reduced to a certain amplitude set-point specified by the researcher (e.g. 80% of the free amplitude). This amplitude set-point was maintained by the controller, allowing the tip to merely brush over the surface as the image was being acquired. The force being applied to the surface was governed by the amplitude set-point (e.g. a large amplitude set-point minimises the force being applied to the surface).

In this research, tapping mode images were constructed from *height data* (as in contact mode); *amplitude data*, which measured the change in amplitude relative to the amplitude set-point; and *phase data*, which measured the cantilever's phase of oscillation relative to the piezo drive signal [154].

Force Spectroscopy

In force spectroscopy, the material properties of the sample are deduced from dynamic interactions between tip and object. This research used two force spectroscopy modes: force volume imaging and nanoindentation. Both rely upon the *force curve*.

Force Curves

A force curve is a plot of the force on the cantilever as it is brought into contact with the sample surface. In essence, it is a representation of the tip-surface interaction, and various mechanical, chemical and electrostatic properties, such as adhesive force and elasticity, can be derived from it.

	Description	Tip-surface interactions	Point on force curve
1	Approach (non-contact) – stage is raised towards tip, starting from ramp size (RS).	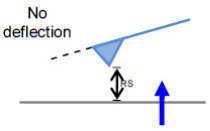	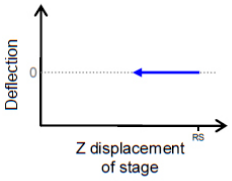
2	Jump to contact – tip deflects downwards due to surface attraction.	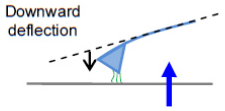	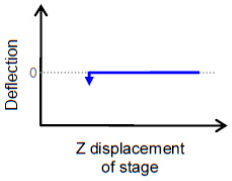
3	Contact – tip is momentarily zero again.		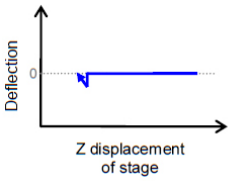
4	Repulsive contact – as stage is raised to the trigger threshold (TT), tip undergoes upward deflection.	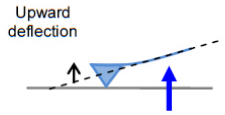	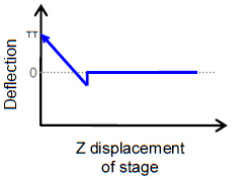
5	Retract – stage is lowered, and upward deflection decreases to zero.		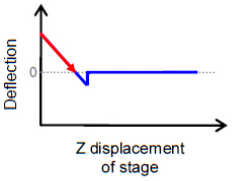
6	Adhesion – as stage moves further away, tip adheres to surface, causing downward deflection.	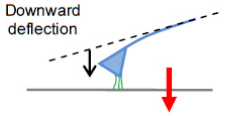	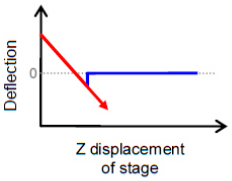
7	Separation – tip pulls away from surface and deflection resumes to zero.	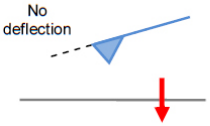	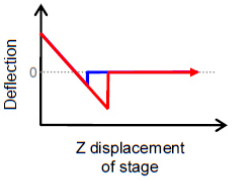

Figure 6.5: Breakdown of a typical force curve relative to tip-surface interactions

Figure 6.5 summarises how a force curve is attained. Initially, the tip is held above the sample at a certain distance called the *ramp size*, specified by the user. In typical cases where long-range attraction or repulsion is absent, the cantilever experi-

ences zero deflection. The stage is then raised towards the tip by the piezocontroller, and due to Van der Waals attractive forces, the tip will experience 'jump-to-contact' motion when in close proximity to the surface [160], causing the tip to deflect downwards. With the tip now in contact with the surface, the piezo raises the stage until the tip reaches a certain deflection, called the *trigger threshold*, also specified by the user. Once the trigger threshold is reached, the stage moves away from the tip until the ramp size is resumed. However, during this retract phase, the tip tends to adhere to the surface, causing the tip to deflect downwards. Finally, once the tip-surface separation is enough to overcome this adhesive force, the tip disengages from the surface and the deflection reverts back to zero. A detailed image of a force curve is given in Figure 6.6.

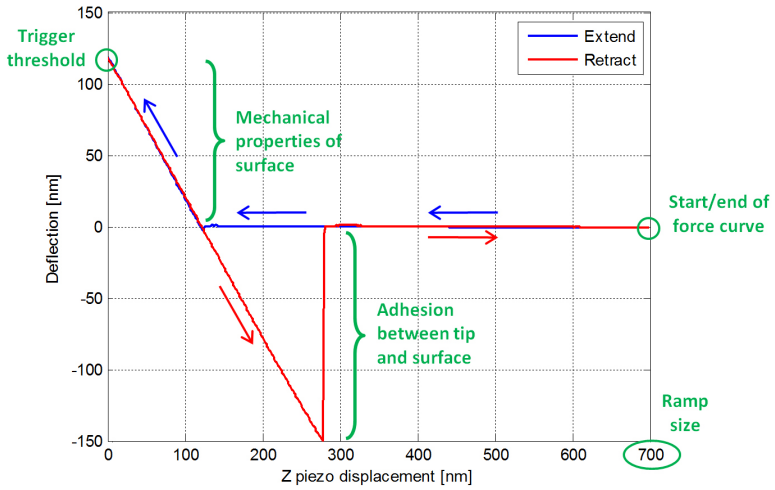

Figure 6.6: A force curve representing z displacement versus tip deflection. The regions of the curve corresponding to the surface's mechanical properties and tip-surface adhesion are highlighted.

Force Volume

Force volume imaging is the process of taking an array of force curves over the entire scan area (Figure 6.7). For each curve, the user can select a particular mechanical property, such as adhesion, and then map the value of that property for each region of the array accordingly. The result is a low-resolution map of the surface, but in terms of mechanical properties rather than topography. In this research, 16×16 and 32×32 force curve arrays were used (Figure 6.8).

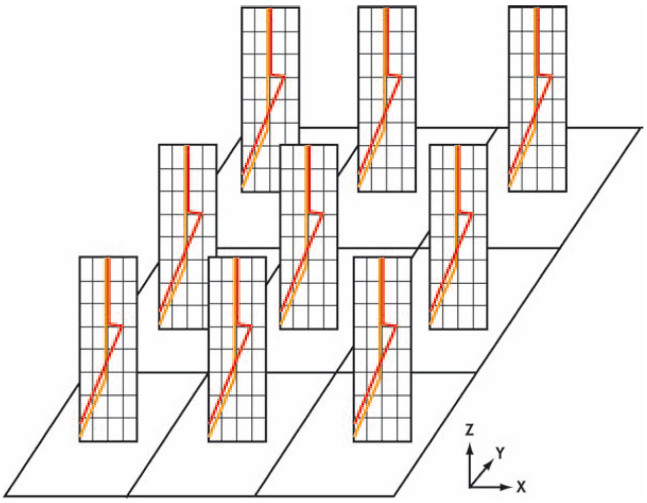

Figure 6.7: Force volume imaging. Force curves are taken over the entire scan area, and then selected parameters, such as adhesion, can be mapped accordingly. (From Heinz et al. [161].)

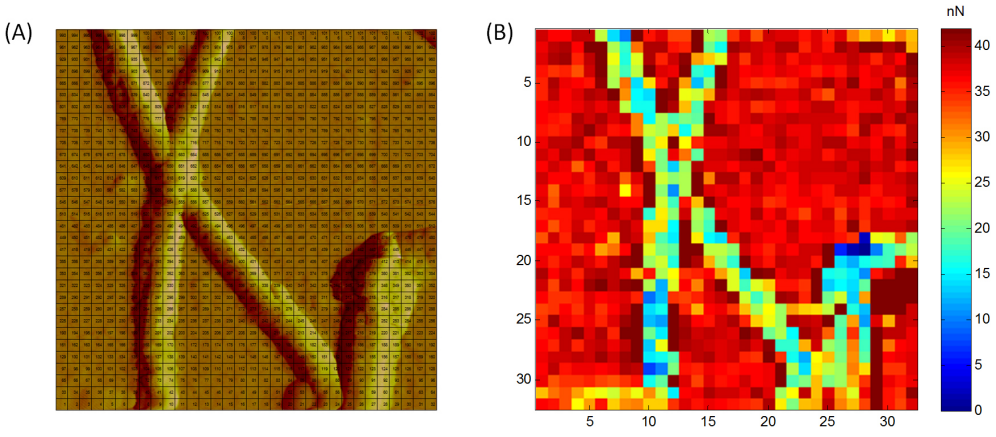

Figure 6.8: Example of force volume imaging for collagen fibrils. (A) 2×2 μm height image of collagen fibrils on mica, divided into a 32×32 array; (B) the corresponding force volume image, representing adhesion between the tip and the sample.

Nanoindentation

If the tip is pushed into the surface with enough force during this force curve process, the surface can be *nanoindented* (Figure 6.9). This function is particularly relevant for this research, because the nanoindentation information can be substituted into an equation, such as the Hertz Model, to indirectly derive the sample's E value. The theory for this model was covered in Section 2.2.4.

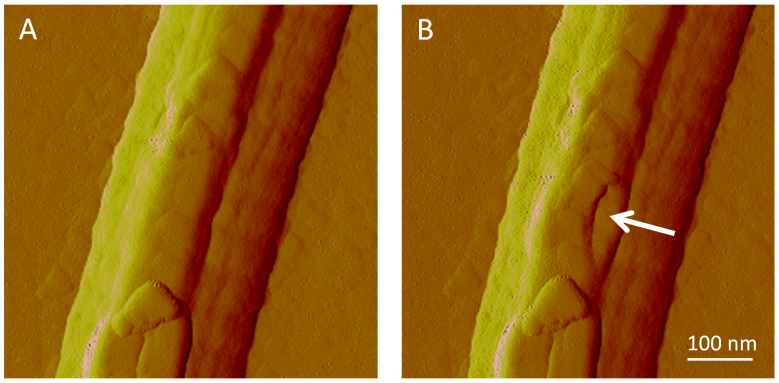

Figure 6.9: Visible indent on a collagen fibril, (A) before and (B) after nanoindentation. Nanoindention is shown by the arrow.

6.2.3 Cantilever Spring Constant Calibration

To determine the force on the cantilever, the deflection and cantilever spring constant, or stiffness, are required (Hooke's Law, Equation 6.1). Deflection is measured by the instrument, and a nominal spring constant value is provided by the tip manufacturer. However, the actual spring constant of the cantilever can vary considerably, so it is necessary to calibrate it independently before the tip is used. Thermal tuning was the primary calibration method used in this research; however, the Sader method was also used on selected AFM tips for verification. These methods are covered in Appendix C.

6.3 Specimen Preparation

To allow a direct comparison between the different structural levels, the collagen fibrils used in the nanoscale experiments were extracted from the fibre bundles used

in the microscale experiments.

The 56 frozen collagen fibre bundle samples from the microscale experiments (healthy N=7, degenerate N=7, from PL, L, AL and A anatomical regions) were thawed at room temperature for approximately 30 minutes. The fibre bundles were then lifted out of the PBS solution and placed onto a board. Fibres were teased out from the mid-region of the sample using surgical needles and tweezers. The fibres were placed onto freshly cleaved mica substrates attached to metal pucks with double-sided tape. The fibres were left to dry for approximately 10 minutes, before a thin layer of nail varnish (Cutex, Connecticut, USA) was painted on two opposite sides, leaving an unvarnished strip down the centre of the puck, 0.5-1.0 mm in width (Figure 6.10). The purpose of the varnish was to hold the fibres onto the surface of the mica.

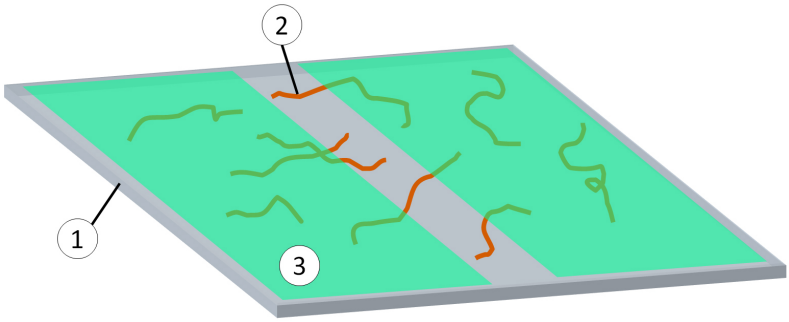

Figure 6.10: Mica surface painted with varnish. (1) Mica surface; (2) fibrils on surface; (3) varnish on sides of the mica, with gap in the middle.

Note that prior to the development of this 'fibre-teasing' technique, the extraction of collagen type I using a neutral salt solvent was attempted, but abandoned due to an inadequate collagen yield. The details of this salt extraction method are given in Appendix D.

6.4 Mechanical Testing: Nanoindentation

A Bruker FMV chip was inserted into the AFM, and the laser was aligned with the cantilever such that the maximum reflection signal was obtained. The vertical and horizontal signals of the photodiode were zeroed.

The sample was placed into the sample stage. A droplet of PBS was deposited on the unvarnished strip and then allowed to evaporate at room temperature. Testing

commenced immediately after the PBS evaporated, which could be clearly seen under an optical microscope (Figure 6.11).

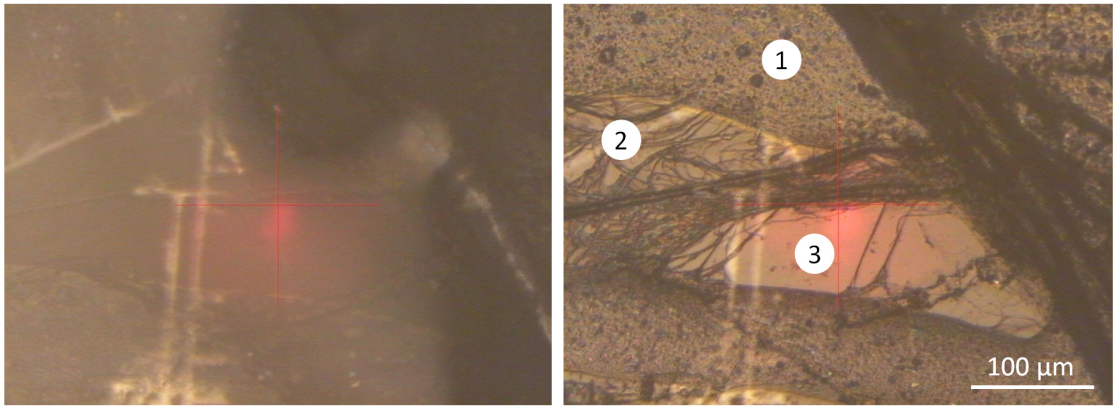

Figure 6.11: Mica surface before (left image) and after (right image) PBS droplet evaporation. (1) Varnish; (2) fibrils; (3) mica surface.

The sample was contact imaged over a large area (e.g. 30×30 μm) to locate the fibrils, which tended to be on the edges of the fibres (scan rate 1 Hz, deflection set-point 0.2 V). Suitable regions were defined as those that contained evenly distributed, single fibrils. Once a suitable region was chosen, the zoom was increased until the scan area was approximately 2×2 μm (Figure 6.12) and contained three individual fibrils.

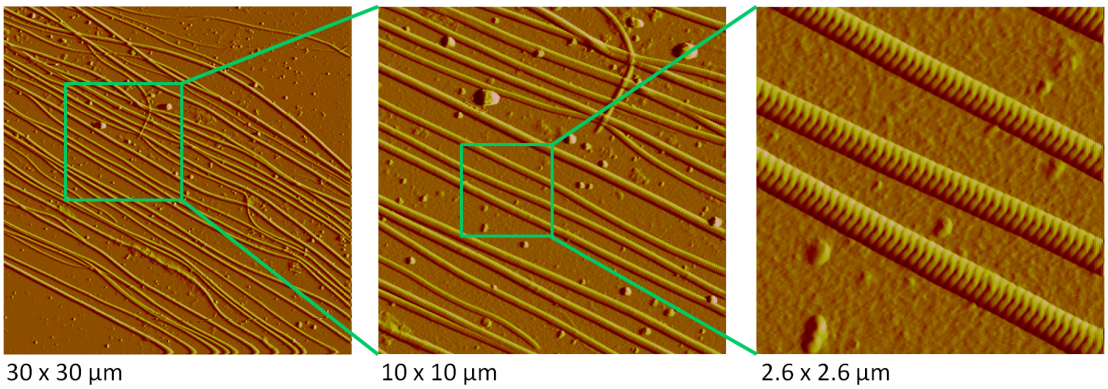

Figure 6.12: AFM images of fibrils on mica surface at scan sizes of 30×30 μm, 10×10 μm and 2.6×2.6 μm.

The width and thickness of the fibrils were measured using the 'dissection' tool in the NanoScope Software, which measured the displacement between two points specified by the user (Figure 6.13).

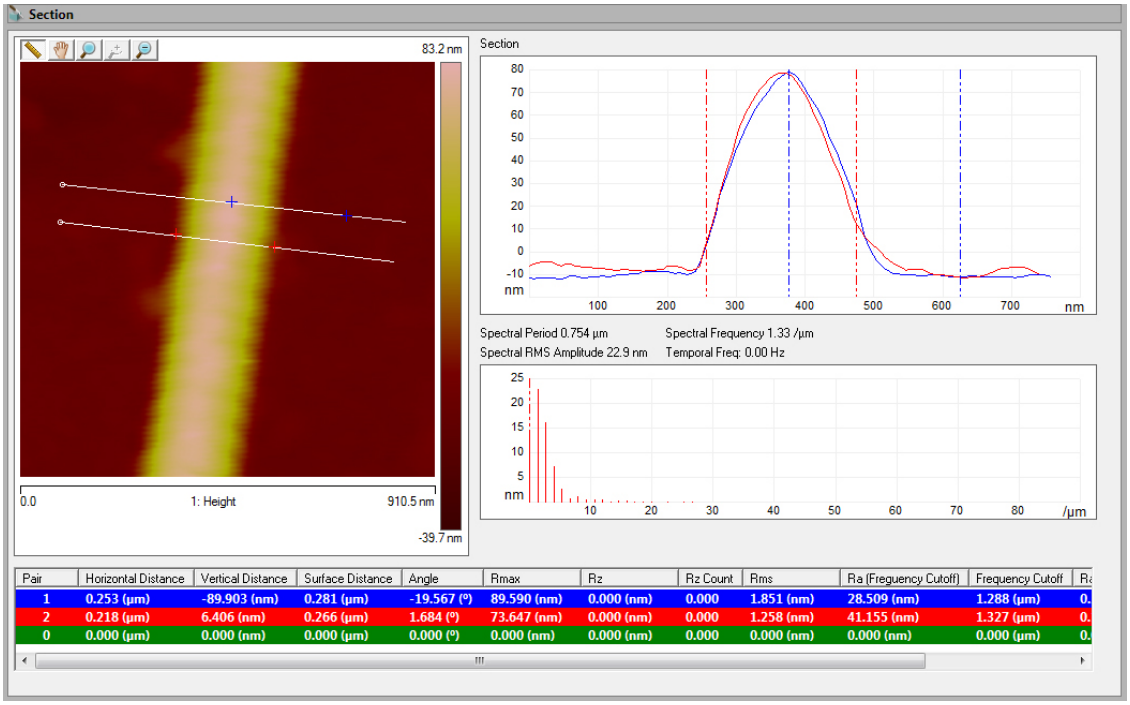

Figure 6.13: Example of fibril dimension (thickness and width) measurement using the NanoScope dissection tool. Thickness is denoted by the vertical distance between the blue markers (89.9 nm), and width by the horizontal distance between the red markers (218 μm).

Nanoindentation was then carried out over a square array consisting of 32×32 nanoindentations (i.e. 1024 nanoindentatons in total). Each nanoindentation was performed in the following way:

- The tip was held above the surface with a ramp size of 500 nm.
- The tip was brought into contact with the surface, at a velocity of 814 nm/s, until a trigger threshold of 100 nm was attained. Pilot tests demonstrated that this threshold was sufficient for the nanoindentation to reach 5% of the fibril diameter, which was where the Hertz Model was valid.
- The tip was lifted from the surface to the 500 nm ramp size again.

A sample force curve was taken from the mica surface to serve as a reference. A curve taken from the collagen surface was then superimposed with the mica curve such that the tip-surface contact point was overlapping (Figure 6.14, left image). The nanoindentation of the collagen was given by the horizontal distance between the mica and collagen curves.

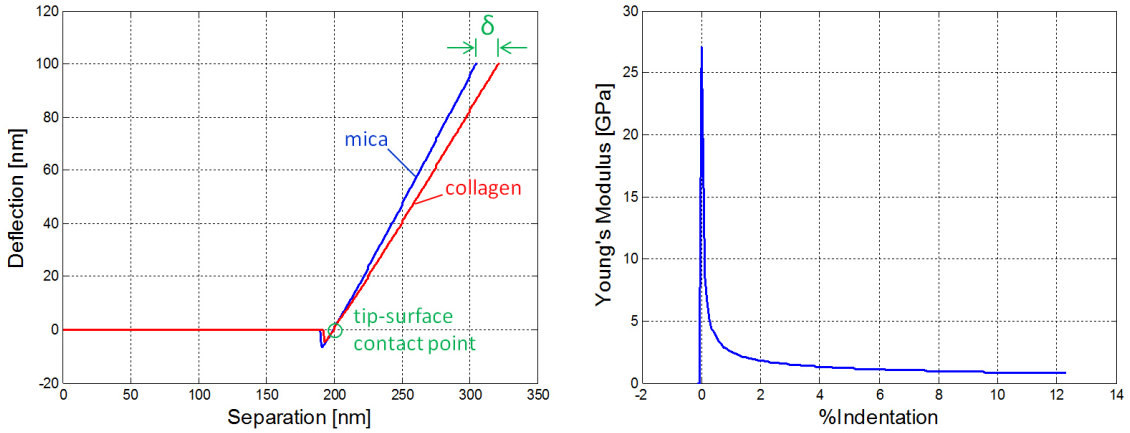

Figure 6.14: Typical nanoindentation force curves. Left image: approach curves, showing tip-surface separation versus tip deflection, for collagen and mica surfaces. The horizontal distance between the two curves represents the indentation (δ) of the collagen surface. Right image: Young's Modulus, E, relative to indentation as a percentage of the fibril height. In this study, E tended to plateau from approximately 5% fibril indentation.

6.4.1 Calculation of *E*

To calculate E, the nanoindentation value was substituted into the Hertz model (Equation 2.5), along with the applied force on the cantilever, nominal tip radius, and a Poisson's Ratio of 0.5.

A plot of E against indentation (relative to the fibril diameter) showed that E plateaued and was relatively constant at small indentation depths; i.e. between approximately 5 and 12% (Figure 6.14, right image). Higher indentation depths tended to produce higher modulus values, most likely due to the influence of the hard substrate underneath. For consistency, all modulus calculations used an indentation depth of 5%. This value is also in relative agreement with other nanoindentation studies [33].

A MATLAB program (Appendix E) was written to locate the points corresponding to the thickest regions of the fibrils; i.e. points located at the centre of the fibril (Figure 6.15). The thinner regions of the fibrils at the edges were not considered, as the hardness of the substrate would be influential here. For consistency, 30 nanoindentation points, taken from the thickest collagen regions, were used for to calculate the average E value for the three fibrils.

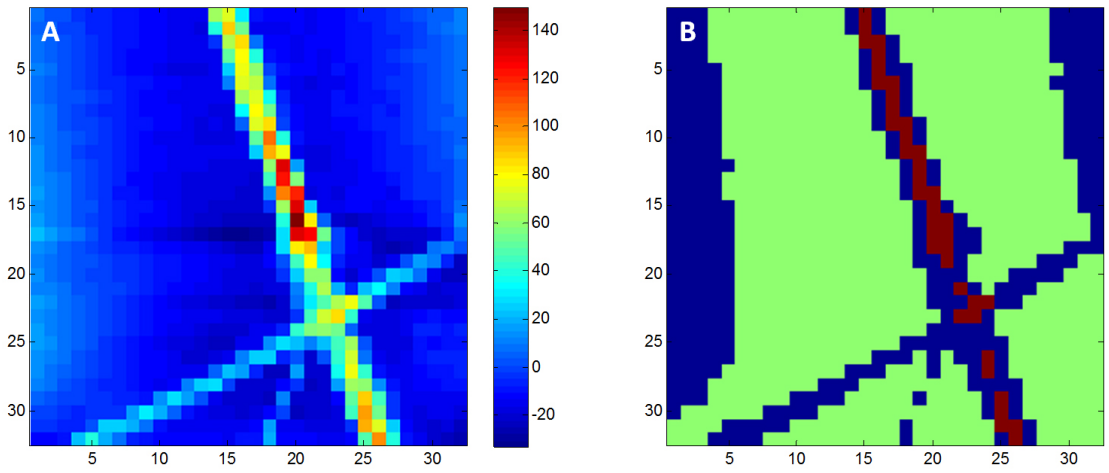

Figure 6.15: (A) Low-resolution (32×32) image of a 2×2μm region with colour bar representing height in nm. (B) Filtered image highlighting the mica and collagen regions, where red=thickest regions of the collagen, green=mica, and blue=collagen edges/thin regions. Debris on the surface of the mica was categorised as blue, and were hence disregarded from the calculations.

6.5 Statistical Analysis

All statistical analyses were performed using IBM SPSS v.20 and were conducted under the advice of a statistician.

To observe the effects of degenerative grade and anatomical region (independent variables) on the width and thickness of the fibrils (dependent variables), the data were analysed using a two-way ANOVA. A Levene's Test of Equality of Error Variances was used to verify normal distribution of the data.

To observe the effects of degenerative grade and anatomical region (independent variables) on E (dependent variable), the data were analysed using a mixed-factor analysis of variance (ANOVA) with one between factor (degenerative grade) and one within factor (anatomical region).

To determine whether any of the mixed-factor ANOVA assumptions were violated, the following tests were conducted:

- Each group and its post-ANOVA standardised residuals were tested for normal distribution using a Shapiro-Wilk test, with any outliers noted.

- Homogeneity of variances within each group was verified using Levene's Test of Equality of Error Variances.

- Homogeneity of variances of the differences between the repeated groups was verified using Mauchly's Test of Sphericity.

A p-value less than 0.05 was considered to be significant. Effect sizes were estimated using the partial eta squared (η^2) value given in SPSS. Small, medium and large effect sizes were defined as $0.01 \leq \eta^2 < 0.06$, $0.06 \leq \eta^2 < 0.14$ and $\eta^2 \geq 0.14$ respectively, in accordance with Kinnear & Gray (2010) [139].

Chapter 7

Nanoscale: Results and Discussion

7.1 Results

7.1.1 Overview

This chapter details the results of the nanoindentation tests on collagen fibrils, as described in Chapter 6.

The most notable findings, with respect to the independent variables, were as follows:

- Degenerative grade did not have a significant effect on *E*.
- Anatomical region did not have a significant effect on *E*.

Full results and statistical analyses can be found under Appendix F.

7.1.2 Verification of Statistical Assumptions

Normal distributions were verified, except for the degenerate posterolateral group (p=0.020). Upon analysing the standardised residuals, normal distributions were verified for all cases.

Homogeneity of variances was verified for all 4 groups, as was homogeneity of variances of the differences between the repeated measures.

Given that the assumptions were verified in all but one case, it was assumed that the violations would have a negligible effect on the statistical outcome. As such, the mixed-factor ANOVA was deemed to be suitable.

Amongst the 4 groups (healthy and degenerate combined, four regions), SPSS identified all of them as containing a small number of outliers. These are given in Appendix F.1.

This outcome is not unexpected, as nanoindentation tends to produce a high degree of variation, and the standard deviations for the groups were relatively large in this case. However, to the author's knowledge, there were no circumstances under which these points could be deemed invalid. A comparison of the original dataset with a revised dataset - with outliers removed - showed that the statistical outcome was not affected. The same significant relationships were present in the revised dataset, with only negligible differences between the values for p and partial η^2 for the main effects and interactions (Appendix F.2.3). As such, the author felt it was unnecessary to remove the points that had been flagged as outliers.

7.1.3 Nanoindentation

Figure 7.1 shows a series of images taken during the nanoindentation process. In this example, the region of interest was selected, and then a 32×32 nanoindentation array was performed, corresponding to Figure 7.1B. Figure 7.1C shows the points that represented the thickest regions on the collagen fibrils. Not all nanoindentations were successfully executed; e.g. in some cases, the resultant force curve yielded a negative modulus value. These invalid force curves were filtered out with the MATLAB program. Figure 7.1D shows the map of E values at every *valid* nanoindentation point on the surface. Note that for the purpose of image clarity, the moduli on the mica regions were set to 0.

The points on the E map that coincided with the thickest collagen areas were identified, and then 30 random values from this array formed the final dataset for that sample. In some cases, there were fewer than 30 valid points, so the maximum possible number was used. The smallest number of viable nanoindentation points was 24. Full results are given in Appendix F.1.

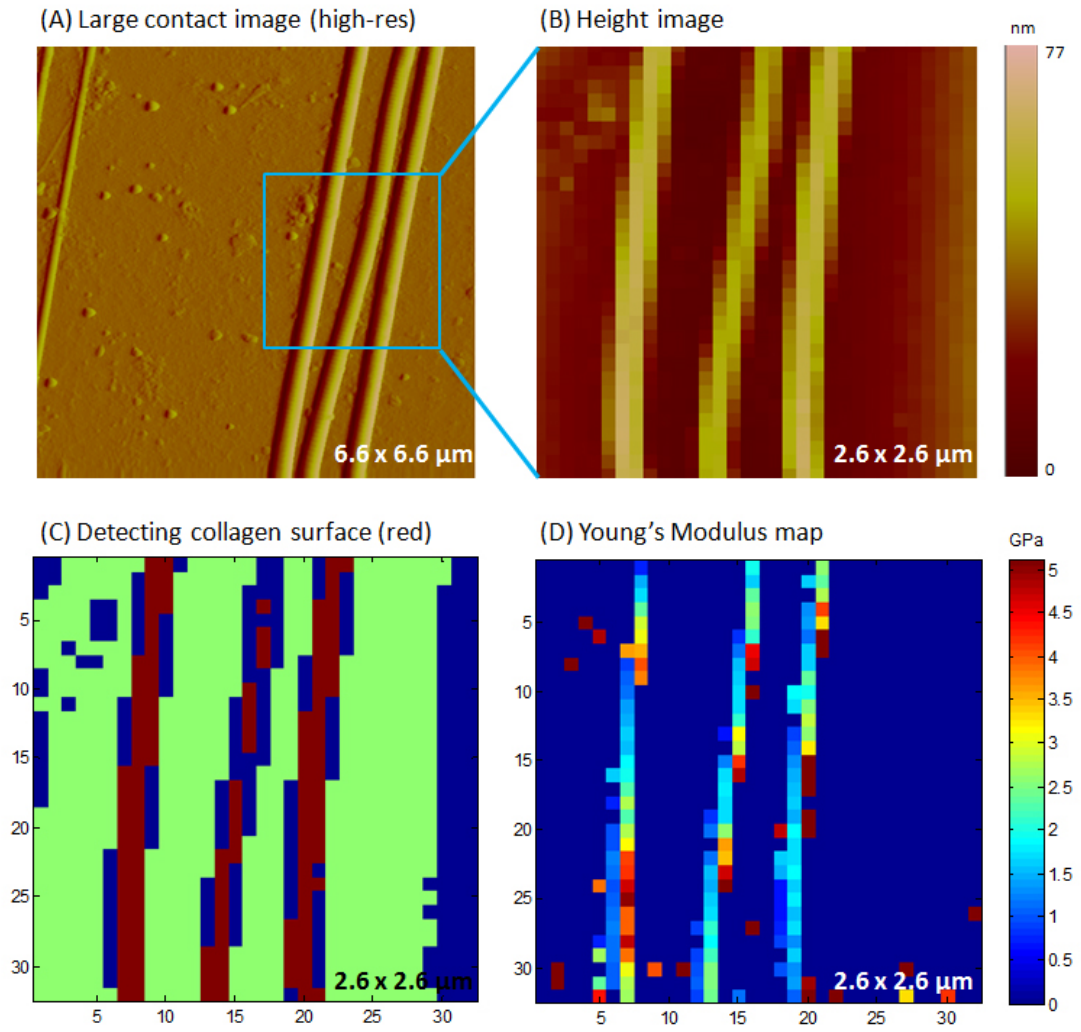

Figure 7.1: Series of images taken during the nanoindentation process. (A) Larger, high-resolution contact image with region of interest, containing three fibrils, highlighted by the blue box; (B) low-resolution (32×32 pixel) image of region of interest showing height in nm; (C) detection of thickest collagen regions, highlighted in red; (D) map of E, calculated from the nanoindentations in each of the 1024 pixels.

7.1.4 The Effects of Disc Degeneration and Anatomical Region

Young's Modulus

Figure 7.2 shows the values for E averaged from the nanoindentations taken from each sample.

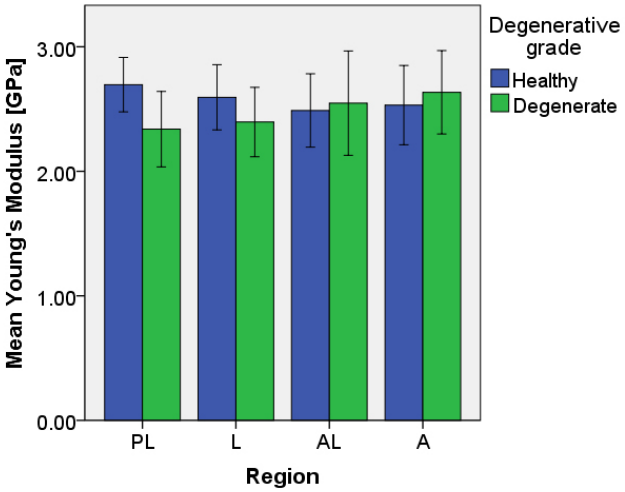

Figure 7.2: Mean (95% CI) Young's Modulus, E, in healthy and degenerate collagen fibrils extracted from four anatomical regions. No significant differences observed.

It was found that E was not significantly affected by degenerative grade (p=0.214), region (p=0.919), nor their interactions (p=0.271).

Thus, much like the collagen fibre bundles, the elastic response of the collagen fibrils is consistent throughout the outer AF, regardless of degenerative grade. This verifies the first and second hypotheses presented in Chapter 3.

Fibril Dimension

The mean±SD widths of the healthy and degenerate fibrils were 213.3±52.8 nm and 203.1±46.9 nm, respectively. Neither degenerative grade (p=0.184), region (p=0.425), nor their interactions (p=0.101) had any significant effect upon the width of the fibrils. However, partial η^2 was $\leq$0.038, suggesting that a larger sample size may have yielded significant statistical outcomes.

The mean±SD thickness of the healthy and degenerate fibrils were 70.4±20.9 nm

and 65.3±20.0 nm, respectively. Similarly, neither degenerative grade (p=0.098), region (p=0.417), nor their interactions (p=0.065) had any significant effect upon the thickness of the fibrils. Though the interaction was only marginally insignificant. Partial η^2 was also found to be small ($\leq$0.052).

It should be noted that a number of groups were not considered to be normally distributed; i.e. the width of degenerate fibrils (p=0.039), width of PL fibrils (p=0.017), and the thickness of AL fibrils (p=0.013). However, given that the majority of groups did not violate any statistical assumptions, it was assumed that the two-way ANOVA was sufficiently robust for such a dataset.

These results indicate that the collagen type I fibril morphology is consistent throughout the outer AF and does not appear to be targeted by degenerative disc disease.

See Appendix F.2.4 for full statistical results.

7.2 Discussion

7.2.1 Preparation

The technique of teasing out the fibrils from the collagen fibres was highly effective with AF tissue. Singular fibrils could be clearly seen along the edges of the fibre, and it was not difficult to isolate fibrils of interest. It has been shown that the collagen content in the outer anulus fibrosus is largely collagen type I [97]. Hence, it was assumed that the fibrils on the fibre edges were of type I. They could also be identified by their characteristic 67 mm D-banding, which was clearly visible on the AFM images (Figure 6.12). Only singular fibrils on clean mica areas were considered for testing.

This technique may also be suitable for other fibrous tissues, such as ligaments and tendons. However, it may not be as effective for gel-like materials like the NP, which would be difficult to tease apart.

One limitation to this technique was the difficulty with testing in fluid. A pilot test was conducted to attempt topographical imaging in PBS; however it was not successful. Due to the fibre simply lying on the surface of the mica, the addition of fluid during testing caused it to float up from the surface and collide with the

tip. The varnish on either side of the fibre held it down more securely, but it did not prevent the fibre from colliding with the tip. Therefore, for the final tests, a droplet of PBS was deposited on the surface of the fibre, and testing commenced immediately after the droplet appeared to evaporate. It was assumed that the fibrils would have retained a small degree of hydration immediately after evaporation.

Contact mode was used to obtain the high-resolution images, as the collagen fibrils were sufficiently robust, and adhered to the mica surface such that contact imaging did not cause any shear movement.

7.2.2 Nanoindentation

As discussed in Section 2.2.4, the direct tensile testing of collagen fibrils presents a number of technical challenges. An attempt at developing a novel tensile testing method will be explored in Chapter 8, but for the purposes of data acquisition, nanoindentation was used in this research, as it is a simple, accepted technique, which has been used in numerous other collagen fibril studies [33, 126–128]. Although the testing technique itself may not be novel, this research was, to the author's knowledge, the first to extract collagen type I fibrils from healthy and degenerate human AF tissue. Furthermore, because the fibrils were extracted from the collagen fibre bundles in the microscale study, this enabled a *direct multiscale comparison* of the AF's mechanical behaviour.

A trigger threshold of 100 nm was enough to ensure that the constant elastic region (i.e. 5% of the fibril diameter) could be reached, as determined by pilot experiments. Additionally, the surface of the collagen fibrils did not appear to be visibly marked after nanoindentation was performed, demonstrating that the elastic region was not exceeded. In order to leave a noticeable imprint on the collagen surface, the trigger threshold needed to be increased to 300 nm, as seen in Chapter 6, Figure 6.9.

Incompressible materials, such as rubber, have a Poisson's Ratio (ν) of 0.5 [162]; i.e. an increase in length by two units will result in a lateral decrease by one unit. Compressive materials, such as soft tissue, are generally reported as having ν values lower than 0.5 [163], though this depends upon the type of tissue and the orientation of testing. Elliott & Setton (2001) [100] found that the ν for multiple outer AF lamellae ranged from 0.14 in the radial-axial direction to 1.77 in the circumferential

direction. These values would take the entire composite of the multiple lamellae into account, however, so it cannot be assumed that ν at the collagen fibril level has the same value. ν for collagen fibrils is yet to be quantified [128], though the majority of nanoindentation papers estimated the value to be 0.5 [126–128]. It seems reasonable to predict that collagen fibrils would be less compressible than composite soft tissues, since they are more homogeneous in structure and do not contain ground substance, which would give soft tissue the propensity to undergo compression under loading. However, it is also fair to speculate that the quarter stagger array of tropocollagen molecules within the fibrils could allow a small degree of compression to occur under loading and thus necessitate a ν value less than 0.5. Nonetheless, in the absence of an accurately determined ν value for collagen fibrils, an estimated value of 0.5 was used in these experiments, in accordance with existing collagen fibril nanoindentation studies.

7.2.3 The Effects of Disc Degeneration and Anatomical Region

The effect of degeneration and anatomical region on E in collagen fibrils, compared with other hierarchical levels in the AF, is summarised in Table 7.1.

Table 7.1: Summary of four hierarchical levels: does disc degeneration and anatomical region affect the value of E in the human AF? Y=yes, as evidenced by at least one study; N=no evidence; blank=unknown.

Level	**Degen. Grade**	**Anat. Region**	References
Multiple lamellae	N	Y	[96, 98–107]
Single lamella		Y	[114]
Fibre bundles	N	N	Current study
Collagen fibrils	N	N	Current study

Though degeneration at the single lamella level has not yet been explored, this comparison suggests that healthy and degenerate AF tissue exhibit the same mechanical behaviour, and this consistency extends from the multiple lamella level down to the collagen fibril level. This observation continues the trend seen in the microscale study; i.e. that degeneration does not target collagen type I in particular, but may have greater impact upon the NP. Furthermore, given that there was

a decreasing, albeit statistically non-significant, trend at the multiple lamella level, degeneration could also target the proteins in the inter- and intra-lamellar ground substance.

It can also be observed that single and multiple lamellae exhibit regional differences in mechanical properties, whereas the regional consistency observed at the fibre bundle level is maintained at the collagen fibril level. This result is understandable, since collagen fibrils are even more homogeneous than fibre bundles, and can be regarded as being the building blocks of connective tissue. Thus, they are likely to have the same properties regardless of the tissue or anatomical region in which they are found. Additionally, the mean±SD value for E found in this study - across both degenerative grades and all anatomical regions - was 2.52±1.47 GPa, which was in agreement with other nanoindentation studies testing in ambient conditions (see Table 2.4), further reinforcing this consistent 'building block' behaviour. In essence, this change in the AF's mechanical behaviour in different regions is more likely caused by a change in the *arrangement* of the collagen fibre bundles and fibrils, rather than a change in the fibre bundles and fibrils themselves.

There exists a number of connective tissue disorders that cause abnormalities in collagen fibril structure, such as Ehlers-Danlos syndrome, wherein the collagen fibrils are much larger in diameter and are spiral and irregularly shaped when viewed longitudinally [164–166]. This can lead to fragility in areas of the body such as the skin, muscles and arteries. It is postulated that this disease may target some of the non-collagenous proteins that comprise the extracellular matrix (ECM) and influence collagen formation [164]. Several studies have investigated deficiencies in biglycan and decorin, the small proteoglycans in the ECM that form crosslinks between collagen fibrils and microfibrils [15, 37, 121]. It has been shown that targeted disruption of these proteoglycans can cause irregularly shaped collagen fibril formation [167]. The extent to which abnormal collagen fibril morphology influences mechanical behaviour is yet to be determined. However, the results for the dimensions and E measurements in this study indicate that degenerative disc disease *may not* target the proteins that aid in collagen fibril formation.

7.2.4 Future Recommendations

The following recommendations have been made for investigating the mechanical properties of collagen fibrils in future research.

- Although the nanoindentations in these experiments were performed immediately after hydration, it was not possible to test under fully hydrated conditions due to the methods used to prepare and isolate the collagen fibrils. It would be more ideal to perform the nanoindentations under conditions that more closely resemble the physiological environment. It is likely that testing in fluid would yield smaller E values, as evidenced by a number of studies comparing dry and hydrated conditions (see Table 2.4).

- A power analysis of the nanoindentation data was performed by running the following test on G*Power v3.1 [148]: ANOVA repeated measures (within-between interaction), α error probability = 0.05, non-sphericity correction = 1. The collagen fibrils were extracted from the 7 healthy and 7 degenerate collagen fibre bundle samples tested in Part II, and to increase the probability of obtaining valid nanoindentation points, three fibrils were tested in each sample. Although this allowed a direct comparison between the microscale and nanoscale of the AF, future studies would benefit from testing a larger number of samples, as the power obtained for these experiments was not sufficiently high (0.09). However, for the observed effect size, the sample size would need to be 96, which would present some practical difficulties given that human tissue was used.

- Although AFM nanoindentation is a commonly used and accepted standard for investigating the mechanical properties of collagen fibrils, it can only indirectly calculate E using models whose assumptions may not necessarily apply to biological tissue. It is also not suitable for very thin fibrils, as the nanoindentation may be influenced by the hard underlying substrate. Direct tensile testing would be more ideal, since it would not rely upon these material assumptions, and, in addition to E, allow E_T, ϵ_M and ϕ to be determined. There is also the potential for strain rate to be altered, since the velocity of tip approach and retract can be adjusted.

- As mentioned in the Future Recommendations for the microscale study in Section 5.2.5, it is ideal for finite-element analyses to use material parameters directly measured from the tissue being modelled. It is uncertain whether considering the properties of the disc at the nanoscale would result in more accurate models, though it is a research question worth investigating, since matrix interactions, such as osmosis, play a critical role in the disc's overall loading response.

- Finally, this research focused primarily on collagen type I, as it is the most prevalent protein in the AF. However, understanding the mechanical contributions of the remaining matrix proteins - and how they interact - is also relevant. Isolated collagen type I fibrils could very well behave differently when interacting with the other proteins in the matrix. It would be interesting to isolate particular protein interactions, such as the attachment of collagen to elastin, using selective digestion, and compare their mechanical properties to those of the individual proteins. The nanoindentation method and Hertz model used in this research may not be the most suitable method for performing such comparisons, since the model assumes the sample is cylindrical and the intertwined proteins may violate this condition. A direct tensile testing method would be more ideal.

7.3 Chapter Summary

This chapter of work further contributes to our understanding of the AF at multiple scales, and reinforces the behavioural observations made at the microscale.

Compared with the collagen fibre bundles, E values at the collagen fibril level have the same distribution throughout the various regions of the disc, and are also unaffected by disc degeneration.

This information could provide some clarification about the types of proteins that are affected by degenerative disc disease, and flag the areas of the disc that need to be targeted if future treatments are to be developed. Furthermore, these findings could influence the way in which healthy and degenerate discs are modelled in finite-element analysis, since noticeable similarities in collagen behaviour are found at more homogeneous levels.

Nanoindentation using AFM presents a number of limitations when biological tissue is concerned. The following chapter explores the development of a novel nano-tensile method for collagen fibrils to allow a more direct calculation of their mechanical behaviour.

Chapter 8

Additional Experiment: Nano-Tensile Testing of Collagen Fibrils

8.1 Introduction

This chapter describes an additional nanoscale experiment that aimed to develop a novel nano-tensile testing method to directly determine E in individual collagen type I fibrils. This experiment was also conducted using AFM, but explored the use of varnish to anchor the collagen fibrils to a substrate, and non-covalent adsorption and anti-collagen coatings to attach the fibrils to the AFM tip.

As mentioned in Section 2.2.4, only a small number of studies have successfully tensile tested collagen fibrils [23, 32, 122, 123]. However, their techniques are arguably difficult to carry out, are performed using either modified AFM setups or custom-made devices, and require days of preparation. This study was an attempt to develop a nano-tensile testing method that would:

- Be relatively simple to carry out;
- Require a short time for sample preparation;
- Be executable on a standard AFM setup;
- Have the option of testing in hydrated conditions.

8.2 Materials and Methods

8.2.1 Experimental Setup

This study used the Bruker MultiMode 8 with NanoScope V Controller as described in Section 6.2. The following functional modes were used:

- Topographical imaging: contact mode, tapping mode
- Force spectroscopy: force volume imaging

8.2.2 Sample Preparation

Fibril Deposition

A frozen human cadaveric lumber intervertebral disc was thawed for ∼2 hours, before outer lamella sections were excised from the anterior region and placed onto a board. The fibres were teased out from lamella sections using surgical needles and tweezers, and placed onto freshly cleaved mica substrates attached to metal pucks with double-sided tape.

The fibres were left to dry for ∼10 minutes, before a thin layer of nail varnish (Cutex, Connecticut, USA) was painted on one half of the mica. The purpose of the varnish was to partially cover some of the fibres, and thus anchor them to surface of the mica (Figure 8.1).

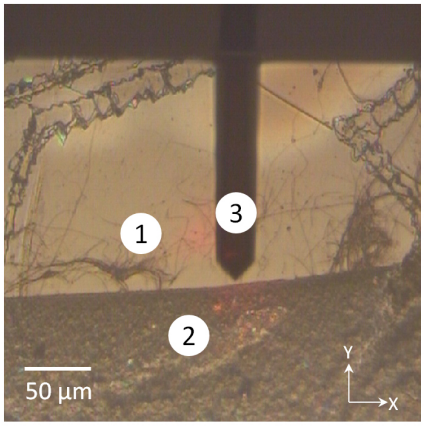

Figure 8.1: Collagen fibrils anchored to the surface of the mica. (1) Collagen fibrils on mica surface; (2) varnish; (3) cantilever.

Fibril Imaging and Cutting

A Bruker FMV chip (see Section 6, Table 6.1) was inserted into the AFM. The laser was aligned with the cantilever such that the maximum reflection signal was obtained, and the vertical and horizontal signals of the photodiode were zeroed. The cantilever spring constant was calibrated using thermal tuning.

Samples were placed onto the sample stage and contact imaged in a direction parallel to the varnish edge to locate singular anchored fibrils that were approximately perpendicular to the varnish edge (scan rate 1 Hz, scan size ~25×25 μm, deflection setpoint ~0.2 V). Once potential fibrils were located, the surface was rescanned from bottom to top (i.e. from varnish side to mica side) and the slow scan axis disabled when the scanner reached a distance approximately 2 μm out from the varnish edge. This forced the tip to scan back and forth continuously over the same line without moving in the Y direction. The deflection setpoint and scan rate were then increased to ~6V and 5Hz respectively, which caused the tip to run back and forth over the fibrils with considerable force, eventually leading to their severence after ~10 seconds (Figure 8.2). An anchored and cut fibril was selected, and then re-imaged at the end farthest from the varnish edge using a smaller scan size of ~500×500 nm (Figure 8.3). In cases where there was image artefact due to fibril movement on the mica surface, tapping mode was used instead.

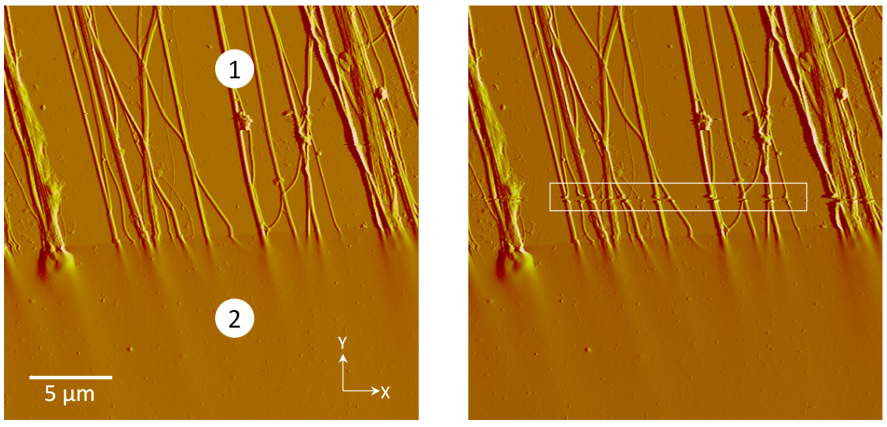

Figure 8.2: Anchored collagen fibrils, before (left) and after (right) dissection. (1) Collagen fibrils on mica surface; (2) varnish. The yellow box shows the dissected fibrils.

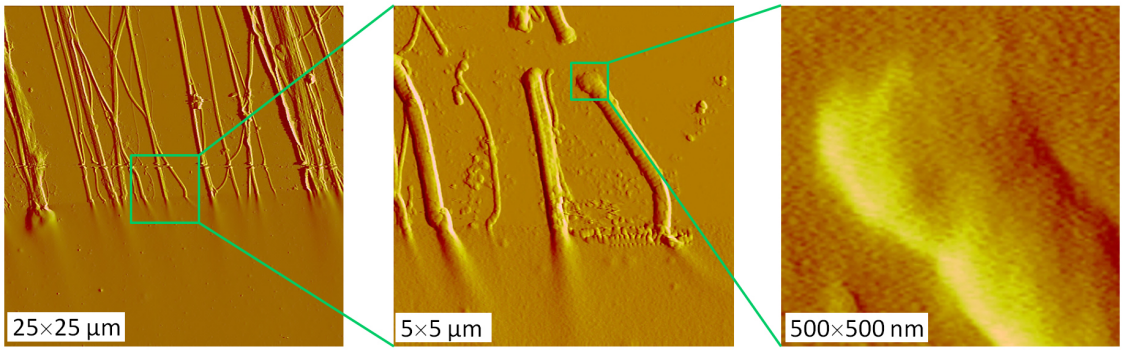

Figure 8.3: Tapping mode images of anchored collagen fibrils after dissection at 25×25 μm, 5×5 μm and 500×500 nm scan sizes.

8.2.3 Nano-Tensile Testing

The AFM was then switched to force spectroscopy mode, where the end of the fibril was force volume imaged with a 16×16 array. However, the force volume procedure was modified to allow the tip to adhere to and pick up the fibril end rather than just perform standard force curves.

Starting with a ramp size of ~1.2 μm, the tip was lowered onto the surface with a velocity of ~822 nm/s, held for 15 secs with a trigger threshold of 350 nm, and then raised to the initial ramp size at the same velocity. This relatively slow velocity was used for the purposes of this preliminary study. However, it should be noted that the Bruker MultiMode allows the velocity to be adjusted, which opens up the possibility of testing under different strain rates.

E was calculated using the standard stress and strain equations as described in Section 2.1. As shown in Figure 8.4, The force on the cantilever was given by F_c=kd, where k is the cantilever stiffness and d is the cantilever deflection. The force along the length of the fibril was therefore given by F=$F_c sin\theta$. The original fibril length, L_O, was measured on the topographical image. The final length was calculated using $L_F = \sqrt{RS^2 + {L_0}^2}$. Stress and strain was then directly calculated from these values.

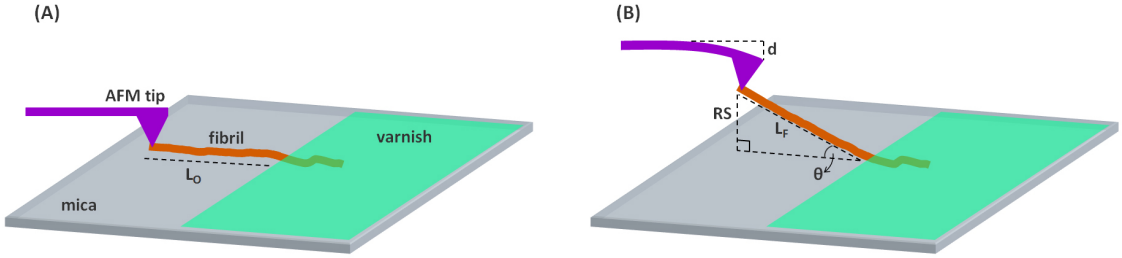

Figure 8.4: Nano-tensile testing procedure. (A) Tip is placed onto the end of the fibril and held for 15 seconds, allowing tip-fibril adsorption; (B) tip is raised to the specified ramp size, stretching the fibril and causing the tip to deflect. L_O=original length of the fibril; L_F=final length of the fibril; RS=ramp size; d=tip deflection; θ=angle between fibril and substrate.

8.2.4 Adhesion Measurement

For the nano-tensile procedure to work most effectively, maximum tip-fibril adhesion is ideal. Using force spectroscopy in force volume imaging mode, the degree of tip-fibril adhesion for a number of different tips was measured.

It was hypothesised that the fibril would adsorb to a standard tip as it was being held on the surface, since this was observed in a number of other fibril testing studies (see Section 2.2.4). However, tip functionalisation with anti-collagen was also explored as a method for better adhesion.

Tip Functionalisation

Anti-collagen is attracted to collagen via specific binding sites [168], demonstrating its potential as an adhesive if applied to the AFM tip. The application of anti-collagen to the AFM tip took the form of physisorption via a biotin-avidin complex, which is the strongest known non-covalent biological interaction between a ligand and a protein [169]. The functionalisation technique attempted in this research was adapted from a number of studies that have attached biotinylated proteins to AFM tips using this biotin-avidin complex [170–173].

The procedure, which was used on three Bruker FMV tips (see Section 6, Table 6.1), consisted of the following four steps, as illustrated in Figure 8.5.

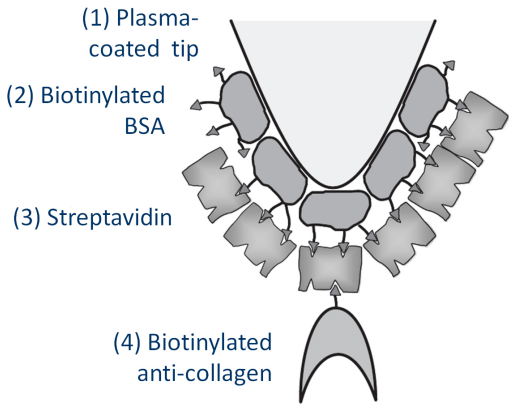

Figure 8.5: Tip functionalisation steps. (Modified from Dupres et al. [174].)

1. **Plasma coating**

   To facilitate the attachment of the proteins, water plasma was applied to the AFM tip to introduce negatively charged hydroxyl groups (-OH) onto its surface. The tips were placed in an open an petri dish, inserted into a water plasma chamber (Eiko Engineering Corporation, Tokyo, Japan) and plasma-cleaned for two minutes under a 9 mA current.

2. **Biotinylated bovine serum albumin (BSA)**

   The plasma-coated tips were immersed in 50 μL of biotin-labelled bovine albumin (Sigma-Aldrich, Missouri, USA; 0.5 mg/mL in 100 mM $NaHCO_3$), covered and left for 24 hours at room temperature. The tips were then rinsed six times using 0.15 M PBS (Australian Chemical Reagents, Queensland, Australia) and dried under N_2 gas.

3. **Streptavidin**

   Streptavidin was then coupled to the tips by placing them in 50 μL of streptavidin solution (Sigma-Aldrich, Missouri, USA; 0.5 mg/mL in 0.15 M PBS) for 5 minutes at room temperature, rinsing once with PBS, and then drying them under N_2 gas.

4. **Biotinylated anti-collagen**

   Finally, the tips were placed in 50 μL of biotin-conjugated anti-collagen type I

antibody (Rockland, Pennsylvania, USA; 0.5 mg/mL in distilled H_2O), covered and left for 24 hours at room temperature. The tips were then rinsed six times using 0.15 M PBS, and dried with N_2 gas.

Adhesion Maps

Force volume imaging was used to measure adhesion between the tip and the collagen/mica surface for the following groups:

Unfunctionalised Tips

1. New tip;
2. Tip after contact imaging;
3. Tip after fibril cutting and extensive contact imaging.

These tests were conducted to determine whether fibril cutting and contact imaging affected the adhesion due to blunting.

A section of collagen on the mica surface (without varnish) measuring 2.6×2.6μm was force volume imaged with each of the three tips (32×32 array, ramp size 800 nm, trigger threshold 100 nm, extend/retract velocity 1.64 μm/s). For consistency, care was taken to approximate the same region for each of the three images.

A custom-written MATLAB program located the regions of the force volume image that corresponded to the thickest collagen regions, mica regions, and any regions in between. A hundred random force curves on the thickest collagen region and mica region were selected for analysis. Another MATLAB program calculated the adhesion of the selected force curves by detecting the lowest point of the retract curve (see Section 6.2.2, Figure 6.6). The code for these programs can be found in Appendix E.

The degree of tip bluntness was verified by taking scanning electron microscopy (SEM) images of the tip using a CAMScan MX2500 (CAMScan Optics, Cambridgeshire, UK).

Data were analysed using IBM SPSS v.20. A Shapiro-Wilk test was conducted to check for normal distribution. Subsequently, it was appropriate for a Mann-Whitney u-test to be conducted to compare adhesions between the collagen and mica surfaces

for each tip. A Kruskal-Wallis test was used to compare the three different tips for the two surfaces. A p-value less than 0.05 was considered to be significant.

Functionalised Tips

1. Before functionalisation;

2. Immediately after functionalisation.

These tests were conducted to verify whether the tip functionalisation procedure increased the degree of tip-surface adhesion.

Similar to the unfunctionalised tip experiments, a section of collagen on the mica surface (without varnish) measuring 1.5×1.5 μm was force volume imaged with the three tips, before and after functionalisation (32×32 array, ramp size 400 nm, trigger threshold 100 nm, extend/retract velocity 822 nm/s). Fifty random force curves on the thickest collagen region and mica region were selected for analysis.

For normally distributed data groups, a paired-samples t-test was used to compare the adhesive forces for each tip before and after functionalisation, and an independent samples t-test used to compare collagen and mica regions for each tip. $P<0.05$ was considered to be significant. For non-normally distributed data groups, as determined by a Shapiro-Wilk test, Wilcoxon Signed rank tests and Mann-Whitney u-tests were performed instead.

8.3 Results and Discussion

8.3.1 Sample Preparation

The method of 'teasing' out the fibrils from the whole fibres was simple and effective for anulus fibrosus tissue, as single fibrils were generally very easy to locate when placed on the mica. This deposition technique may, however, be less effective for less fibrous tissues, in which case collagen type I may have to be extracted in its pure form. For most samples, an abundant number of singular collagen fibrils were distributed at the edge of the varnish; thus, anchored fibrils could be easily selected. The use of the AFM tip to dissect the fibrils worked exceptionally well, as the fibrils were cut quickly and cleanly. The fibrils were also sufficiently bound to the mica surface such that there was little or no lateral movement when contact imaging was performed, as seen by the before and after images of the fibrils.

8.3.2 Adhesion Measurement

Unfunctionalised Tips

Full adhesion data for the unfunctionalised tips are given in Appendix G.1. Figure 8.6, Part A shows the three unfunctionalised tips with varying degrees of prior usage. The SEM images demonstrated that contact imaging alone and combined contact imaging and fibril cutting noticeably blunted the tip. Residual debris, possibly consisting of collagen, could also been seen on the very end of the tip.

A prominent wave could be seen in the non-contact region of the force curves for Tip #1 (Figure 8.6, Part E). These waves were often observed when brand new tips were used, and may be have been due to the surface of the cantilever being particularly clean and reflective, causing interference of the laser light.

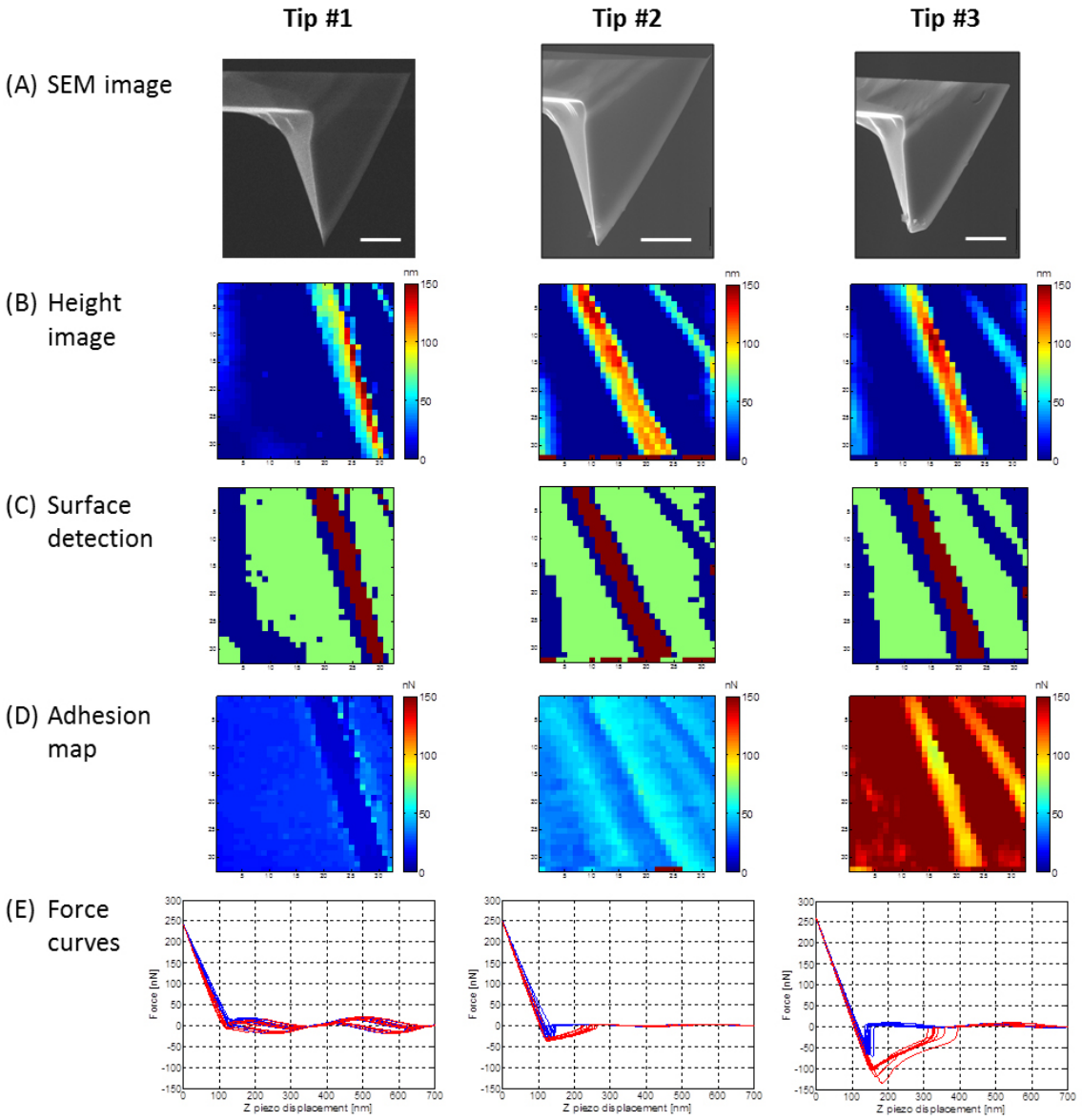

Figure 8.6: Comparison of the three unfunctionalised tips with varying degrees of prior usage. Tip #1 was new, Tip #2 had been used for contact imaging, and Tip #3 had been used for fibril cutting and extensive contact imaging. (A) SEM images, demonstrating increasing bluntness with usage. The bar in the SEM images represents a length of 4 μm. (B) Topographical height images. The blue regions denote mica; the multi-coloured regions collagen. (C) Surface detection. Red=thick collagen regions; green=mica; blue=thin collagen regions (disregarded). (D) Adhesion maps. Note that the bottom-most lines of Tips #2 and #3 were disregarded, as they were erroneous. (E) A sample of 10 force curves taken from the collagen region, demonstrating increasing adhesion force with increasing tip bluntness.

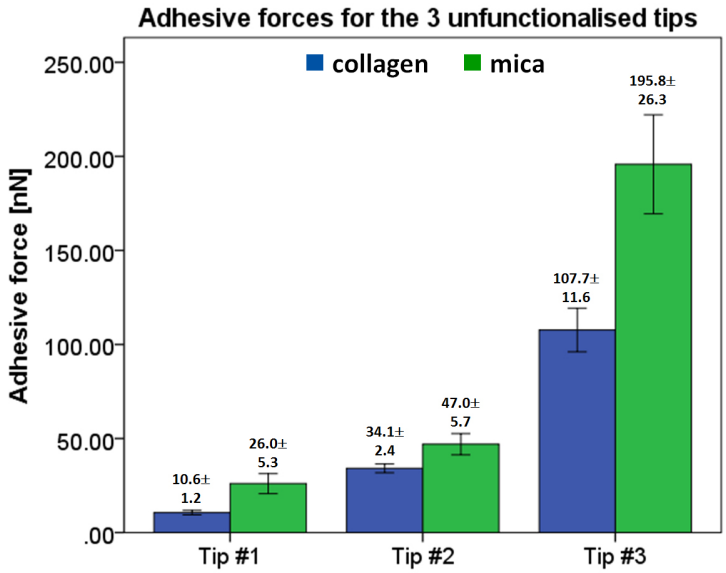

Figure 8.7: Mean±SD adhesive forces for three unfunctionalised tips with varying degrees of prior usage. Blunter tips yielded significantly greater adhesion for both collagen and mica surfaces.

The adhesion maps indicated that the degree of tip-surface adhesion increased significantly for both collagen and mica surfaces as the tip became blunter (Figure 8.7, $p<0.001$).

FMV tips have a nominal tip width of 10 nm, and the two blunt tips were measured to be 180 nm (Tip #2) and 1600 nm (Tip #3) in width. This result was expected, since the blunter tips had greater surface areas to instigate adhesion. Adhesion to mica for all three tips was greater than collagen ($p<0.001$ in all cases). Cleaved mica is negatively charged [175], whereas collagen fibrils are positively charged [176], indicating that the charge on the tip was likely to be predominantly positive.

These results demonstrate that blunting the tip was a simple, effective way of significantly increasing adhesion strength, and that blunt tips could potentially be used for nano-tensile testing of collagen fibrils.

Functionalised Tips

Adhesions maps for the three tips conducted before and after functionalisation are shown in Figure 8.8. Adhesion values are given in Figure 8.9.

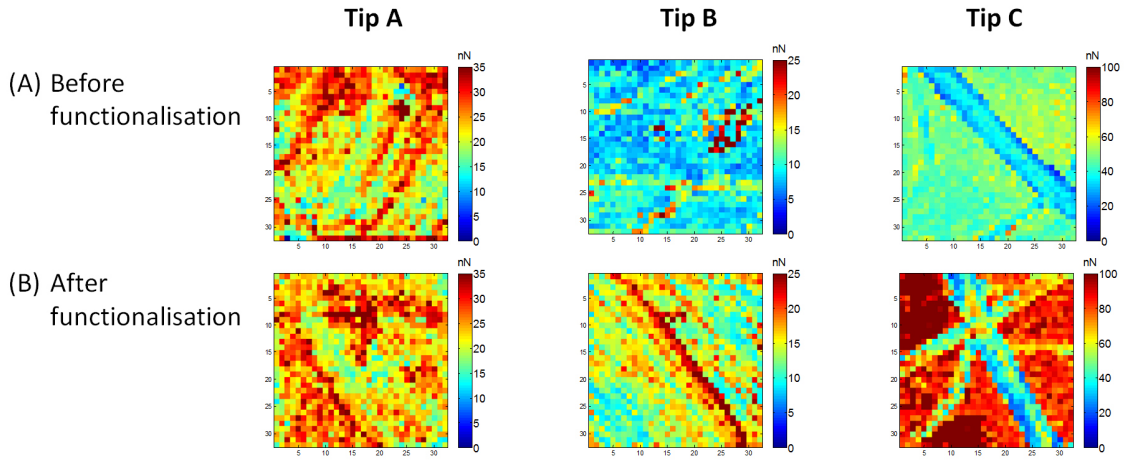

Figure 8.8: Comparison of adhesive forces for three tips, (A) before and (B) after anti-collagen functionalisation.

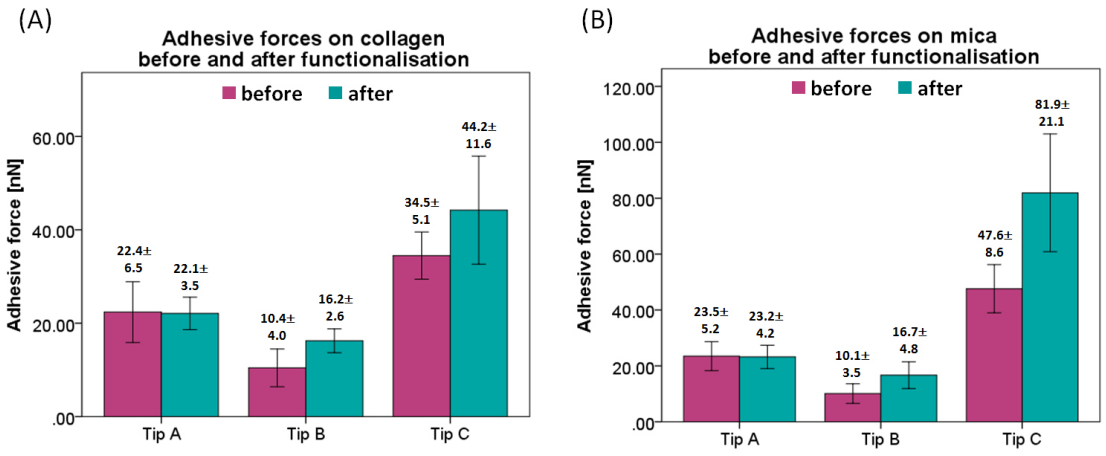

Figure 8.9: Mean±SD adhesive forces on (A) collagen and (B) mica surfaces, before and after anti-collagen functionalisation. Note the difference in scale for the Y-axes.

For collagen surfaces, adhesion significantly increased after functionalisation for Tip B and Tip C ($p<0.001$ in both cases). Tip A's adhesion did not change significantly ($p=0.988$). For mica surfaces, the same observations were made - adhesion significantly increased for Tip B and Tip C ($p<0.001$ in both cases) and Tip A did

not change (p=0.792). Full adhesion data for the unfunctionalised tips are given in Appendix G.2.

For Tips A and B, adhesion on mica was not significantly greater than that on collagen, regardless of whether they had been functionalised (all cases p>0.400). For unfunctionalised Tip C, adhesion on mica was slightly higher than that on collagen, but not significant (p=0.097). Functionalised Tip C was the only case where adhesion on mica was significantly greater than adhesion on collagen (p<0.001).

These results indicate that the functionalisation process only had a modest effect on the degree of tip-collagen adhesion. This could have been due to the following reasons:

- Antibody reactions only occur in the presence of a buffer [177], but the method of depositing the collagen on the substrate in its macroscopic fibre form meant that testing in fluid was not a possibility. When a droplet of PBS was placed on the sample and imaging was attempted, the fibres, being relatively large in size, tended to float away from the surface. Despite one end of the fibre being anchored with the varnish, the loose end collided with the tip, making imaging impossible. As such, all testing was conducted in ambient conditions, which is likely to have affected the antibody reaction. Future investigations could explore alternative sample preparation techniques that better suit hydrated conditions, and perhaps experiment with different contact times between the tip and collagen to achieve maximum adhesion.

- As there were four different steps in the process, it was unknown whether each step within the process was effectively applied, as this was not tested. Verifying the presence of each layer/protein at each step is recommended for future attempts at this procedure. Having additional control groups, such as anti-collagen type II as a negative control, could also help differentiate between specific and non-specific binding between the tip and fibres.

8.3.3 Nano-Tensile Testing

The results of the adhesion tests indicated that the greatest tip-fibril adhesions were achieved using blunted tips, and that the modest increase in tip-fibril adhesion was not enough to justify the expensive, time-consuming functionalisation procedure.

Thus, the nano-tensile tests were performed using plain, blunt tips that had been previously used for extensive contact imaging and cutting.

Successful fibril pick-up was indicated by **two observations**.

The **first observation** was that there was a sudden change in the force curve's retract phase; i.e. it was assumed that the fibril had adhered to the tip and was lifted from the surface when the retract signal did not snap back to zero deflection/force, but underwent continuous downward deflection. Figure 8.10 shows the typical response of a fibril when being picked up.

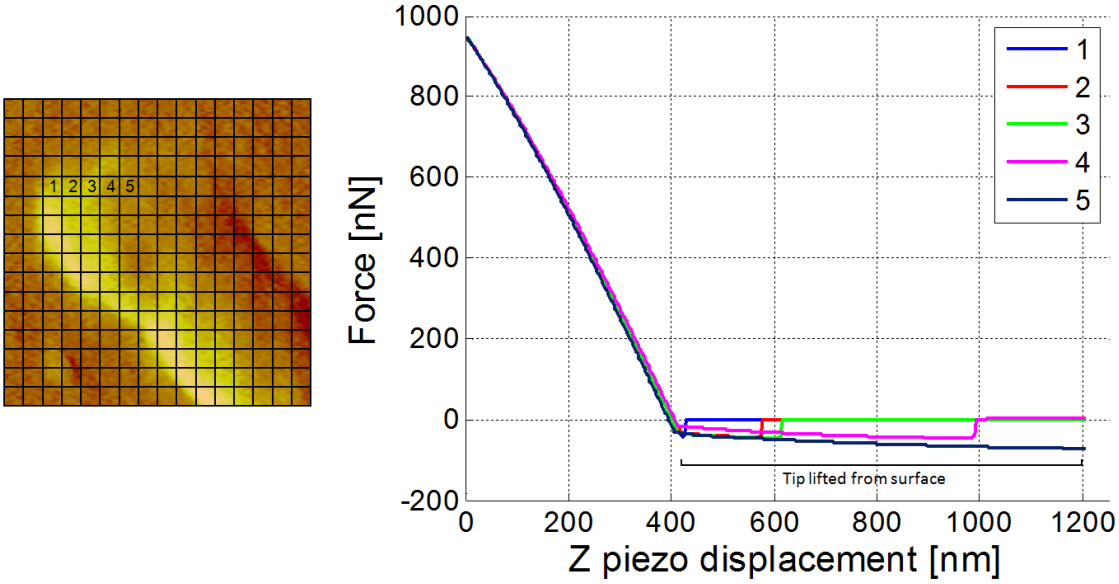

Figure 8.10: Sequence of force curves (retract phase) leading to fibril pick-up. Plot 1 denotes a force curve where the fibril was not picked up. Fibril pick-up duration is gradually increased in plots 2,3 and 4, before being successfully picked up and constantly held in plot 5.

The image on the left shows the end of the fibril divided into the 16×16 array. In this case, the force curves were performed from left to right, top to bottom. The force (retract) curves on the right side of the figure represent the boxes labelled 1 to 5 on the array. Plot 1 denotes a force curve that has not picked up the fibril, since the signal snaps back to zero force. In plot 2, the downward deflection of the tip is slightly prolonged, suggesting that something is holding onto the tip momentarily before eventually snapping back to zero force, most likely due to the fibril being dropped. This prolonged downward deflection gradually increases with each subsequent force curve (plots 3 and 4). Finally, the fibril is successfully picked up, as evidenced by the continuous downward tip deflection that does not snap back to

zero force (plot 5).

Fibril pick-up was observable for 8 tensile tests using 7 different fibrils (see Appendix G for individual results), with the number of valid tensile force curves ranging from 8 to 55 for each fibril. Once the fibril was picked up successfully, downward tip deflection was maintained for all remaining force curves in that image; i.e. the tip did not revert back to zero force. The pick-up response was only observed when the tip was positioned at the end of the fibril; this response was never observed at the anchored end or for any other region along the length of the fibril, providing further evidence that this response corresponded to fibril pick-up.

The force-displacement (stretch) information was obtained by extracting the region of the force curve where the tip was being lifted from the surface (see Figure 8.10) and inverting the force axis. Figure 8.11 shows an example of 7 different force curves for a fibril.

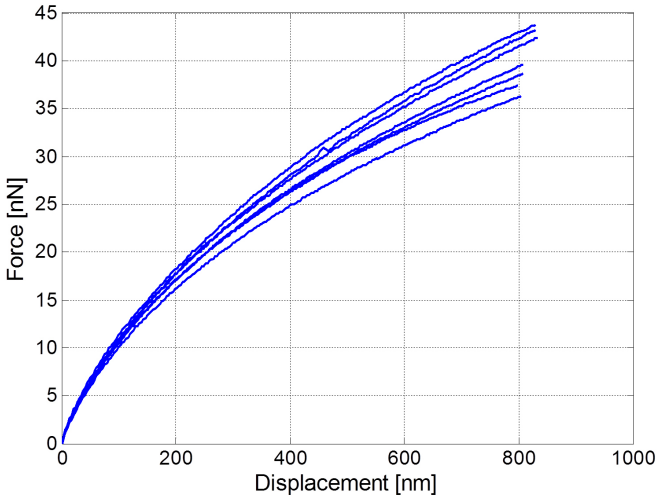

Figure 8.11: Example of 7 consecutive force-displacement curves for nano-tensile testing on a fibril.

They were repeatable and exhibited the same curvature. It was, however, observed that they did not take the form of a typical force-displacement curve that one would see with soft tissue; i.e. a toe-region that gradually turns linear. As such, it postulated that the curves were representing fibril stretching in addition to *peeling*, with peel-off never quite reaching the varnish edge. This meant that the E value could not be calculated accurately, since the change in length of the fibril (ΔL) was constantly changing over time. In some cases, the force-displacement curves were

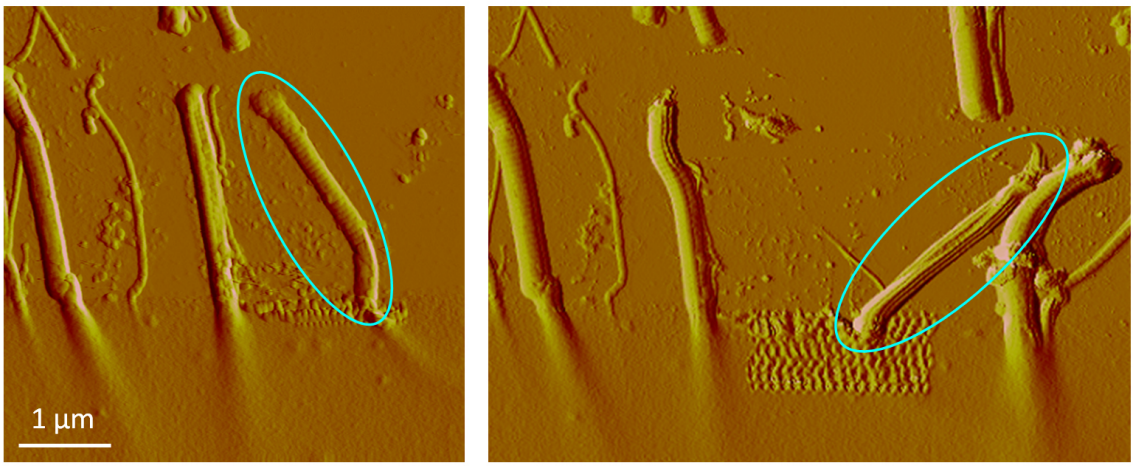

Figure 8.12: Example of collagen fibril manipulation before (left) and after (right) testing. Fibril movement is circled in blue.

erratic rather than smooth (see Appendix G, Figures G.1-G.3). It is postulated that the peeling of the fibril from the surface may not have been smooth and consistent in these cases, causing the tip to jump erratically as it moved away from the surface.

The tests were then repeated using higher ramp sizes ($\sim$1.8 μm) and fibrils that had been cut to shorter lengths, in an attempt to lift the fibril entirely from the mica surface and reach the varnish edge. However, fibril pick-up was not successful for this group of tests. Every attempt was made to keep the conditions of the experiments consistent with the first series of tests; however, the nano-tensile tests could not be replicated. This could have been due to the varying degrees of bluntness and adhesive strength for each tip. Additionally, the AFM was not enclosed in an environment where temperature and humidity could be controlled. The first series of tests were conducted in a dry, warm environment, whereas the second series was conducted in a cooler, more humid environment. These changes in conditions could have affected the degree of adhesion between the tip and the fibril, but also the adhesion between the fibril and the mica. Drier conditions would have caused the fibrils to dehydrate more quickly, so they would have been less tightly bound to the substrate. More humid conditions - like those in the second series of experiments - would have caused the fibrils to stick more readily to the substrate. To address the fibril-mica adhesion, the use of a neutrally charged silicon sample substrate was explored, though fibril pick-up was still unsuccessful.

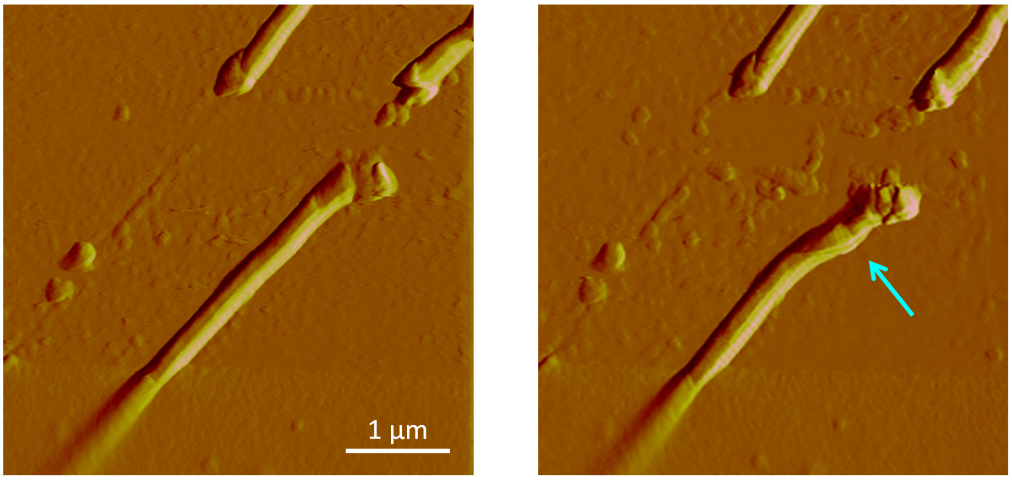

Figure 8.13: Example of collagen fibril movement before (left) and after (right) testing. Fibril movement is shown by the arrow.

The **second observation** was the ability to manoeuvre the fibril on the surface of the mica. The fibril was tensile tested, and instead of immediately retracting the tip after the final force curve in the array, the scanner was moved to the far left or right (i.e. on the x-axis) and then retracted. Figure 8.12 shows an example of the fibril being manoeuvred to the right after tensile testing, indicating that the fibril had been picked up successfully. The ability to manoeuvre the fibril was only demonstrated on this one occasion, though in other tests it was evident that the fibril had undergone movement on the mica surface during tensile testing (Figure 8.13).

As mentioned previously, the method of fibril deposition made testing in fluid difficult, so nano-tensile testing was conducted in air. However, if a single layer of collagen fibrils were deposited on the surface, which has been achieved using other studies (albeit using different tissue), there is the potential for this technique to be conducted under hydration. It is also possible for this technique to be used for other proteins or nano-fibres.

8.4 Chapter Summary

These experiments indicated that this nano-tensile testing technique could potentially be used for collagen type I fibrils and other rope-like fibres or proteins. A standard AFM setup could be used, and preparation and execution, compared with

the existing tensile testing methods, were arguably quicker and simpler to carry out. However, the technique does require further refinement.

The 'teasing' method of fibril deposition was effective for anulus fibrosus tissue, and the varnish firmly anchored the fibrils to the mica surface. However, the only caveat to this preparation technique was that the fibres, due to their large size, tended to float away from the surface when placed in PBS, so testing under hydration was not possible in this series of tests.

AFM tips that had been blunted by excessive imaging and fibril cutting were shown to have the greatest adhesion to collagen and mica, and were therefore used for the nano-tensile experiments. Functionalisation using anti-collagen had potential, but the process was expensive and time-consuming, and the increase in tip-collagen adhesion was only modest, most likely due to the antibody reaction requiring a buffer. The methodology also needed to be further refined to ensure that all protein layers were applied successfully.

During testing, the constant downward deflection of the force curves suggested that the tip had attached itself to the fibril and was peeling it from the surface while stretching it at the same time. This demonstrates that non-covalent adsorption between the tip and the fibril may be enough to bind them together sufficiently. However, the fibril needed to be lifted further to reach the varnish anchor point.

The tests could not be replicated, possibly due to changes in humidity and temperature, which seemed to affect the adhesions between collagen, the tip and the mica surface. A more controlled testing environment could allow more consistent results.

Although the prospects were promising, this nano-tensile technique needed to be improved considerably, and in the interests of time, it was abandoned in favour of nanoindentation, which was discussed in the previous chapter. Nonetheless, it is anticipated that, with further development, this could be an effective technique for tensile testing fibrillar proteins at the nanoscale, and perhaps other nanoscopic fibres, such as silk proteins and synthetic materials.

8.5 Acknowledgements

The author acknowledges Dr Christopher Gibson, School of Chemical and Physical Sciences, Flinders University for his valuable advice and expertise in completing this chapter of work.

Part IV

Conclusion

Chapter 9

Conclusion

The aim of this research was to determine the effect of anatomical region, degenerative grade and strain rate on the multiscale mechanical properties of collagen type I in the human anulus fibrosus. It is anticipated that this information will give clarity to the AF's composite structure, and improve our understanding of the origins of disc degeneration. The principal findings, contributions and recommendations for future work are presented in this concluding chapter.

9.1 Principal Findings

- Degenerative grade had no significant effect on E_T, E, ϵ_M or ϕ in collagen type I, regardless of whether it was in its fibre bundle form at the microscale, or fibril form at the nanoscale. This finding appears to be consistent with studies that have examined the mechanical properties of degenerate multiple-lamella samples, suggesting that disc degeneration may have a more profound impact upon the NP, whilst the AF is less noticeably affected. Furthermore, the obvious physical differences that are observed at the whole-disc level are not necessarily present at the microscale and nanoscale.

- Anatomical region had no significant effect on E_T, E, ϵ_M or ϕ at the collagen fibre bundle and fibril levels. This contrasts with the studies examining the AF at single and multiple lamella levels, which have reported significant regional differences. Since the amount of ground substance and arrangement of the fibre bundles also varies from region to region, it is postulated these two factors play

an important role in lamellar mechanics.

- A fast strain rate significantly affected E and ϕ at the collagen fibre bundle level. This demonstrates that collagen fibre bundles exhibit viscoelastic behaviour, although the extent of viscoelasticity is considerably lower than that at the whole-disc level.

9.2 Contributions to Biomechanics

Although the AF has been explored at various hierarchical levels, this is the first study to specifically extract and investigate individual collagen type I fibre bundles in the AF. Quantifying the mechanical behaviour of the fibre bundles, and then comparing it to single and multiple lamellae, has augmented our understanding of the AF's composite structure; provided insight to the interactions between the fibre bundles and the ground substance; and highlighted the significance of fibre bundle arrangement within the lamellae. This information could also provide a reference for the development of artificial tissue scaffolds and finite-element models of the disc.

This research extracted and investigated collagen fibrils from the same collagen fibre bundle samples, enabling a direct, multiscale analysis of the AF with greater consistency and control. To the author's knowledge, no existing studies have made a direct comparison between two different hierarchical levels in the AF. In essence, the investigation of the AF at the microscale and nanoscale has helped clarify the extent to which the various components within the AF contribute to the disc's overall mechanical response. Additionally, the use of human specimens - both healthy and degenerate - has given this research strong clinical relevance, as it offers a more accurate representation of the human disc's behaviour *in vivo* compared with animal specimens. Indeed, prior to this study, no other studies measuring the mechanical properties of collagen type I fibrils have used human AF tissue.

The comparison between healthy and degenerate specimens at the microscale and nanoscale has helped identify the disc components that are specifically targeted by this disease. A thorough understanding of the aetiology of disc degeneration could provide grounding for the development of more effective treatments, which would ideally halt the progression of the disease in its initial pre-symptomatic stages. Although such a treatment may not eventuate for some time, the findings from this

research may provide some useful insights to the underlying mechanisms of disc degeneration.

Finally, it has been demonstrated that the various testing techniques used in this research hold much potential for the testing of soft tissue samples. Hitherto, the CellScale BioTester apparatus has only been used for larger samples, such as multiple lamella sections. It has now been demonstrated that samples as small as collagen fibre bundles can also be tested with this setup. The nanotensile testing technique developed in this study could be a potentially viable method for directly determining the elastic properties of collagen fibrils, as well as other fibrillar proteins and synthetic materials. Although it is not yet suitable for final testing, this technique in its preliminary state could possibly serve as a platform for subsequent developments. Additionally, the method for isolating collagen fibrils by prising them apart and depositing them on a substrate has the potential to be used for other fibrous tissues, such as ligaments and tendons.

9.3 Recommendations for Future Research

This research is but a small contribution to our overall knowledge of how the disc behaves under loading, and how disc degeneration manifests. The outcomes from this research demonstrate that two main issues still need to be resolved: (1) some aspects of the AF testing techniques and methodology require considerable improvement; and (2) a number of gaps in the literature pertaining to other hierarchical levels and regions in the disc still exist, and they need to be addressed if a more complete multiscale analysis is to be conducted.

9.3.1 Improve Mechanical Testing Techniques

The CellScale BioTester has been shown to be an effective apparatus for the tensile testing of individual collagen fibre bundles, though the testing technique could be improved by using a more secure gripping mechanism to allow the ultimate tensile strength to be measured. With regard to collagen fibrils, AFM nanoindentation is a commonly used testing method, but can only be used to indirectly calculate E. Tensile techniques are favoured because they enable the direct measurement of E_T, E, ϵ_M and ϕ, and open up the possibility of testing under different strain rates.

The nanotensile testing technique using AFM holds considerable promise, due to its relatively simplistic method of preparation using easily sourced materials. However, significant refinements are required before it can be deemed usable. Irrespective of the testing technique, future studies should consider testing collagen fibrils under fully hydrated conditions to better replicate the physiological environment.

Human cadaver specimens provide greater clinical relevancy compared to animal tissue. However, the specimens were thawed from a frozen state, and testing fresh specimens immediately after surgical excision would be more ideal. Sourcing enough human specimens to achieve sufficient statistical power presents practical challenges, though it is necessary to achieve a more robust set of results.

9.3.2 Complete the Multiscale Picture

This research focused on one particular aspect of the AF: the collagen fibre bundles and fibrils in the outer region. For a more comprehensive analysis, it would be pertinent to also consider the inner AF, since its physical characteristics have been shown to be noticeably different to those in the outer AF. Exploring the tissue in the transition zone could clarify how mechanical properties differ when the AF and NP coalesce. It was also difficult to extract intact posterior collagen fibre bundles in this research, so it would be worthwhile for future studies to explore this region if an effective method of extraction is devised.

It would be insightful to explore the possible correlation between mechanical properties of collagen fibre bundles and their biochemical composition. Proteins that have strong interactions with collagen, such as elastin and proteoglycans, could be of particular interest, since they have been shown to affect the mechanical properties of the AF at higher hierarchical levels.

The nanoscale study focused primarily on collagen type I, but the remaining proteins in the matrix also need to be taken into consideration. A comparison of how collagen type I mechanically behaves on it own, and how it behaves when interacting with other proteins, such as elastin and proteoglycans, could directly demonstrate the effect of these matrix interactions.

Finally, the properties at the microscale and nanoscale could be used to augment current finite-element models. A number of models consider the microstructure of the AF, but use material parameters taken from other types of tissue. Using values

that have been directly measured from the human AF could allow more accurate loading predictions to be made. It is also worth exploring whether the inclusion of the nanoscale properties is necessary to achieve even greater predictive accuracy in these models.

9.4 Closing Statement

There remains a multitude of unanswered questions relating to the structure and mechanics of the human intervertebral disc and the aetiology of disc degeneration. Indeed, if time and resources were of no concern, the most ideal method of testing would be to directly measure the multiscale mechanics of disc tissue *in vivo* in human subjects with varying degrees of disc degeneration. Additionally, it would be insightful to explore whether additional factors such as sex, age and the presence of other co-morbidities, such as obesity or connective tissue disease, have any confounding effects upon disc mechanics. With the obvious practical and ethical difficulties in mind, *in vitro* testing using human specimens can be considered to be a reasonable alternative to *in vivo* experimentation, though the continued refinement of finite-element models may even lead to the eventual abandonment of mechanical testing altogether.

The development of an effective treatment for disc degeneration to reduce the incidence of low-back pain is unlikely to be realised for some time, and requires a multidisciplinary approach. Nonetheless, helping to uncover the microscopic and nanoscopic mechanical behaviours of the AF could aid in the future development of such treatments, and shed light upon what is undoubtedly a complex and challenging frontier of our knowledge of the human anatomy.

Part V

Appendices and References

Appendix A

MATLAB Code: Microscale

A.1 Setup File for Each Experiment

```
% Session 84_000
% Material: HUMAN75, spec D7, ant
% Load cells: 23 N

x_axis = 1; % 1 if yes, 0 if no
y_axis = 0;

samples = [601;230;230;230]
cycles = [1;5;5;5]
phase_count = numel(samples)

T = 0.52e-3; % thickness
W = 1.64*1e-3; % width

path(path,'F:\phd\cellscale\SESSION 84\session84_000')
M = importdata('session84_000Data.csv');

plot_phases = ones(phase_count,1); % plot all phases by default
calc_young = ones(phase_count,1);

A = 1 % apply slack correction
slack_fix = 1
AD = 381
slack_fix_2 = 1
new_S_pre = 1.894*1e-3;
```

A.2 Plot Stress-Strain Curves

```
% Plotting force (mN) vs. displacement (mm)

% STRETCH phase

if numel(cycles) >= 4
    find_four = strmatch('five', M.textdata(1:end, 1));
    find_5stretch = strmatch('5-Stretch', M.textdata(1:end, 2));
    final_stretch = intersect(find_four, find_5stretch); % last cycle only
else if numel(cycles) == 3
        find_three = strmatch('three', M.textdata(1:end, 1));
        find_5stretch = strmatch('5-Stretch', M.textdata(1:end, 2));
        final_stretch = intersect(find_three, find_5stretch);
    else end
end

actual_disp = [0:(AD/(numel(final_stretch)-1)):AD];

if x_axis == 1
    new_force_stretch = M.data(final_stretch,6);
else if y_axis == 1
        new_force_stretch = M.data(final_stretch,7);
    else end
end

figure(1), plot(new_force_stretch, 'b', 'LineWidth', 1), grid on,
title('Checking slack', 'FontSize', 16), xlabel('Points', 'FontSize', 14),
ylabel('Force [mN]', 'FontSize', 14), hold on

actual_disp_adj = actual_disp(1:end-(slack_fix_2));
new_force_stretch_adj = new_force_stretch(slack_fix_2+1:end);

figure(2), plot(actual_disp_adj, new_force_stretch_adj, 'b', 'LineWidth', 2),
grid on

% Polyfit of new_force_stretch_adj

d = numel(new_force_stretch_adj);
filt_x = (1:d)';
```

```
filt_y = new_force_stretch_adj;

p = polyfit(filt_x, filt_y, 4);

result1 = polyval(p,filt_x);
figure(9), plot(actual_disp_adj, result1, 'k', 'LineWidth', 2), hold on

% RECOVER phase

find_5recover = strmatch('5-Recover', M.textdata(1:end, 2));

if numel(cycles) >= 4
    final_recover = intersect(find_four, find_5recover); % last cycle only
else if numel(cycles) == 3
        final_recover = intersect(find_three, find_5recover);
    else end
end

if x_axis == 1
    new_force_recover = M.data((final_recover(1)-1):end,6);
else if y_axis == 1
        new_force_recover = M.data((final_recover(1)-1):end,7);
    else end
end

if numel(new_force_recover) > numel(new_force_stretch_adj)
    q = numel(new_force_recover)-numel(new_force_stretch_adj);
    new_force_recover_pre = new_force_recover(1:end-q);
    new_force_recover_adj = flipud(new_force_recover_pre);
    figure(9), plot(actual_disp_adj, new_force_recover_adj, 'r', 'LineWidth', 2),
    grid on, title('Force vs. displacement', 'FontSize', 16),
    xlabel('Displacement [um]', 'FontSize', 14), ylabel('Force [mN]',
    'FontSize', 14), hold on
else
    actual_disp2 = [0:(AD/(numel(final_recover)-1)):AD];
    new_force_recover_adj = flipud(new_force_recover);
    figure(9), plot(actual_disp2, new_force_recover_adj, 'r', 'LineWidth', 2),
    grid on, title('Force vs. displacement', 'FontSize', 16),
    xlabel('Displacement [um]', 'FontSize', 14), ylabel('Force [mN]',
    'FontSize', 14), hold on
```

```
end

% Plotting stress and strain - EXTEND

% Stress

area = T*W;
new_stress_stretch = (new_force_stretch_adj/1E3)/area;

% Strain

new_S = new_S_pre + ((slack_fix_2/numel(actual_disp))*(AD*1e-6)); % negate slack
new_strain_stretch = (actual_disp_adj/1E6)/new_S;

figure(10), plot(new_strain_stretch*100, new_stress_stretch*1E-6, 'r',
'LineWidth', 2), grid on, title('Final stress vs. strain', 'FontSize', 16),
xlabel('Strain [\%]', 'FontSize', 18), ylabel('Stress [MPa]', 'FontSize', 18),
hold on

% Plotting stress and strain - RETRACT

new_stress_recover = (new_force_recover_adj/1E3)/area;

if numel(new_force_recover) > numel(new_force_stretch_adj)
    new_strain_recover = (actual_disp_adj/1E6)/new_S;
else
    new_strain_recover = (actual_disp2/1E6)/new_S;
end

figure(10), plot(new_strain_recover*100, new_stress_recover*1E-6, 'b',
'LineWidth', 2), hold on

% Polyfit of new_stress_stretch_adj

d = numel(new_stress_stretch);

filt_x = (1:d)';
filt_y = new_stress_stretch;

p = polyfit(filt_x, filt_y, 4)
```

```
result2 = polyval(p,filt_x);
figure(10), plot(new_strain_stretch*100, result2*1E-6, 'k', 'LineWidth', 2),
hold on
```

A.3 Calculating E_T, E and ϵ_M (Moving Cell Linear Regression)

```
% John Martin - johnma@mail.med.upenn.edu - November 2013

Rsq_lim = 0.995;
toe_value = 0.005;

function [toe_mod, linear_mod, trans_strain] = lachlan_bilinear_fit(strain,
stress, Rsq_lim)

% This function takes stress and strain (both positive, pre-failure) as
% inputs and returns the modulus in the toe and linear regions and also the
% transition strain. Strain and stress are input as vectors. Rsq_lim defines the
% R^2 value for the toe and linear region fits. Rsq_lim = 0.995 is a good
% starting point.

% Fit toe region

R_sq(1)=1;
for i=1:length(strain)
    [p(i,:),zz] = polyfit(strain(1:i),stress(1:i),1);
    Etoe(i) = p(i,1);

    corrcoeff_matrix = corrcoef(strain(1:i),stress(1:i));

    if length(strain(1:i))~=1
        R_sq(i) = corrcoeff_matrix(2)^2;
        end

end

R_sq = R_sq - Rsq_lim;
[zz,index_toe] = min(abs(R_sq));
```

```
stress_toe = polyval(p(index_toe,:), strain(1:index_toe));

toe_mod = Etoe(index_toe);

% Fit linear region

clear Rsq

R_sq(1)=1;
j=1;
for i=length(strain):-1:1
    [q(i,:),zz] = polyfit(strain(i:length(strain)),stress(i:length(strain)),1);
    Elinear(i) = q(i,1);

    corrcoeff_matrix = corrcoef(strain(i:length(strain)),stress(i:length
    (strain)));

    if length(strain(i:length(strain))) ~= 1
        R_sq(i) = corrcoeff_matrix(2)^2;
        end
end

R_sq = R_sq - Rsq_lim;
[zz,index_linear] = min(abs(R_sq));
stress_linear = polyval(q(index_linear,:), strain(index_linear:length
(strain)));

linear_mod = Elinear(index_linear);
figure
plot(strain(1:index_toe),stress_toe,'-k', strain(index_linear:length
(strain)), stress_linear,'-k', strain, stress,'ob')
ylabel('Stress (MPa)')
xlabel('Strain (mm/mm)')
title('Stress vs. Strain')

trans_strain = (q(index_linear,2)-p(index_toe,2))/(p(index_toe,1)-
q(index_linear,1))*100;

end
```

A.4 Calculating ϕ (Cross Spectral Density Estimate Function)

```
% Marcos Duarte - mduarte@usp.br - July 2002

function [phi, frq, cxy] = relphase(x,y,freq,show)

% RELPHASE finds the relative phase, PHI, between the vectors X and Y.
% The frequency, FRQ, and strength, CXY, of the coupling are also given.
% FREQ (optional, default is 2) is the sampling frequency of the vectors X and Y.
% SHOW (optional, default is do not show) plots the results if SHOW is input.

if ~exist('freq','var'), freq = 2; end
x = detrend(x);
y = detrend(y);
if length(x) > 1024
    nfft = round(length(x)/2);
    nfft2 = 512;
elseif length(x) > 256
    nfft = 256;
    nfft2 = 256;
else
    nfft = length(x);
    nfft2 = length(x);
end

% Cross Spectral Density of X and Y

[Pxy,F] = csd(x,y,nfft,freq,nfft,round(nfft/2),'linear');
ang = angle(Pxy)*180/pi;
[m,i] = max(abs(Pxy));

% Phase between X and Y at their maximum cross-spectral density

phi = ang(i);
frq = F(i);

% Coherence of X and Y (Coherence is a function of frequency with values
% between 0 and 1 that indicate how well X corresponds to Y at each frequency)
```

```
[Cxy,F2] = cohere(x,y,nfft2,freq,nfft2,round(nfft2/2),'linear');
[tmp,i] = min(abs(F2-frq));

% Strength of the coupling

cxy = Cxy(i);

% Plot

if exist('show','var')
    figure
    subplot(3,1,1)
    plot(F,abs(Pxy),frq,m,'ro')
    ylabel('Cross Spectral Density')
    title(['Phase between X and Y: ' num2str(round(100*phi)/100),...
            '^o at ' num2str(round(100*frq)/100),...
            ' Hz with a coherence of ' num2str(round(100*cxy)/100)])
    subplot(3,1,2)
    plot(F2,Cxy,F2(i),cxy,'ro')
    xlabel('Frequency (Hz)')
    ylabel('Coherence')
    subplot(3,1,3)
    t =linspace(0,length(x)/freq,length(x));
    plot(t,x,'k',t,y,'r')
    xlabel('Time (s)')
    ylabel('X and Y')
    legend('X','Y',0)
end
```

Appendix B

Collagen Fibre Bundle Data

This appendix presents the full results and statistical analyses for the microscale experiments discussed in Chapter 5.

B.1 Microscale Data

B.1.1 Toe Modulus

Table B.1: Full results for toe modulus, E_T, for healthy (N=7) and degenerate (N=7) samples in posterolateral (P), lateral (L), anterolateral (AL) and anterior (A) regions. Values highlighted in blue were flagged as potential outliers.

TOE MODULUS [MPa]													
	SLOW				MED				FAST				
	PL	L	AL	A	PL	L	AL	A	PL	L	AL	A	
HEALTHY	3.51	0.28	1.43	2.07	4.94	0.48	2.61	2.30	0.16	5.64	2.19	1.17	
	3.41	6.80	0.26	0.13	0.68	5.51	4.56	0.75	5.98	1.79	0.22	0.45	
	3.56	5.69	3.23	0.98	8.51	3.61	1.12	3.99	4.11	1.71	3.15	4.37	
	0.85	2.29	0.36	2.55	0.35	2.03	2.40	3.96	0.27	0.76	2.56	2.03	
	2.83	3.66	5.92	3.02	3.28	5.70	4.96	4.21	1.71	3.40	4.90	0.62	
	5.16	4.00	2.90	3.71	4.29	6.33	3.12	2.87	2.43	8.78	3.75	4.90	
	2.72	0.86	0.42	2.58	3.24	3.24	0.63	2.79	0.39	2.38	1.89	1.25	
	3.15	**3.37**	**2.08**	**2.15**	**3.61**	**3.84**	**2.77**	**2.98**	**2.15**	**3.49**	**2.67**	**2.11**	mean
	1.29	**2.40**	**2.09**	**1.22**	**2.76**	**2.14**	**1.61**	**1.22**	**2.21**	**2.81**	**1.48**	**1.80**	SD
DEGENERATE	3.38	3.40	1.68	1.67	4.93	1.85	4.36	5.65	2.56	4.46	0.32	0.46	
	3.77	2.63	1.54	1.77	2.83	1.41	5.47	4.89	1.69	2.13	4.03	4.00	
	3.89	4.74	2.88	4.88	1.36	2.74	1.38	1.05	0.26	3.06	3.01	3.17	
	0.53	5.68	4.02	2.20	1.39	6.58	0.59	0.50	2.93	5.36	3.03	2.90	
	1.90	1.12	0.33	1.87	1.97	3.79	1.81	0.39	2.13	2.99	3.83	0.29	
	0.59	4.60	6.34	0.52	1.13	2.98	3.75	2.46	0.55	3.31	2.84	1.41	
	6.34	2.16	0.17	1.86	2.43	1.51	0.86	1.74	3.86	1.16	1.31	0.60	
	2.91	**3.47**	**2.42**	**2.11**	**2.29**	**2.98**	**2.60**	**2.38**	**2.00**	**3.21**	**2.62**	**1.83**	mean
	2.07	**1.62**	**2.20**	**1.33**	**1.32**	**1.81**	**1.91**	**2.11**	**1.28**	**1.39**	**1.34**	**1.50**	SD

B.1.2 Young's Modulus

Table B.2: Full results for Young's Modulus, E, for healthy (N=7) and degenerate (N=7) samples in posterolateral (P), lateral (L), anterolateral (AL) and anterior (A) regions. Values highlighted in blue were flagged as potential outliers.

YOUNG'S MODULUS [MPa]

	SLOW				MED				FAST				
	PL	L	AL	A	PL	L	AL	A	PL	L	AL	A	
HEALTHY	70.58	49.53	36.04	42.79	73.15	61.63	43.72	40.51	79.18	55.42	35.12	48.67	
	61.51	47.98	56.78	56.35	63.39	58.42	53.50	54.02	77.80	55.94	66.58	58.65	
	50.87	51.86	57.57	47.61	50.09	50.65	63.89	59.32	59.98	67.90	49.44	61.34	
	41.28	17.87	46.58	21.69	42.46	18.42	43.73	34.02	51.58	23.59	57.11	23.24	
	17.14	25.66	31.79	31.62	18.11	18.43	26.55	30.35	23.89	31.51	38.00	70.85	
	63.27	63.93	26.29	56.32	69.81	48.61	18.42	45.15	35.37	64.05	32.41	68.44	
	39.75	30.53	28.35	29.51	30.18	30.18	25.52	21.71	45.63	39.43	32.59	12.77	
	49.20	**41.05**	**40.49**	**40.84**	**49.60**	**40.91**	**39.33**	**40.72**	**53.35**	**48.26**	**44.46**	**49.14**	mean
	18.21	**16.56**	**13.16**	**13.60**	**20.71**	**18.33**	**16.50**	**13.27**	**20.67**	**16.89**	**13.48**	**22.65**	SD
DEGENERATE	23.40	34.50	41.29	88.57	20.08	30.89	36.12	84.60	27.74	52.16	50.80	127.7	
	58.87	83.41	50.55	83.62	66.66	78.24	39.79	56.97	65.92	82.41	53.25	67.58	
	38.54	59.33	14.05	26.47	39.77	82.74	11.34	22.41	40.80	26.25	26.52	37.63	
	27.91	55.20	41.07	40.43	25.55	51.74	30.84	39.63	29.75	63.70	44.32	48.96	
	57.31	38.01	44.37	56.20	67.84	39.15	41.08	54.17	84.50	46.52	53.07	61.99	
	20.17	50.18	61.15	27.78	18.25	62.56	65.99	19.14	59.25	52.45	55.61	33.64	
	54.80	24.20	44.69	56.01	63.66	21.01	50.70	46.92	34.37	31.93	45.35	48.58	
	40.14	**49.26**	**42.45**	**54.16**	**43.12**	**52.33**	**39.41**	**46.26**	**48.90**	**50.77**	**46.99**	**60.87**	mean
	16.79	**19.48**	**14.34**	**24.87**	**22.57**	**23.51**	**16.88**	**22.34**	**21.43**	**18.92**	**9.95**	**31.85**	SD

B.1.3 Extensibility

Table B.3: Full results for extensibility, ϵ_M, for healthy (N=7) and degenerate (N=7) samples in posterolateral (P), lateral (L), anterolateral (AL) and anterior (A) regions. Values highlighted in blue were flagged as potential outliers.

EXTENSIBILITY [%]

	SLOW				MED				FAST				
	PL	L	AL	A	PL	L	AL	A	PL	L	AL	A	
HEALTHY	6.68	5.23	5.43	5.15	7.10	5.97	5.94	5.07	6.29	5.63	5.17	4.70	
	2.23	2.78	3.30	5.18	1.90	2.89	2.94	5.03	2.98	2.54	3.35	5.04	
	3.02	4.85	3.23	3.29	3.36	4.43	3.85	3.65	3.12	5.11	2.92	3.97	
	4.20	6.69	3.39	6.47	4.13	6.66	4.16	6.49	4.19	6.38	4.51	5.45	
	6.67	5.10	4.92	6.70	6.77	4.64	3.26	6.55	6.52	4.77	4.95	4.87	
	7.59	3.39	8.50	3.57	7.90	2.80	7.24	2.88	6.32	2.85	9.20	3.93	
	6.03	4.65	6.22	5.48	4.85	4.85	5.60	4.57	5.87	4.65	6.35	2.79	
	5.20	**4.67**	**5.00**	**5.12**	**5.15**	**4.61**	**4.71**	**4.89**	**5.04**	**4.56**	**5.21**	**4.40**	mean
	2.05	**1.28**	**1.94**	**1.30**	**2.19**	**1.44**	**1.58**	**1.36**	**1.57**	**1.40**	**2.10**	**0.90**	SD
DEGENERATE	8.32	6.05	4.82	4.00	8.44	5.25	4.63	4.33	7.44	5.39	5.82	5.97	
	2.90	4.67	4.27	4.53	3.17	4.69	3.94	3.70	3.36	4.41	4.27	3.92	
	6.30	4.89	5.97	6.00	6.12	5.73	4.59	4.79	6.09	4.02	5.81	5.51	
	3.68	2.03	9.72	7.20	3.39	1.87	7.73	6.92	3.87	2.13	8.55	6.64	
	9.32	5.28	4.93	3.66	10.40	5.83	4.80	3.67	9.19	4.72	4.54	3.60	
	7.43	4.16	7.32	9.31	6.34	4.00	7.11	6.83	7.78	3.70	5.53	8.79	
	4.30	7.84	8.75	8.65	4.04	6.78	7.38	8.51	8.74	7.63	8.90	6.66	
	6.03	**4.99**	**6.54**	**6.19**	**5.98**	**4.88**	**5.74**	**5.54**	**6.64**	**4.57**	**6.20**	**5.87**	mean
	2.46	**1.77**	**2.11**	**2.27**	**2.71**	**1.59**	**1.59**	**1.88**	**2.29**	**1.69**	**1.83**	**1.77**	SD

B.1.4 Phase Shift

Table B.4: Full results for phase, ϕ, for healthy (N=7) and degenerate (N=7) samples in posterolateral (P), lateral (L), anterolateral (AL) and anterior (A) regions.

PHASE SHIFT [°]													
	SLOW				MED				FAST				
	PL	L	AL	A	PL	L	AL	A	PL	L	AL	A	
HEALTHY	4.34	6.02	5.32	4.62	4.57	4.32	4.15	3.68	2.23	1.31	1.71	1.52	
	5.82	5.21	4.86	4.56	5.42	4.23	3.05	3.78	2.59	2.50	1.96	1.02	
	5.31	6.10	5.21	4.74	5.09	5.19	5.21	4.44	1.73	3.41	2.10	2.83	
	5.52	5.35	5.51	4.69	5.29	5.38	5.31	4.80	2.57	2.43	2.11	2.08	
	5.24	5.27	4.45	5.92	4.82	6.94	4.08	6.28	1.05	2.50	0.64	1.45	
	5.34	6.53	4.25	5.23	5.46	5.96	4.72	5.35	2.87	4.30	1.45	2.00	
	5.03	6.03	4.69	4.17	5.71	4.05	4.94	3.94	1.37	2.08	1.20	1.71	
	5.23	**5.79**	**4.90**	**4.85**	**5.19**	**5.15**	**4.49**	**4.61**	**2.06**	**2.65**	**1.60**	**1.80**	mean
	0.46	**0.51**	**0.47**	**0.57**	**0.40**	**1.05**	**0.80**	**0.95**	**0.69**	**0.96**	**0.54**	**0.58**	SD
DEGENERATE	5.26	5.04	4.18	5.76	5.83	4.62	4.04	5.25	2.03	0.51	1.09	3.05	
	5.01	6.27	4.16	4.67	3.91	6.48	4.16	5.01	1.87	2.10	1.05	2.06	
	5.51	4.20	5.41	3.89	5.11	5.41	6.04	4.46	2.10	2.23	1.73	0.41	
	5.72	4.61	4.97	5.21	4.35	3.95	4.73	4.47	1.82	1.31	1.61	2.27	
	4.40	5.07	5.49	5.63	3.49	4.91	5.91	4.69	0.80	2.13	2.24	1.91	
	6.47	5.42	6.27	3.98	6.17	4.21	5.10	4.37	3.22	0.44	2.69	0.50	
	5.09	4.96	2.98	4.20	5.12	4.67	2.86	4.10	0.68	0.11	0.48	0.30	
	5.35	**5.08**	**4.78**	**4.76**	**4.85**	**4.89**	**4.69**	**4.62**	**1.79**	**1.26**	**1.56**	**1.50**	mean
	0.65	**0.65**	**1.09**	**0.78**	**0.99**	**0.84**	**1.12**	**0.39**	**0.86**	**0.91**	**0.76**	**1.09**	SD

B.1.5 Sample Dimensions

Table B.5: Dimensions for healthy (N=7) and degenerate (N=7) samples in posterolateral (P), lateral (L), anterolateral (AL) and anterior (A) regions.

HEALTHY			
	Sample #	Width (mm)	Thickness (mm)
PL	1	1.27	0.25
	2	2.23	0.57
	3	1.43	0.58
	4	1.43	0.42
	5	2.47	0.81
	6	1.90	0.58
	7	1.85	0.53
L	1	1.07	0.63
	2	1.68	0.45
	3	0.74	0.37
	4	1.59	0.67
	5	1.50	0.69
	6	1.93	0.46
	7	2.35	0.57
AL	1	1.68	0.74
	2	2.06	0.55
	3	1.48	0.56
	4	1.96	0.55
	5	2.22	0.50
	6	1.55	0.39
	7	2.47	0.49
A	1	1.43	0.64
	2	0.89	0.49
	3	1.57	0.35
	4	2.12	0.49
	5	1.82	0.44
	6	1.77	0.48
	7	2.65	0.76
Mean ± SD		1.75 ± 0.47	0.54 ± 0.13

DEGENERATE			
	Sample #	Width (mm)	Thickness (mm)
PL	1	1.64	0.32
	2	1.57	0.38
	3	2.65	0.35
	4	1.69	1.00
	5	2.33	0.37
	6	1.48	0.49
	7	1.64	0.44
L	1	1.59	0.54
	2	1.20	0.44
	3	1.27	0.55
	4	1.85	0.46
	5	1.60	0.40
	6	1.80	0.55
	7	2.63	0.73
AL	1	1.38	0.65
	2	1.38	0.31
	3	1.75	0.47
	4	1.53	0.53
	5	1.57	0.34
	6	1.46	0.31
	7	2.47	0.56
A	1	1.01	0.29
	2	1.93	0.30
	3	2.12	0.29
	4	1.57	0.62
	5	1.69	0.49
	6	2.24	0.56
	7	1.64	0.52
Mean ± SD		1.74 ± 0.41	0.47 ± 0.16

B.2 Statistical Analyses

B.2.1 Tests of Assumptions

Normal Distribution (Shapiro-Wilk Test)

Table B.6: Shapiro-Wilk Test for toe modulus, Young's Modulus, extensibility and phase shift. Groups that violated this assumption ($p<0.05$) are shown in red.

Strain Rate	Region	Degen State	Toe Modulus			Young's Modulus			Extensibility			Phase Shift		
			Statistic	df	Sig.	Statistic	df	Sig.	Statistic	df	Sig.	Statistic	df	Sig.
SLOW	PL	H	.923	7	.496	.942	7	.654	.909	7	.388	.917	7	.449
		D	.926	7	.520	.862	7	.157	.939	7	.632	.975	7	.929
	L	H	.960	7	.821	.940	7	.637	.952	7	.745	.881	7	.229
		D	.968	7	.883	.964	7	.853	.969	7	.892	.946	7	.690
	AL	H	.860	7	.152	.878	7	.216	.881	7	.231	.957	7	.796
		D	.919	7	.459	.867	7	.174	.910	7	.399	.966	7	.869
	A	H	.949	7	.719	.921	7	.479	.912	7	.408	.891	7	.282
		D	.786	7	.030	.902	7	.341	.914	7	.427	.896	7	.309
MED	PL	H	.931	7	.562	.943	7	.665	.952	7	.750	.965	7	.856
		D	.842	7	.104	.831	7	.082	.917	7	.447	.956	7	.786
	L	H	.940	7	.639	.872	7	.193	.933	7	.574	.919	7	.465
		D	.847	7	.115	.950	7	.728	.928	7	.533	.920	7	.469
	AL	H	.947	7	.702	.942	7	.659	.933	7	.575	.912	7	.408
		D	.901	7	.337	.973	7	.917	.832	7	.084	.954	7	.766
	A	H	.894	7	.297	.980	7	.961	.937	7	.615	.910	7	.393
		D	.866	7	.172	.949	7	.718	.886	7	.255	.951	7	.740
FAST	PL	H	.878	7	.217	.950	7	.727	.818	7	.062	.930	7	.548
		D	.965	7	.856	.901	7	.340	.905	7	.363	.911	7	.403
	L	H	.869	7	.182	.925	7	.509	.922	7	.482	.939	7	.634
		D	.975	7	.933	.962	7	.838	.954	7	.763	.853	7	.131
	AL	H	.988	7	.990	.868	7	.177	.912	7	.412	.905	7	.363
		D	.889	7	.269	.809	7	.051	.856	7	.139	.978	7	.947
	A	H	.833	7	.086	.868	7	.178	.933	7	.577	.963	7	.842
		D	.880	7	.226	.795	7	.037	.947	7	.702	.878	7	.217

Table B.7: Shapiro-Wilk Test on standardised residuals for toe modulus, Young's Modulus, extensibility and phase shift. Groups that violated this assumption ($p<0.05$) are shown in red.

Strain Rate	Region	Toe Modulus			Young's Modulus			Extensibility			Phase Shift		
		Statistic	df	Sig.	Statistic	df	Sig.	Statistic	df	Sig.	Statistic	df	Sig.
SLOW	PL	.941	14	.426	.931	14	.320	.920	14	.218	.965	14	.799
	L	.973	14	.918	.953	14	.609	.978	14	.963	.964	14	.790
	AL	.883	14	.064	.963	14	.765	.892	14	.085	.964	14	.787
	A	.959	14	.710	.959	14	.706	.953	14	.602	.923	14	.243
MED	PL	.937	14	.384	.884	14	.066	.955	14	.636	.978	14	.963
	L	.977	14	.951	.938	14	.390	.960	14	.723	.918	14	.205
	AL	.927	14	.274	.979	14	.967	.884	14	.066	.964	14	.781
	A	.953	14	.603	.974	14	.929	.933	14	.335	.941	14	.425
FAST	PL	.921	14	.230	.950	14	.562	.915	14	.184	.950	14	.562
	L	.910	14	.158	.963	14	.774	.977	14	.954	.953	14	.609
	AL	.959	14	.714	.982	14	.984	.904	14	.129	.978	14	.961
	A	.863	14	.034	.924	14	.252	.946	14	.507	.967	14	.828

Homogeneity of Variances (Levene's Test of Equality of Error Variances)

Table B.8: Levene's Test of Equality of Error Variances for toe modulus, Young's Modulus, extensibility and phase shift. Groups that violated this assumption ($p<0.05$) are shown in red.

Strain Rate	Region	Toe Modulus			Young's Modulus			Extensibility			Phase Shift		
		F	df	Sig.	F	df	Sig.	F	df	Sig.	F	df	Sig.
SLOW	PL	2.097	12	.173	.005	12	.944	.383	12	.548	.681	12	.425
	L	1.158	12	.303	.013	12	.912	.276	12	.609	.000	12	.995
	AL	.005	12	.947	.298	12	.595	.289	12	.601	4.351	12	.059
	A	.064	12	.805	2.088	12	.174	3.615	12	.082	1.918	12	.191
MED	PL	1.950	12	.188	.398	12	.540	.187	12	.673	6.479	12	.026
	L	.577	12	.462	.392	12	.543	.048	12	.831	.506	12	.491
	AL	.931	12	.354	.173	12	.685	.123	12	.732	.670	12	.429
	A	2.341	12	.152	1.109	12	.313	2.183	12	.165	4.361	12	.059
FAST	PL	2.029	12	.180	.104	12	.753	1.312	12	.274	.007	12	.933
	L	2.593	12	.133	.021	12	.886	.025	12	.877	.113	12	.743
	AL	.014	12	.908	1.785	12	.206	.002	12	.968	.692	12	.422
	A	.116	12	.739	.131	12	.724	1.844	12	.199	6.733	12	.023

Homogeneity of Variances of the Differences between Groups (Mauchly's Test of Sphericity)

Table B.9: Mauchly's Test of Sphericity for toe modulus, Young's Modulus, extensibility and phase shift. Groups that violated this assumption ($p<0.05$) are shown in red.

	Within subjects effect	Mauchly's W	Approx. Chi-Square	df	Sig.
Toe Modulus	Strain rate	.952	.546	2	.761
	Region	.680	4.134	5	.532
	Strain rate * Region	.095	22.999	20	.314
Young's Modulus	Strain rate	.705	3.848	2	.146
	Region	.846	1.798	5	.877
	Strain rate * Region	.005	51.007	20	.000
Extensibility	Strain rate	.949	.580	2	.748
	Region	.620	5.124	5	.403
	Strain rate * Region	.014	41.714	20	.004
Phase Shift	Strain rate	.760	3.016	2	.221
	Region	.717	3.562	5	.615
	Strain rate * Region	.091	23.434	20	.292

B.2.2 Mixed-Factor Repeated Measures ANOVA

Toe Modulus

Table B.10: SPSS output for mixed-factor repeated measures ANOVA. Main effects of between factor (degenerative grade).

Tests of Between-Subjects Effects

Measure: Elasticity

Transformed Variable: Average

Source	Type III Sum of Squares	df	Mean Square	F	Sig.	Partial Eta Squared	Noncent. Parameter	Observed Power[a]
Intercept	1240.484	1	1240.484	161.285	.000	.931	161.285	1.000
degen_state	3.629	1	3.629	.472	.505	.038	.472	.097
Error	92.295	12	7.691					

a. Computed using alpha = .05

Table B.11: SPSS output for mixed-factor repeated measures ANOVA. Main effects of within factors (anatomical region and strain rate) and interactions.

Tests of Within-Subjects Effects

Measure: Elasticity

Source		Type III Sum of Squares	df	Mean Square	F	Sig.	Partial Eta Squared	Noncent. Parameter	Observed Power[a]
Strain_Rate	Sphericity Assumed	5.001	2	2.501	1.327	.284	.100	2.655	.259
	Greenhouse-Geisser	5.001	1.908	2.622	1.327	.284	.100	2.532	.252
	Huynh-Feldt	5.001	2.000	2.501	1.327	.284	.100	2.655	.259
	Lower-bound	5.001	1.000	5.001	1.327	.272	.100	1.327	.186
Strain_Rate * degen_state	Sphericity Assumed	4.526	2	2.263	1.201	.318	.091	2.402	.237
	Greenhouse-Geisser	4.526	1.908	2.373	1.201	.317	.091	2.291	.232
	Huynh-Feldt	4.526	2.000	2.263	1.201	.318	.091	2.402	.237
	Lower-bound	4.526	1.000	4.526	1.201	.295	.091	1.201	.173
Error(Strain_Rate)	Sphericity Assumed	45.217	24	1.884					
	Greenhouse-Geisser	45.217	22.891	1.975					
	Huynh-Feldt	45.217	24.000	1.884					
	Lower-bound	45.217	12.000	3.768					
Region	Sphericity Assumed	29.596	3	9.865	2.221	.102	.156	6.662	.517
	Greenhouse-Geisser	29.596	2.500	11.838	2.221	.116	.156	5.552	.465
	Huynh-Feldt	29.596	3.000	9.865	2.221	.102	.156	6.662	.517
	Lower-bound	29.596	1.000	29.596	2.221	.162	.156	2.221	.279
Region * degen_state	Sphericity Assumed	2.043	3	.681	.153	.927	.013	.460	.075
	Greenhouse-Geisser	2.043	2.500	.817	.153	.899	.013	.383	.073
	Huynh-Feldt	2.043	3.000	.681	.153	.927	.013	.460	.075
	Lower-bound	2.043	1.000	2.043	.153	.702	.013	.153	.065
Error(Region)	Sphericity Assumed	159.923	36	4.442					
	Greenhouse-Geisser	159.923	30.001	5.331					
	Huynh-Feldt	159.923	36.000	4.442					
	Lower-bound	159.923	12.000	13.327					
Strain_Rate * Region	Sphericity Assumed	8.479	6	1.413	.522	.790	.042	3.132	.198
	Greenhouse-Geisser	8.479	3.747	2.263	.522	.709	.042	1.956	.160
	Huynh-Feldt	8.479	6.000	1.413	.522	.790	.042	3.132	.198
	Lower-bound	8.479	1.000	8.479	.522	.484	.042	.522	.102
Strain_Rate * Region * degen_state	Sphericity Assumed	1.181	6	.197	.073	.998	.006	.436	.066
	Greenhouse-Geisser	1.181	3.747	.315	.073	.987	.006	.272	.063
	Huynh-Feldt	1.181	6.000	.197	.073	.998	.006	.436	.066
	Lower-bound	1.181	1.000	1.181	.073	.792	.006	.073	.057
Error (Strain_Rate*Region)	Sphericity Assumed	194.938	72	2.707					
	Greenhouse-Geisser	194.938	44.961	4.336					
	Huynh-Feldt	194.938	72.000	2.707					
	Lower-bound	194.938	12.000	16.245					

a. Computed using alpha = .05

Pairwise comparisons for E_T were omitted, as no significant main effects were observed.

Young's Modulus

Table B.12: SPSS output for mixed-factor repeated measures ANOVA. Main effects of between factor (degenerative grade).

Tests of Between-Subjects Effects

Measure: Elasticity

Transformed Variable: Average

Source	Type III Sum of Squares	df	Mean Square	F	Sig.	Partial Eta Squared	Noncent. Parameter	Observed Power[a]
Intercept	360671.640	1	360671.640	237.899	.000	.952	237.899	1.000
degen_state	406.104	1	406.104	.268	.614	.022	.268	.076
Error	18192.833	12	1516.069					

a. Computed using alpha = .05

Table B.13: SPSS output for mixed-factor repeated measures ANOVA. Main effects of within factors (anatomical region and strain rate) and interactions.

Tests of Within-Subjects Effects

Measure: Elasticity

Source		Type III Sum of Squares	df	Mean Square	F	Sig.	Partial Eta Squared	Noncent. Parameter	Observed Power[a]
Strain_Rate	Sphericity Assumed	1365.473	2	682.737	7.473	.003	.384	14.945	.911
	Greenhouse-Geisser	1365.473	1.544	884.254	7.473	.007	.384	11.539	.845
	Huynh-Feldt	1365.473	1.876	727.721	7.473	.004	.384	14.022	.896
	Lower-bound	1365.473	1.000	1365.473	7.473	.018	.384	7.473	.709
Strain_Rate * degen_state	Sphericity Assumed	6.589	2	3.294	.036	.965	.003	.072	.055
	Greenhouse-Geisser	6.589	1.544	4.267	.036	.933	.003	.056	.054
	Huynh-Feldt	6.589	1.876	3.511	.036	.958	.003	.068	.055
	Lower-bound	6.589	1.000	6.589	.036	.853	.003	.036	.054
Error(Strain_Rate)	Sphericity Assumed	2192.726	24	91.364					
	Greenhouse-Geisser	2192.726	18.531	118.331					
	Huynh-Feldt	2192.726	22.516	97.383					
	Lower-bound	2192.726	12.000	182.727					
Region	Sphericity Assumed	1020.772	3	340.257	.466	.708	.037	1.398	.135
	Greenhouse-Geisser	1020.772	2.691	379.326	.466	.688	.037	1.254	.129
	Huynh-Feldt	1020.772	3.000	340.257	.466	.708	.037	1.398	.135
	Lower-bound	1020.772	1.000	1020.772	.466	.508	.037	.466	.096
Region * degen_state	Sphericity Assumed	1747.512	3	582.504	.798	.503	.062	2.393	.204
	Greenhouse-Geisser	1747.512	2.691	649.388	.798	.492	.062	2.147	.194
	Huynh-Feldt	1747.512	3.000	582.504	.798	.503	.062	2.393	.204
	Lower-bound	1747.512	1.000	1747.512	.798	.389	.062	.798	.131
Error(Region)	Sphericity Assumed	26287.015	36	730.195					
	Greenhouse-Geisser	26287.015	32.292	814.037					
	Huynh-Feldt	26287.015	36.000	730.195					
	Lower-bound	26287.015	12.000	2190.585					
Strain_Rate * Region	Sphericity Assumed	335.695	6	55.949	.629	.707	.050	3.774	.235
	Greenhouse-Geisser	335.695	3.062	109.618	.629	.604	.050	1.926	.170
	Huynh-Feldt	335.695	4.573	73.405	.629	.665	.050	2.877	.205
	Lower-bound	335.695	1.000	335.695	.629	.443	.050	.629	.113
Strain_Rate * Region * degen_state	Sphericity Assumed	303.289	6	50.548	.568	.754	.045	3.410	.214
	Greenhouse-Geisser	303.289	3.062	99.036	.568	.643	.045	1.740	.157
	Huynh-Feldt	303.289	4.573	66.319	.568	.709	.045	2.599	.187
	Lower-bound	303.289	1.000	303.289	.568	.465	.045	.568	.107
Error (Strain_Rate*Region)	Sphericity Assumed	6404.210	72	88.947					
	Greenhouse-Geisser	6404.210	36.749	174.270					
	Huynh-Feldt	6404.210	54.878	116.698					
	Lower-bound	6404.210	12.000	533.684					

a. Computed using alpha = .05

Table B.14: SPSS output for mixed-factor repeated measures ANOVA. Pairwise comparisons for strain rate. 1=slow; 2=medium; 3=fast strain rate.

Pairwise Comparisons

Measure: Elasticity

(I) Strain_Rate	(J) Strain_Rate	Mean Difference (I-J)	Std. Error	Sig.[b]	95% Confidence Interval for Difference[b]	
					Lower Bound	Upper Bound
1	2	.738	1.247	1.000	-2.727	4.204
	3	-5.645*	1.925	.038	-10.996	-.293
2	1	-.738	1.247	1.000	-4.204	2.727
	3	-6.383*	2.128	.033	-12.297	-.469
3	1	5.645*	1.925	.038	.293	10.996
	2	6.383*	2.128	.033	.469	12.297

Based on estimated marginal means

*. The mean difference is significant at the .05 level.

b. Adjustment for multiple comparisons: Bonferroni.

Extensibility

Table B.15: SPSS output for mixed-factor repeated measures ANOVA. Main effects of between factor (degenerative grade).

Tests of Between-Subjects Effects

Measure: Elasticity

Transformed Variable: Average

Source	Type III Sum of Squares	df	Mean Square	F	Sig.	Partial Eta Squared	Noncent. Parameter	Observed Power[a]
Intercept	4758.421	1	4758.421	401.920	.000	.971	401.920	1.000
degen_state	32.966	1	32.966	2.784	.121	.188	2.784	.336
Error	142.071	12	11.839					

a. Computed using alpha = .05

Table B.16: SPSS output for mixed-factor repeated measures ANOVA. Main effects of within factors (anatomical region and strain rate) and interactions.

Tests of Within-Subjects Effects

Measure: Elasticity

Source		Type III Sum of Squares	df	Mean Square	F	Sig.	Partial Eta Squared	Noncent. Parameter	Observed Power[a]
Strain_Rate	Sphericity Assumed	2.234	2	1.117	2.965	.071	.198	5.929	.523
	Greenhouse-Geisser	2.234	1.902	1.174	2.965	.074	.198	5.640	.508
	Huynh-Feldt	2.234	2.000	1.117	2.965	.071	.198	5.929	.523
	Lower-bound	2.234	1.000	2.234	2.965	.111	.198	2.965	.354
Strain_Rate * degen_state	Sphericity Assumed	.798	2	.399	1.058	.363	.081	2.117	.213
	Greenhouse-Geisser	.798	1.902	.419	1.058	.360	.081	2.013	.208
	Huynh-Feldt	.798	2.000	.399	1.058	.363	.081	2.117	.213
	Lower-bound	.798	1.000	.798	1.058	.324	.081	1.058	.158
Error(Strain_Rate)	Sphericity Assumed	9.043	24	.377					
	Greenhouse-Geisser	9.043	22.828	.396					
	Huynh-Feldt	9.043	24.000	.377					
	Lower-bound	9.043	12.000	.754					
Region	Sphericity Assumed	23.348	3	7.783	.928	.437	.072	2.783	.233
	Greenhouse-Geisser	23.348	2.443	9.556	.928	.423	.072	2.266	.210
	Huynh-Feldt	23.348	3.000	7.783	.928	.437	.072	2.783	.233
	Lower-bound	23.348	1.000	23.348	.928	.355	.072	.928	.144
Region * degen_state	Sphericity Assumed	6.667	3	2.222	.265	.850	.022	.795	.096
	Greenhouse-Geisser	6.667	2.443	2.729	.265	.811	.022	.647	.091
	Huynh-Feldt	6.667	3.000	2.222	.265	.850	.022	.795	.096
	Lower-bound	6.667	1.000	6.667	.265	.616	.022	.265	.076
Error(Region)	Sphericity Assumed	302.065	36	8.391					
	Greenhouse-Geisser	302.065	29.321	10.302					
	Huynh-Feldt	302.065	36.000	8.391					
	Lower-bound	302.065	12.000	25.172					
Strain_Rate * Region	Sphericity Assumed	3.558	6	.593	1.186	.324	.090	7.115	.438
	Greenhouse-Geisser	3.558	2.429	1.465	1.186	.327	.090	2.880	.259
	Huynh-Feldt	3.558	3.344	1.064	1.186	.329	.090	3.966	.310
	Lower-bound	3.558	1.000	3.558	1.186	.298	.090	1.186	.171
Strain_Rate * Region * degen_state	Sphericity Assumed	2.616	6	.436	.872	.520	.068	5.230	.323
	Greenhouse-Geisser	2.616	2.429	1.077	.872	.447	.068	2.118	.199
	Huynh-Feldt	2.616	3.344	.782	.872	.474	.068	2.915	.233
	Lower-bound	2.616	1.000	2.616	.872	.369	.068	.872	.138
Error (Strain_Rate*Region)	Sphericity Assumed	36.010	72	.500					
	Greenhouse-Geisser	36.010	29.151	1.235					
	Huynh-Feldt	36.010	40.134	.897					
	Lower-bound	36.010	12.000	3.001					

a. Computed using alpha = .05

Pairwise comparisons for ϵ_M were omitted, as no significant main effects were observed.

Phase Shift

Table B.17: SPSS output for mixed-factor repeated measures ANOVA. Main effects of between factor (degenerative grade).

Tests of Between-Subjects Effects

Measure: Phase

Transformed Variable: Average

Source	Type III Sum of Squares	df	Mean Square	F	Sig.	Partial Eta Squared	Noncent. Parameter	Observed Power[a]
Intercept	2547.486	1	2547.486	1824.786	.000	.993	1824.786	1.000
degen_state	2.939	1	2.939	2.105	.172	.149	2.105	.267
Error	16.753	12	1.396					

a. Computed using alpha = .05

Table B.18: SPSS output for mixed-factor repeated measures ANOVA. Main effects of within factors (anatomical region and strain rate) and interactions.

Tests of Within-Subjects Effects

Measure: Phase

Source		Type III Sum of Squares	df	Mean Square	F	Sig.	Partial Eta Squared	Noncent. Parameter	Observed Power[a]
Strain_Rate	Sphericity Assumed	378.976	2	189.488	472.824	.000	.975	945.647	1.000
	Greenhouse-Geisser	378.976	1.613	234.934	472.824	.000	.975	762.720	1.000
	Huynh-Feldt	378.976	1.982	191.238	472.824	.000	.975	936.993	1.000
	Lower-bound	378.976	1.000	378.976	472.824	.000	.975	472.824	1.000
Strain_Rate * degen_state	Sphericity Assumed	1.225	2	.613	1.529	.237	.113	3.058	.293
	Greenhouse-Geisser	1.225	1.613	.760	1.529	.241	.113	2.466	.261
	Huynh-Feldt	1.225	1.982	.618	1.529	.237	.113	3.030	.291
	Lower-bound	1.225	1.000	1.225	1.529	.240	.113	1.529	.207
Error(Strain_Rate)	Sphericity Assumed	9.618	24	.401					
	Greenhouse-Geisser	9.618	19.357	.497					
	Huynh-Feldt	9.618	23.780	.404					
	Lower-bound	9.618	12.000	.802					
Region	Sphericity Assumed	7.785	3	2.595	2.100	.117	.149	6.301	.492
	Greenhouse-Geisser	7.785	2.461	3.164	2.100	.131	.149	5.169	.438
	Huynh-Feldt	7.785	3.000	2.595	2.100	.117	.149	6.301	.492
	Lower-bound	7.785	1.000	7.785	2.100	.173	.149	2.100	.266
Region * degen_state	Sphericity Assumed	3.954	3	1.318	1.067	.375	.082	3.200	.264
	Greenhouse-Geisser	3.954	2.461	1.607	1.067	.368	.082	2.625	.238
	Huynh-Feldt	3.954	3.000	1.318	1.067	.375	.082	3.200	.264
	Lower-bound	3.954	1.000	3.954	1.067	.322	.082	1.067	.159
Error(Region)	Sphericity Assumed	44.481	36	1.236					
	Greenhouse-Geisser	44.481	29.532	1.506					
	Huynh-Feldt	44.481	36.000	1.236					
	Lower-bound	44.481	12.000	3.707					
Strain_Rate * Region	Sphericity Assumed	.447	6	.075	.291	.939	.024	1.746	.124
	Greenhouse-Geisser	.447	3.563	.125	.291	.863	.024	1.037	.105
	Huynh-Feldt	.447	5.674	.079	.291	.933	.024	1.651	.122
	Lower-bound	.447	1.000	.447	.291	.599	.024	.291	.079
Strain_Rate * Region * degen_state	Sphericity Assumed	1.829	6	.305	1.191	.321	.090	7.143	.440
	Greenhouse-Geisser	1.829	3.563	.513	1.191	.327	.090	4.241	.322
	Huynh-Feldt	1.829	5.674	.322	1.191	.322	.090	6.755	.425
	Lower-bound	1.829	1.000	1.829	1.191	.297	.090	1.191	.171
Error (Strain_Rate*Region)	Sphericity Assumed	18.436	72	.256					
	Greenhouse-Geisser	18.436	42.751	.431					
	Huynh-Feldt	18.436	68.092	.271					
	Lower-bound	18.436	12.000	1.536					

a. Computed using alpha = .05

Table B.19: SPSS output for mixed-factor repeated measures ANOVA. Pairwise comparisons for strain rate. 1=slow; 2=medium; 3=fast strain rate.

Pairwise Comparisons

Measure: Phase

(I) Strain_Rate	(J) Strain_Rate	Mean Difference (I-J)	Std. Error	Sig.[b]	95% Confidence Interval for Difference[b]	
					Lower Bound	Upper Bound
1	2	.278	.118	.110	-.051	.607
	3	3.316*	.092	.000	3.061	3.571
2	1	-.278	.118	.110	-.607	.051
	3	3.038*	.143	.000	2.640	3.436
3	1	-3.316*	.092	.000	-3.571	-3.061
	2	-3.038*	.143	.000	-3.436	-2.640

Based on estimated marginal means

*. The mean difference is significant at the .05 level.

b. Adjustment for multiple comparisons: Bonferroni.

B.2.3 Consideration of Outliers

Table B.20: Comparison of main effects with and without outliers.

		Toe modulus p-value {partial η^2}	Young's Modulus p-value {partial η^2}	Extensibility p-value {partial η^2}	Phase shift p-value {partial η^2}
Degenerative grade	Original data set	0.505 {0.038}	0.614 {0.022}	0.121 {0.189}	0.172 {0.149}
	Revised data set	0.377 {0.066}	0.935 {0.001}	0.124 {0.186}	0.137 {0.174}
Anatomical region	Original data set	0.102 {0.156}	0.708 {0.037}	0.437 {0.072}	0.117 {0.149}
	Revised data set	0.219 {0.114}	0.205 {0.118}	0.148 {0.136}	0.894 {0.017}
Strain rate	Original data set	0.284 {0.100}	0.003 {0.384}	0.071 {0.198}	0.000 {0.975}
	Revised data set	0.301 {0.095}	0.039 {0.183}	0.298 {0.096}	0.000 {0.932}

B.2.4 Pilot Test: Refreezing

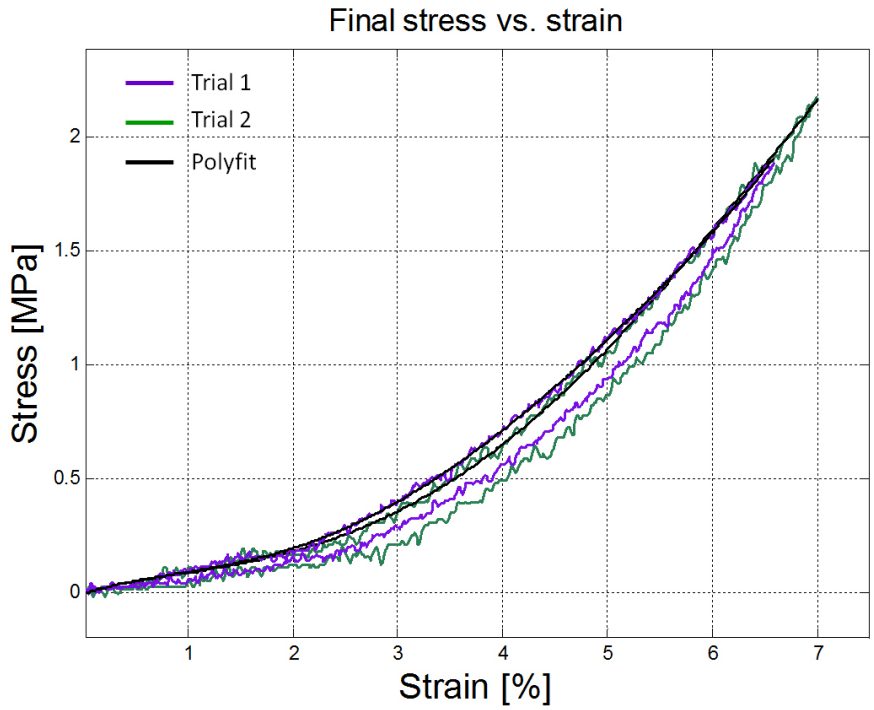

Figure B.1: Example of stress-strain curves for sample before and after refreezing. In Trial 1, a frozen disc was thawed and the fibre bundles extracted and tested. The sample was then refrozen, thawed and tested again for Trial 2. The results for E_T, E, ϵ_M and ϕ were found to be comparable.

Table B.21: Results for E_T, E, ϵ_M and ϕ before (Trial 1) and after (Trial 2) refreezing.

	E_T [MPa]	$\boldsymbol{E}$ [MPa]	ϵ_M [%]	ϕ
Trial 1	7.24	54.3	4.78	5.06
Trial 2	8.76	52.0	5.34	5.01

Appendix C

Cantilever Stiffness Calibration

C.1 Introduction

Two methods of AFM tip calibration were used in this research to determine the cantilever spring constant, a parameter that needs to be accurately measured for force spectroscopy. The primary method was *thermal tuning*, which is the standard method for calibration on the Bruker MultiMode instrument; however, the *Sader* method was also used on a number of tips for the purpose of validation.

C.2 Thermal Tuning

Thermal tuning is a widely used and accepted calibration method that derives the stiffness of the cantilever from its mechanical response to thermal noise. This technique, which is the default calibration program on the NanoScope software, is based upon the principle that "a harmonic oscillator, in equilibrium with its surroundings, will fluctuate in response to thermal noise" [178]. Assuming the cantilever is a simple harmonic oscillator with one degree of freedom, thermal noise is applied to the cantilever, and its fluctuations are measured with respect to time. One can then deduce the frequency spectrum, to which a Lorentzian model is fitted (Figure C.1).

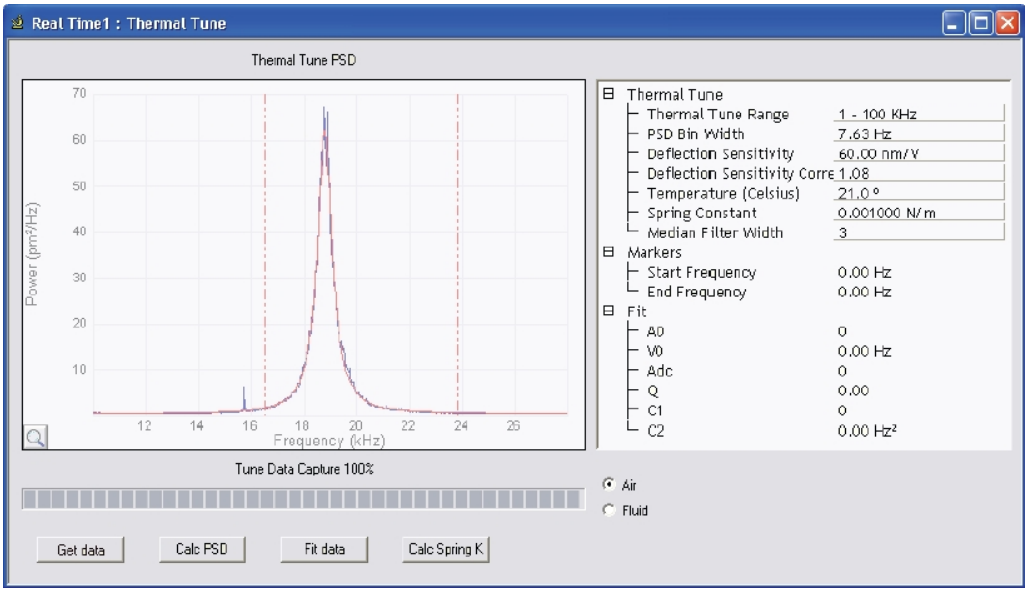

Figure C.1: Example of thermal tuning data (power spectral density, blue plot) fitted with a Lorentzian curve (red plot). The peak of the curve is the resonant frequency of the cantilever. (From Serry [179]).

The peak of this spectrum is the cantilever's resonant frequency, and the area underneath the curve, P, is a measure of the power of the fluctuations. The spring constant of the cantilever, k, can then be calculated using Equation C.1.

$$k = k_B T / P \tag{C.1}$$

where k_B is the Boltzmann Constant, and T is temperature, assumed to be 21°C.

C.3 Sader Method

The Sader method [180] is an alternative calibration technique that derives the spring constant from the interaction between the cantilever's physical dimensions and the surrounding fluid medium, which is air in this case. This method accounts for the errors that may be associated with the cantilever mass and density, and change in resonant frequency due to the surrounding medium. The spring constant is calculated from Equation C.2.

$$k = 0.1906\rho_f b^2 L Q_f \Gamma_i(\omega_f)\omega_f^2 \tag{C.2}$$

where ρ_f is the density of the medium, b is the width of the cantilever, L is the length of the cantilever, Q_f is the quality factor in the medium, Γ_i is the imaginary component of the hydrodynamic function Γ, and ω_f is the resonant frequency.

The calibration was carried out using the Sader online calibration program [181]. The quality factor and resonant frequency were measured with the NanoScope software. Tip dimensions were measured using a WITec Alpha optical microscope (WITec, Ulm, Germany) set to x40 magnification. For calibrating in air, fluid density and fluid viscosity were assumed to be 1.18 kg/m^3 and 1.86×10^{-5} kg/m/s, respectively.

C.4 Tip Calibration

To validate the Bruker MultiMode's standard thermal tuning calibration technique, four AFM tips were calibrated using both the thermal and Sader methods. The tips were Bruker FMVs (see Section 6, Table 6.1), with nominal spring constants of 2.8 N/m (min. 1 N/m, max. 5 N/m).

Table C.1 summarises the calibration parameters and spring constant calculations for the four FMV tips. The relationship between the thermal and Sader methods were investigated using Pearson correlation. There was a strong, positive correlation between thermal and Sader methods (R=0.790), indicating that the two methods were in good agreement. As such, the standard thermal tuning method was deemed to be sufficiently accurate for calibrating the tips in this research. The calculated spring constants for all tips used in this research are given in Figure C.2. Six tips in total were used to conduct the 56 AFM experiments (14 discs, 4 regions).

Table C.1: Calibration parameters for AFM tips. Δ is the percentage difference in k relative to the thermal tuning method, $\mathbf{k}_{thermal}$.

Tip	**Cantilever length, L [μm]**	**Cantilever width, b [μm]**	**Resonant freq, ω_f [kHz]**	**Q-factor, Q_f**	**$\mathbf{k}_{thermal}$ [N/m]**	**$\mathbf{k}_{Sader}$ [N/m] {Δ}**
1	208	35.3	79.670	174.2	2.62	2.51 {-4.2%}
2	208	35.9	77.180	168.6	2.26	2.36 {+4.4%}
3	208	35.4	78.473	171.8	2.56	2.43 {-5.1%}
4	208	35.3	78.718	170.2	2.59	2.41 {-6.9%}

	PL	L	AL	A
H1	1	1	2	2
H2	2	2	2	2
H3	2	2	2	2
H4	2	2	3	3
H5	3	3	3	3
H6	4	4	5	5
H7	5	5	5	5
D1	3	3	3	3
D2	3	3	3	3
D3	3	3	3	3
D4	5	5	5	5
D5	5	5	5	5
D6	6	6	6	6
D7	6	6	6	6

	k [N/m]
1	4.1731
2	4.1866
3	3.5021
4	3.3893
5	3.6738
6	3.3848

Figure C.2: Spring cantilever constants for all 6 FMV tips used for nanoindentation, as calculated using thermal tuning. H1-H7 and D1-D7 represent the 7 healthy and 7 degenerate discs, respectively. PL=posterolateral; L=lateral; AL=anterolateral; A=anterior. The nominal spring constant for FMV tips is 2.8 N/m (min. 1, max. 5).

C.5 Conclusion

Thermal tuning was an accurate method for calibrating the AFM tips used for nanoindentation, as it produced spring constant values that were in close agreement with those produced using the Sader method.

Appendix D

Salt Extraction of Collagen Type I Fibrils

D.1 Introduction

This appendix describes a pilot test that attempted to extract pure collagen type I fibrils from ovine anulus fibrosus tissue. The resultant extract was not used in the final nanoscale tests, as the amount of collagen produced was inadequate.

Fibrillar collagens (i.e. types I, II, III, V, XI, XXIV and XXVII [20]) are widely distributed throughout the body, and the types of collagen present in a particular tissue or organ can vary enormously, as can the form in which the collagens are found. As such, the extraction of a specific collagen type cannot be narrowed down to a single, standard procedure for any given tissue. Rather, the following chemical extraction procedure, as described by Miller and Kent Rhodes [182], is a technique that can be applied to a variety of different tissues, and should extract any native fibrillar collagens present, though efficiency may vary depending upon the type of tissue.

In general, there are three different solvents that can be used for the chemical extraction of fibrillar collagens from soft tissue: (1) neutral salt solvent; (2) dilute acetic acid solvent; and (3) dilute acetic acid solvent with pepsin.

Neutral salt solvent is considered to be the method with the lowest capacity to solubilise collagen, because it is only capable of extracting collagen fibrils that are present in the ground substance and not bound within the fibres. This is the gentlest

solvent that can be used, though the proportion of free collagen is generally quite small.

Dilute acetic acid solvent is more effective at solubilising collagen, and is able to extract fibrils that are bound in the fibres themselves, but this method can only be used in tissues, like dermis and tendons from young organisms, which are bound by weak intermolecular crosslinks, such as aldimine. Acetic acid is not effective at dissociating stronger crosslinks, such as ketoamines, which are present in tissues like bone, cartilage and material from older animals [182, 183].

Finally, *dilute acetic acid/pepsin* is the most effective solvent for collagen extraction; however, pepsin breaks down the collagen to the tropocollagen level, so the fibril structure is not maintained.

Only a few studies have attempted to extract collagen fibrils from the intervertebral disc. A study by Bushell et al. [184] investigating idiopathic scoliosis extracted collagen from freeze-dried anulus and nucleus using a sodium chloride salt solvent; and Aladin et al. [185] used the same salt solvent to successfully extract collagen from fresh nucleus pulposus. As such, it was concluded that using a neutral salt solvent on fresh anulus fibrosus tissue would be the simplest and most logical method to attempt first.

D.2 Materials and Methods

D.2.1 Tissue Preparation

An ovine lumbar intervertebral disc, frozen at -30°C, was thawed at room temperature for approximately 30 mins, until the disc was semi-frozen. Using a surgical scalpel, the outer anulus was scraped from the anterior region of the disc producing a finely shredded paste. This was divided into two portions: Sample 1 and Sample 2.

D.2.2 Collagen Extraction

An extraction buffer containing 0.15 M NaCl, 2 mM Na_3PO_4 and protease inhibitor cocktail (P8340, Sigma-Aldrich, Missouri, USA) was prepared. The ground anulus samples were homogenised in 14 volumes of extraction buffer for 1-2 minutes a using

a Heidolph Silent Crusher S fitted with a Type 5F generator (Heidolph, Bavaria, Germany).

The resultant solutions were placed in two test tubes, such that the volumes were equal in weight. The test tubes were placed in an ultracentrifuge fitted with a Type 70 Ti Rotor (Beckman Coulter, California, USA) and centrifuged at 16,000 rpm at 4°C for 30 minutes. The supernatant was collected, and 14 volumes of fresh extraction buffer was added to the test tubes. Centrifugation was performed again at the same speed, temperature and duration. Once again, the supernatant was collected, the extraction buffer topped up, and the test tubes centrifuged. The three resultant supernatant volumes were combined and transferred to two new test tubes, which were centrifuged at 33,500 rpm at 4°C for 2 hours. The final supernatant was removed, leaving two small resultant masses of protein in the two test tubes. The final masses were combined and suspended in PBS such that the concentration was 200μg/mL.

D.2.3 SDS-PAGE Analysis

The composition and purity of the final mass was analysed using sodium dodecyl sulfate polyacrylamide gel electrophoresis (SDS-PAGE), which identifies the types of proteins present in a sample based upon their molecular weight. The final masses were first digested in a solution of pepsin (1mg/mL acetic acid) at 4°C for 24 hours. Analysis was conducted using a 5% SDS running gel consisting of 40% acryl/bisacryl, 1.5M tris(hydroxymethyl)aminomethane (Tris), 20% SDS, tetramethylethylenediamine (TEMED) and 10% ammonium sulphate; and proteins were visualised using Coomassie Blue staining. Gels were run at 40 mA/200 V.

D.2.4 AFM Imaging

A small portion of the final mass was deposited onto freshly cleaved mica substrates and allowed to dry at room temperature. The sample was AFM imaged in air using a MikroMasch NSC15 tip in intermittent mode and an AS-12VLR ('E') scanner. The scan rate was 0.4 Hz and scan size 5×5μm.

D.3 Results

Table D.1 summarises the initial weight of the two ground anulus samples, and their respective final mass weights after salt extraction was performed. The final weights were extremely small, making SDS-PAGE analysis ineffective. There were no visible bands at the regions expected for collagen type I's alpha-1 and alpha-2 polypeptide chains. The AFM image revealed that no collagen fibrils were present in the final mass (Figure D.1). Only general surface debris could be seen.

Table D.1: Initial weights of the ground anulus samples, and final mass weights after salt extraction.

Sample	**Initial sample weight [mg]**	**Final mass weight [mg]**
1	182.9	8.79
2	191.2	9.56

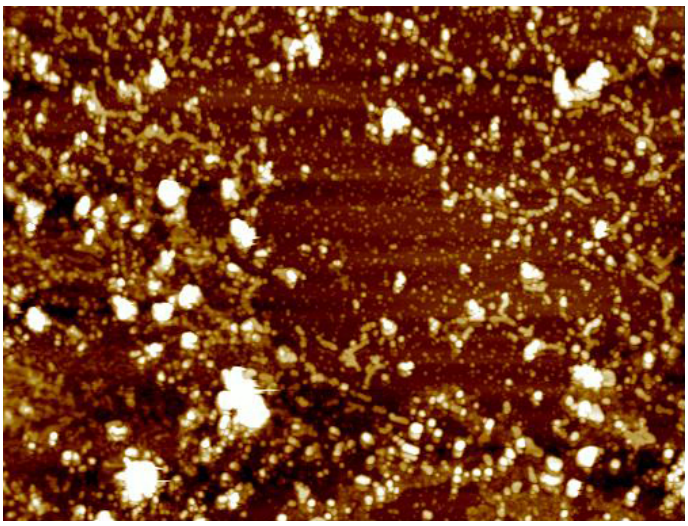

Figure D.1: AFM image of final mass showing general debris. No collagen fibrils were present.

D.4 Discussion

The neutral salt solvent method was shown to be ineffective for extracting fibrillar collagen from fresh anulus fibrosus tissue. The anulus, when fully thawed, was difficult to break down due to its fibrous, viscoelastic disposition, so to facilitate this step, the anulus was ground into a paste when it was still in a semi-frozen state.

Bushell et al. [184] used freeze-dried tissue, which would have made the tissue easier to break down and homogenise. Aladin et al. [185] used fresh tissue, but, similarly, the tissue would have been easier to homogenise due to the nucleus being non-fibrous in structure.

Despite grinding the anulus down very finely, the final protein yield was extremely small after the final centrifugation step, so it was difficult to analyse with SDS-PAGE. If collagen type I were present, one would expect bands at the alpha-1 and alpha-2 bands, corresponding to molecular weights of 139 kDa and 129 kDa, respectively. However, these could not be seen at all, and this is likely to be because the tissue was not homogenised properly at the beginning and/or the amount of unbound collagen in these samples was negligible.

The absence of collagen fibrils in the AFM image verified that the technique was not successful.

D.5 Conclusion

Though it has been used for collagen extraction from disc tissue in other studies, this attempt with neutral salt solvent was not successful, as evidenced by the lack of visible bands during SDS-PAGE analysis and the absence of collagen fibrils in the AFM image. This may have been attributable to the way in which the anulus was prepared, or the lack of unbound collagen in the tissue itself.

This unsuccessful attempt was not consequential, as an alternative method for isolating collagen fibrils was eventually devised (see Section 6.3).

D.6 Acknowledgements

The author acknowledges Dr Sharon Byers for her valuable guidance and expertise, and for allowing the use of her laboratory at The Matrix Biology Unit, The Women's and Children's Hospital.

Appendix E

MATLAB Code: Nanoscale

E.1 Nanoindentation

E.1.1 Setup File for Each Experiment

```
% Session 114A
% diana_collagen_114_human10b_A.004
% FV image

session_title = 'session114A';
RS = 500;
TT = 100;
K = 4.1731;
fibril_thickness = 83.0;
v = 0.5;
Rt = 1e-8;
coll_start = 100;

surface_threshold = 50;

% Setting path

path(path,'.\2012-09-27_collagen_114_human10b_pbs')
heightdata = importdata('height114A.txt');
path(path,'.\2012-09-27_collagen_114_human10b_pbs\
forcecurves114A')
sub = importdata('diana_collagen_114_human10b_pbs_A-BF4A-907.spm.txt'),
sub = sub.data;  \% Loading the substrate (reference) force curve
```

E.1.2 Collagen Surface Detection

```
data2 = flipud(heightdata.data);
data3 = rot90(data2, -1);
min(data3(:));
collagen = [];
mica = [];

f = 1;
g = 1;
e = 1;

while f < 1025;
    if data3(f) > surface_threshold % collagen region
        collagen(g) = f;
        g = g+1;
        whole1(f) = 10;
    else whole1(f) = 0;
    end

    if data3(f) < 0  % mica region
        mica(e) = f;
        e = e+1;
        whole2(f) = 5;
    else whole2(f) = 0;
    end

    f = f+1;
end

whole = whole1 + whole2;
check_pre = reshape(whole, 32, 32);
check = flipud(check_pre');

figure(5), imagesc(data2), axis square, caxis([0, 50]), colorbar;
H = colorbar;
title(H, 'nm', 'FontSize', 10);
set(H, 'FontSize', 10);

figure(6), imagesc(check), axis square;
```

E.1.3 Nanoindentation Plots

```
% Approach

baseline_sub_ext = mean(sub(300:305,1)); % take average value of flat region..
sub_ext = sub(coll_start:end,1)-baseline_sub_ext; % ..to normalise sub force curve.
baseline_coll_ext = mean(coll(300:305,1)); % same for collagen force curve
coll_ext = coll(coll_start:end,1)-baseline_coll_ext;

% Retract

coll_ret = coll(1:end,2)-baseline_coll_ext;
coll_ret = flipud(coll_ret);


% Adjusting COLLAGEN curve

% Approach

diff_coll_ext = diff(coll_ext); % differentiate coll curve
p = find(diff_coll_ext==min(diff_coll_ext));
% find index of minimum value of coll diff function (tip breakaway pt)
short_diff_c = coll_ext(p(1)+1:end); % plot breakaway point + 1 --> end
x_int_c = min(abs(short_diff_c-0)); % find value with modulus closest to 0
x_int_c_index = find(abs(short_diff_c)==x_int_c)+p(1)-1; % find index

% Retract

diff_coll_ret = diff(coll_ret);
pr = find(diff_coll_ret==min(diff_coll_ret));
short_diff_c_ret = coll_ret(pr(1)+1:end);
x_int_c_ret = min(abs(short_diff_c_ret-0));
x_int_c_index_ret = find(abs(short_diff_c_ret)==x_int_c_ret)+pr(1)-1;

% Adjusting SUBSTRATE curve

diff_sub_ext = diff(sub_ext); % repeat everything for substrate
q = find(diff_sub_ext==min(diff_sub_ext)); % index of min value of sub diff function
short_diff_s = sub_ext(q(1)+1:end);
x_int_s = min(abs(short_diff_s-0));
```

```
x_int_s_index = find(abs(short_diff_s)==x_int_s)+q(1)-1;

% Shifting curves so they overlap

sub_start = coll_start+(x_int_s_index - x_int_c_index);
% shift sub curve left/right so its x-int coincides with that of the coll curve

RS_temp = 512;

D = 0:511;
D1 = D*(RS_temp/512);

% Plot adjusted curves

sub_ext = sub(sub_start:end,1)-baseline_sub_ext; %new, adjusted sub_ext
figure(1), plot(D1(1:numel(sub_ext)), sub_ext, 'b', 'LineWidth', 2),
title('Deflection Vs. Separation [RS = 512]', 'FontSize', 18),
xlabel('Points', 'FontSize', 14), ylabel('Deflection [nm]', 'FontSize', 14),
grid on, hold on
figure(1), plot(D1(1:numel(coll_ext)), coll_ext, 'r', 'LineWidth', 2)

% Plot indentation (modulus) vs. separation

% Approach

force = K*coll_ext(1:end,1);
sub_final = sub_ext(x_int_c_index:end);
coll_final = coll_ext(x_int_c_index:end);
force_final = force(x_int_c_index:end);

% Retract

coll_final_ret = coll_ret(x_int_c_index_ret:end);

D1 = D*(RS/512);

figure(3), plot(D1(1:numel(sub_ext)), sub_ext, 'b', 'LineWidth', 2),
title('Deflection Vs. Separation [Proper RS]', 'FontSize', 18),
xlabel('Separation [nm]', 'FontSize', 14), ylabel('Deflection [nm]',
'FontSize', 14), grid on, hold on
```

```
figure(3), plot(D1(1:numel(coll_ext)), coll_ext, 'r', 'LineWidth', 2), hold on
legend('Substrate deflection', 'Collagen deflection');

indent_table = [];
b = numel(coll_final);

while b > 0
    coll_value_target = coll_final(b);
    match = abs(sub_final - coll_value_target);
    [where where] = min(match);
    indent = D1(b) - D1(where);
    indent_table(b,1) = indent;
    b = b-1;
end

figure(4), plot((D1(1:length(sub_final))), sub_final, 'b', 'LineWidth', 2) %sub
hold on
plot((D1(1:length(coll_final))), coll_final, 'r', 'LineWidth', 2) %coll
grid on
hold on
plot((D1(1:length(indent_table))), indent_table, 'k', 'LineWidth', 2) %indent
title('Indentation', 'FontSize', 18), xlabel('Separation [nm]', 'FontSize', 14),
ylabel('Distance [nm]', 'FontSize', 14)
legend('Substrate deflection', 'Collagen deflection', 'Indentation');

% Smoothing out indentation curve

filt_x = (1:numel(indent_table))';
filt_y = indent_table;
p = polyfit(filt_x, filt_y, 3);
warning ('off');
indent_smooth = polyval(p,filt_x); %filtered signal becomes the new indent signal
figure(4), plot((D1(1:length(indent_smooth))), indent_smooth, 'g', 'LineWidth', 1)

% Calculating Young's Modulus

youngs_mod = [];

for w = 1:length(indent_smooth)
    if indent_smooth(w) < 0 %to prevent generating imaginary numbers
```

```
        youngs_mod(w,1) = 0;
    else
        E = (3/4)*((force_final(w)*1e-9)*(1-(v^2)))/((Rt^0.5)*
        (indent_smooth(w)*1e-9)^(3/2));
        youngs_mod(w,1) = E;
    end
end

% Plotting indentation data

figure(5), plot(youngs_mod(1:end)*1e-9, 'b', 'LineWidth', 2)
grid on
hold on
title('Young''s Modulus ', 'FontSize', 18), xlabel('Points', 'FontSize', 14),
ylabel('Young''s Modulus [GPa]', 'FontSize', 14)

figure(6), plot((indent_smooth/fibril_thickness)*100, youngs_mod(1:end)*1e-9, 'b',
'LineWidth', 2)
grid on
hold on
title('Young''s Modulus ', 'FontSize', 18), xlabel('Indentation', 'FontSize', 14),
ylabel('Young''s Modulus [GPa]', 'FontSize', 14)

% Finding Young's Modulus for particular value

target_value_nm = desired_percentage*fibril_thickness/100;
margin = abs(indent_smooth - target_value_nm); %find indent value closest to target
[place place] = min(margin);

closest_value_nm = indent_smooth(place);
actual_percentage = closest_value_nm/fibril_thickness*100;
force_nN = force_final(place);
Young_GPa = youngs_mod(place)*1e-9;

nano_table = [coll_final indent_smooth force_final youngs_mod];
```

E.1.4 Nanoindentation Calculations

```
desired_percentage = 5; %i.e. 5% of fibril diameter

young_table = [];

for a = 1:numel(J)
    coll_curve = J(a)
    run(session_title)
    nanoindent_auto_2
    young_table(coll_curve,1) = Young_GPa;
    young_table(coll_curve,2) = actual_percentage;
end

nonzero = find(young_table(1:end,1));
young_table_final = [nonzero young_table(nonzero,1) young_table(nonzero,2)];

if isempty(young_table_final) == 0
    approx = find(young_table_final(1:end, 3)>desired_percentage-0.2 &
    young_table_final(1:end, 3)<desired_percentage+0.2);
    young_table_short = [young_table_final(approx,1) young_table_final(approx,2)
    young_table_final(approx,3)];
    avg_young = mean(young_table_short(1:end,2));
    std_young = std(young_table_short(1:end,2));
    min_young = min(young_table_short(1:end,2));
    max_young = max(young_table_short(1:end,2));

    display(['---------------'])
    display(['Average Young''s Modulus (taken from shortlist) = ', num2str
    (avg_young), ' GPa'])
    display(['Standard Deviation = ', num2str(std_young), ' GPa'])
    display(['Min. value = ', num2str(min_young), ' GPa'])
    display(['Max. value = ', num2str(max_young), ' GPa'])
    display(['---------------'])

else
    display(['---------------'])
    display(['No indents have reached desired percentage'])
    display(['---------------'])
end
```

E.2 Nano-Tensile Testing

E.2.1 Plot Nano-Tensile Curves

```
% TO PLOT FORCE CURVES FROM NANOSCOPE (16x16)
% (1) Obtain force curves from Nanoscope V5.30. Export raw ASCII file.
% (2) Import ASCII file into MATLAB (delimited, header 608, space). This
% file will be called 'data'.
% (3) Open 'force volume grid' Word file.
% (4) Paste in JPEG form of high resolution topographical image, resize to
% 32x32cm
% (5) Highlight regions for which you want to plot force curves. Copy.
% (6) Paste as an array into MATLAB as 'J' (i.e. J = [...]).
% (7) State ramp size (see Parameters in Nanoscope). Name this variable 'RS'.
% (8) State trigger threshold deflection (see Parameters in Nanoscope).
% Name this variable 'TT'.
% (9) State spring constant of the cantilever (see Parameters in
% Nanoscope). Name this variable 'K'.
% (10) Run this M-file.

% Sort and find dimensions of 'J'.

J = sort(J);
[X,Y] = size(J);

% Reshape matrix into single column vector.

J1 = reshape(J,X*Y,1);
A = zeros(X*Y,1);

% Create a matrix 'D1' that scales the Separation (X) axis. Uses RS.

D = 0:511;
D1 = D*(RS/512);

% Plot all selected force curves. Starts at bottom of J1, ends at top.

k = X*Y;
young = [];
```

```
while k > 0
    a = J1(k);

    baseline_ext = mean(data((2*a)+512, 420:470));
    DATA_EXT = (data((2*a)+511, 1:512))-baseline_ext;
    s_ext = (DATA_EXT(1))/TT;

    baseline_ret = mean(data((2*a)+512, 420:470));
    DATA_RET = (data((2*a)+512, 1:512))-baseline_ret;
    s_ret = (DATA_RET(1))/TT;

    plot_ext = (DATA_EXT/s_ext)*K;
    plot_ret = (DATA_RET/s_ret)*K;

    figure(1), plot(D1, plot_ext, 'b', 'LineWidth', 2), grid on,
    title('Plot of Selected Force Curves', 'FontSize', 18),
    xlabel('Z piezo displacement [nm]', 'FontSize', 16),
    ylabel('Force [nN]', 'FontSize', 16);
    hold on
    plot(D1, plot_ret, 'g', 'LineWidth', 2), legend('Extend', 'Retract');
    k = k-1;

end
```

E.2.2 Plot Force-Displacement Region from Force Curves

```
% Locating where tension starts in the force curve

difference = diff(diff(plot_ret));
[value,pre_start] = max(difference);
start = pre_start+2;

% For plotting stress vs. strain

pull = (-1)*plot_ret(1, start:512);
norm_pull = pull - pull(1);
stress = (norm_pull*(1E-9)/area)*1e-6;

ramp = zeros(1, numel(pull));
count = 1;
```

```
while count < numel(pull)+1
    ramp(count+1) = RS/512 + ramp(count);
    count = count+1;
end

strain = zeros(1, numel(pull));
count1 = 1;

while count1 < numel(pull)+1
    strain(count1) = (((sqrt((length^2) + ((ramp(count1))*1e-9)^2))-length)/length);
    count1 = count1+1;
end

% Plot

figure(10), plot(ramp(1:numel(norm_pull)), norm_pull, 'LineWidth', 2), grid on,
xlabel('Displacement [nm]', 'FontSize', 16), ylabel('Force [nN]', 'FontSize', 16)
hold on
```

Appendix F

Collagen Fibril Data: Nanoindentation

This appendix presents the full results for the nanoindentation experiments described in Chapter 7.

F.1 Nanoscale Data

Table F.1: Summary of mean Young's Modulus values for healthy and degenerate collagen fibrils in posterolateral (P), lateral (L), anterolateral (AL) and anterior (A) regions. Values highlighted in blue were flagged as potential outliers.

	YOUNG'S MODULUS [GPa]				
	PL	L	AL	A	
HEALTHY	2.54	2.57	2.61	2.65	
	2.74	2.56	2.58	2.37	
	3.11	2.64	2.12	2.19	
	2.89	2.08	2.93	2.44	
	2.51	2.76	2.48	2.13	
	2.63	2.53	2.02	3.00	
	2.45	3.02	2.68	2.94	
	2.69	**2.59**	**2.49**	**2.53**	mean
	0.24	**0.28**	**0.32**	**0.34**	SD
DEGENERATE	2.64	2.79	1.71	2.62	
	1.64	2.21	2.33	2.97	
	2.31	2.69	2.69	2.84	
	2.33	2.17	2.46	1.92	
	2.50	2.61	2.70	2.86	
	2.46	2.31	2.78	2.43	
	2.49	1.99	3.16	2.80	
	2.34	**2.40**	**2.55**	**2.63**	mean
	0.33	**0.30**	**0.45**	**0.36**	SD

F.2 Statistical Analyses

F.2.1 Tests of Assumptions

Normal Distribution (Shapiro-Wilk Test)

Table F.4: Shapiro-Wilk Test for Young's Modulus. Groups that violated this assumption ($p<0.05$) are shown in red.

Region	Degen State	Young's Modulus		
		Statistic	df	Sig.
PL	H	.919	7	.461
	D	.769	7	.020
L	H	.924	7	.499
	D	.931	7	.558
AL	H	.934	7	.590
	D	.938	7	.621
A	H	.918	7	.455
	D	.847	7	.115

Table F.5: Shapiro-Wilk Test for standardised residuals for Young's Modulus.

Region	Young's Modulus		
	Statistic	df	Sig.
PL	.933	14	.341
L	.971	14	.891
AL	.956	14	.665
A	.963	14	.775

Table F.2: Full results for E [GPa] for 7 healthy discs (H1-H7) in posterolateral (P), lateral (L), anterolateral (AL) and anterior (A) regions. Up to 30 nanoindentations were taken from each sample, which contained 3 fibrils.

	H1				H2				H3				H4				H5				H6				H7			
	PL	L	AL	A	PL	L	AL	A	PL	L	AL	A	PL	L	AL	A	PL	L	AL	A	PL	L	AL	A	PL	L	AL	A
1	0.89	0.26	0.67	0.23	0.21	0.78	0.25	0.13	0.14	0.66	0.30	0.25	0.43	0.44	0.25	0.11	0.34	1.10	0.33	0.25	0.25	0.95	0.43	0.36	0.41	0.25	0.70	0.80
2	0.91	0.41	1.19	0.27	0.22	0.81	0.34	0.43	0.45	0.78	0.63	0.50	0.85	0.45	0.27	0.29	0.59	1.11	0.36	0.46	1.21	1.38	0.71	0.51	0.56	0.39	1.17	1.18
3	0.95	0.43	1.35	1.31	0.35	0.88	0.51	0.75	0.58	0.85	0.81	0.62	0.87	0.83	0.33	0.59	0.71	1.37	0.57	0.54	1.21	1.42	0.82	0.54	0.82	0.52	1.57	1.22
4	0.97	0.45	1.38	1.42	0.60	0.90	0.52	0.77	0.65	0.91	0.83	0.68	1.31	1.13	0.75	0.92	0.77	1.59	0.62	0.76	1.25	1.55	1.11	0.75	1.10	0.66	1.58	1.24
5	1.01	0.60	2.05	1.95	0.63	0.92	0.84	0.80	0.73	1.03	0.87	0.75	1.36	1.21	0.86	1.04	0.83	1.64	0.79	0.93	1.29	1.67	1.43	0.83	1.21	0.72	1.60	1.36
6	1.18	0.81	2.07	2.04	1.00	1.02	1.01	1.09	0.79	1.25	0.95	0.80	1.54	1.28	1.14	1.11	0.88	1.69	1.20	1.01	1.34	1.67	1.51	0.88	1.27	0.95	1.78	1.57
7	1.43	0.88	2.10	2.06	1.03	1.04	1.29	1.48	1.28	1.34	1.04	1.24	1.61	1.49	1.19	1.13	1.02	1.84	1.22	1.10	1.47	1.79	1.57	0.92	1.28	1.02	2.15	1.67
8	1.43	0.92	2.19	2.26	1.21	1.09	1.61	1.62	1.80	1.37	1.07	1.71	1.65	1.96	1.26	1.40	1.12	2.17	1.33	1.23	1.52	1.88	1.63	1.13	1.52	1.14	2.23	2.26
9	1.53	1.28	2.29	2.27	1.21	1.29	1.74	1.67	1.94	1.45	1.15	1.83	1.89	2.64	1.35	1.54	1.24	2.65	1.33	1.54	1.61	1.93	1.69	1.30	1.64	1.35	2.35	2.37
10	1.57	1.71	2.37	2.59	1.30	1.35	1.77	1.78	2.23	1.73	1.43	2.09	1.93	2.69	1.79	1.64	1.76	2.68	1.64	1.67	2.37	2.02	1.73	1.37	1.72	1.45	2.51	2.42
11	1.81	1.82	2.41	2.63	1.48	1.47	2.26	1.90	2.52	1.86	1.56	2.34	2.10	2.73	2.06	1.83	1.98	2.71	1.78	1.83	2.40	2.20	1.98	1.55	1.88	1.57	2.73	2.59
12	1.82	1.94	2.52	2.75	1.48	1.63	2.36	2.13	2.91	1.92	1.62	2.69	2.18	2.76	2.11	1.93	2.01	2.73	1.90	1.93	2.46	2.29	2.18	1.66	1.97	2.01	2.80	2.74
13	2.15	2.00	2.63	2.81	1.61	1.64	2.58	2.21	3.02	2.10	1.80	2.79	2.19	2.70	2.26	2.37	2.14	2.75	2.17	2.02	2.51	2.32	2.35	1.67	2.35	2.03	2.80	2.88
14	2.25	2.01	2.74	2.82	1.73	1.66	2.68	2.23	3.02	2.11	1.81	2.79	2.28	2.79	2.63	2.38	2.22	2.75	2.30	2.12	2.59	2.35	2.42	1.69	2.36	2.13	3.26	2.89
15	2.32	2.10	2.75	2.84	1.75	2.00	3.13	2.30	3.12	2.14	1.84	2.88	2.34	3.17	2.88	2.57	2.39	3.02	2.30	2.22	2.82	2.50	2.50	1.72	2.52	2.81	3.35	2.90
16	2.45	2.50	2.77	2.93	2.38	2.18	3.40	2.44	3.42	2.46	2.16	3.15	2.36	3.33	3.30	2.57	2.31	3.13	2.44	2.43	2.83	2.61	2.78	1.94	2.53	2.47	3.43	2.92
17	2.68	2.72	2.90	2.96	2.48	2.31	3.41	2.56	3.49	2.60	2.30	3.21	2.51	3.37	3.46	2.62	2.22	3.16	2.55	2.50	2.84	2.69	2.82	2.00	2.57	2.51	3.68	2.98
18	2.89	2.73	2.92	3.02	2.69	2.32	3.48	3.19	3.64	2.63	2.33	3.35	2.65	3.55	3.60	2.63	2.43	3.29	2.69	2.67	3.20	2.96	3.17	2.14	2.83	2.61	3.68	2.98
19	2.98	2.78	3.30	3.03	2.73	2.35	3.78	3.31	3.68	3.08	2.78	3.38	2.67	3.60	3.62	3.02	2.63	3.45	2.88	2.70	3.27	3.04	3.33	2.16	2.91	2.89	3.78	3.31
20	3.19	3.27	3.44	3.08	2.99	2.88	3.90	4.07	3.75	3.18	2.88	3.44	2.74	3.84	3.65	3.18	2.82	3.49	3.12	2.71	3.30	3.04	3.47	2.18	3.05	3.08	3.80	3.39
21	3.22	3.37	3.65	3.51	3.07	3.21	3.90	4.09	3.91	3.18	2.88	3.58	2.92	3.85	3.89	3.35	2.98	3.50	3.12	2.84	3.31	3.06	3.49	2.42	3.19	3.19	3.85	3.49
22	3.39	3.44	3.77	3.62	3.23	3.33	3.98	4.38	4.17	3.34	3.04	3.81	3.15	4.00	4.10	3.55	3.11	3.60	3.30	2.86	3.39	3.16	3.51	2.54	3.36	3.22	3.92	3.59
23	3.58	4.55	3.94	3.75	3.67	3.49	4.03	4.39	4.20	3.69	3.39	3.84	3.28	4.17	4.29	3.76	3.23	3.73	3.34	2.93	3.53	3.26	3.51	2.55	3.54	3.32	4.00	3.68
24	3.63	4.90	4.11	3.81	4.29	3.53	4.16	4.52	4.21	3.73	6.19	3.85	3.30	4.20	4.72	3.96	3.37	3.82	3.62	2.97	3.80	3.34	3.60	2.80	3.72	3.34	4.17	3.77
25	3.91	4.93	4.40	4.16	4.61	3.65	4.21	5.28	4.30	3.91	6.43	3.93	3.36	4.57	4.73	4.05	3.65	4.01	3.64	3.01	3.81	3.56	3.98	3.14	3.80	3.44	4.20	3.85
26	3.97	4.95	4.48	4.29	4.75	3.85		7.21		4.16		4.02	3.43	4.71	4.75	4.20	4.40	4.10	4.01		3.86	3.89	3.99	3.63	3.92	3.45	4.52	3.89
27	4.02	5.37	4.87	5.10	5.42	4.30				4.64		4.03	3.45	4.73	5.17	4.22	4.08	4.12	4.13		3.86	3.99		4.52	3.94	3.52	5.36	4.24
28	4.03	5.63	5.82	5.14	5.64	4.89				5.43		4.03	3.69	4.79		4.30		4.16	4.19		3.89	4.09		4.89	4.31	3.66		4.53
29	4.05	6.48	5.87	5.28	5.73	8.59				5.80		4.06	5.91	4.80		5.00		4.17	5.21		3.91	4.44		5.85	4.51			4.69
30	5.84	6.92	6.32		5.77	9.64				5.85		7.08	5.95	4.90		6.01		4.43	6.45		5.41	4.44		6.18				6.70
Mean	**2.54**	**2.74**	**3.11**	**2.89**	**2.51**	**2.63**	**2.45**	**2.57**	**2.56**	**2.64**	**2.08**	**2.76**	**2.53**	**3.02**	**2.61**	**2.58**	**2.12**	**2.93**	**2.48**	**2.02**	**2.68**	**2.65**	**2.37**	**2.19**	**2.44**	**2.13**	**3.00**	**2.94**
SD	**1.26**	**1.94**	**1.40**	**1.25**	**1.76**	**2.11**	**1.37**	**1.69**	**1.39**	**1.50**	**1.52**	**1.50**	**1.25**	**1.39**	**1.55**	**1.47**	**1.12**	**0.99**	**1.47**	**0.79**	**1.15**	**0.95**	**1.06**	**1.51**	**1.17**	**1.12**	**1.14**	**1.26**

Table F.3: Full results for E [GPa] for 7 degenerate discs (D1-D7) in posterolateral (P), lateral (L), anterolateral (AL) and anterior (A) regions. Up to 30 nanoindentations were taken from each sample, which contained 3 fibrils.

	D1				D2				D3				D4				D5				D6				D7			
	PL	L	AL	A	PL	L	AL	A	PL	L	AL	A	PL	L	AL	A	PL	L	AL	A	PL	L	AL	A	PL	L	AL	A
1	0.28	0.79	0.28	0.24	0.48	0.25	0.20	0.39	0.25	0.53	0.35	0.39	0.73	0.23	0.12	0.34	0.52	0.57	0.16	0.64	0.87	0.85	0.24	0.70	0.31	1.04	0.55	0.90
2	0.98	0.83	0.36	0.40	0.55	0.26	0.79	0.71	0.36	1.04	0.55	0.49	0.98	0.45	0.22	0.43	0.59	0.71	0.48	0.65	1.18	1.19	0.46	0.87	0.44	1.16	0.69	1.12
3	1.40	0.94	0.41	0.41	0.68	0.31	1.00	0.80	0.46	1.15	0.65	0.67	1.04	0.65	0.35	0.49	0.86	0.80	0.74	1.11	1.25	1.30	0.48	0.89	0.63	1.24	0.78	1.14
4	1.59	0.96	0.45	0.47	0.79	0.55	1.22	0.98	0.67	1.50	0.66	0.83	1.09	0.72	0.45	0.53	0.96	0.82	1.41	1.36	1.30	1.37	0.49	0.93	0.73	1.46	0.88	1.30
5	1.66	0.96	0.80	0.55	0.86	0.65	1.26	1.08	0.98	1.56	0.69	0.87	1.14	0.94	0.50	0.96	1.02	0.87	1.49	1.47	1.37	1.41	0.71	1.01	0.85	1.70	0.93	1.47
6	1.77	1.05	0.82	0.59	0.97	0.95	1.27	1.24	1.12	1.64	0.90	0.87	1.22	1.06	0.54	0.97	1.04	1.06	1.55	1.65	1.46	1.73	0.73	1.23	0.93	1.91	0.96	1.52
7	1.85	1.12	0.93	0.64	1.01	0.96	1.27	1.46	1.26	1.65	1.00	1.04	1.23	1.08	0.59	1.11	1.09	1.09	1.69	1.82	1.47	1.98	0.81	1.34	0.94	1.97	1.10	1.53
8	1.88	1.18	1.15	0.67	1.06	1.13	1.28	1.53	1.32	1.79	1.05	1.05	1.24	1.13	0.62	1.16	1.37	1.17	1.93	2.01	1.49	2.02	0.84	1.75	1.18	1.99	1.14	1.91
9	2.12	1.18	1.16	1.44	1.07	1.37	1.41	1.63	1.37	1.90	1.06	1.30	1.36	1.26	0.74	1.38	1.49	1.59	2.11	2.04	1.63	2.11	1.15	1.95	1.27	2.13	1.24	2.08
10	2.19	1.23	1.23	1.46	1.08	1.37	1.71	1.73	1.38	2.12	1.35	1.30	1.38	1.30	1.02	1.46	1.73	1.70	2.34	2.06	1.65	2.14	1.24	2.11	1.32	2.17	1.54	2.14
11	2.24	1.30	1.25	1.48	1.25	1.56	1.72	1.90	1.51	2.15	1.51	1.40	1.54	1.43	1.13	1.48	1.90	1.72	2.42	2.25	1.85	2.45	1.35	2.29	1.33	2.48	2.34	2.24
12	2.31	1.36	1.61	1.48	1.26	1.67	1.85	2.14	1.67	2.20	1.73	1.41	1.58	1.48	1.22	1.62	1.92	1.74	2.68	2.26	1.90	2.61	1.42	2.42	1.53	2.79	2.34	2.33
13	2.36	1.51	2.01	1.63	1.29	1.86	2.28	2.17	1.82	2.20	1.85	1.81	1.83	1.54	1.31	2.39	2.06	1.77	2.72	2.51	2.40	2.71	1.78	2.60	1.63	3.13	2.43	2.34
14	2.38	1.51	2.43	1.65	1.31	2.12	2.43	2.36	1.95	2.25	2.15	2.04	1.03	1.73	1.45	2.69	2.34	2.10	3.04	2.61	2.51	2.73	2.81	2.69	1.71	3.48	2.49	2.40
15	2.39	1.66	2.62	2.16	1.62	2.15	2.62	2.39	2.08	2.26	2.37	2.05	2.00	1.83	1.59	3.12	2.37	2.17	3.19	2.69	2.54	2.82	2.83	2.69	1.84	3.54	2.60	2.49
16	2.50	1.69	2.65	2.37	1.73	2.35	2.63	2.76	2.25	2.42	2.46	2.18	2.10	2.01	1.66	3.15	2.42	2.17	3.32	2.98	2.56	2.85	2.92	3.04	1.92	3.54	2.69	2.65
17	2.52	1.69	2.70	2.46	1.79	2.39	2.71	3.01	2.56	2.63	2.58	2.73	2.12	2.22	1.72	3.23	2.80	2.18	3.34	3.12	2.72	2.86	4.37	3.08	2.24	3.63	3.08	2.66
18	2.57	1.71	2.88	2.50	1.95	2.79	2.79	3.05	2.65	2.82	2.74	2.87	2.33	2.23	1.84	3.44	2.80	2.36	3.35	3.18	3.13	2.92	5.13	3.11	2.85	3.71	3.13	2.66
19	2.57	1.76	2.89	2.79	2.10	3.07	2.93	3.15	2.81	2.85	2.78	4.06	2.47	2.26	1.97	3.52	2.81	2.31	3.36	3.22	3.32	2.92	5.70	3.12	2.39	3.76	3.53	2.91
20	3.14	1.81	2.96	2.91	2.56	3.11	3.32	3.22	2.89	3.19	2.92	4.76	2.61	2.38	2.02	3.60	2.91	2.61	3.44	3.24	3.36	2.98	6.89	4.51	2.43	3.81	3.64	2.97
21	3.53	1.85	3.10	3.07	2.89	3.23	3.56	3.67	3.03	3.31	3.07	4.88	2.77	2.62	2.09	3.70	2.92	2.89	3.80	3.40	3.40	3.10	6.95	4.69	2.43	3.93	3.68	3.04
22	3.55	1.95	3.11	3.24	4.69	3.30	3.57	4.47	3.22	3.41	3.15	4.96	2.80	2.62	2.21	3.99	3.06	2.94	4.08	3.40	3.50	3.33	7.26	4.72	2.52	4.02	3.89	3.30
23	3.62	2.02	3.27	3.34	5.67	3.35	3.58	4.52	3.31	3.55	3.47	5.12	2.83	2.68	2.23	4.07	3.57	3.05	4.21	3.63	3.96	3.57	7.34	5.39	2.77	4.04	4.10	3.53
24	3.75	2.03	3.35	3.41	6.94	3.36	3.85	4.64	3.47	3.78	3.74	6.10	3.12	3.17	2.39	4.31	3.79	3.12	4.39	3.76	6.15	3.60	7.38	5.42	2.96	4.29	5.44	3.86
25	3.82	2.07	3.38	3.47	7.15	3.57	3.92	4.76	3.68	3.83	3.88	6.32	3.30	3.21	2.61	5.06	3.93	4.37	4.50	3.87	6.47	3.71		5.56	3.06	4.46	5.48	4.13
26	3.82	2.16	3.68	3.54	7.29	3.62	3.97	7.29	3.88	4.00	3.95	6.39	3.75	3.54	2.73		3.94	4.46	4.56	4.17	8.07	6.99		5.64	3.41			4.28
27	3.88	2.38	4.05	3.56	7.56	3.76	5.20	8.34	4.02	4.15	4.10		5.13				4.00	4.64		4.27	8.36				3.47			4.45
28	4.03	2.72	4.42	3.75		5.89	5.32			4.24	4.12		5.39				6.57	4.71		4.37	8.60				4.72			4.89
29	4.09	2.83	4.51	5.64		6.47				4.57			6.73				6.98	5.96		4.58								5.57
30	4.35	3.06	4.84	8.64		6.51				6.14							7.02	6.23		4.94								6.23
Mean	**2.64**	**1.64**	**2.31**	**2.33**	**2.50**	**2.46**	**2.49**	**2.79**	**2.21**	**2.69**	**2.17**	**2.61**	**2.31**	**1.99**	**1.71**	**2.33**	**2.69**	**2.46**	**2.70**	**2.78**	**3.16**	**2.62**	**2.97**	**2.84**	**1.92**	**2.86**	**2.43**	**2.80**
SD	**1.02**	**0.60**	**1.36**	**1.78**	**2.33**	**1.71**	**1.32**	**1.92**	**1.04**	**1.23**	**1.23**	**1.99**	**1.45**	**0.77**	**0.60**	**1.43**	**1.75**	**1.54**	**1.25**	**1.16**	**2.27**	**1.19**	**2.64**	**1.62**	**1.06**	**1.09**	**1.45**	**1.34**

Homogeneity of Variances (Levene's Test of Equality of Error Variances)

Table F.6: Levene's Test of Equality of Error Variances for Young's Modulus.

	Young's Modulus		
Region	F	df	Sig.
PL	.055	12	**.818**
L	.736	12	**.408**
AL	.437	12	**.521**
A	.031	12	**.863**

Homogeneity of Variances of the Differences between Groups (Mauchly's Test of Sphericity)

Table F.7: Mauchly's Test of Sphericity for Young's Modulus.

	Within subjects effect	Mauchly's W	Approx. Chi-Square	df	Sig.
Young's Modulus	Region	.660	4.449	5	**.488**

F.2.2 Mixed-Factor ANOVA

Young's Modulus

Table F.8: SPSS output for mixed-factor ANOVA. Main effects of between factor (degenerative grade) is highlighted in green.

Tests of Between-Subjects Effects

Measure: Elasticity

Transformed Variable: Average

Source	Type III Sum of Squares	df	Mean Square	F	Sig.	Partial Eta Squared	Noncent. Parameter	Observed Power[a]
Intercept	357.945	1	357.945	4534.087	.000	.997	4534.087	1.000
degen_state	.136	1	.136	1.723	.214	.126	1.723	.227
Error	.947	12	.079					

a. Computed using alpha = .05

Table F.9: SPSS output for mixed-factor ANOVA. Main effects of within factor (anatomical region) and interactions are highlighted in green.

Tests of Within-Subjects Effects

Measure: Elasticity

Source		Type III Sum of Squares	df	Mean Square	F	Sig.	Partial Eta Squared	Noncent. Parameter	Observed Power[a]
Region	Sphericity Assumed	.060	3	.020	.165	.919	.014	.495	.078
	Greenhouse-Geisser	.060	2.499	.024	.165	.890	.014	.413	.075
	Huynh-Feldt	.060	3.000	.020	.165	.919	.014	.495	.078
	Lower-bound	.060	1.000	.060	.165	.692	.014	.165	.066
Region * degen_state	Sphericity Assumed	.497	3	.166	1.358	.271	.102	4.075	.330
	Greenhouse-Geisser	.497	2.499	.199	1.358	.274	.102	3.394	.298
	Huynh-Feldt	.497	3.000	.166	1.358	.271	.102	4.075	.330
	Lower-bound	.497	1.000	.497	1.358	.266	.102	1.358	.189
Error(Region)	Sphericity Assumed	4.395	36	.122					
	Greenhouse-Geisser	4.395	29.989	.147					
	Huynh-Feldt	4.395	36.000	.122					
	Lower-bound	4.395	12.000	.366					

a. Computed using alpha = .05

F.2.3 Consideration of Outliers

Table F.10: Comparison of main effects with and without outliers.

		Young's Modulus p-value {partial η^2}
Degenerative grade	Original data set	0.214 {0.126}
	Revised data set	0.565 {0.028}
Anatomical region	Original data set	0.919 {0.014}
	Revised data set	0.747 {0.033}

F.2.4 Sample Dimensions

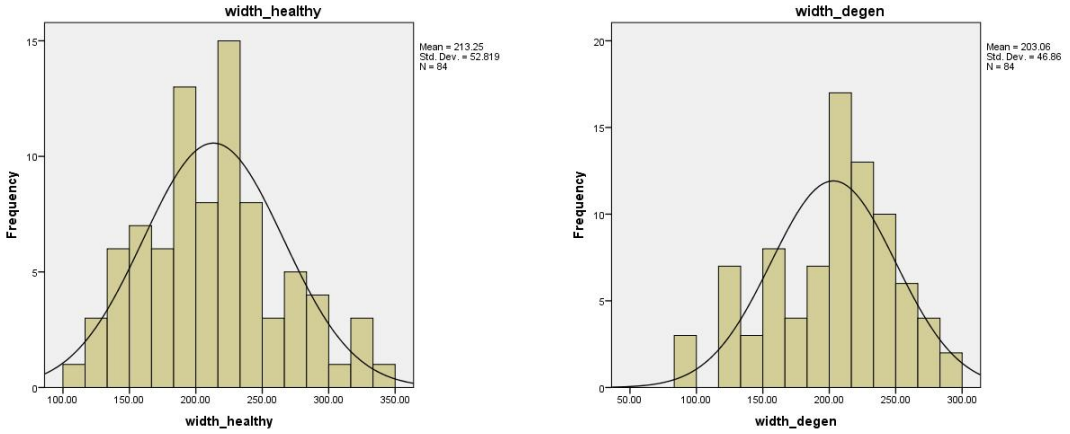

Figure F.1: Histograms for healthy (left) and degenerate (right) collagen fibril width. Measurements given in nm.

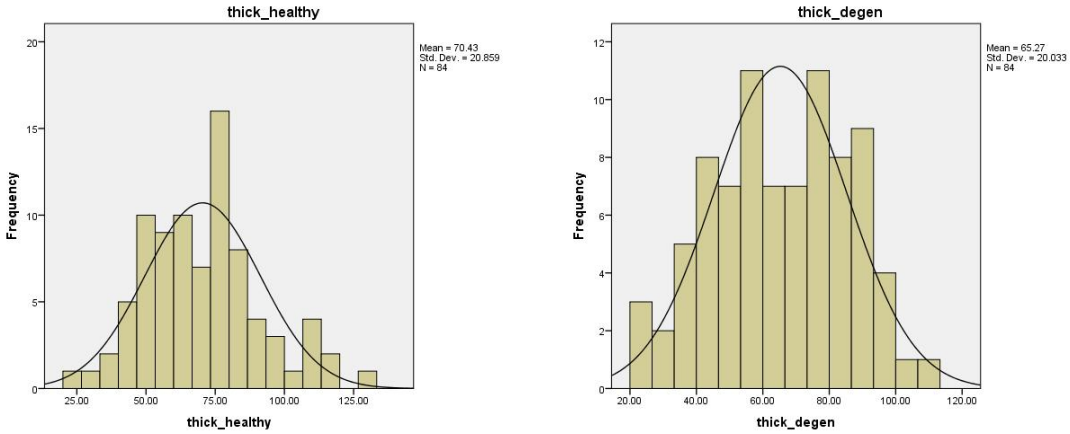

Figure F.2: Histograms for healthy (left) and degenerate (right) collagen fibril thickness. Measurements given in nm.

Table F.11: Shapiro-Wilk Test of normal distribution for fibril width and thickness.

Tests of Normality

	degen_grade	Kolmogorov-Smirnov[a] Statistic	df	Sig.	Shapiro-Wilk Statistic	df	Sig.
width	healthy	.066	84	.200*	.984	84	.376
	degen	.112	84	.011	.969	84	.039
thickness	healthy	.075	84	.200*	.979	84	.178
	degen	.075	84	.200*	.982	84	.285

*. This is a lower bound of the true significance.

a. Lilliefors Significance Correction

Tests of Normality

	region	Kolmogorov-Smirnov[a] Statistic	df	Sig.	Shapiro-Wilk Statistic	df	Sig.
width	PL	.148	42	.021	.933	42	.017
	L	.126	42	.094	.978	42	.571
	AL	.131	42	.070	.970	42	.331
	A	.075	42	.200*	.981	42	.682
thickness	PL	.073	42	.200*	.983	42	.770
	L	.148	42	.021	.949	42	.058
	AL	.111	42	.200*	.930	42	.013
	A	.105	42	.200*	.973	42	.429

*. This is a lower bound of the true significance.

a. Lilliefors Significance Correction

Table F.12: Levene's Test of Equality of Error Variances for fibril width and thickness

Levene's Test of Equality of Error Variances[a]

Dependent Variable: width

F	df1	df2	Sig.
1.279	7	160	.264

Tests the null hypothesis that the error variance of the dependent variable is equal across groups.

a. Design: Intercept + degen_grade + region + degen_grade * region

Levene's Test of Equality of Error Variances[a]

Dependent Variable: thickness

F	df1	df2	Sig.
1.769	7	160	.097

Tests the null hypothesis that the error variance of the dependent variable is equal across groups.

a. Design: Intercept + degen_grade + region + degen_grade * region

Table F.13: Two-way ANOVA examining the effects of degenerative grade and anatomical region (independent variables) on fibril width and thickness

Tests of Between-Subjects Effects

Dependent Variable: width

Source	Type III Sum of Squares	df	Mean Square	F	Sig.	Partial Eta Squared	Noncent. Parameter	Observed Power[b]
Corrected Model	26730.116[a]	7	3818.588	1.561	.151	.064	10.926	.638
Intercept	7279380.180	1	7279380.180	2975.404	.000	.949	2975.404	1.000
degen_grade	4358.467	1	4358.467	1.781	.184	.011	1.781	.264
region	6868.082	3	2289.361	.936	.425	.017	2.807	.253
degen_grade * region	15503.566	3	5167.855	2.112	.101	.038	6.337	.532
Error	391442.914	160	2446.518					
Total	7697553.210	168						
Corrected Total	418173.030	167						

a. R Squared = .064 (Adjusted R Squared = .023)

b. Computed using alpha = .05

Tests of Between-Subjects Effects

Dependent Variable: thickness

Source	Type III Sum of Squares	df	Mean Square	F	Sig.	Partial Eta Squared	Noncent. Parameter	Observed Power[b]
Corrected Model	5845.787[a]	7	835.112	2.065	.050	.083	14.457	.783
Intercept	773435.720	1	773435.720	1912.723	.000	.923	1912.723	1.000
degen_grade	1120.134	1	1120.134	2.770	.098	.017	2.770	.380
region	1155.824	3	385.275	.953	.417	.018	2.858	.257
degen_grade * region	3569.830	3	1189.943	2.943	.065	.052	8.828	.690
Error	64698.192	160	404.364					
Total	843979.700	168						
Corrected Total	70543.980	167						

a. R Squared = .083 (Adjusted R Squared = .043)

b. Computed using alpha = .05

Appendix G

Collagen Fibril Data: Nano-Tensile Testing

This appendix presents the full results for the nano-tensile testing experiments described in Chapter 8.

G.1 Unfunctionalised Tips

Table G.1: Adhesion forces (nN) for unfunctionalised AFM tips on collagen and mica.

Curve	Tip #1		Tip #2		Tip #3	
	collagen	mica	collagen	mica	collagen	mica
1	10.29	19.52	37.22	52.18	126.62	181.81
2	10.51	23.92	34.06	55.91	112.97	217.07
3	10.67	21.42	31.64	52.59	104.69	152.24
4	10.77	22.58	37.77	45.67	107.97	147.00
5	10.99	23.31	34.82	43.36	114.99	162.11
6	11.06	24.56	34.64	44.50	125.06	157.97
7	10.98	18.35	34.66	48.31	108.99	149.05
8	11.15	24.58	36.61	50.44	104.64	154.07
9	11.21	34.79	36.90	36.11	108.74	149.32
10	10.89	24.46	34.95	55.67	115.83	183.98
11	11.13	24.57	32.32	42.07	120.45	173.80
12	11.28	33.88	37.72	37.42	107.06	229.53
13	11.31	18.61	35.54	36.65	117.24	179.67
14	11.30	19.48	33.76	40.63	99.37	179.55
15	11.35	23.73	35.39	43.60	100.57	176.22
16	11.69	23.83	34.08	57.97	105.92	181.81
17	11.81	24.34	36.12	44.93	111.49	210.15
18	12.64	23.47	33.59	36.65	98.31	189.23
19	11.90	21.49	33.85	51.77	107.13	184.42
20	11.97	25.50	32.25	55.95	140.87	190.28

(continued next page)

Curve	Tip #1		Tip #2		Tip #3	
	collagen	mica	collagen	mica	collagen	mica
21	11.60	35.58	33.99	53.77	107.52	160.33
22	12.03	25.20	34.45	38.89	99.92	253.97
23	11.88	24.46	33.64	53.21	101.10	193.52
24	11.80	24.37	33.38	53.02	129.84	164.86
25	11.90	33.91	31.33	36.37	103.69	170.02
26	11.84	25.31	32.97	39.19	107.00	191.29
27	11.64	22.59	33.79	41.88	113.25	218.05
28	11.72	23.19	32.54	56.45	104.38	200.47
29	12.06	23.64	35.81	50.41	118.83	203.06
30	11.64	23.42	34.38	34.94	103.75	187.21
31	11.38	24.78	34.23	40.29	101.76	164.20
32	11.67	50.99	33.42	54.06	105.55	211.21
33	11.45	24.19	32.02	42.22	122.68	181.05
34	11.46	25.88	36.67	41.11	101.99	161.38
35	11.50	24.56	32.72	46.22	102.13	210.21
36	11.23	24.94	30.94	50.72	111.74	236.74
37	11.49	40.16	37.25	46.69	113.12	205.75
38	11.43	25.26	32.85	43.63	99.31	204.58
39	11.37	28.94	30.81	49.73	102.97	179.38
40	11.57	24.56	35.77	56.21	137.00	249.08
41	11.28	25.93	34.20	40.52	104.76	193.25
42	11.32	37.50	33.32	44.00	102.76	196.95
43	11.46	24.48	37.62	52.06	105.16	238.07
44	11.14	22.47	33.78	42.61	97.19	213.08
45	11.21	23.13	33.45	41.93	116.26	198.10
46	11.58	23.76	35.27	43.83	100.13	173.62
47	11.29	24.81	33.47	41.09	99.76	210.95
48	10.99	26.51	30.93	37.38	107.98	215.06
49	11.24	30.69	30.45	39.58	93.12	231.58
50	10.87	22.98	33.45	51.48	99.77	184.19
51	10.63	23.27	36.50	53.91	107.51	232.47
52	10.81	22.04	32.28	50.35	135.37	195.55
53	10.49	29.73	30.03	46.53	99.53	170.55
54	10.43	33.99	35.07	42.47	119.83	167.98
55	10.53	27.94	33.48	36.46	100.51	233.42
56	10.21	23.58	37.95	47.80	98.38	180.96
57	10.13	25.17	36.03	48.35	100.69	234.50
58	9.90	22.57	32.63	45.29	134.61	237.06
59	10.66	24.96	30.83	53.67	97.53	203.57
60	10.34	27.06	36.68	51.91	95.63	172.20
61	10.03	22.74	31.98	45.58	114.75	223.37
62	16.48	22.92	37.54	42.06	98.13	177.70
63	10.49	21.95	39.15	46.58	93.31	202.86
64	10.12	22.26	36.91	47.53	96.40	227.38
65	10.00	33.77	33.85	42.99	102.14	224.32
66	10.21	22.63	32.85	48.38	91.10	197.39
67	9.87	23.67	36.91	51.06	90.82	178.03
68	9.67	26.48	35.50	44.07	100.22	222.11
69	10.05	23.41	34.52	46.52	131.29	217.54
70	9.71	32.31	36.44	45.51	95.58	205.31
71	9.56	24.78	35.08	43.81	87.57	213.31
72	9.64	21.69	33.52	46.98	90.46	240.42
73	9.33	27.19	35.94	55.93	117.34	210.22
74	9.09	32.65	32.82	47.13	89.89	195.92
75	9.81	27.39	31.92	45.91	93.16	200.50
76	9.55	22.26	35.14	47.60	105.29	174.56
77	9.28	27.05	34.86	45.42	88.90	204.53
78	9.14	42.71	30.39	52.40	134.76	220.61
79	8.72	24.57	30.25	46.42	98.45	200.90
80	9.51	21.71	36.57	48.09	95.92	175.55

(continued next page)

Curve	Tip #1		Tip #2		Tip #3	
	collagen	mica	collagen	mica	collagen	mica
81	9.41	26.73	31.35	48.73	120.06	179.07
82	9.13	23.89	29.63	50.07	97.81	198.88
83	9.41	27.98	35.50	61.90	94.11	204.27
84	9.59	22.92	34.43	55.63	109.70	273.45
85	9.41	22.02	29.12	47.73	100.86	227.62
86	9.09	22.51	37.84	45.84	105.47	185.46
87	11.22	25.77	31.66	49.60	104.75	221.83
88	9.78	26.51	30.74	53.20	102.93	170.88
89	9.49	29.13	41.94	49.90	119.09	207.05
90	9.29	40.08	34.68	48.50	103.43	146.85
91	9.04	25.56	31.25	53.99	106.01	179.61
92	8.88	25.11	32.60	49.80	114.65	196.58
93	9.21	26.67	34.39	47.65	125.97	207.56
94	9.03	37.78	31.97	47.63	108.89	180.00
95	8.81	26.13	36.55	47.56	109.13	206.24
96	10.06	24.51	37.39	46.82	119.88	171.46
97	8.97	22.47	33.87	41.68	111.97	162.71
98	8.83	21.92	33.48	50.95	113.17	209.77
99	8.60	22.28	30.71	46.14	120.98	198.30
100	8.21	22.94	34.36	41.62	117.91	156.36
Mean±SD	10.6±1.2	26.0±5.3	34.1±2.4	47.0±5.7	107.7±11.6	195.8±26.3

Table G.2: Test for normal distribution for each AFM tip. P>0.05 signified normal distribution.

	Tip #1	Tip #2	Tip #3
Shapiro-Wilk significance	0.000	0.000	0.000
Normal distribution?	N	N	N

Table G.3: Test for normal distribution for collagen and mica surfaces (all three tips combined). P>0.05 signified normal distribution.

	Collagen	Mica
Shapiro-Wilk significance	0.000	0.000
Normal distribution?	N	N

G.2 Functionalised Tips

Table G.4: Adhesion forces (nN) for AFM Tip A on collagen and mica (before and after functionalisation).

Curve	**Tip A**			
	coll before	**coll after**	**mica before**	**mica after**
1	24.81	23.89	10.22	16.42
2	31.40	22.85	9.15	19.26
3	30.52	24.42	19.31	13.41
4	13.65	27.62	11.42	10.22
5	17.48	18.96	8.86	11.57
6	21.73	24.84	10.68	15.20
7	19.53	28.46	10.98	12.41
8	29.06	19.24	11.22	15.80
9	18.59	24.13	7.61	15.09
10	17.02	22.37	9.57	14.65
11	17.94	27.54	8.64	14.25
12	17.58	21.33	8.22	17.38
13	18.38	23.64	8.66	17.41
14	18.87	25.06	9.99	19.38
15	17.62	16.90	9.98	16.04
16	15.56	24.29	6.59	16.13
17	16.51	24.13	7.65	15.85
18	20.28	17.02	8.65	17.00
19	24.65	23.72	25.77	14.65
20	22.83	22.31	11.76	14.97
21	21.24	18.45	9.38	21.22
22	27.06	19.47	8.24	13.24
23	19.50	20.53	23.09	16.02
24	13.73	17.41	8.88	15.85
25	25.37	24.28	6.59	19.46
26	21.62	22.93	8.02	15.87
27	31.65	25.39	9.11	15.83
28	21.23	17.61	9.95	16.43
29	24.33	15.66	11.02	13.59
30	24.26	20.53	8.14	18.56
31	22.62	18.76	10.19	15.12
32	25.22	20.41	10.70	19.85
33	34.58	17.58	10.91	18.60
34	18.23	24.12	17.10	18.31
35	23.70	20.79	6.26	15.34
36	36.58	19.61	8.98	20.20
37	19.47	19.48	10.42	14.56
38	22.17	20.49	12.82	12.46
39	17.71	17.12	4.59	20.85
40	26.64	17.72	8.13	15.45
41	42.01	17.90	19.67	14.22
42	17.35	21.27	9.62	17.96
43	30.37	27.86	10.43	14.57
44	21.91	24.76	7.87	18.78
45	12.83	27.09	7.01	17.88
46	19.43	20.91	14.12	16.91
47	6.73	25.27	9.08	17.57
48	22.51	24.67	10.10	15.47
49	23.61	27.27	8.57	12.75
50	31.78	27.12	8.11	21.97
Mean±SD	22.4±6.5	22.1±3.5	23.5±5.2	23.2±4.2

Table G.5: Adhesion forces (nN) for AFM Tip B on collagen and mica (before and after functionalisation).

Curve	**Tip B**			
	coll before	**coll after**	**mica before**	**mica after**
1	37.13	61.31	36.73	26.30
2	40.81	63.72	29.41	20.59
3	36.86	37.63	18.93	25.78
4	32.73	29.23	17.67	23.80
5	42.21	58.87	32.37	23.23
6	37.30	35.71	30.59	21.28
7	34.28	33.23	20.97	25.62
8	39.42	56.59	24.16	28.28
9	33.96	48.42	22.95	23.22
10	39.60	32.77	30.38	26.98
11	32.51	47.26	23.20	17.35
12	38.72	27.38	14.51	25.03
13	30.89	41.75	15.27	24.79
14	23.89	37.05	19.62	22.50
15	30.35	35.61	20.21	18.01
16	22.65	38.52	18.58	24.84
17	42.60	47.88	18.00	30.02
18	33.45	30.29	26.04	28.19
19	38.71	33.77	21.75	20.74
20	29.22	47.26	23.08	12.91
21	37.02	41.53	16.13	21.80
22	29.94	23.31	18.41	22.08
23	41.75	60.34	20.43	26.00
24	35.73	39.43	22.21	33.34
25	40.50	41.47	18.59	28.48
26	31.26	54.58	28.23	22.89
27	35.66	29.53	30.49	17.30
28	41.81	29.78	26.62	22.81
29	34.61	57.29	21.88	23.85
30	37.15	49.38	23.67	27.90
31	30.41	48.20	26.55	13.28
32	35.92	52.34	30.89	17.39
33	38.12	63.47	19.66	22.55
34	32.57	50.81	15.63	21.19
35	37.40	54.44	19.15	17.26
36	37.95	56.05	24.58	21.78
37	28.06	53.91	28.14	19.34
38	36.47	60.81	19.55	22.48
39	37.67	31.71	27.02	20.96
40	34.61	52.36	19.43	21.56
41	28.09	65.46	17.66	21.09
42	27.74	35.55	24.62	23.63
43	32.70	50.16	28.88	28.77
44	37.98	44.36	28.77	26.24
45	28.06	29.70	18.68	26.88
46	39.02	49.19	27.78	26.18
47	37.31	30.08	21.47	22.94
48	29.21	26.46	29.88	24.18
49	22.93	40.57	25.55	29.31
50	29.35	43.98	28.96	17.96
Mean±SD	10.4±4.0	16.2±2.6	10.2±3.5	16.7±4.8

Table G.6: Adhesion forces (nN) for AFM Tip C on collagen and mica (before and after functionalisation).

Curve	**Tip C**			
	coll before	**coll after**	**mica before**	**mica after**
1	13.64	15.48	41.17	107.90
2	11.80	25.81	46.51	84.65
3	10.16	11.96	48.19	103.63
4	7.41	16.92	46.28	76.99
5	11.06	26.25	51.01	87.44
6	8.08	14.74	40.11	86.18
7	10.41	16.16	44.29	79.74
8	10.78	8.92	51.97	79.37
9	8.32	17.71	51.45	91.28
10	10.75	13.52	50.20	99.09
11	9.19	18.69	46.71	85.05
12	9.21	15.85	34.96	87.32
13	8.02	12.44	53.75	72.87
14	6.14	22.93	30.23	87.83
15	14.79	9.70	18.92	70.05
16	10.83	10.78	36.12	91.11
17	10.15	15.38	45.31	89.13
18	14.35	15.60	55.04	33.98
19	19.50	24.35	14.67	83.83
20	10.30	23.75	48.17	79.86
21	9.29	10.31	51.14	55.14
22	9.32	16.84	52.52	86.29
23	8.87	15.02	48.31	84.76
24	8.56	18.67	41.67	107.26
25	6.44	19.12	50.56	123.94
26	6.35	24.17	55.01	125.99
27	6.12	14.97	50.78	60.22
28	7.20	13.01	58.47	40.39
29	9.12	13.17	56.33	74.72
30	10.10	12.44	50.86	94.75
31	8.68	11.34	50.64	75.86
32	9.66	17.72	55.60	92.22
33	12.21	11.92	53.85	94.35
34	8.43	13.64	44.87	84.77
35	5.26	13.63	52.11	101.01
36	18.41	14.76	51.60	109.67
37	5.66	12.64	52.79	59.45
38	19.23	16.90	54.11	80.37
39	14.59	22.37	53.50	51.45
40	11.88	17.11	61.44	108.40
41	15.69	18.41	51.19	42.53
42	8.23	18.57	49.95	65.96
43	4.84	12.46	47.01	74.25
44	12.17	14.93	45.66	111.23
45	8.57	16.08	44.55	62.59
46	10.60	15.50	52.88	69.42
47	7.64	32.41	49.93	78.81
48	14.71	21.20	47.33	106.99
49	4.47	17.32	43.17	41.26
50	8.34	19.60	47.08	54.53
Mean±SD	34.5±5.1	44.2±11.6	47.6±8.6	81.9±21.1

Table G.7: Test for normal distribution for each AFM tip, on collagen and mica. P>0.05 signified normal distribution.

	Tip A		**Tip B**		**Tip C**	
	collagen	**mica**	**collagen**	**mica**	**collagen**	**mica**
Shapiro-Wilk significance	0.004	0.832	0.015	0.002	0.000	0.000
Normal distribution?	N	Y	N	N	N	N

Table G.8: Test for normal distribution for each AFM tip, before and after functionalisation. P>0.05 signified normal distribution.

	Tip A		**Tip B**		**Tip C**	
	before	**after**	**before**	**after**	**before**	**after**
Shapiro-Wilk significance	0.058	0.676	0.000	0.000	0.129	0.001
Normal distribution?	Y	Y	N	N	Y	N

G.3 Nano-Tensile Tests

Table G.9: Dimensions and number of successful pick-up curves for collagen fibrils. Note that cases 2 and 3 were the same fibril.

#	**Width [nm]**	**Thickness [nm]**	**Length [μm]**	**# of curves**
1	158	46	2.07	23
2	219	38	2.57	55
3	219	38	2.57	39
4	133	10	2.28	24
5	175	20	1.59	22
6	280	75	2.91	32
7	193	47	2.25	43
8	245	37	2.37	8

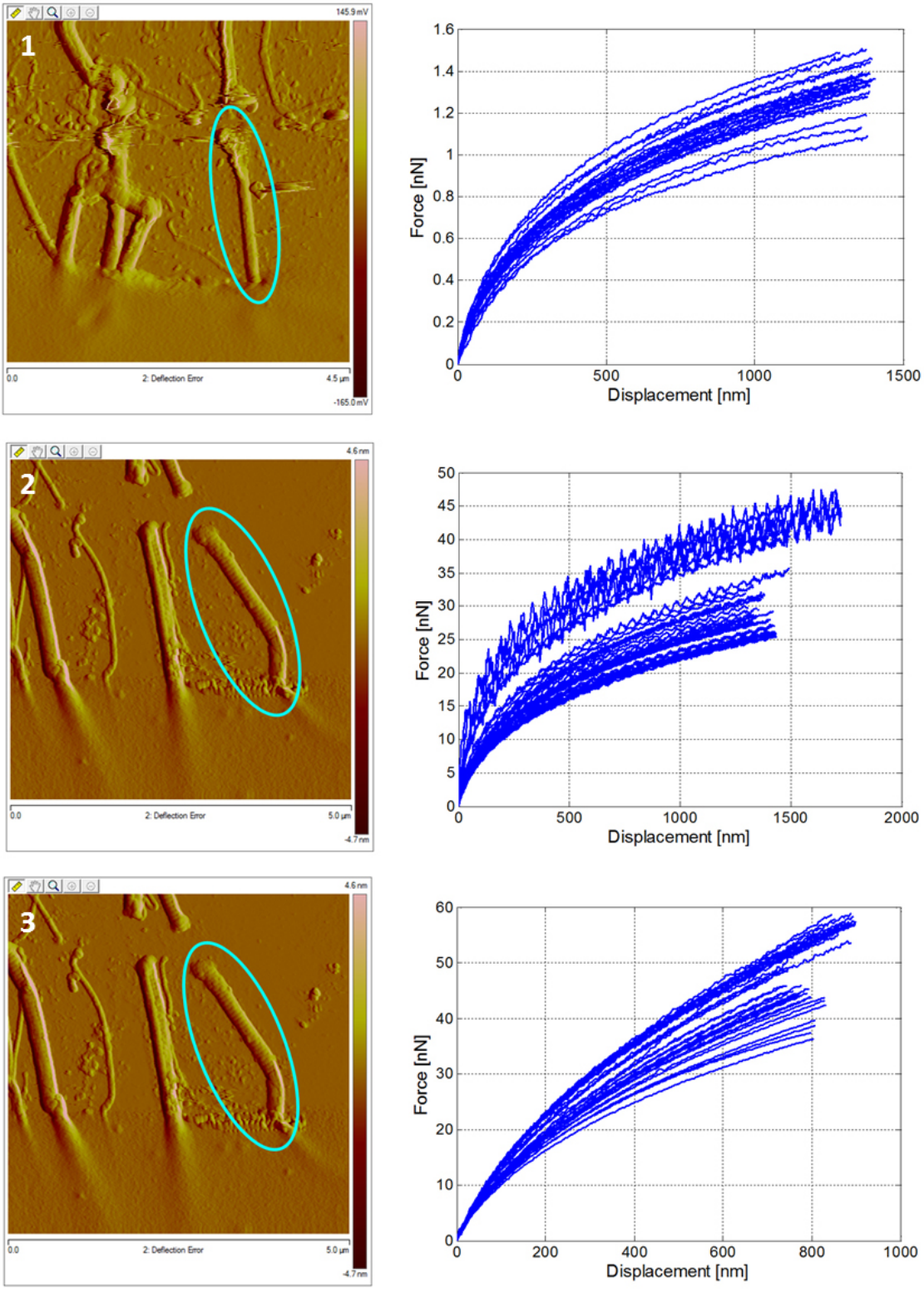

Figure G.1: Fibrils 1, 2 and 3 (from Table G.9) and their corresponding nano-tensile force curves.

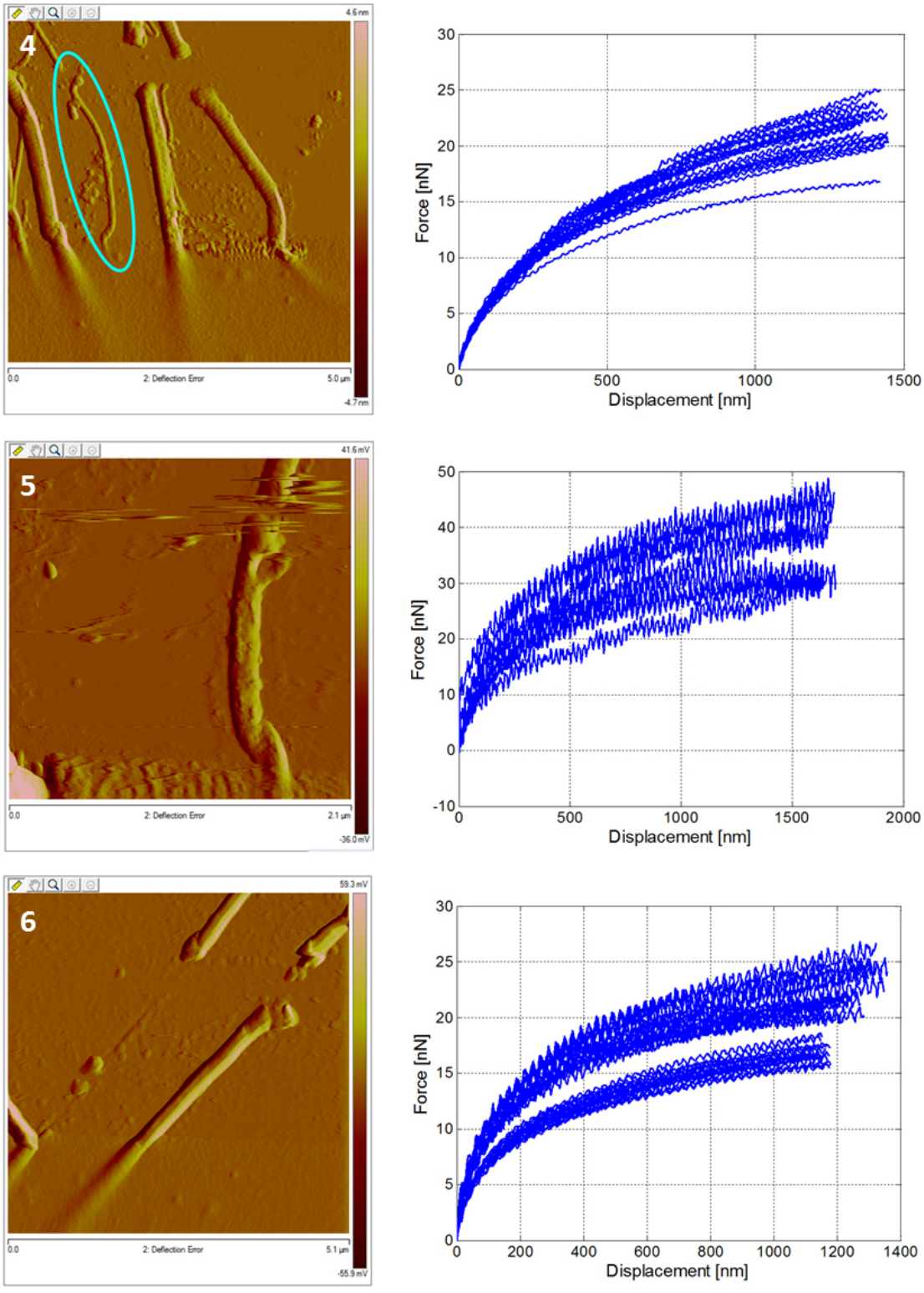

Figure G.2: Fibrils 4, 5 and 6 (from Table G.9) and their corresponding nano-tensile force curves.

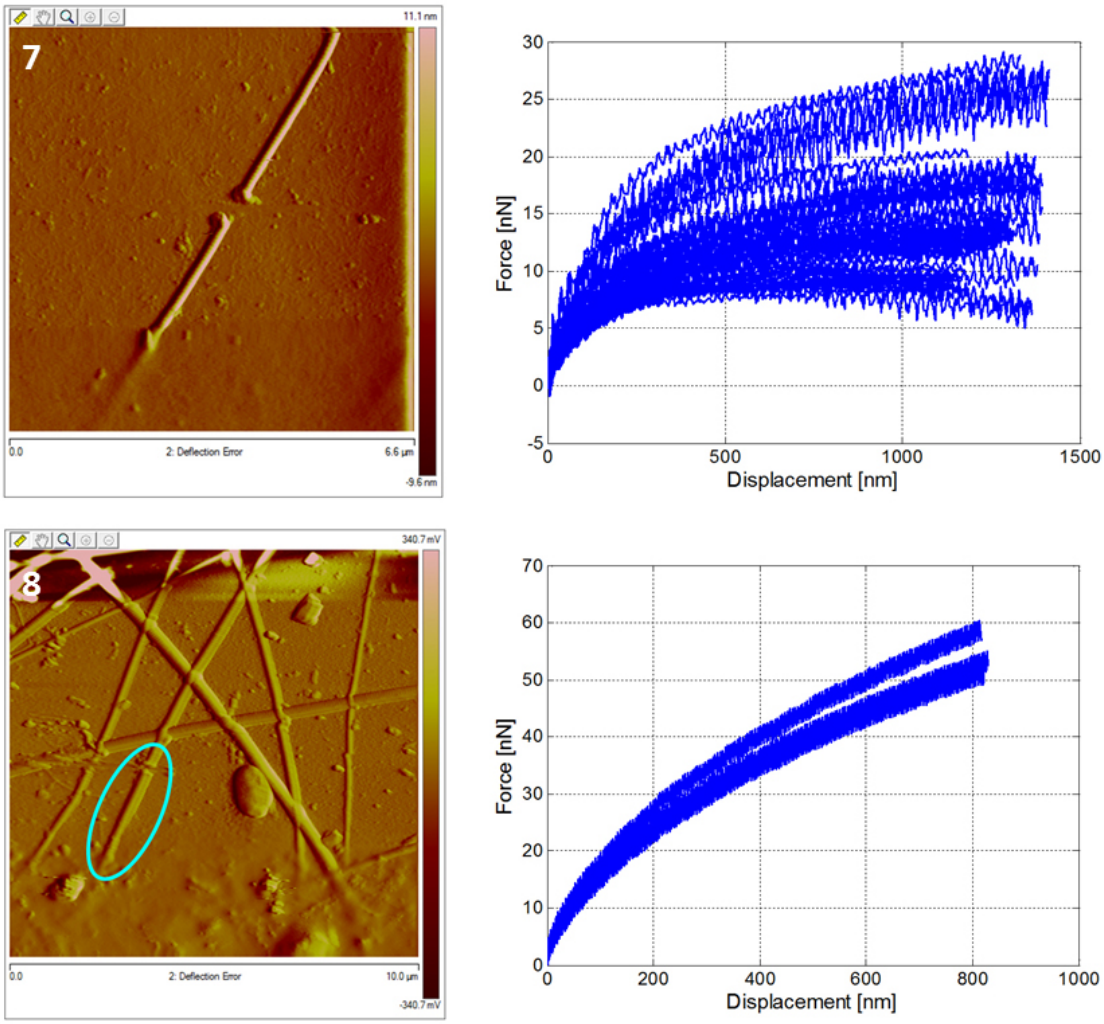

Figure G.3: Fibrils 7 and 8 (from Table G.9) and their corresponding nano-tensile force curves.

References

[1] Gille U. Vertebral column. http://en.wikipedia.org/wiki/Image:Gray_111_-_Vertebral_column-coloured.png (2006). Accessed September 2008.

[2] Bogduk N. *Clinical Anatomy of the Lumbar Spine and Sacrum*. 3rd edition. Churchill Livingstone, Edinburgh, UK (2002).

[3] Gray H. Fifth lumbar vertebra, from above. http://www.bartleby.com/107/illus94.html (2008). Accessed October 2008.

[4] Adams MA, Bogduk N, Burton K & Dolan P. *The Biomechanics of Back Pain*. Churchill Livingstone, Edinburgh, UK (2002).

[5] Ashton-Miller JA & Schultz AB. *Biomechanics of the human spine*, chapter 10, 353–393. 2nd edition. Lippincott-Raven, Philadelphia, USA (1997).

[6] Fritz JM, Erhard RE & Hagen BF. Segmental instability of the lumbar spine. *Physical Therapy* **78**(8): 889–896 (1998).

[7] Hansen L, de Zee M, Rasmussen J, Andersen TB, Wong C & Simonsen EB. Anatomy and biomechanics of the back muscles in the lumbar spine with reference to biomechanical modeling. *Spine* **31**(17): 1888–1899 (2006).

[8] Gray H. Lateral view of the vertebral column. http://www.bartleby.com/107/illus111.html (2008). Accessed October 2008.

[9] Urban JP & Roberts S. Degeneration of the intervertebral disc. *Arthritis Research and Therapy* **5**(3): 120–130 (2003).

[10] Fazzalari NL, Costi JJ, Hearn TC, Fraser RD, Vernon-Roberts B, Hutchinson J, Manthey BA, Parkinson IH & Sinclair C. Mechanical and pathologic consequences of induced concentric anular tears in an ovine model. *Spine* **26**(23): 2575–2581 (2001).

[11] Edmondston SJ & Singer KP. Thoracic spine: anatomical and biomechanical considerations for manual therapy. *Manual Therapy* **2**(3): 132–143 (1997).

[12] Pooni JS, Hukins DWL, Harris PF, Hilton RC & Davies KE. Comparison of the structure of human intervertebral discs in the cervical, thoracic and lumbar regions of the spine. *Surgical and Radiologic Anatomy* **8**(3): 175–182 (1986).

[13] Melrose J, Ghosh P & Taylor TK. A comparative analysis of the differential spatial and temporal distributions of the large (aggrecan, versican) and small (decorin, biglycan, fibromodulin) proteoglycans of the intervertebral disc. *Journal of Anatomy* **198**(1): 3–15 (2001).

[14] Hadjipavlou AG, Tzermiadianos MN, Bogduk N & Zindrick MR. The pathophysiology of disc degeneration: a critical review. *Journal of Bone and Joint Surgery (British)* **90**(10): 1261–1270 (2008).

[15] Scott JE & Thomlinson AM. The structure of interfibrillar proteoglycan bridges ('shapes modules') in extracellular matrix of fibrous connective tissues and their stability in various chemical environments. *Journal of Anatomy* **192**(3): 391–405 (1998).

[16] Marchand F & Ahmed AM. Investigation of the laminate structure of lumbar disc anulus fibrosus. *Spine* **15**(5): 402–410 (1990).

[17] Roughley PJ. Biology of intervertebral disc aging and degeneration. *Spine* **29**(23): 2691–2699 (2004).

[18] Moore RJ. The vertebral end-plate: what do we know? *European Spine Journal* **9**(2): 92–96 (2000).

[19] Costi J, Stokes I, Gardner-Morse M & Iatridis J. Frequency-dependent behavior of the intervertebral disc in response to each of six degree of freedom dynamic loading: solid phase and fluid phase contributions. *Spine* **33**(16): 1731–1738 (2008).

[20] Fratzl P. *Collagen: Structure and Mechanics*. Springer (2008).

[21] Bozec L & Horton M. Topography and mechanical properties of single molecules of type I collagen using atomic force microscopy. *Biophysical Journal* **88**(6): 4223–4231 (2005).

[22] Nimni ME. Collagen, structure and function. In *Encyclopaedia of Human Biology*, volume 2, 559–574. Academic Press, Inc., California, USA (1991).

[23] Graham JS, Vomund AN, Phillips CL & Grandbois M. Structural changes in human type I collagen fibrils investigated by force spectroscopy. *Experimental Cell Research* **299**(2): 335–342 (2004).

[24] Gutsmann T, Fantner GE, Kindt JH, Venturoni M, Danielsen S & Hansma PK. Force spectroscopy of collagen fibers to investigate their mechanical properties and structural organization. *Biophysical Journal* **86**(5): 3186–3193 (2004).

[25] Ottani V, Martini D, Franchi M, Ruggeri A & Raspanti M. Hierarchical structures in fibrillar collagens. *Micron* **33**(7-8): 587–596 (2002).

[26] Junqueira LC & Carneiro J. *Basic Histology: Text and Atlas*. 11th edition. McGraw-Hill, Inc., USA (2005).

[27] Mallery C. Collagen. `http://porpax.bio.miami.edu/~cmallery/150/physiol/40x2collagen.gif` (2007). Accessed October 2008.

[28] Kadler KE, Holmes DF, Trotter JA & Chapman JA. Collagen fibril formation. *Biochemical Journal* **316**(1): 1–11 (1996).

[29] Viidik A. Functional properties of collagenous tissues. *International Review of Connective Tissue Research* **6**: 127–215 (1973).

[30] Chen JM, Kung CE, Feairheller SH & Brown EM. An energetic evaluation of a "smith" collagen microfibril model. *Journal of Protein Chemistry* **10**(5): 535–552 (1991).

[31] Wess TJ, Hammersley AP, Wess L & Miller A. Molecular packing of type I collagen in tendon. *Journal of Molecular Biology* **275**(2): 255–267 (1998).

[32] van der Rijt JA, van der Werf KO, Bennink ML, Dijkstra PJ & Feijen J. Micromechanical testing of individual collagen fibrils. *Macromolecular Bioscience* **6**(9): 697–702 (2006).

[33] Heim AJ & Matthews WG. Determination of the elastic modulus of native collagen fibrils via radial indentation. *Applied Physics Letters* **89**(18): 181902 (2006).

[34] Eyre DR, Paz MA & Gallop PM. Cross-linking in collagen and elastin. *Annual Review of Biochemistry* **53**: 717–748 (1984).

[35] Meisenberg G & Simmons WH. *Principles of Medical Biochemistry.* Mosby Elsevier, Philadelphia (2006).

[36] Tan CI, Kent GN, Randall AG, Edmondston SJ & Singer KP. Age-related changes in collagen, pyridinoline, and deoxypyridinoline in normal human thoracic intervertebral discs. *Journal of Gerontology, Biological Sciences and Medical Sciences* **58**(5): B387–B393 (2003).

[37] Feng H, Danfelter M, Stromqvist B & Heinegard D. Extracellular matrix in disc degeneration. *Journal of Bone and Joint Surgery (American)* **88**(Suppl. 2): 25–29 (2006).

[38] Heinegard D, Aspberg A, Franzen A & Lorenzo P. Glycosylated matrix proteins. In Royce PM & Steinmann B (eds.), *Connective Tissue and its Heritable Disorders: Molecular, Genetic, and Medical aspects*, chapter 4, 271–291. Wiley-Liss, New York, USA (2002).

[39] Scott JE. Proteodermatan and proteokeratan sulfate (decorin, lumican/fibromodulin) proteins are horseshoe shaped: Implications for their interactions with collagen. *Biochemistry* **35**(27): 8795–8799 (1996).

[40] Pezowicz CA, Robertson PA & Broom ND. The structural basis of interlamellar cohesion in the intervertebral disc wall. *Journal of Anatomy* **208**(3): 317–330 (2005).

[41] Australian Bureau of Statistics. 2011-2012 ABS National Health Survey: First Results (2012).

[42] Australian Institute of Health and Welfare. Health-care expenditure on arthritis and other musculoskeletal conditions 2008-09 (2014).

[43] Walker BF, Muller R & Grant WD. Low back pain in Australian adults: the economic burden. *Asia-Pacific Journal of Public Health* **15**(2): 79–87 (2003).

[44] Guyer RD & Ohnmeiss DD. Lumbar discography. *Spine Journal* **3**(Suppl. 3): 11S–27S (2003).

[45] Luoma K, Riihimaki H, Luukkonen R, Raininko R, Viikari-Juntura E & Lamminen A. Low back pain in relation to lumbar disc degeneration. *Spine* **25**(4): 487–492 (2000).

[46] Jensen MC, Brant-Zawadzki MN, Obuchowski N, Modic MT, Malkasian D & Ross JS. Magnetic resonance imaging of the lumbar spine in people without back pain. *New England Journal of Medicine* **331**(2): 69–73 (1994).

[47] Carragee EJ, Tanner CM, Khurana S, Hayward C, Welsh J, Date E, Truong T, Rossi M & Hagle C. The rates of false-positive lumbar discography in select patients without low back symptoms. *Spine* **25**(11): 1373–1381 (2000).

[48] Carragee EJ, Don AS, Hurwitz EL, Cuellar JM, Carrino J & Herzog R. 2009 issls prize winner: does discography cause accelerated pro-

gression of degeneration changes in the lumbar disc: a ten-year matched cohort study. *Spine* **34**(21): 2338–2345 (2009).

[49] Fagan A, Moore R, Roberts B, Blumbergs P & Fraser RD. ISSLS prize winner: the innervation of the intervertebral disc: a quantitative analysis. *Spine* **28**(23): 2570–2576 (2003).

[50] Rajasekaran S, Bajaj N, Tubaki V, Kanna RM & Shetty AP. Issls prize winner: the anatomy of failure in lumbar disc herniation: an in vivo, multimodal, prospective study of 181 subjects. *Spine* **38**(17): 1491–1500 (2013).

[51] Ullrich Jnr PF. Lumbar herniated disc. `http://www.spine-health.com/conditions/herniated-disc/lumbar-herniated-disc` (2001). Accessed July 2009.

[52] Adams MA & Roughley PJ. What is intervertebral disc degeneration, and what causes it? *Spine* **31**(18): 2151–2161 (2006).

[53] Adams MA, Freeman BJ, Morrison HP, Nelson IW & Dolan P. Mechanical initiation of intervertebral disc degeneration. *Spine* **25**(13): 1625–1636 (2000).

[54] Adams MA, McNally DS & Dolan P. 'Stress' distributions inside intervertebral discs: the effects of age and degeneration. *Journal of Bone and Joint Surgery* **78B**(6): 965–972 (1996).

[55] Brinckmann P & Grootenboer H. Change of disc height, radial disc bulge, and intradiscal pressure from discectomy an in vitro investigation on human lumbar discs. *Spine* **16**(6): 641–646 (1991).

[56] Wang JC. Progressive back pain in a 26-year-old male. `http://www.spineuniverse.com/professional/case-studies/wang/progressive-back-pain-26-year-old-male` (2009). Accessed October 2009.

[57] Pfirrmann CW, Metzdorf A, Zanetti M, Hodler J & Boos N. Magnetic resonance classification of lumbar intervertebral disc degeneration. *Spine* **26**(17): 1873–1878 (2001).

[58] Haughton V. Imaging intervertebral disc degeneration. *Journal of Bone and Joint Surgery* **88**(Suppl. 2): 15–20 (2006).

[59] Martin JT, Collins CM, Ikuta K, Mauck RL, Elliott DM, Zhang Y, Anderson DG, Vaccaro AR, Albert TJ, Arlet V *et al.* Population average t2 mri maps reveal quantitative regional transformations in the degenerating rabbit intervertebral disc that vary by lumbar level. *Journal of Orthopaedic Research* **33**(1): 140–148 (2015).

[60] Nguyen AM, Johannessen W, Yoder JH, Wheaton AJ, Vresilovic EJ, Borthakur A & Elliott DM. Noninvasive quantification of human nucleus pulposus pressure with use of t1ρ-weighted magnetic resonance imaging. *Journal of Bone & Joint Surgery* **90**(4): 796–802 (2008).

[61] Thompson JP, Pearce RH, Schechter MT, Adams ME, Tsang IK & Bishop PB. Preliminary evaluation of a scheme for grading the gross morphology of the human intervertebral disc. *Spine* **15**(5): 411–415 (1990).

[62] Nachemson A. Lumbar intradiscal pressure: experimental studies on postmortem material. *Acta Orthopaedica Scandinavia Supplementum* **43**: 1–104 (1960).

[63] Mimura M, Panjabi MM, Oxland TR, Crisco JJ, Yamamoto I & Vasavada A. Disc degeneration affects the multidirectional flexibility of the lumbar spine. *Spine* **19**(12): 1371–1380 (1994).

[64] Battie MC, Videman T, Gibbons LE, Fisher LD, Manninen H & Gill K. 1995 Volvo Award in Clinical Sciences. Determinants of lumbar disc degeneration: a study relating lifetime exposures and magnetic resonance imaging findings in identical twins. *Spine* **20**(24): 2601–2612 (1995).

[65] Sambrook PN, MacGregor AJ & Spector TD. Genetic influences on cervical and lumbar disc degeneration: a magnetic resonance imaging study in twins. *Arthritis and Rheumatism* **42**(2): 366–372 (1999).

[66] Takahashi M, Haro H, Wakabayashi Y, Kawa-uchi T, Komori H & Shinomiya K. The association of degeneration of the intervertebral disc with

5a/6a polymorphism in the promoter of the human matrix metalloproteinase-3 gene. *Journal of Bone and Joint Surgery (British)* **83**(4): 491–495 (2001).

[67] Battie MC, Videman T, Kaprio J, Gibbons LE, Gill K, Manninen H, Saarela J & Peltonen L. The twin spine study: contributions to a changing view of disc degeneration. *Spine Journal* **9**(1): 47–59 (2009).

[68] Adams P & Muir H. Qualitative changes with age of proteoglycans of human lumbar discs. *Annals of the Rheumatic Diseases* **35**(4): 289–296 (1976).

[69] Holm S, Maroudas A, Urban JP, Selstam G & Nachemson A. Nutrition of the intervertebral disc: solute transport and metabolism. *Connective Tissue Research* **8**(2): 101–119 (1981).

[70] Akmal M, Kesani A, Anand B, Singh A, Wiseman M & Goodship A. Effect of nicotine on spinal disc cells: a cellular mechanism for disc degeneration. *Spine* **29**(5): 568–575 (2004).

[71] Ishihara H & Urban JP. Effects of low oxygen concentrations and metabolic inhibitors on proteoglycan and protein synthesis rates in the intervertebral disc. *Journal of Orthopaedic Research* **17**(6): 829–835 (1999).

[72] Gorth DJ, Lothstein KE, Chiaro JA, Farrell MJ, Dodge GR, Elliott DM, Malhotra NR, Mauck RL & Smith LJ. Hypoxic regulation of functional extracellular matrix elaboration by nucleus pulposus cells in long-term agarose culture. *Journal of Orthopaedic Research* **33**(5): 747–754 (2015).

[73] Miller JAA, Schmatz C & Schultz AB. Lumbar disc degeneration: correlation with age, sex, and spine level in 600 autopsy specimens. *Spine* **13**(2): 173–178 (1988).

[74] Handa T, Ishihara H, Ohshima H, Osada R, Tsuji H & Obata K. Effects of hydrostatic pressure on matrix synthesis and matrix metalloproteinase production in the human lumbar intervertebral disc. *Spine* **22**(10): 1085–1091 (1997).

[75] Iatridis JC, Mente PL, Stokes IA, Aronsson DD & Alini M. Compression-induced changes in intervertebral disc properties in a rat tail model. *Spine* **24**(10): 996–1002 (1999).

[76] Walsh AJ & Lotz JC. Biological response of the intervertebral disc to dynamic loading. *Journal of Biomechanics* **37**(3): 329–337 (2004).

[77] Farfan HF, Cossette JW, Robertson GH, Wells RV & Kraus H. The effects of torsion on the lumbar intervertebral joints: the role of torsion in the production of disc degeneration. *Journal of Bone and Joint Surgery (American)* **52**(3): 468–497 (1970).

[78] Pope MH & Hansson TH. Vibration of the spine and low back pain. *Clinical Orthopaedics and Related Research* **279**: 49–59 (1992).

[79] Bovenzi M & Zadini A. Self-reported low back symptoms in urban bus drivers exposed to whole-body vibration. *Spine* **17**(9): 1048–1059 (1992).

[80] Raj PP. Intervertebral disc: anatomy-physiology-pathophysiology-treatment. *Pain Practice* **8**(1): 18–44 (2008).

[81] Zdeblick TA. The treatment of degenerative lumbar disorders: a critical review of the literature. *Spine* **20**(Suppl. 24): 126S–137S (1995).

[82] An H, Boden SD, Kang J, Sandhu HS, Abdu W & Weinstein J. Summary statement: emerging techniques for treatment of degenerative lumbar disc disease. *Spine* **28**(Suppl. 15): S24–S25 (2003).

[83] Mirza SK & Deyo RA. Systematic review of randomized trials comparing lumbar fusion surgery to nonoperative care for treatment of chronic back pain. *Spine* **32**(7): 816–823 (2007).

[84] Andersson GB, Mekhail NA & Block JE. Treatment of intractable discogenic low back pain. A systematic review of spinal fusion and intradiscal electrothermal therapy (idet). *Pain Physician* **9**(3): 237–248 (2006).

[85] Brox JI, Reikeras O, Nygaard O, Sorensen R, Indahl A, Holm I, Keller A, Ingebrigtsen T, Grundnes O, Lange JE & Friis A. Lumbar instrumented fusion compared with cognitive intervention and exercises

in patients with chronic back pain after previous surgery for disc herniation: a prospective randomized controlled study. *Pain* **122**(1-2): 145–155 (2006).

[86] Anderson PA & Rouleau JP. Intervertebral disc arthroplasty. *Spine* **29**(23): 2779–2786 (2004).

[87] Costi JJ, Freeman BJ & Elliott DM. Intervertebral disc properties: challenges for biodevices. *Expert Review of Medical Devices* **8**(3): 357–376 (2011).

[88] Paesold G, Nerlich AG & Boos N. Biological treatment strategies for disc degeneration: potentials and shortcomings. *European Spine Journal* **16**(4): 447–468 (2007).

[89] Sobajima S, Vadala G, Shimer A, Kim JS, Gilbertson LG & Kang JD. Feasibility of a stem cell therapy for intervertebral disc degeneration. *The Spine Journal* **8**(6): 888–896 (2008).

[90] Masuda K, Oegema Jr TR & An HS. Growth factors and treatment of intervertebral disc degeneration. *Spine* **29**(23): 2757–2769 (2004).

[91] Nagae M, Ikeda T, Mikami Y, Hase H, Ozawa H, Matsuda KI, Sakamoto H, Tabata Y, Kawata M & Kubo T. Intervertebral disc regeneration using platelet-rich plasma and biodegradable gelatin hydrogel microspheres. *Tissue Engineering* **13**(1): 147–158 (2007).

[92] Nerurkar NL, Mauck RL & Elliott DM. ISSLS prize winner: Integrating theoretical and experimental methods for functional tissue engineering of the annulus fibrosus. *Spine* **33**(25): 2691–2701 (2008).

[93] Mow VC & Huiskes R. *Basic Orthopaedic Biomechanics and Mechanobiology*, chapter 5. Lippincott Williams and Wilkins (2005).

[94] Lakes R. *Viscoelastic Materials*. Cambridge University Press, New York, USA (2009).

[95] Hasan A, Ragaert K, Swieszkowski W, Selimović Š, Paul A, Camci-Unal G, Mofrad MR & Khademhosseini A. Biomechanical

properties of native and tissue engineered heart valve constructs. *Journal of Biomechanics* **47**(9): 1949–1963 (2014).

[96] Smith L, Byers S, Costi J & Fazzalari N. Elastic fibers enhance the mechanical integrity of the human lumbar anulus fibrosus in the radial direction. *Annals of Biomedical Engineering* **36**(2): 214–223 (2008).

[97] Adams P, Eyre DR & Muir H. Biochemical aspects of development and ageing of human lumbar intervertebral discs. *Rheumatology* **16**(1): 22–29 (1977).

[98] Acaroglu E, Latridis J, Setton L, Foster R, Mow V & Weidenbaum M. Degeneration and aging affect the tensile behavior of human lumbar anulus fibrosus. *Spine* **20**(24): 2690–2701 (1995).

[99] Ebara S, Iatridis JC, Setton LA, Foster RJ, Mow VC & Weidenbaum M. Tensile properties of nondegenerate human lumbar anulus fibrosus. *Spine* **21**(4): 452–461 (1996).

[100] Elliott DM & Setton LA. Anisotropic and inhomogeneous tensile behavior of the human anulus fibrosus: experimental measurement and material model predictions. *Journal of Biomechanical Engineering* **123**(3): 256–263 (2001).

[101] Fujita Y, Duncan N & Lotz J. Radial tensile properties of the lumbar annulus fibrosus are site and degeneration dependent. *Journal of Orthopaedic Research* **15**(6): 814–819 (1997).

[102] Guerin HAL & Elliott DM. Degeneration affects the fiber reorientation of human annulus fibrosus under tensile load. *Journal of Biomechanics* **39**(8): 1410–1418 (2006).

[103] O'Connell GD, Guerin HL & Elliott DM. Theoretical and uniaxial experimental evaluation of human annulus fibrosus degeneration. *Journal of Biomechanical Engineering* **131**(11): 111007 (2009).

[104] Wagner DR & Lotz JC. Theoretical model and experimental results for the

nonlinear elastic behavior of human annulus fibrosus. *Journal of orthopaedic research* **22**(4): 901–909 (2004).

[105] Skrzypiec D, Tarala M, Pollintine P, Dolan P & Adams MA. When are intervertebral discs stronger than their adjacent vertebrae? *Spine* **32**(22): 2455–2461 (2007).

[106] Gregory D & Callaghan J. An examination of the influence of strain rate on subfailure mechanical properties of the annulus fibrosus. *Journal of Biomechanical Engineering* **132**(9): 091010 (2010).

[107] Gregory D & Callaghan J. A comparison of uniaxial and biaxial mechanical properties of the annulus fibrosus: a porcine model. *Journal of Biomechanical Engineering* **133**: 0245031–0245035 (2011).

[108] Tsuji H, Hirano N, Ohshima H, Ishihara H, Terahata N & Motoe T. Structural variation of the anterior and posterior anulus fibrosus in the development of human lumbar intervertebral disc: a risk factor for intervertebral disc rupture. *Spine* **18**(2): 204–210 (1993).

[109] Pezowicz C. Analysis of selected mechanical properties of intervertebral disc annulus fibrosus in macro and microscopic scale. *Journal of Theoretical and Applied Mechanics* **48**(4): 917–932 (2010).

[110] Adams M & Green T. Tensile properties of the annulus fibrosus: I. the contribution of fibre-matrix interactions to tensile stiffness and strength. *European Spine Journal* **2**(4): 203–208 (1993).

[111] Pezowicz CA, Robertson PA & Broom ND. The structural basis of interlamellar cohesion in the intervertebral disc wall. *Journal of Anatomy* **208**(3): 317–330 (2006).

[112] Sen S, Jacobs NT, Boxberger JI & Elliott DM. Human annulus fibrosus dynamic tensile modulus increases with degeneration. *Mechanics of Materials* **44**: 93–98 (2012).

[113] Holzapfel GA, Schulze-Bauer CAJ, Feigl G & Regitnig P. Single

lamellar mechanics of the human lumbar anulus fibrosus. *Biomechanics and Modeling in Mechanobiology* **3**(3): 125–140 (2005).

[114] Skaggs DL & Weidenbaum M. Regional variation in tensile properties and biochemical composition of the human lumbar anulus fibrosus. *Spine* **19**(12): 1310–1319 (1994).

[115] Callaghan JP & McGill SM. Frozen storage increases the ultimate compressive load of porcine vertebrae. *Journal of Orthopaedic Research* **13**(5): 809–812 (1995).

[116] Panjabi MM, Krag M, Summers D & Videman T. Biomechanical time-tolerance of fresh cadaveric human spine specimens. *Journal of Orthopaedic Research* **3**(3): 292–300 (1985).

[117] Smeathers J & Joanes D. Dynamic compressive properties of human lumbar intervertebral joints: a comparison between fresh and thawed specimens. *Journal of Biomechanics* **21**(5): 425–433 (1988).

[118] Thomas S & Pothan LA. *Natural Fibre Reinforced Polymer Composites: From Macro to Nanoscale*. Archives Contemporaines, Paris, France (2009).

[119] Woo SY, Gomez M & Akeson W. The time and history-dependent viscoelastic properties of the canine medial collateral ligament. *Journal of Biomechanical Engineering* **103**(4): 293–298 (1981).

[120] Woo SL, Debski RE, Withrow JD & Janaushek MA. Biomechanics of knee ligaments. *American Journal of Sports Medicine* **27**(4): 533–543 (1999).

[121] Schönherr E, Witsch-Prehm P, Harrach B, Robenek H, Rauterberg J & Kresse H. Interaction of biglycan with type I collagen. *Journal of Biological Chemistry* **270**(6): 2776–2783 (1995).

[122] Yang L. *Mechanical properties of collagen fibrils and elastic fibers explored by AFM*. Ph.D. thesis, University of Twente, Enschede, The Netherlands (2008).

[123] Yang L, van der Werf K, Dijkstra P, Feijen J & Bennink M. Micromechanical analysis of native and cross-linked collagen type i fibrils sup-

ports the existence of microfibrils. *Journal of the Mechanical Behavior of Biomedical Materials* **6**: 148–158 (2012).

[124] Heim AJ, Koob TJ & Matthews WG. Low strain nanomechanics of collagen fibrils. *Biomacromolecules* **8**(11): 3298–3301 (2007).

[125] Yang L, van der Werf KO, Koopman BF, Subramaniam V, Bennink ML, Dijkstra PJ & Feijen J. Micromechanical bending of single collagen fibrils using atomic force microscopy. *Journal of Biomedical Materials Research, Part A* **82**(1): 160–168 (2007).

[126] Grant CA, Brockwell DJ, Radford SE & Thomson NH. Tuning the elastic modulus of hydrated collagen fibrils. *Biophysical Journal* **97**(11): 2985–2992 (2009).

[127] Strasser S, Zink A, Janko M, Heckl WM & Thalhammer S. Structural investigations on native collagen type I fibrils using AFM. *Biochemical and Biophysical Research Communications* **354**(1): 27–32 (2007).

[128] Wenger MP, Bozec L, Horton MA & Mesquida P. Mechanical properties of collagen fibrils. *Biophysical Journal* **93**(4): 1255–1263 (2007).

[129] Bella J, Brodsky B & Berman HM. Hydration structure of a collagen peptide. *Structure* **3**(9): 893–906 (1995).

[130] Svensson RB, Hassenkam T, Hansen P & Peter Magnusson S. Viscoelastic behavior of discrete human collagen fibrils. *Journal of the Mechanical Behavior of Biomedical Materials* **3**(1): 112–115 (2010).

[131] Eppell SJ, Smith BN, Kahn H & Ballarini R. Nano measurements with micro-devices: mechanical properties of hydrated collagen fibrils. *Journal of the Royal Society Interface* **3**(6): 117–121 (2006).

[132] Shen ZL, Kahn H, Ballarini R & Eppell SJ. Viscoelastic properties of isolated collagen fibrils. *Biophysical Journal* **100**(12): 3008–3015 (2011).

[133] Hertz H. On the contact of elastic solids. *Journal fuer die Reine und Angewandte Mathematik* **92**: 156–171 (1881).

[134] Mahaffy R, Shih C, MacKintosh F & Käs J. Scanning probe-based frequency-dependent microrheology of polymer gels and biological cells. *Physical Review Letters* **85**(4): 880–883 (2000).

[135] Radmacher M. Measuring the elastic properties of living cells by the atomic force microscope. *Methods in Cell Biology* **68**: 67–90 (2002).

[136] Johnson K, Kendall K & Roberts A. Surface energy and the contact of elastic solids. *Proceedings of the Royal Society of London Series A: Mathematical and Physical Sciences* **324**(1558): 301–313 (1971).

[137] Oliver WC & Pharr GM. Improved technique for determining hardness and elastic modulus using load and displacement sensing indentation experiments. *Journal of Materials Research* **7**(6): 1564–1583 (1992).

[138] Lewis NT, Hussain MA & Mao JJ. Investigation of nano-mechanical properties of annulus fibrosus using atomic force microscopy. *Micron* **39**(7): 1008–1019 (2008).

[139] Kinnear PR & Gray CD. *PASW Statistics 17 Made Simple*. Psychology Press, Hove, NY (2010).

[140] Iatridis JC, MacLean JJ, O'Brien M & Stokes IA. Measurements of proteoglycan and water content distribution in human lumbar intervertebral discs. *Spine* **32**(14): 1493–1497 (2007).

[141] Smith LJ & Fazzalari NL. Regional variations in the density and arrangement of elastic fibres in the anulus fibrosus of the human lumbar disc. *Journal of Anatomy* **209**(3): 359–367 (2006).

[142] Stokes IA. Surface strain on human intervertebral discs. *Journal of Orthopaedic Research* **5**(3): 348–355 (1987).

[143] Green T, Adams M & Dolan P. Tensile properties of the annulus fibrosus: Ii. ultimate tensile strength and fatigue life. *European Spine Journal* **2**(4): 209–214 (1993).

[144] Hirsch C, Paulson S, Sylvén B & Snellman O. Biophysical and physiological investigations on cartilage and other mesenchymal tissues vi. characteristics of human nuclei pulposi during aging. *Acta Orthopaedica* **22**(1-4): 175–183 (1952).

[145] Naylor A, Happey F & Macrae T. The collagenous changes in the intervertebral disk with age and their effect on its elasticity. *British Medical Journal* **2**(4887): 570 (1954).

[146] Johannessen W & Elliott DM. Effects of degeneration on the biphasic material properties of human nucleus pulposus in confined compression. *Spine* **30**(24): E724–E729 (2005).

[147] Taylor DC, Dalton JD, Seaber AV, Garrett WE *et al.* Viscoelastic properties of muscle-tendon units the biomechanical effects of stretching. *American Journal of Sports Medicine* **18**(3): 300–309 (1990).

[148] Faul F, Erdfelder E, Buchner A & Lang AG. G*power 3: A flexible statistical power analysis program for the social, behavioral, and biomedical sciences. *Behavior Research Methods* **39**(2): 175–191 (2007).

[149] Szczesny SE & Elliott DM. Interfibrillar shear stress is the loading mechanism of collagen fibrils in tendon. *Acta Biomaterialia* **10**(6): 2582–2590 (2014).

[150] Schroeder Y, Wilson W, Huyghe J & Baaijens F. Osmoviscoelastic finite element model of the intervertebral disc. *European Spine Journal* **15**(Suppl. 3): S361–S371 (2006).

[151] Little J, Adam C, Evans J, Pettet G & Pearcy M. Nonlinear finite element analysis of anular lesions in the L4/5 intervertebral disc. *Journal of Biomechanics* **40**(12): 2744–2751 (2007).

[152] Lu Y, Hutton W & Gharpuray V. Do bending, twisting, and diurnal fluid changes in the disc affect the propensity to prolapse? a viscoelastic finite element model. *Spine* **21**(22): 2570–2579 (1996).

[153] Silver FH, Ebrahimi A & Snowhill PB. Viscoelastic properties of self-assembled type i collagen fibers: molecular basis of elastic and viscous behaviors. *Connective Tissue Research* **43**(4): 569–580 (2002).

[154] Bruker Corporation. *MultiMode 8 Instruction Manual* (2010).

[155] Khulbe KC, Feng CY & Matsuura T. *Synthetic polymeric membranes: characterization by atomic force microscopy*. Springer, Berlin (2008).

[156] Bruker Corporation. OTR8-10 tip specifications. `http://www.brukerafmprobes.com/p-3438-otr8-10.aspx` (2013). Accessed July 2013.

[157] Bruker Corporation. SNL-10 tip specifications. `http://www.brukerafmprobes.com/p-3693-snl-10.aspx` (2013). Accessed July 2013.

[158] Bruker Corporation. FMV tip specifications. `https://www.brukerafmprobes.com/Product.aspx?ProductID=3268` (2013). Accessed July 2013.

[159] MikroMasch. NSC15 tip specifications. `http://www.spmtips.com/afm-tip-hq-nsc15-al-bs` (2013). Accessed July 2013.

[160] Cappella B & Dietler G. Force-distance curves by atomic force microscopy. *Surface Science Reports* **34**(1-3): 1–104 (1999).

[161] Heinz WF, A-Hassn E, Hoh JH & Serry F. Applications of force volume imaing with atomic force microscopes. Technical report, Bruker Corporation, Billerica, USA (2004).

[162] Greaves GN, Greer A, Lakes R & Rouxel T. Poisson's ratio and modern materials. *Nature Materials* **10**(11): 823–837 (2011).

[163] Fung YC. *Biomechanics: Mechanical Properties of Living Tissues*. Springer, New York (2010).

[164] Vogel A, Holbrook K, Steinmann B, Gitzelmann R & Byers P. Abnormal collagen fibril structure in the gravis form (type i) of ehlers-danlos syndrome. *Laboratory Investigation: A Journal of Technical Methods and Pathology* **40**(2): 201–206 (1979).

[165] Wenstrup RJ, Murad S & Pinnell SR. Ehlers-danlos syndrome type vi: clinical manifestations of collagen lysyl hydroxylase deficiency. *Journal of Pediatrics* **115**(3): 405–409 (1989).

[166] Hausser I & Anton-Lamprecht I. Differential ultrastructural aberrations of collagen fibrils in ehlers-danlos syndrome types i-iv as a means of diagnostics and classification. *Human Genetics* **93**(4): 394–407 (1994).

[167] Danielson KG, Baribault H, Holmes DF, Graham H, Kadler KE & Iozzo RV. Targeted disruption of decorin leads to abnormal collagen fibril morphology and skin fragility. *Journal of Cell Biology* **136**(3): 729–743 (1997).

[168] Morgan K. What do anti-collagen antibodies mean? *Annals of the Rheumatic Diseases* **49**(1): 62–65 (1990).

[169] Haugland RP & You WW. Coupling of antibodies with biotin. In McMahon RJ (ed.), *Avidin-Biotin Interactions*, 13–23. Humana Press, New York, USA (2008).

[170] Florin EL, Moy VT & Gaub HE. Adhesion forces between individual ligand-receptor pairs. *Science* **264**(5157): 415–417 (1994).

[171] Lo YS, Huefner ND, Chan WS, Stevens F, Harris JM & Beebe TP. Specific interactions between biotin and avidin studied by atomic force microscopy using the Poisson Statistical Analysis method. *Langmuir* **15**(4): 1373–1382 (1999).

[172] Moy VT, Florin EL & Gaub HE. Adhesive forces between ligand and receptor measured by afm. *Colloids and Surfaces A: Physicochemical and Engineering Aspects* **93**: 343–348 (1994).

[173] Yuan C, Chen A, Kolb P & Moy VT. Energy landscape of streptavidin-biotin complexes measured by atomic force microscopy. *Biochemistry* **39**(33): 10219–10223 (2000).

[174] Dupres V, Verbelen C & Dufrene YF. Probing molecular recognition sites on biosurfaces using AFM. *Biomaterials* **28**(15): 2393–2402 (2007).

[175] Maslova M, Gerasimova L & Forsling W. Surface properties of cleaved mica. *Colloid Journal* **66**(3): 322–328 (2004).

[176] Relini A, Canale C, De Stefano S, Rolandi R, Giorgetti S, Stoppini M, Rossi A, Fogolari F, Corazza A, Esposito G *et al.* Collagen plays an active role in the aggregation of β2-microglobulin under physiopathological conditions of dialysis-related amyloidosis. *Journal of Biological Chemistry* **281**(24): 16521–16529 (2006).

[177] Browning-Kelley ME, Wadu-Mesthrige K, Hari V & Liu GY. Atomic force microscopic study of specific antigen/antibody binding. *Langmuir* **13**(2): 343–350 (1997).

[178] Hutter JL & Bechhoefer J. Calibration of atomic-force microscope tips. *Review of Scientific Instruments* **64**: 1868–1873 (1993).

[179] Serry F. Improving the accuracy of AFM measurements: the thermal tune solution to the cantilever spring constant problem. Technical report, Bruker Corporation, Billerica, USA (2010).

[180] Sader JE, Chon JW & Mulvaney P. Calibration of rectangular atomic force microscope cantilevers. *Review of Scientific Instruments* **70**: 3967–3969 (1999).

[181] Sader J. AFM cantilevers: Calibration method of Sader. `http://www.ampc.ms.unimelb.edu.au/afm/calibration.html` (2012). Accessed November 2011.

[182] Miller EJ & Kent Rhodes R. *Preparation and characterization of the different types of collagen*, volume 82, 33–64. Academic Press (1982).

[183] Wnek G & Bowlin G. *Encyclopedia of Biomaterials and Biomedical Engineering*, volume 1. Marcel Dekker AG (2008).

[184] Bushell GR, Ghosh P, Taylor TK & Sutherland JM. The collagen of the intervertebral disc in adolescent idiopathic scoliosis. *Journal of Bone and Joint Surgery (British)* **61**(4): 501–508 (1979).

[185] Aladin DM, Cheung KM, Ngan AH, Chan D, Leung VY, Lim CT, Luk KD & Lu WW. Nanostructure of collagen fibrils in human nucleus pulposus and its correlation with macroscale tissue mechanics. *Journal of Orthopaedic Research* **28**(4): 497–502 (2009).